FERMILAB-THESIS-2024-06

ANGULAR DISTRIBUTION OF DIMUONS FROM DRELL-YAN PRODUCTION IN P+FE INTERACTIONS AT 120 GEV BEAM ENERGY

BY

MD FORHAD HOSSAIN, B.S., M.S.

A dissertation submitted to the Graduate School
in partial fulfillment of the requirements
for the degree
Doctor of Philosophy

Major: Physics

NEW MEXICO STATE UNIVERSITY
LAS CRUCES, NEW MEXICO
May 2024

Md Forhad Hossain

Candidate

Physics

Major

This Dissertation is approved on behalf of the faculty of New Mexico State University, and it is acceptable in quality and form for publication:

Approved by the Dissertation Committee:

Dr. Stephen Pate

Chairperson

Dr. Vassili Papavassiliou

Committee Member

Dr. Matthew Sievert

Committee Member

Dr. Andreas Gross

Dean's Representative

ACKNOWLEDGMENTS

I am profoundly grateful for the privilege of having Dr. Stephen Pate, an exceptional professor, as my advisor. Thank you for teaching me what it takes to be a good researcher. His constant support, encouragement, and guidance have been instrumental in shaping my personal and professional growth. Dr. Pate consistently ensured that I received the necessary support throughout my Ph.D. journey. I am particularly thankful to him for frequently visiting Fermilab, despite his teaching duties. These visits provided valuable opportunities to learn from him and work on detector and trigger-related tasks, as well as to discuss numerous physics projects that I have been engaged in throughout my Ph.D. journey. I also thank him for being a very kind person and a great listener. I want to thank another very talented professor, Dr. Vassili Papavassiliou, who provided invaluable advice on numerous E906/SeaQuest and E1039/SpinQuest projects. His questions in the NMSU weekly meetings were challenging at times, but they were crucial in deepening my understanding of the physics problems I was addressing. I would like to thank Dr. Matthew Sievert and Dr. Andreas Gross for serving on my PhD committee and for their time.

Thank you very much to the E906/SeaQuest Collaborators for welcoming me and our NMSU group. This opportunity has allowed me to work on my Ph.D. dissertation project. The weekly Tuesday meetings were very productive; I received many great suggestions that helped me understand the physics I was working with or resolve analysis issues. Special thanks to Dr. Paul Reimer, Dr. Donald Geesaman, Dr. Jen-Chieh Peng, Dr. Toshi-Aki Shibata, and Dr. Arun Tadepalli for their invaluable assistance. Additionally, I am grateful to Dr. Dustin Keller, Dr. Kun Liu, and the E1039/SpinQuest collaboration for allowing me to participate

in the E1039/SpinQuest projects. Although my Ph.D. thesis is based on E906/SeaQuest, the similar analysis framework and spectrometer in E1039/SpinQuest helped me quickly adapt to new analyses in E906/SeaQuest.

When I first came to Fermilab for the SpinQuest project in 2018, Dr. Chuck Brown and Dr. Rick Tesarek provided me with a deeper understanding of the NIM and CAMAC electronics-based trigger systems, as well as essential details about the hodoscopes. I was fortunate to spend a significant amount of time with Dr. Brown at the NM4 building, learning from him throughout the day. I have also learned a great deal from Andrew Chen about the DAQ system.

I must thank Dr. Kenichi Nakano, who made my Ph.D. life easier by providing me with extensive, module-based analysis code. I believe this has made me more efficient. I have completed many projects with him and learned a great deal. I appreciate his help, as he was always willing to assist me whenever I needed any computational support. The same goes for Dr. Haiwang Yu, with whom I worked at the very beginning of my Ph.D. projects. Thank you, Dr. Nakano and Dr. Yu, for frequently reviewing my code.

During the later stages of my Ph.D., I extensively discussed the physics related to my dissertation with Dr. Abinash Pun. As the analysis of angular distributions from the dump data proved challenging, we discussed daily how to tackle unfolding, acceptance correction, and the event mixing method for E906/SeaQuest. I learned a great deal from him during this time. I will miss his frequent dinner invitations where he cooked very delicious dumplings.

I want to thank Dinupa for working with me on numerous trigger and hodoscope-related problems. He was always there to fix any detector issues and to cross-check some of my Ph.D. analysis results. Thanks also for taking on a lot of responsibility for the hodoscope

system, allowing me to focus on writing my Ph.D. dissertation.

I have learned a lot from Dr. Kei Nagai, especially regarding the E906/SeaQuest simulation framework. His advice on analysis, particularly on event selections and the acceptance correction method, has been very helpful in understanding the analysis chain for angular distributions.

I want to thank Hugo, Noah, Nuwan, Helen, Harsha, Zong-Wei, Ishara, Vibodha, Zulkaida, Anchit, and Waqar for the good times during the E1039/SpinQuest Experiment. Special appreciation goes to Minuddin, Tomal, and Samantha from the NMSU Graduate School. I am particularly grateful to Minuddin, with whom I have spent countless hours preparing for qualifying exams and completing homework.

Finally, I am deeply grateful for the profound emotional support and dedication my parents, Nilufa Yeasmin and Jahangir Alom, have shown. Words can't express my appreciation for my mother's unwavering support in the face of adversity. Nadia, my wife, has also been a constant source of strength during this time. Thank you all for being on this journey with me.

VITA

2012 B.S., Jagannath University, Dhaka, Bangladesh

2014 M.S., Jagannath University, Dhaka, Bangladesh

2021 M.S., New Mexico State University, Las Cruces, New Mexico

PUBLICATIONS

1. M.F. Hossain et al. Angular distribution of Drell-Yan muon pairs produced in proton-iron interactions with a 120 GeV proton beam at SeaQuest. (To be soon submitted to Physical Review Letters.)

2. Stephen Pate et al. Estimation of Combinatoric Background in SeaQuest using an Event-Mixing Method. 2023. arXiv:2302.04152, DOI 10.1088/1748-0221/18/10/P10032

3. Andrew Chen et al. Probing nucleon's spin structures with polarized Drell-Yan in the Fermilab SpinQuest experiment. PoS, SPIN2018:164, 2019. arXiv:1901.09994, doi:10.22323/1.346.0164.

ABSTRACT

ANGULAR DISTRIBUTION OF DIMUONS FROM DRELL-YAN PRODUCTION IN P+FE INTERACTIONS AT 120 GEV BEAM ENERGY

BY

MD FORHAD HOSSAIN, B.S., M.S.

Doctor of Philosophy

New Mexico State University

Las Cruces, New Mexico, 2022

Dr. Stephen Pate, Chair

In the E906/SeaQuest Fermilab experiment, we report a measurement of the angular distributions by measuring the angular parameters λ, μ, and ν of Drell-Yan dimuons produced using a 120 GeV proton beam incident on an iron target. The angular distribution in the naive Drell-Yan model does not show any $\cos 2\phi$ dependency, where ϕ denotes the azimuthal angle of dimuons in the Collins-Soper frame. However, pion-induced Drell-Yan experiments, such as NA10 and E615, have observed a significant dependence on $\cos 2\phi$. The Boer–Mulders function, a transverse momentum-dependent distribution function, represents the correlation between the transverse spin and the transverse momentum of the quark. A non-zero Boer-Mulders function or an improved higher-order Drell-Yan model considering

QCD effects can produce a $\cos 2\phi$ modulation in the Drell-Yan angular distribution. To measure the angular distributions, we have used an event mixing method to construct the combinatorial background, which was then subtracted from the data to isolate the Drell-Yan signal. Following this, we corrected the detector, trigger, and reconstruction efficiencies using a doubly-iterative Bayesian Unfolding method. This iterative unfolding technique improves the response matrix based on the results of the previous unfolding step, ensuring robust convergence without exaggeration of uncertainties. The angular distributions of the dimuons were measured over the invariant mass range $5.0 < M_{\mu^+\mu^-} < 8.0\ GeV/c^2$, with dimuon transverse momentum $P_T < 2$ GeV/c and Feynman-x $-0.18 < x_F < 0.9$. The measured angular distributions are then compared with the QCD calculations for $p+$Fe interactions, and proton-induced angular distribution measurements from other experiments. We have observed weak $\cos 2\phi$ modulations as a function of P_T. For $P_T > 1.0\,\mathrm{GeV}/c$, the predicted NNLO perturbative QCD value of ν is larger than what we have measured at E906/SeaQuest. Moreover, we have not observed a strong dependence of ν on the kinematic variables, such as dimuon mass $M_{\mu^+\mu^-}$ and Bjorken-x. The spin alignment of the virtual photon, λ, measured from the SeaQuest Drell-Yan $p+$Fe data, is found to be strongly dependent on P_T, decreasing as P_T increases. λ also holds to the upper bound condition $\lambda < 1.0$ within the statistical uncertainty, showing a trend similar to that predicted by NNLO perturbative QCD. However, for $1.0 < P_T < 2.0\,\mathrm{GeV}/c$, the extracted λ value from SeaQuest is smaller than that predicted by perturbative QCD at NNLO.

CONTENTS

LIST OF TABLES xiii

LIST OF FIGURES xxxi

1 Introduction 1

1.1 Deep Inelastic Scattering and the Nucleon Structure . . . 3

1.2 Drell-Yan Process . . . 9

1.3 Collins-Soper Frame . . . 10

1.4 Angular Distribution of the DY Process . . . 13

1.4.1 Boer-Mulder Function . . . 21

2 The E906/SeaQuest Experiment 24

2.1 E906/SeaQuest Spectrometer Overview . . . 25

2.2 Beam Monitor . . . 25

2.3 Targets . . . 27

2.4 Magnet . . . 27

2.5 Hodoscopes . . . 30

2.6 Tracking Chambers . . . 41

2.7 Muon Identification . . . 47

2.8 Trigger . . . 49

2.8.1 NIM-Based Trigger . . . 49

2.8.2 FPGA-Based Trigger . . . 50

2.9 Data Acquisition Systems . . . 52

2.9.1 Event DAQ . . . 53
2.9.2 Scaler DAQ . . . 54
2.9.3 Beam DAQ . . . 55

3 Analysis Method **56**

3.1 Data Set . . . 56
3.2 Event Reconstruction . . . 56
3.2.1 Pre-tracking Analysis . . . 57
3.2.1.1 Hit Removal . . . 57
3.2.1.2 Occupancy Cuts . . . 58
3.2.2 Track Reconstruction . . . 59
3.2.3 Single Track Vertex Reconstruction . . . 61
3.2.4 Dimuon Vertex Reconstruction . . . 64
3.2.5 Monte Carlo Simulation . . . 65
3.3 Event Selections . . . 67
3.3.1 Track Level Selections (μ^+) . . . 71
3.3.2 Track Level Selections (μ^-) . . . 71
3.3.3 Dimuon Level Selections . . . 72
3.4 Estimation of Combinatoric Background . . . 74
3.4.1 Tracks Types in SeaQuest . . . 75
3.4.2 Event Mixing Steps . . . 76
3.4.3 Mixing Method: Mathematical Argument for Normalization and Approximation . . . 78

3.4.4 Method Validation with Simulated Event . . . 80
3.4.4.1 Type I Test . . . 80
3.4.4.2 Type II Test . . . 85
3.4.5 Validity of the Event Mixing method for the SeaQuest experiment . . 91
3.5 Unfolding . . . 92
3.5.1 Building Response Matrix . . . 93
3.5.2 The Unfolding Procedure in Analysis . . . 96
3.5.3 Interative Bayesian Unfolding . . . 99
3.5.4 Retraining the Response Matrix . . . 101
3.6 Event Reweighting Overview . . . 104
3.6.1 Event Reweighting in SeaQuest dump MC . . . 106
3.6.2 Preserving the Statistical Uncertainty after Reweighting . . . 106
3.7 Systematic Uncertainties . . . 110
3.7.1 Monte Carlo Closure Test . . . 110
3.7.2 Acceptance Effect . . . 111
3.7.3 Kinematic Dependence of ν . . . 115
3.7.4 Secondary Beam Effect . . . 124
3.7.4.1 Yield Estimation of Secondary Beam P_T Hadrons . . . 124
3.7.4.2 (λ, μ, ν) extractions . . . 129
3.8 Combinatorial Background Subtraction . . . 135

4 Results **141**

4.1 Steps to Extract the (λ, μ, ν) from Fe (dump) Data . . . 141

4.2 Source of Uncertainties in Extracted Parameters 142

4.3 The Lam-Tung (LT) Quantity in SeaQuest 145

4.4 Extracting ν in different kinematics 146

5 Discussion & Conclusion **150**

5.1 Comparing E906/SeaQuest Proton-induced Drell-Yan Angular Distributions with E866/NuSea 150

5.2 Conclusion 155

LIST OF TABLES

1 Kinematical variables are listed to describe a DIS process. 7

2 Kinematical variables are listed to describe a Drell-Yan process. 10

3 Best fit values of the Boer-Mulders functions [78]. 23

4 SeaQuest target features. Taken from the Ref. [3]. 30

5 Summary of Spectrometer Magnet Configurations. 30

6 Details about the number and sizes of scintillators at each hodoscope plane are shown. Values in the table are taken from [3]. 40

7 Parameters of all chambers. The table is taken from [3]. 46

8 Performance metrics for the drift chambers in the SeaQuest experiment (April 2014 - June 2015). The numbers are taken from [3]. 46

9 Trigger configurations used in the SeaQuest experiment [3]. 49

10 Upper limits of the occupancy of each drift chamber. The numbers are taken from [67]. 59

11 Vertex fitting parameters and variables. 63

12 List of variables and descriptions. 70

13 Area of each histogram in Figs. 55 and 56 as a function of the normalization factor NM. 87

14 A list of residual signals is provided for the fixed embedding and for the random embedding using the Type I test. This Table is taken from Ref. [70]. 91

15 After event selection, all data events, combinatorial background events, and signal events are listed. 140

16 SeaQuest results for angular coefficients from a two-dimensional fit of $\cos\theta$ vs. ϕ for $p+Fe$ Drell-Yan in the Collins-Soper frame. Uncertainties are statistical only. The response matrix was built within $\cos\theta \in (-0.425, 0.425)$, and the fit was performed within the range $cos\theta \in (-0.325, 0.325)$. 144

17 The systematic uncertainties are taken from the sections 3.7.1, 3.7.2. 144

18 The central and systematic values are given for the Lam-Tung quantity $2\nu - (1 - \lambda)$. 146

19 Uncertainties for different kinematic variables. 148

LIST OF FIGURES

1 Feynman diagram of deep inelastic scattering. It shows a high-energy electron scattering from a quark in the proton. 5

2 The spectrum of scattered electrons for an incident beam energy of 4.879 GeV and an incident beam angle of 10 degrees [9]. 6

3 The left figure shows $F(x, Q^2)$ vs. x, illustrating the constituents inside the proton [7]. The right figure displays the ratio of the structure functions $2xF_1(x)$ and $F_2(x)$. Within experimental uncertainty, the ratio is consistent with unity. The plot is taken from [73]. 8

4 Feynman diagram of Leading Order Drell-Yan Process. 9

5 Higher order corrections to the leading order Drell-Yan process that include additional gluon diagrams. The figure is taken from [72]. 11

6 The polar and azimuthal angles θ and ϕ are shown in the Collins–Soper frame. P_1 and P_2 represent the beam and target hadron momenta. The z-axis is the bisector of the two interacting hadron momenta, and the x-axis aligns with the transverse momentum of the dimuon P_T. The momenta l and l' correspond to the lepton and antilepton, respectively. The angular difference between the leptons and the beam/z-axis is denoted as θ in the Collins–Soper frame, while ϕ measures the angles between the lepton and the hadron plane. The Figure is taken from [17]. 12

7 The three graphs show measurements of the angular distributions of the Drell-Yan process in the Collins-Soper frame as a function of the dimuon's transverse momentum P_T, at different π^- beam energies that impinged on tungsten, deuterium, and tungsten targets respectively. The error bars represent statistical uncertainties only, and the dashed curves show perturbative QCD predictions [27]. The figure is taken from [52]. 16

8 The two figures are taken from the E866/NuSea experiments [80, 79], where the angular distributions of the Drell-Yan process have been measured in the Collins-Soper frame as a function of the dimuon's transverse momentum P_T. The left plot shows the results for $p + p$ and $p + d$ measured in the E866 experiment, and the right one shows the pion-induced Drell-Yan interactions $\pi^- + \mathrm{W}$ events from CERN-NA10 [45, 52] (blue star) and from E615 [33](red diamond). The figure is taken from [80, 79]. 17

9 A comparison is made between the NLO (red points) and NNLO (blue points) fixed-order pQCD calculations with the E615 [33] and NA10 [45, 52] data. The figure is taken from [25]. 18

10 A comparison is made between the NLO (red points) and NNLO (blue points) fixed-order pQCD calculations with the E866 data [80, 79]. The figure is taken from [25]. 19

11 Leading-twist transverse momentum-dependent (TMD) distributions, classified by the polarizations of quarks (f, g, h) and nucleons (U, L, T), include $f_\perp^{1T}$ and $h_\perp^1$, termed naive time-reversal-odd TMD distributions, with a corresponding classification for gluons. Plot from Reference [2] 21

12 The plot has been taken from the NuSea/E866 experiment [81], where ν is shown as a function of dimuon P_T for $p+d$ and $p+p$ Drell-Yan data. The dotted and solid curves represent calculations [78] for $p+d$ and $p+p$ processes, respectively, using parameterizations based on a fit to the $p+d$ data. The red dot-dashed curve corresponds to the contribution from the perturbative QCD at $\mathcal{O}(\alpha_s)$ [16, 30]. 23

13 Fermilab accelerator complex. The figure is taken from Ref. [3]. 24

14 A detailed schematic representation of the SeaQuest spectrometer. The figure is taken from Ref. [3]. 26

15 Beam Intensity Monitor (BIM) Cherenkov counter. The figure is taken from Ref. [3]. 27

16 The figure shows the protons per RF bucket vs. RF Bucket Index, which were measured by the Beam DAQ Cerenkov counter. The red line indicates the threshold for trigger inhibition. No data will be recorded if the intensity exceeds the red line. However, the lower plot shows that the number is quite high. The figure is taken from Ref. [3]. 28

17 The figure presents a top-view diagram of the adjustable target table, illustrating the seven distinct positions. The figure is taken from Ref. [3]. 29

18 The figure shows the scintillator hodoscopes for Station 1, denoted as H1X and H1Y. They are also known as the X and Y measuring hodoscopes. The figure is taken from Ref. [67]. 32

19 The figure shows the scintillator hodoscopes for Station 2, denoted as H2X and H2Y. The figure is taken from Ref. [67]. 33

20 The figure shows the scintillator hodoscopes for Station 3, denoted as H3X. The figure is taken from Ref. [67]. 34

21 The figure shows the scintillator hodoscopes for Station 4, denoted as H4X and H4Y. The figure is taken from Ref. [67]. 35

22 TDC time distributions of the top (H1T) and bottom (H1B) hodoscope planes. The left plot shows TCD time distributions for the FPGA trigger hits, and the right plot shows the Distributions (red) after applying the RF-based in-time cut. 36

23 TDC time distributions of the top (H2T) and bottom (H2B) hodoscope planes. The left plot shows TCD time distributions for the FPGA trigger hits, and right plot shows the Distributions (red) after applying the RF-based in-time cut. 37

24 TDC time distributions of the top (H3T) and bottom (H3B) hodoscope planes. The left plot shows TCD time distributions for the FPGA trigger hits, and right plot shows the Distributions (red) after applying the RF-based in-time cut. 38

25 TDC time distributions of the top (H4T) and bottom (H4B) hodoscope planes. The left plot shows TCD time distributions for the FPGA trigger hits, and right plot shows the Distributions (red) after applying the RF-based in-time cut. 39

26 Drawing of the chamber readout electronics system. The figure is taken from Ref. [67]. 42

27 Configuration of the St. 1 drift chamber is illustrated in (a) for the V plane, where the wires are tilted by approximately 14 degrees from the vertical direction. In (b), the X plane is shown with vertical wires. The figure is taken from Ref. [67]. 43

28 Configuration of the St. 2 drift chamber is illustrated in (a) for the V plane, where the wires are tilted by approximately 14 degrees from the vertical direction. In (b), the X plane is shown with vertical wires. The figure is taken from Ref. [67]. 43

29 Configuration of the St. 3+ drift chamber is illustrated in (a) for the V plane, where the wires are tilted by approximately 14 degrees from the vertical direction. In (b), the X plane is shown with vertical wires. The St. 3+ drift chamber covers upper half of St. 3. The figure is taken from Ref. [67]. 44

30 Configuration of the St. 3- drift chamber is illustrated in (a) for the V plane, where the wires are tilted by approximately 14 degrees from the vertical direction. In (b), the X plane is shown with vertical wires. The St. 3+ drift chamber covers lower half of St. 3. The figure is taken from Ref. [67]. 44

31 Drift Chamber Resolutions in Different Planes. The figure is taken from Ref. [3] 45

32 Layout of the proportional tubes showing the top (x-z) and side (y-z) views. [3] 48

33 Schematic of NIM3 trigger [76]. 50

34 The hit patterns of positive muons on the X-hodoscopes are visualized here. In a top view, scintillator paddles are shown as black points. The red line highlights the 10 most frequently hit patterns, and the blue lines show the subsequent 10 most frequent patterns. All other patterns are represented in gray [42]. 52

35 Trigger hardware schematic [63]. 53

36 A chain of VME crates. 54

37 Procedure of the dimuon reconstruction based on the kTracker [67]. 57

38 The global track reconstruction uses the sagitta ratio. The figure is taken from [67]. 61

39 Vertex reconstruction at FMag slice is shown where the P_T^{Kick} is applied. . . 62

40 The resolutions of the μ^+ and μ^- tracks. 64

41 Vertex reconstructions method. The left figure is taken from [65]. 65

42 The plot shows the range of Bjorken-x-Beam versus Bjorken-x-Target for the beam dump target location using the Drell-Yan process. The black points represent the generated 4π GMC events, while the red points represent the reconstructed GMC. 67

43 The plot illustrates the range of true $\cos\theta$ versus the reconstructed distribution for the beam dump target location using the Drell–Yan process. The blue histogram represents the generated 4π GMC events, while the red histogram represent the reconstructed GMC. Both histograms are scaled to Y_{max} yield of 1. 68

44 This figure shows the track multiplicities for positive (left) and negative (right) tracks across various D1 occupancies. The color coding is as follows: blue represents low occupancy, black denotes medium occupancy, and red indicates high occupancy. Generally, there are more positive tracks than negative tracks, which can be attributed to the higher production of positive pions compared to negative pions in proton-nucleus collisions. The plot is taken from Ref. [70]. 76

45 All positive tracks from event i and all negative tracks from event $i+1$ are combined into a new mixed event. This combination assumes that event sorting based on occupancy has already been done. 77

46 The steps show the Type I test, and at the end of the steps, the recovered signals can be obtained by taking the subtraction between the yields of $Yield^{\text{comb}}_{\text{embed}}$ and $Yield^{\text{comb}}_{\text{normal}}$. 82

47 The left histogram shows mixing events from real data, whereas the right histogram shows simulated signals intended for embedding in those mixing events. This figure comes from Ref. [70]. 83

48 The left black and green histograms represent the sum of embedded simulated events and mixed events, respectively, while the right blue histogram shows the signal events obtained by subtracting the mixed events from the GMC embedded data. This figure is taken from Ref. [70]. 83

49 The blue histogram represents the signal recovered using the mixing method, as shown in Fig. 48 (right), and the red histogram displays the embedded simulated events, as shown in Fig. 47 (right). This figure is taken from Ref. [70]. 84

50 The steps show the Type II test, and at the end of the steps, the recovered signals can be obtained by taking the subtraction between the yields of Signal1 and Signal2. 86

51 The left histogram displays the dimuon mass distributions for normal data (shown in black) and mixed data (shown in green) from 10 runs. The right histogram presents the signal, obtained by subtracting the mixed data from the normal data. This figure comes from Ref. [70]. 87

52 The figure shows a simulated resonance signal peaking at 6 GeV/c^2, which will be embedded into the data shown in Fig. 51. This figure comes from Ref. [70]. 88

53 The left black histogram shows the dimuon distribution after embedding the simulated signals from Fig. 52 into the data from Fig. 51. The green histogram represents the corresponding combinatorial background. The right magenta histogram represents the signal obtained by subtracting the combinatorial background (green) from the total data (black). This figure is taken from Ref. [70]. 88

54 The figure shows a comparison of signals from different analysis stages. On the left, the blue histogram represents the signal (Signal1) from the 10 normal runs, and the magenta histogram represents the signal from the simulated data (Signal 2). Both of these were obtained after combinatorial background subtraction. The red histogram represents the embedded simulated signal, same as Fig. 52. The right histogram shows the difference (Signal2 - Signal1). This figure comes from Ref. [70]. 89

55 From the right side of Fig. 54, this figure illustrates the difference between the embedded GMC and the recovered simulated signal. This figure comes from Ref. [70]. 89

56 From the right side of Fig. 54, this figure illustrates the difference between the embedded GMC and the recovered simulated signal with different normalization factors (NM). This figure comes from Ref. [70]. 90

57 In the figure, we can see three kinds of distributions for the $cos\theta_{CS}$ in the Collins-Soper frame. It displays the true, reconstructed, and unfolded distributions. 93

58 Using the Monte Carlo events, the response matrix plots show bin-to-bin migration probabilities in 2D. The reconstructed dimuon mass chosen for this case ranges from 5 GeV/c^2 to 8 GeV/c^2. All the participated events went through the reconstructed cuts, so we don't have any inefficient events included in the response matrix. 95

59 Resolution plots of ϕ and $\cos\theta$ in the Collins-Soper frame for the Drell–Yan dimuon P_T range of (0.0, 2.0) GeV/c and in the mass range of (5.0, 8.0) GeV/c^2. 97

60 In this response matrix plot, the 2D bins represent the bin-to-bin migration probabilities without considering the inefficiency. x^T and x^R represent the true and reconstructed first 20×20 bin combinations from the two-dimensional variable response matrix $\phi \times \cos\theta$. 98

61 A flowchart of the Bayesian Iterative Unfolding method with iterative retraining of the response matrix. 101

62 (λ, μ, ν) were extracted in the p_T range of (0.0, 2.0) GeV/c from a simulated test dataset using Bayesian Unfolding with unfolding regularization iteration 2. 103

63 Illustration of the reweighting of dimuon mass, Feynman-x (x_F), Bjorken target (x_T) and Bjorken beam (x_B) variables. The MC default (red) and the reweighted MC (magenta) distributions are scaled to match the total counts of the signal (black) events. The signal events are obtained after subtracting the combinatorial events from all the data, which is represented by "Unmix-Mix" events. 105

64 (λ, μ, ν) were extracted in the P_T range of (0.0, 2.0) GeV/c from independent test MC datasets. The injected values of (λ, μ, ν) into the MC test dataset were (1.0, 0.0, 0.0). The total data size in each MC test dataset was 50k events. The left column shows the unfolded (λ, μ, ν) extractions in the $\cos\theta$ range (-0.325, 0.325) with no additional weight, while the right column shows the same extraction with reweighted events. 108

65 (λ, μ, ν) were extracted in the P_T range of (0.0, 2.0) GeV/c from independent test MC datasets. The injected values of (λ, μ, ν) into the MC test dataset were (0.5, 0.2, 0.1). The total data size in each MC test dataset was 50k events. The left column shows the unfolded (λ, μ, ν) extractions in the $\cos\theta$ range (-0.325, 0.325) with no additional weight, while the right column shows the same extraction with reweighted events. 109

66 The y-axis shows the total number of independent test unfolded histograms in the p_T range of (0.1, 0.5) GeV/c. The injected (λ, μ, ν) into the MC test dataset were (0.862, 0.0511, 0.0256). The total event size in each MC test unfolded histogram is about $80k$ for each histogram, and listed in the table 15. The left column shows the unfolded (λ, μ, ν) extractions in the $\cos\theta_{CS}$ range (-0.325, 0.325), and the right column shows the difference of the unfolded parameters between the two $\cos\theta_{CS}$ ranges (-0.325, 0.325) and (-0.275, 0.275). 112

67 The y-axis shows the total number of independent test unfolded histograms in the p_T range of (0.5, 1.0) GeV/c. The injected (λ, μ, ν) into the MC test dataset were (0.724, -0.009, 0.0187). The total event size in each MC test unfolded histogram is about $130k$ for each histogram, and listed in the table 15. The left column shows the unfolded (λ, μ, ν) extractions in the $\cos\theta_{CS}$ range (-0.325, 0.325), and the right column shows the difference of the unfolded parameters between the two $\cos\theta_{CS}$ ranges (-0.325, 0.325) and (-0.275, 0.275). 113

68 The y-axis shows the total number of independent test unfolded histograms in the p_T range of (1.0, 2.0) GeV/c. The injected (λ, μ, ν) into the MC test dataset were (0.281, 0.032, 0.038). The total event size in each MC test unfolded histogram is about $70k$ for each histogram, and listed in the table 15. The left column shows the unfolded (λ, μ, ν) extractions in the $\cos\theta_{CS}$ range (-0.325, 0.325), and the right column shows the difference of the unfolded parameters between the two $\cos\theta_{CS}$ ranges (-0.325, 0.325) and (-0.275, 0.275). 114

69 In each figure, ν values were extracted in the p_T range of (0.0, 2.0) GeV/c from independent test MC datasets using Bayesian Iterative Unfolding with 2 unfolding regularization iterations. The difference between the injected ν parameter and the mean of the unfolded distribution is used as the systematic bias coming from the unfolding method. 116

70 In each figure, ν values were extracted in the p_T range of (0.0, 2.0) GeV/c from independent test MC datasets using Bayesian Iterative Unfolding with 2 unfolding regularization iterations. Each plot shows the difference between the extracted ν parameters using two $\cos\theta$ fit ranges, namely (-0.325, 0.325) and (-0.275, 0.275). 117

71 In each figure, ν values were extracted in the p_T range of (0.0, 2.0) GeV/c from independent test MC datasets using Bayesian Iterative Unfolding with 2 unfolding regularization iterations. The difference between the injected ν parameter and the mean of the unfolded distribution is used as the systematic bias coming from the unfolding method. 118

72 In each figure, ν values were extracted in the p_T range of (0.0, 2.0) GeV/c from independent test MC datasets using Bayesian Iterative Unfolding with 2 unfolding regularization iterations. Each plot shows the difference between the extracted ν parameters using two $\cos\theta$ fit ranges, namely (-0.325, 0.325) and (-0.275, 0.275). 119

73 In each figure, ν values were extracted in the p_T range of (0.0, 2.0) GeV/c from independent test MC datasets using Bayesian Iterative Unfolding with 2 unfolding regularization iterations. The difference between the injected ν parameter and the mean of the unfolded distribution is used as the systematic bias coming from the unfolding method. 120

74 In each figure, ν values were extracted in the p_T range of (0.0, 2.0) GeV/c from independent test MC datasets using Bayesian Iterative Unfolding with 2 unfolding regularization iterations. Each plot shows the difference between the extracted ν parameters using two $\cos\theta$ fit ranges, namely (-0.325, 0.325) and (-0.275, 0.275). 121

75 In each figure, ν values were extracted in the p_T range of (0.0, 2.0) GeV/c from independent test MC datasets using Bayesian Iterative Unfolding with 2 unfolding regularization iterations. The difference between the injected ν parameter and the mean of the unfolded distribution is used as the systematic bias coming from the unfolding method. 122

76 In each figure, ν values were extracted in the p_T range of (0.0, 2.0) GeV/c from independent test MC datasets using Bayesian Iterative Unfolding with 2 unfolding regularization iterations. Each plot shows the difference between the extracted ν parameters using two $\cos\theta$ fit ranges, namely (-0.325, 0.325) and (-0.275, 0.275). 123

77 The left plots show the P_T vs. P_z distributions of direct secondary protons, neutrons, π^+, and π^-. The right plots represent the corresponding 1D projections, displaying the P_z distributions. The total count of the P_z distributions is scaled by 1/10,000. The Geant4 physics list used was QBBC. 126

78 The left plots show the P_T vs. P_z distributions of direct secondary protons, neutrons, π^+, and π^-. The right plots represent the corresponding 1D projections, displaying the P_z distributions. The total count of the P_z distributions is scaled by 1/10,000. The Geant4 physics list used was FTFP_BERT. 127

79 The left plots show the P_T vs. P_z distributions of direct secondary protons, neutrons, π^+, and π^-. The right plots represent the corresponding 1D projections, displaying the P_z distributions. The total count of the P_z distributions is scaled by 1/10,000. The Geant4 physics list used was QGSP_BERT. . . . 128

80 This shows the ratio between the 2D ϕ-$\cos\theta$ histograms for unsmeared and smeared ones. 130

81 This shows the ratio between the 2D ϕ-$\cos\theta$ histograms for unsmeared and smeared ones. 131

82 (λ, μ, ν) were extracted in the P_T range of (0.0, 2.0) GeV/c from independent test MC datasets. The injected values of (λ, μ, ν) into the MC test dataset were (0.95, 0.03, 0.02). The total data size in each MC test dataset was 90k events. The left column shows the unfolded (λ, μ, ν) extractions in the $\cos\theta$ range (-0.325, 0.325) with no P_T^{beam} smearing, while the right column shows the same extraction with P_T^{beam} smeared events. The P_T^{beam} distributions were uniformly taken in the range (0.0, 0.5). 133

83 (λ, μ, ν) were extracted in the P_T range of (0.0, 2.0) GeV/c from independent test MC datasets. The injected values of (λ, μ, ν) into the MC test dataset were (0.95, 0.03, 0.02). The total data size in each MC test dataset was 90k events. The left column shows the unfolded (λ, μ, ν) extractions in the $\cos\theta$ range (-0.325, 0.325) with no P_T^{beam} smearing, while the right column shows the same extraction with P_T^{beam} smeared events. The P_T^{beam} distributions were uniformly taken in the range (0.0, 1.0). 134

84 We show here the 2D histogram of $\cos\theta - \phi$ after applying the event conditions outlined in Section 3.3 for the p_T range of (0.1, 2.0) GeV/c. 136

85 We show here the 2D histogram of $\cos\theta - \phi$ after applying the event conditions outlined in Section 3.3 for the p_T range of (0.1, 0.5) GeV/c. 137

86 We show here the 2D histogram of $\cos\theta - \phi$ after applying the event conditions outlined in Section 3.3 for the p_T range of (0.5, 1.0) GeV/c. 138

87 We show here the 2D histogram of $\cos\theta - \phi$ after applying the event conditions outlined in Section 3.3 for the p_T range of (1.0, 2.0) GeV/c. 139

88 Unfolded Results: The left columns represent the unfolded results in different pT ranges, while the right columns are the corresponding correlation coefficients between the unfolded parameters 143

89 Parameters λ, μ, and ν, and the Lam-Tung quantity $2\nu - (1 - \lambda)$ versus p_T in the Collins-Soper frame. The blue line represents results from SeaQuest $p + Fe$ (Dump target) at 120 GeV when the (LH_2) target was present. The vertical blue error bars are statistical only, and the shaded blue area represents the combination of statistical uncertainty (σ_{stat}) and systematic uncertainties (σ_{unfold}, σ_{acc}). 147

90 Parameter ν versus $M_{\mu^+\mu^-}, x_F, x_B,$ and x_T in the Collins-Soper frame. The blue line represents results from SeaQuest $p + Fe$ (Dump target) at 120 GeV when the (LH_2) target was present. The vertical blue error bars are statistical only, and the shaded blue area represents the combination of statistical uncertainty (σ_{stat}) and systematic uncertainties (σ_{sys1}, σ_{sys2}). 149

91 Parameters λ, μ, and ν, and the Lam-Tung quantity $2\nu - (1 - \lambda)$ versus P_T in the Collins-Soper frame. The blue line represents results from SeaQuest $p + Fe$ (dump target) at 120 GeV when the (LH_2) target was present. The vertical blue error bars are statistical only, and the shaded blue area represents the combination of statistical uncertainty (σ_{stat}) and systematic uncertainties (σ_{unfold}, σ_{acc}). The magenta-colored data points represent the NNLO perturbative QCD predicted values of λ, μ, and ν as a function of P_T [43]. The results from the E866 experiments [79, 80] in the $P_T \in (0.0, 2.0) GeV/c$ are also added for comparison. 153

92 Parameter ν versus $M_{\mu^+\mu^-}, x_F, x_B,$ and x_T in the Collins-Soper frame. The blue line represents results from E906/SeaQuest $p + Fe$ (dump target) at 120 GeV when the (LH_2) target was present. The vertical blue error bars are statistical only, and the shaded blue area represents the combination of statistical uncertainty (σ_{stat}) and systematic uncertainties (σ_{sys1}, σ_{sys2}). The magenta-colored data points represent the NNLO perturbative QCD predicted values [43]. The results from the E866 experiments [79, 80] in the $P_T \in (0.0, 2.0) GeV/c$ are also added for comparison. 154

1 Introduction

The exploration of nucleon and nuclear structure stands as a key objective in nuclear physics. The spin-$\frac{1}{2}$ particle, the proton, was considered a fundamental particle upon its discovery by Rutherford in 1917 [44]. As spin-1/2 particles, where the magnetic moment is expressed as $\mu = \frac{g}{2}\frac{e\hbar}{2m}$, with g expected to be 2.0. However, in later years, measurements of its magnetic moment [39] showed a significant deviation from the prediction of Dirac's point-like particle theory [34]. This discrepancy kept physicists motivated to understand the structure of the proton and the origin of the nuclear magnetic moment. In the 1950s, Hofstadter et al. [54, 62] performed an elastic scattering of a 188 MeV electron beam with gaseous targets of hydrogen, obtaining the first determination of the root-mean-squared charge radius of the proton, which was found to be 0.74 ± 0.24 femtometers (fm). In a few years, a classification of particles known as the "Eightfold Way" was independently developed by both Murray Gell-Mann [49] and Yuval Ne'eman [69]. They plotted charge vs. strangeness in a hexagonal pattern for several groups of particles that have the same spin, which is similar to what Mendeleev did for chemistry. According to this classification scheme, there exist three fundamental quarks: the "up" quark (u), the "down" quark (d), and the "strange" quark (s), along with their corresponding antiparticles, the antiquarks. Baryons are made of three quarks, while mesons are bound states of a quark and an antiquark. The success of the Eightfold Way and the symmetry group SU(3) led to the development of the quark model proposed by Gell-Mann [50] and George Zweig [82, 83]. Originally, three quarks were proposed: up, down, and strange. Later evidence indicates the existence of three more: top, bottom, and charm. The proton is a dynamic bound system, which was first experimentally proven at

SLAC through inelastic electron scattering experiments [19, 13]. Based on the discovery of quarks, the Quark-Parton Model was developed by Feynman, Bjorken et al. [47, 11].

Understanding how a proton, a spin-1/2 particle, acquires its total spin is a fundamental aspect of nuclear structure. The European Muon Collaboration (EMC) [6] at CERN measured that the contribution from the quark to the total proton's spin accounts for a small fraction of the total proton spin using polarized deep-inelastic scattering of muons by longitudinally polarized protons. The integral of the spin-dependent structure function of the proton was deduced in the experiment to investigate the contribution of the spin of the quarks to the proton spin. The proton spin can be decomposed as [55]: $J = \frac{1}{2}\Delta\Sigma + L_Q^{JM} + \Delta G + L_G$, where $\frac{1}{2}\Delta\Sigma(\Delta G)$ represents the quark (glue) spin contributions, and $L_Q^{JM}(L_G)$ represents the quark (glue) orbital angular momentum contributions. The EMC experiment motivated many other experiments in which researchers investigated cross-sections and angular distributions in various processes, including deep inelastic scattering (DIS), the Drell-Yan process, electron-positron annihilation, etc.

Significant progress has been made in understanding the partonic structure of hadrons, relying on parton distribution functions (PDFs). However, to better understand the theoretical predictions and experimental results, physicists consider the transverse motion of partons inside the nucleon. Transverse Momentum Dependent (TMD) parton distribution functions and Generalized Parton Distributions (GPDs) offer complementary information about the transverse momentum and spatial distribution of partons, allowing for a more comprehensive understanding of hadron structure, including its spin decomposition and orbital angular momentum. In recent years, there has been considerable interest in transverse-momentum-

dependent parton distribution functions (TMDs) because they describe the relationship between the transverse spin and transverse momentum of the partons and nucleons.

This thesis will mainly focus on extracting the angular distributions from the proton-induced Drell-Yan process. There are several aspects to extracting the angular distributions: (1) There are no experiments that provide complete descriptions of the angular distributions for unpolarized proton-induced Drell-Yan with a heavy nuclear target. Therefore, the results will exhibit nuclear effects and quark energy loss in different kinematic variables, especially in higher x_F Feynman regions. (2) This study will also focus on understanding the perturbative QCD effects in the extracted angular distributions. This could connect us with the Boer-Mulder effect [14], which is one of the Transverse Momentum Dependent distributions (TMD). We aim to understand if the Boer-Mulder effect is necessary to explain any asymmetry, especially if the asymmetry arises from the modulations of the $\cos 2\phi$ in higher transverse momentum. Here, ϕ represents the azimuthal angle between the lepton and hadron planes in the virtual photon's rest frame. Another aspect of this thesis is the challenge posed by the measurement of angular distributions. Small systematic effects from detectors, the quality of simulated data, or reconstruction quality could introduce biases in the measurement if not properly accounted for. To address this challenge, we have incorporated many systematic studies and examined these effects using a data unfolding technique.

1.1 Deep Inelastic Scattering and the Nucleon Structure

In a scattering process, for example, between an electron and a nuclear target (proton), if the invariant mass of the nuclear target doesn't change, then the process is called elastic scattering. If sufficient energy is transferred from the electron to the nuclear target ($lp \rightarrow$

$l'p'$), then the target can be in the excited state. This is an inelastic regime, the invariant mass of the hadronic state can be written as:

$$W^2 = (P+q)^2 = M^2 + \underbrace{2M\nu - Q^2}_{>0}, \tag{1}$$

where W is determined by q and P, which are the four-momenta of the gauge boson and the incoming parton, respectively. The invariant mass of the final state (W) will no longer be the same as the initial state's proton mass (M), and ν is a Lorentz invariant quantity, which is defined as $\nu = \frac{P\cdot q}{M}$. The vector q here is space-like and once can write $q^2 = -Q^2$.

With further increasing energy transfer by the lepton, the nuclear target (proton) will undergo hadronization, and the process will be referred to as deep-inelastic scattering (DIS), as shown in Figure 1. The reaction is described as follows:

$$l(\mathbf{k}) + N(\mathbf{P}) \Longrightarrow l(\mathbf{k}^{'}) + X \tag{2}$$

Where the hadronic final state X in equation (2) will no longer represent the invariant mass of the proton or a resonant state.

In inclusive DIS, only the lepton in the final state $l^{'}$ is detected. Now if the initial and the final momentum of the electron are k and $k^{'}$, the transferred momentum by the virtual photon to the hadronic system would be $q = k - k^{'}$.

The transition from the elastic regime via the resonance region into the DIS regime is illustrated in Figure 2, which is taken from an electron-proton scattering experiment [9, 71]. In the figure, we see several peaks corresponding to excited states of the nucleon, also known as nucleon resonances. It shows the spectrum of scattered electrons for an incident beam energy

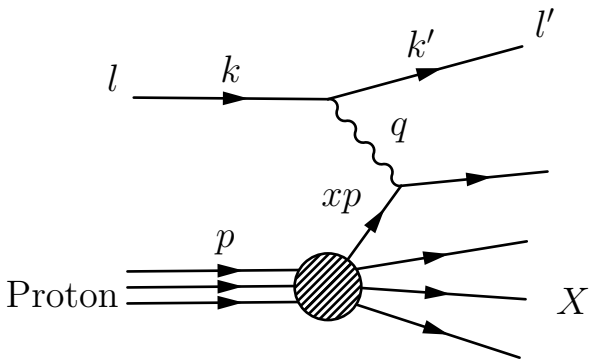

Figure 1: Feynman diagram of deep inelastic scattering. It shows a high-energy electron scattering from a quark in the proton.

of 4.879 GeV and a scattering angle of 10°. The far-right portion of the spectrum displays the elastic scattering peak at the proton mass $W \approx 0.938$ GeV, scaled down by a factor of 15 to fit within the graph. Additionally, several broad inelastic nucleon excitations can be observed at lower scattering energies, near $W = 1.236$, $W = 1.52$, and $W = 1.68$ GeV, where W represents the invariant mass of the hadron's final state. The excited states of the proton show that it is a composite system.

The DIS cross-section [12] in the laboratory frame can be written as :

$$\frac{d\sigma}{dE'd\Omega} = \frac{\alpha^2}{4E^2\sin^4(\theta/2)}\left[W_2(\nu, q^2)\cos^2(\theta/2) + 2W_1(\nu, q^2)\sin^2(\theta/2)\right], \tag{3}$$

where W_1 and W_2 denote the unpolarized structure functions [47], and α is the fine structure constant. The structure functions, $F_1(x)$ and $F_2(x)$, can be expressed as their limits in the Deep Inelastic Scattering (DIS) regime:

$$MW_1(\nu, Q^2) \to F_1(x) = \frac{1}{2x}F_2(x) \quad \text{and} \quad \nu W_2(\nu, Q^2) \to F_2(x) = \sum_i e_i^2 x f_i(x), \tag{4}$$

where:

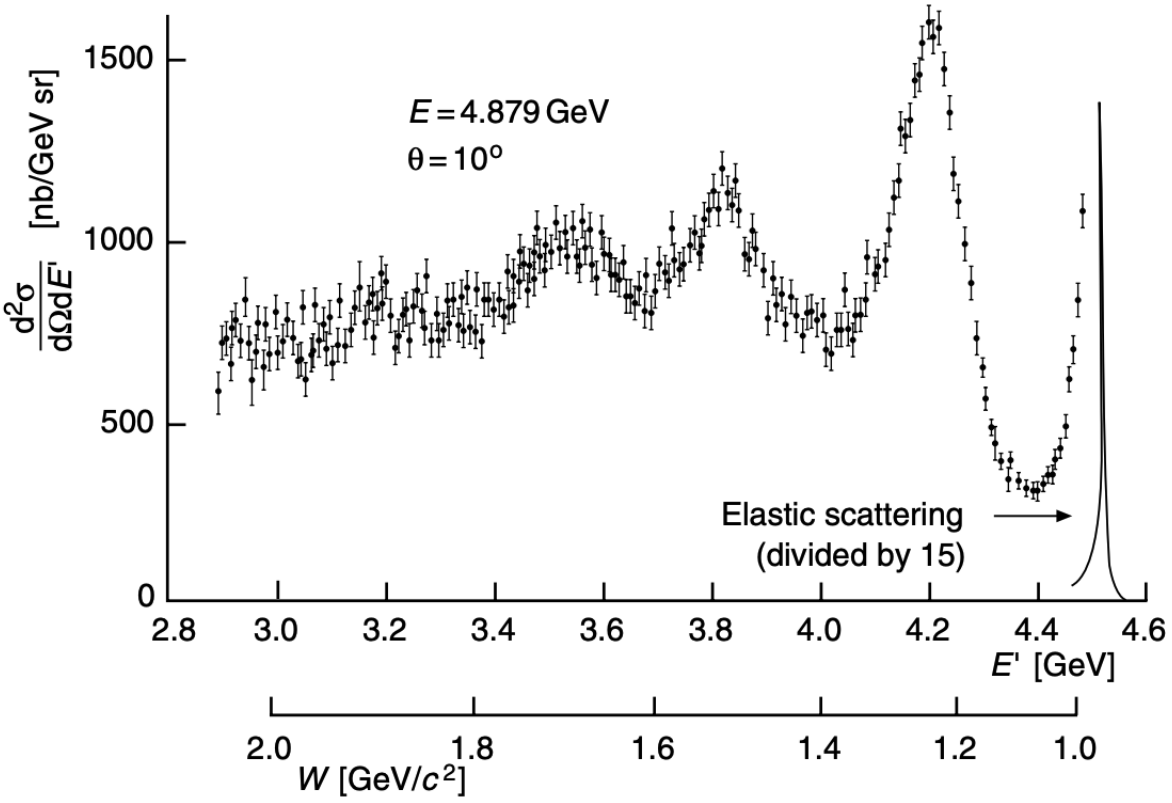

Figure 2: The spectrum of scattered electrons for an incident beam energy of 4.879 GeV and an incident beam angle of 10 degrees [9].

- e_i represents quark charge with flavor index i.
- $f_i(x)$: Parton distribution functions (PDFs).
- x: The Bjorken scaling variable, defined as $x = \frac{Q^2}{2M\nu}$.
- Lorentz-invariant quantity $\nu = (E - E')$ in lab frame.

Variables	**Notations**
P, q	Four momentum vector of nucleon and exchanged gauge boson.
θ	Lepton scattering angle in laboratory frame.
$k = k - k^{'}$	4-momentum transfer from the lepton to the target.
E, E'	Energy of the incident and the scattered electron.
$\nu = E - E'$	Energy transfer between lepton and nucleon.
M	Rest mass of the nucleon.
$W^2 = (P+q)^2 = M^2 + 2M\nu - Q^2$	Invariant mass squared of the hadronic state
$Q^2 = -q^2 \approx 4EE' \sin^2(\theta/2)$	Squared momentum transferred.
$x = \frac{Q^2}{2M\nu}$	Bjorken scaling variable

Table 1: Kinematical variables are listed to describe a DIS process.

In the equation (4), F_1 and F_2 vary slowly with Q^2, and this behavior is known as Bjorken scaling [10]. In this regime, the structure functions become independent of Q^2, and it means the electrons are scattered off a point charge.

In naive quark parton model, $2x\ F_1(x) = F_2(x)$ is known as Callan-Gross relationship [22].

$$\text{elastic: } 2M\nu - Q^2 = 0, \quad W^2 = Q^2, \quad x = 1 \tag{5}$$

$$\text{inelastic: } 2M\nu - Q^2 > 0, \quad W^2 > Q^2, \quad 0 < x < 1. \tag{6}$$

In Figure 2, the electron beam energy is about 5 GeV, and no resonances or structures are observed in the deep inelastic scattering (DIS) regions ($W > 2$ GeV). To understand the

spectrum of the scattered electrons at higher beam energies, we can observe in an SLAC experiment with an electron beam energy of 20 GeV and a liquid hydrogen target. It is shown in the left plot of Figure 3 that $F_2(x, Q^2)$ remains independent of Q^2 and exhibits a point-like structure in position space. On the other hand, the right plot is consistent with the Callan-Gross relation, as expected for spin-1/2 particles, because the F_1 structure function represents the magnetic interaction, and it vanishes for scattering off spin-zero particles. Since the ratio is consistent with unity, we can say that constituents of the nucleon have spin 1/2. The combination of the two plots manifests that the substructure of the nucleons is point-like spin-1/2 particles. This point-like structure, which is also independent of the Q^2, is predicted by the "Parton Model" [47], proposed by Feynman in 1969. A nice introduction to the Deep Inelastic Scattering process can be found in Refs. [71, 73].

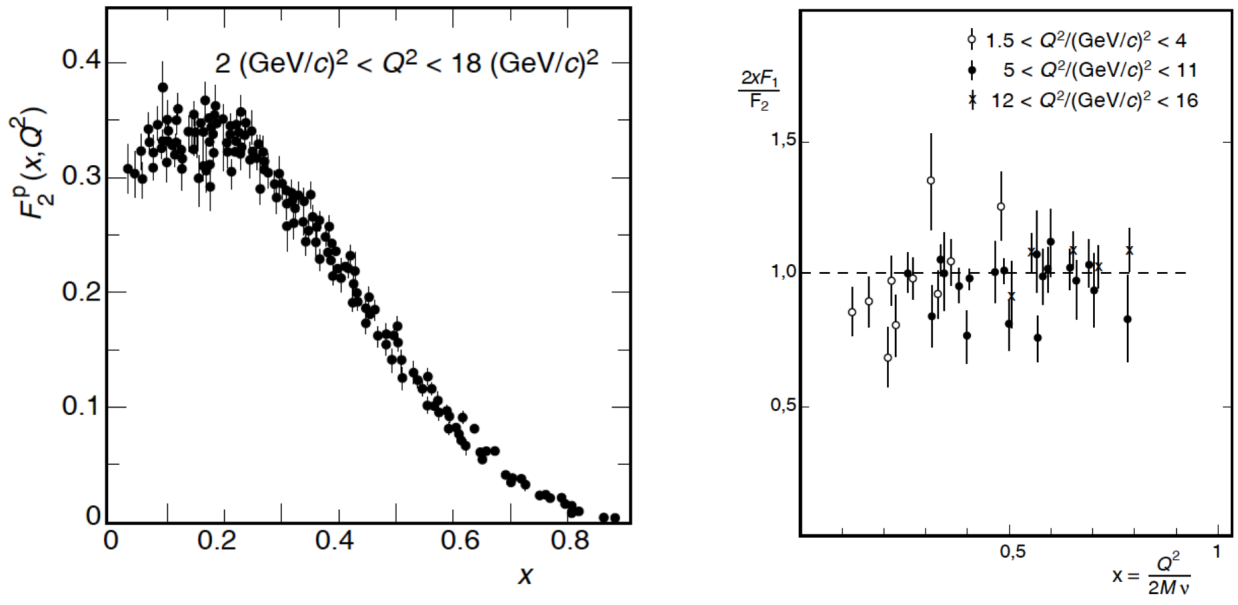

Figure 3: The left figure shows $F(x, Q^2)$ vs. x, illustrating the constituents inside the proton [7]. The right figure displays the ratio of the structure functions $2xF_1(x)$ and $F_2(x)$. Within experimental uncertainty, the ratio is consistent with unity. The plot is taken from [73].

1.2 Drell-Yan Process

The first measurement of high-mass muon pairs from hadron-hadron collisions was conducted in 1970 by Christenson et al [28]. They found that the continuum cross section was decreasing with increasing invariant dimuon mass. They also observed a shoulder around 3.1 GeV/c^2, which is known as the resonant state of J/ψ particle. This decay process was first suggested by Sidney D. Drell and Tung-Mow Yan [36]. The Drell-Yan process generally involves a quark-antiquark pair, denoted by $q\bar{q}$, that originates from the collision of two hadrons, labeled as H_A and H_B. This interaction is depicted in Figure 4. The advantage of the Drell-Yan process is that it provides access to the antiquark PDF, and the kinematics are simple and can be determined experimentally. The leading order Drell-Yan scattering cross section can be written as:

$$\frac{d^2\sigma}{dx_1 dx_2} = \frac{4\pi\alpha^2}{9x_1x_2s}\sum_i e_i^2[q_i(x_1)\bar{q}_i(x_2) + \bar{q}_i(x_1)q_i(x_2)], \tag{7}$$

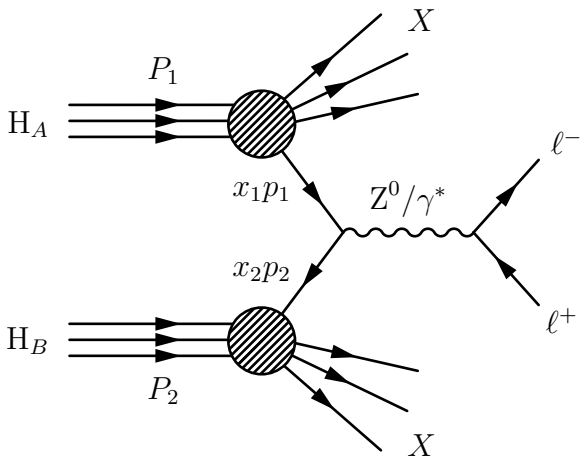

Figure 4: Feynman diagram of Leading Order Drell-Yan Process.

where x_1 and x_2 are the momentum fractions of the beam and target partons participating in the reaction, respectively. e_i is the charge of quark flavor i. $q(x)$ and $\bar{q}(x)$ are the probability distributions for quarks and antiquarks of flavor q in the proton. α is the fine-structure

constant, and s is the square of the center-of-mass energy of the beam and target. In the large x region, the quark distributions are primarily dominated by the valence quark, whereas at small x, sea quarks and gluons are more dominant. Details of the kinematic explanation are given in reference [57].

Variables	**Notations**
P_1, P_2	Beam and target hadron momenta.
l^-,l^+	Lepton and antilepton momenta.
y	Rapidity: $y = \frac{1}{2}\ln\left(\frac{E+p_l}{E-p_l}\right)$.
q	Virtual photon momentum, $q = l^- + l^+$.
Q^2	Dimuon invariant mass, $Q^2 = q^2 = M^2$.
q_T, $\lvert q_T\rvert$	Transverse component of q, where $q = (q^0, \vec{q})$.
$\tau = \frac{M^2}{s} = x_1 x_2$	
$x_1 = \sqrt{\tau}e^y$, $x_2 = \sqrt{\tau}e^{-y}$	Bjorken variable for beam and target x_1 (x_2).
$x_F = \frac{2q_L}{\sqrt{s}}$	The Feynman variable, where q_L is the longitudinal momentum of the dimuon.
θ, ϕ	Polar and azimuthal angles of l^- in the Collins-Soper frame.

Table 2: Kinematical variables are listed to describe a Drell-Yan process.

Higher Order Diagrams: Although the leading-order formula provides reasonable results for the Drell-Yan cross-section, as depicted in Figure 4, it does not predict well the transverse momenta of the dileptons, angular distributions, etc., because the model neglects interactions between the partons that constitute each of the hadrons. Therefore, it is important to include the QCD contributions to account for the remainder of the cross-section. Figures 5(a) and 5(b) show the QCD Compton diagram, while Figures 5(c) and 5(d) depict gluon production, and Figure 5(e) shows the vertex correction.

1.3 Collins-Soper Frame

Extracting the angular distributions of dilepton is typically done in a frame where the virtual photon is at rest. The coordinate system can be arbitrary, but depending on the chosen

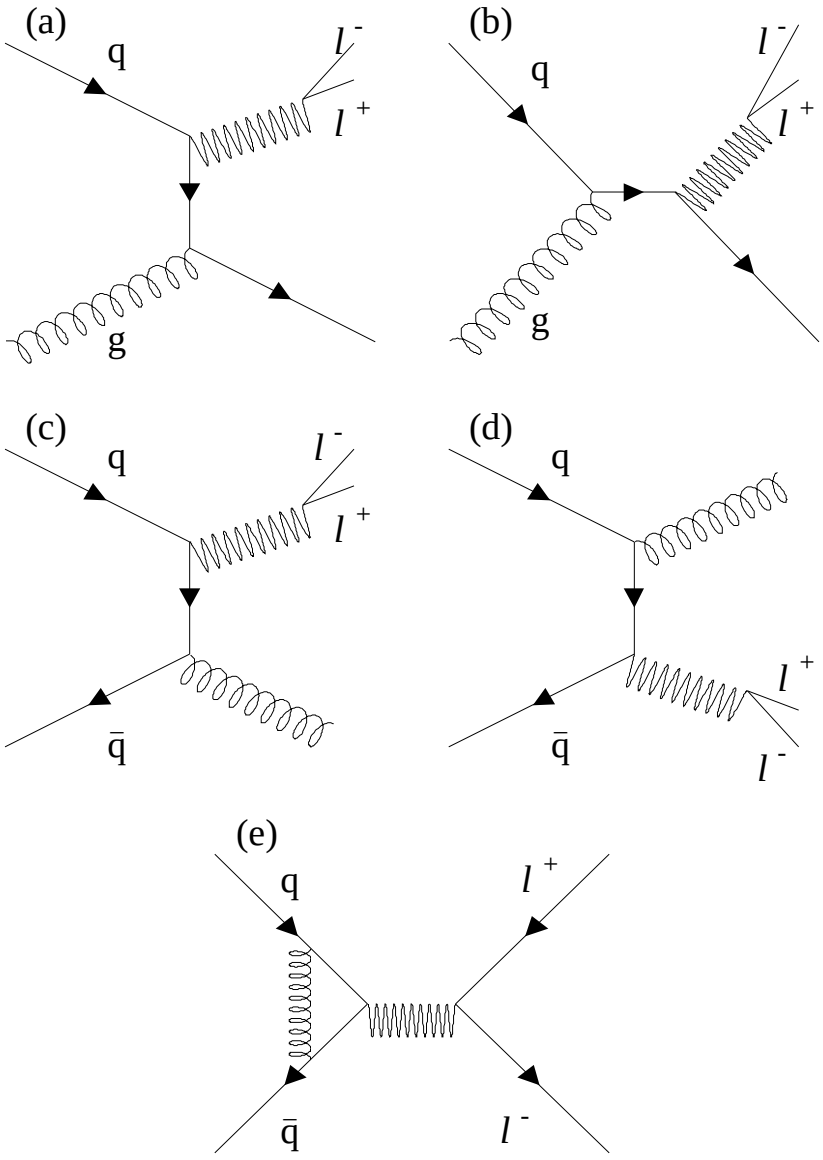

Figure 5: Higher order corrections to the leading order Drell-Yan process that include additional gluon diagrams. The figure is taken from [72].

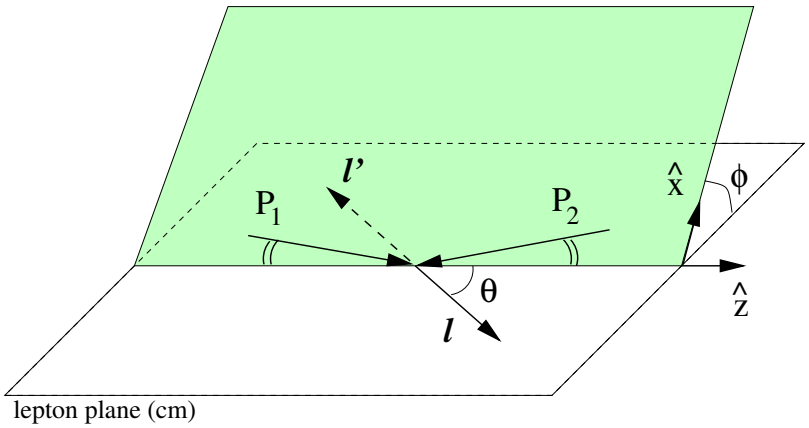

Figure 6: The polar and azimuthal angles θ and ϕ are shown in the Collins–Soper frame. P_1 and P_2 represent the beam and target hadron momenta. The z-axis is the bisector of the two interacting hadron momenta, and the x-axis aligns with the transverse momentum of the dimuon P_T. The momenta l and l' correspond to the lepton and antilepton, respectively. The angular difference between the leptons and the beam/z-axis is denoted as θ in the Collins–Soper frame, while ϕ measures the angles between the lepton and the hadron plane. The Figure is taken from [17].

coordinate system, we may have different numerical values for the parameters. To report the parameter values of the angular distribution of the dimuons, we have chosen a particular rest frame of the virtual photon, known as the Collins-Soper frame, where the z-axis is defined as the bisector of the two interacting hadron momenta. It can be obtained through two successive boosts as follows:

- The first boost along the beam direction, to the interaction center-of-mass frame, sets the z-momentum of the virtual photon to zero ($Q_z^* = 0$ or $Q^* = Q_T$).
- The second boost is applied along the transverse momenta, setting the muon pair back-to-back.

The detailed derivation of the angular distribution variables can be found in Ref. [31]. Accordingly, the polar and azimuthal angles of the dimuons can be calculated using the formula in laboratory frame variables below:

$$\cos\theta = \frac{2(l_1^+ l_2^- - l_1^- l_2^+)}{Q\sqrt{Q^2 + Q_T^2}} \tag{8a}$$

$$\tan\phi = \frac{\sqrt{Q^2 + Q_T^2}}{Q} \frac{\Delta_T \cdot \hat{R}_T}{\Delta_T \cdot \hat{Q}_T} \tag{8b}$$

$$l^{\pm} = \frac{l^0 \pm l_z}{\sqrt{2}} \tag{9a}$$

$$Q = l_1 + l_2, \quad \Delta = l_1 - l_2 \tag{9b}$$

$$\hat{R} = \frac{P_A \times Q}{|P_A \times Q|}, \quad \hat{Q_T} = \frac{Q_T}{|Q_T|} \tag{9c}$$

$\hat{Q}_T$, $\hat{R}_T$ are the transverse unit vector in the direction of $\vec{Q}_T$ and $\vec{P}_T \times \vec{Q}$ respectively. The Collins-Soper frame is illustrated in the Figure 6 [15]. Unless specified otherwise, the angular distribution analysis is performed in the Collins-Soper frame.

1.4 Angular Distribution of the DY Process

The general expression for the angular distribution of the leptons in unpolarized Drell-Yan process has been extensively discussed in the following references [15, 31, 58] and can be written as:

$$\frac{dN}{d\Omega} = \frac{3}{4\pi} \frac{1}{\lambda + 3} \left[1 + \lambda \cos^2\theta + \mu \sin 2\theta \cos\phi + \frac{\nu}{2} \sin^2\theta \cos 2\phi\right], \tag{10}$$

where $d\Omega = dcos\theta\ d\phi$ is a solid angle of the lepton in terms of its polar and azimuthal angles in the center of mass frame of the lepton pair. A different parameterization [31] form is often used as:

$$\frac{dN}{d\Omega} = \frac{3}{16\pi}\left[1 + \cos^2\theta + \frac{A_0}{2}(1 - 3\cos^2\theta) + A_1 \sin 2\theta \cos\phi + \frac{A_2}{2}\sin^2\theta \cos 2\phi\right] . \quad (11)$$

The A_n coefficients can be written as $A_n(s, Q^2, y, \vec{Q}_T^2)$ with $n = 0, 1, 2$, and can be related to the angular coefficients as follows:

$$\lambda = \frac{2 - 3A_0}{2 + A_0} , \quad \mu = \frac{2A_1}{2 + A_0} , \quad \nu = \frac{2A_2}{2 + A_0} , \quad (12)$$

In the case of the naive Drell-Yan model, which does not consider the transverse motion of the quark and also doesn't account for gluon interactions in the production of the dimuons, $\lambda = 1$, and $\mu = \nu = 0$. However, once the QCD effect is included, and the non-zero intrinsic transverse momentum of the quarks is considered, the ν parameter is no longer zero [29]. Regarding the QCD effect that appears in the ν coefficients, an interesting relationship known as the Lam-Tung relation was obtained in Ref. [59], which shows that

$$1 - \lambda - 2\nu = 0, \quad (13)$$

and this relationship holds in LO QCD corrections [77], and even at NLO QCD, the numerical violation is small [5, 64].

The first experiment on angular distributions for Drell Yan was conducted by the NA10 Collaboration [45, 52] for $\pi^- + \mathrm{W}$ at 140, 194, and 286 GeV/c. In the experiment, in the

Collins-Soper frame, λ was found to be close to 1 and substantially independent of P_T as shown in Figure 7. μ was found to be zero. One of the striking results from the experiment is that large $\cos 2\phi$ modulations were observed, leading to sizable values of ν that increase with the dimuon transverse momentum P_T. The extracted ν parameter is larger than the predicted value from leading-order perturbative QCD, which considers the resummation of soft gluons [27]. Another pion-induced Drell-Yan experiment at Fermilab, Experiment-615 (E615) [33], observed non-zero values of ν, clearly violating the Lam-Tung relation $1 - \lambda - 2\nu = 0$ for the E615 data, as shown in Figure 8.

However, the first measurement of the proton-induced Drell-Yan angular distributions in the Fermilab experiment found small violations of the Lam-Tung relationship compared to the pion-induced Drell-Yan process in the NA10 and E615 experiments. The NuSea/E866 experiment used an 800 GeV proton beam interacting with hydrogen and deuterium targets, as shown in Figure 8.

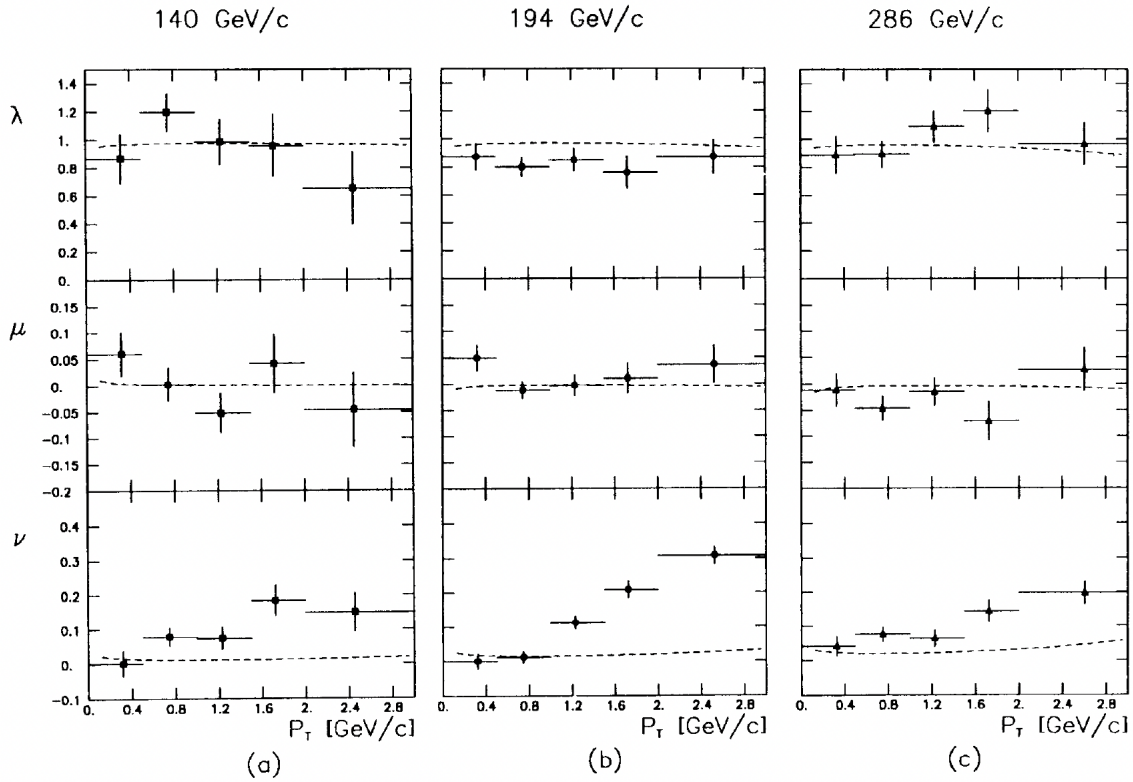

Figure 7: The three graphs show measurements of the angular distributions of the Drell-Yan process in the Collins-Soper frame as a function of the dimuon's transverse momentum P_T, at different π^- beam energies that impinged on tungsten, deuterium, and tungsten targets respectively. The error bars represent statistical uncertainties only, and the dashed curves show perturbative QCD predictions [27]. The figure is taken from [52].

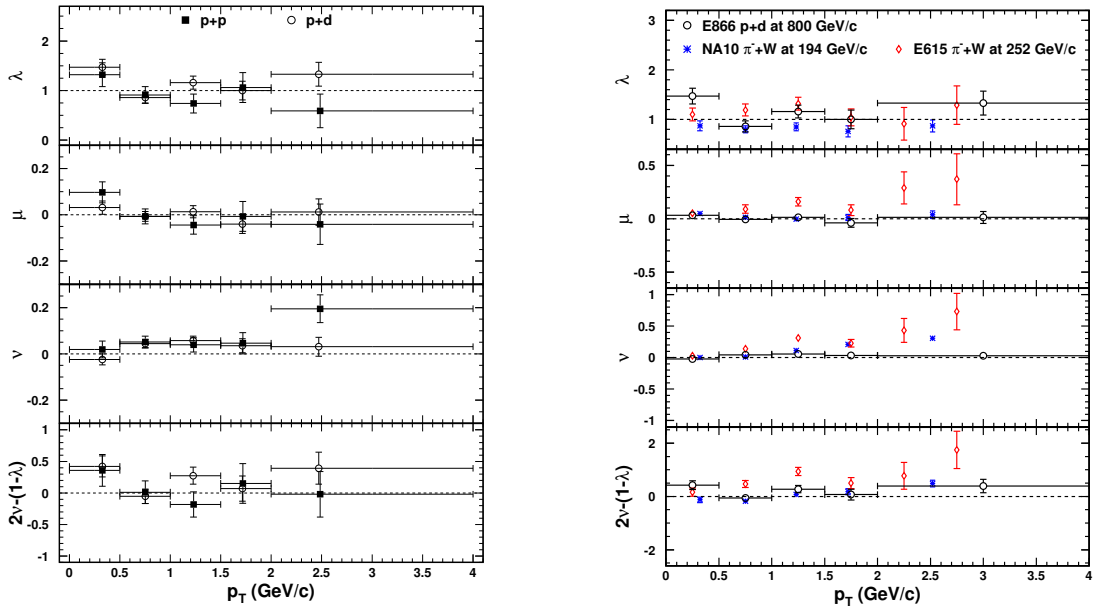

Figure 8: The two figures are taken from the E866/NuSea experiments [80, 79], where the angular distributions of the Drell-Yan process have been measured in the Collins-Soper frame as a function of the dimuon's transverse momentum P_T. The left plot shows the results for $p+p$ and $p+d$ measured in the E866 experiment, and the right one shows the pion-induced Drell-Yan interactions $\pi^- + \mathrm{W}$ events from CERN-NA10 [45, 52] (blue star) and from E615 [33](red diamond). The figure is taken from [80, 79].

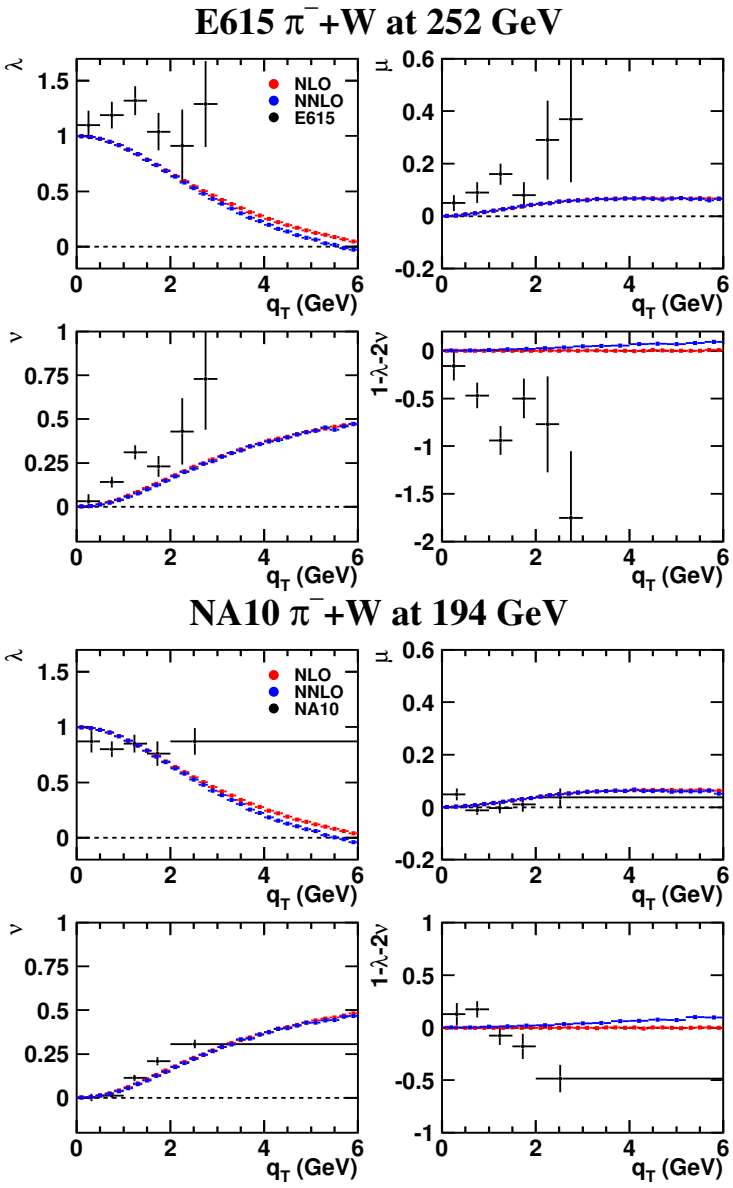

Figure 9: A comparison is made between the NLO (red points) and NNLO (blue points) fixed-order pQCD calculations with the E615 [33] and NA10 [45, 52] data. The figure is taken from [25].

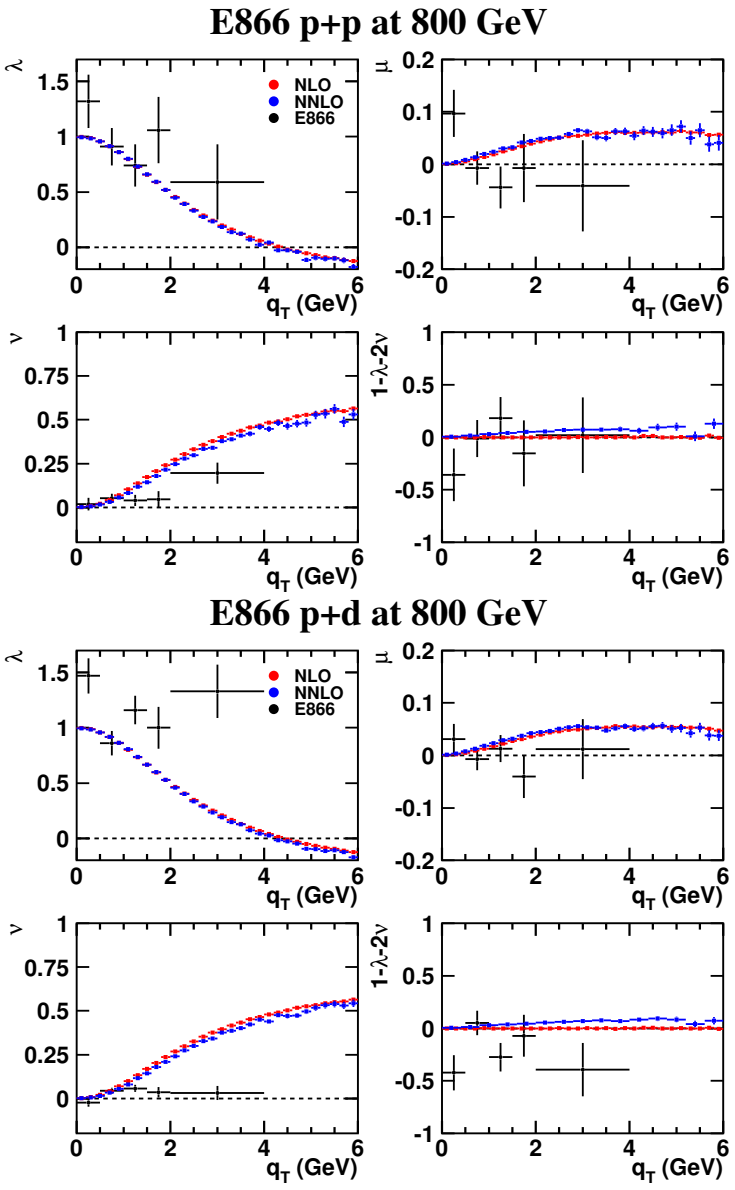

Figure 10: A comparison is made between the NLO (red points) and NNLO (blue points) fixed-order pQCD calculations with the E866 data [80, 79]. The figure is taken from [25].

Figure 9 shows the results of the angular distribution coefficients compared with the QCD-predicted values using NLO and NNLO fixed-order perturbative QCD calculations from the E615 and E866 pion-induced Drell-Yan experiments. The author of the paper [25] concludes with a few remarks for Figure 9:

- There could be some systematic effects in the data, as the λ value doesn't decrease as QCD predicts.
- Agreement on the μ parameter is better for the NA10 experiment than for E615.
- The extracted ν parameter at E615 is larger than the perturbative QCD predicted one, but NA10 shows reasonable agreement.
- In NA10 and E615, both datasets predict larger Lam-Tung violations than NNLO pQCD, and also the predicted Lam-Tung quantity shows the opposite trend compared to the data.
- Since ν increases as the transverse momentum increases, one must account for the pQCD effect before extracting the Boer-Mulder Function.

On the other hand for the E866 experiments, the remarks are below:

- Large lambda values ($\lambda > 1.0$) did not follow the positive constraint for λ. For example, according to the [58, 60], we must have $\lambda \leq 1$.
- Since the predicted ν from pQCD is larger than the data suggests, it implies a negative contribution from the Boer-Mulder effect, which exhibits the opposite trend compared to the pion-induced Drell-Yan process.

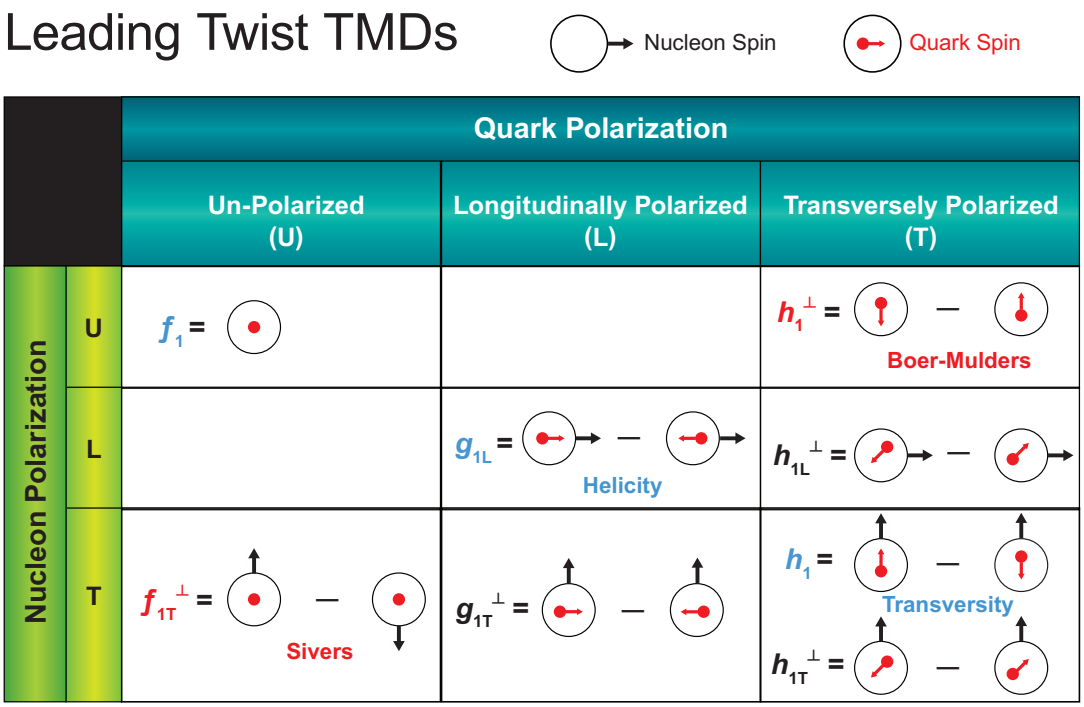

Figure 11: Leading-twist transverse momentum-dependent (TMD) distributions, classified by the polarizations of quarks (f, g, h) and nucleons (U, L, T), include $f_{\perp}^{1T}$ and $h_{\perp}^{1}$, termed naive time-reversal-odd TMD distributions, with a corresponding classification for gluons. Plot from Reference [2]

1.4.1 Boer-Mulder Function

The Transverse Momentum Dependent distribution functions (TMDs) represents the probability of a parton in a hadron with a longitudinal momentum fraction x and transverse momentum k_T, along the direction of the hadron's momentum [32, 8]. It provides three-dimensional densities in momentum space. From the TMDs, one could learn about the various correlations among quark spin, hadron momentum, and hadron spin. The Boer-Mulders function, $h_{\perp}^{1}$, is one of the TMDs [17], which describes the correlation between k_T and the quark's transverse spin, $s_{\perp}$, in an unpolarized nucleon. The function is shown in Figure 11, along with other TMDs.

The first extraction of the Boer-Mulders function is provided in reference [17], where the Transverse Momentum Dependent (TMD) function $h_1^{\perp,q}(x, \mathbf{k}_T^2)$ is factorized into x and k_T based on a Gaussian model with width k_{bm}^2 [78]:

$$h_1^{\perp,q}(x, \mathbf{k}_T^2) = h_1^{\perp,q}(x) \frac{\exp(-\mathbf{k}_T^2/k_{bm}^2)}{\pi k_{bm}^2}. \tag{14}$$

Using a simple parametrization, the x-dependence of the Boer–Mulders functions can be expressed in terms of the unpolarized integrated distribution function $f_1^q(x)$ as follows: $h_1^{\perp,q}(x, p_\perp^2) = H_q\, x^c\, (1-x)\, f_1^q(x) \exp\left(-p_\perp^2/p_{bm}^2\right)$, aiming to fit the data points of the asymmetry coefficient ν versus p_T, x_1, and x_2, where q stands for the u, d, $\bar{u}$, or $\bar{d}$ quarks. The inclusion of the coefficient $(1-x)$ is necessary to ensure the correct large-x behavior [20] for $h_1^\perp$ compared to the unpolarized distribution.

The best fitting values for the parameters are provided in Table 3. Figure 12 shows ν versus p_T for the $p+p$ and $p+d$ Drell-Yan data [80, 79]. Using the E866 $(p+d)$ data, the Boer-Mulders functions were parametrized. Then, the solid (black) and dotted (red) curves were calculated for the $(p+p)$ and $(p+d)$ data. The prediction from the Boer-Mulder function in the region of $\sim 1.5 GeV/c$ is higher for $p+p$ interactions than for $p+d$. However, the experimental extraction of the value ν does not reflect this.

H_u	3.99
H_d	3.83
$H_{\bar{u}}$	0.91
$H_{\bar{d}}$	-0.96
p_{bm}^2	0.161
c	0.45
$\chi^2/d.o.f.$	0.79

Table 3: Best fit values of the Boer-Mulders functions [78].

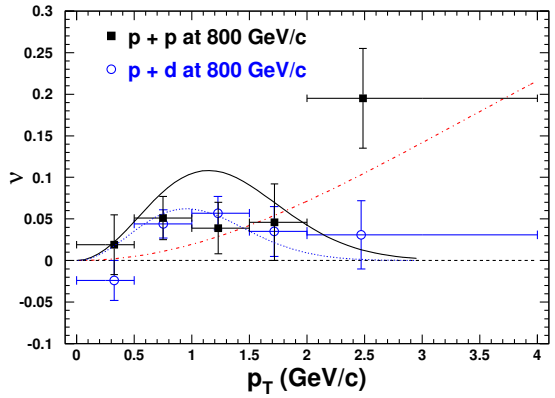

Figure 12: The plot has been taken from the NuSea/E866 experiment [81], where ν is shown as a function of dimuon P_T for $p+d$ and $p+p$ Drell-Yan data. The dotted and solid curves represent calculations [78] for $p+d$ and $p+p$ processes, respectively, using parameterizations based on a fit to the $p+d$ data. The red dot-dashed curve corresponds to the contribution from the perturbative QCD at $\mathcal{O}(\alpha_s)$ [16, 30].

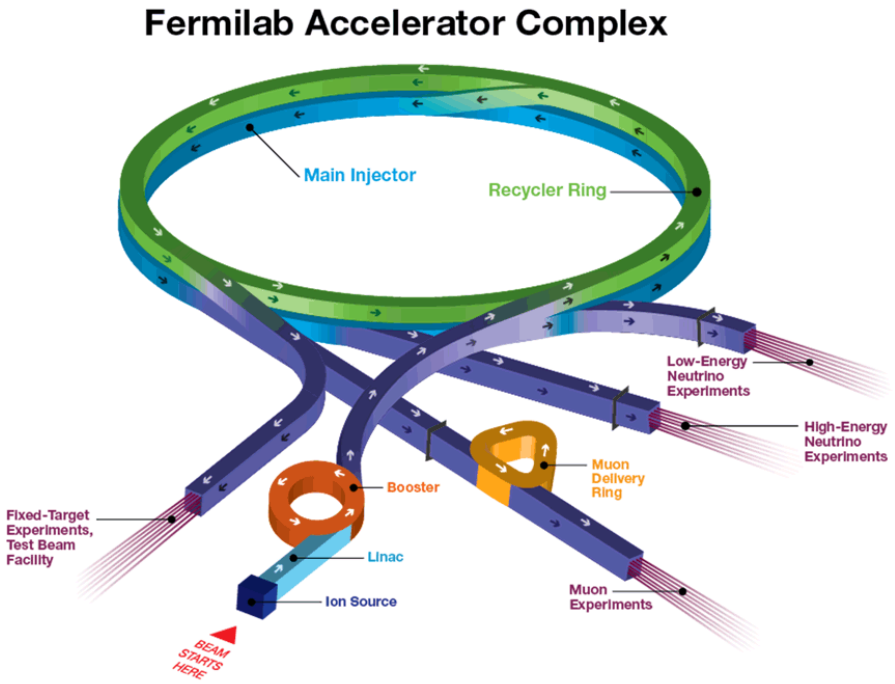

Figure 13: Fermilab accelerator complex. The figure is taken from Ref. [3].

2 The E906/SeaQuest Experiment

The Fermilab-based E906 SeaQuest experiment is a fixed-target dimuon experiment designed to produce dimuon pairs through the Drell–Yan process. The experiment is located near the KTeV hall and uses a 120 GeV unpolarized proton beam from the Fermilab Main Injector, whereas the earlier experiment E866/NuSea used an 800 GeV proton beam. The origin of the 120 GeV proton beam is shown in Figure 13. This chapter provides an overview of SeaQuest's experimental setup. Key elements, including the beam structure, target design, and advanced detector technology in the muon spectrometer, are highlighted. Further details can be found in the article [3].

2.1 E906/SeaQuest Spectrometer Overview

The SeaQuest spectrometer, approximately 25 meters in length, incorporates a variety of liquid and solid targets, two dipole magnets, four tracking/triggering stations, and two hadron absorbers. The spectrometer is designed to detect high dimuon mass through four tracking/triggering stations, where photomultiplier tube (PMT)-based trigger detectors are used to detect the muon signal. Field Programmable Gate Array (FPGA)-based triggers are employed for physics data taking, while Nuclear Instrument Modules (NIM)-based triggers are used and heavily prescaled to register other triggers.

The magnet, known as KMag and located between stations 1 and 2, is used for momentum measurement. The other magnet, FMag, located upstream of the target positions, is used as a hadron absorber, and it is also known as the focusing magnet. The other hadron absorber, positioned between stations 3 and 4, is employed for muon identification. The details are shown in the Figure 14.

2.2 Beam Monitor

SeaQuest receives a 5-second spill approximately once per minute, and during this time, it is not guaranteed that we receive protons uniformly in different RF buckets. This poses significant disadvantages for the DAQ, triggers, and reconstructions. Since one of the main goals of the SeaQuest experiment is to extract the ratio of $\frac{\bar{d}}{\bar{u}}$, it is important to monitor the beam buckets, as this information is required later for normalizing events originating from different target locations. To measure the protons from RF bucket to RF bucket, a Cherenkov counter was located upstream of the test. The Cherenkov counter is shown in Figure 15. As illustrated in the figure, the aluminized Kapton mirror is held at a 45° angle,

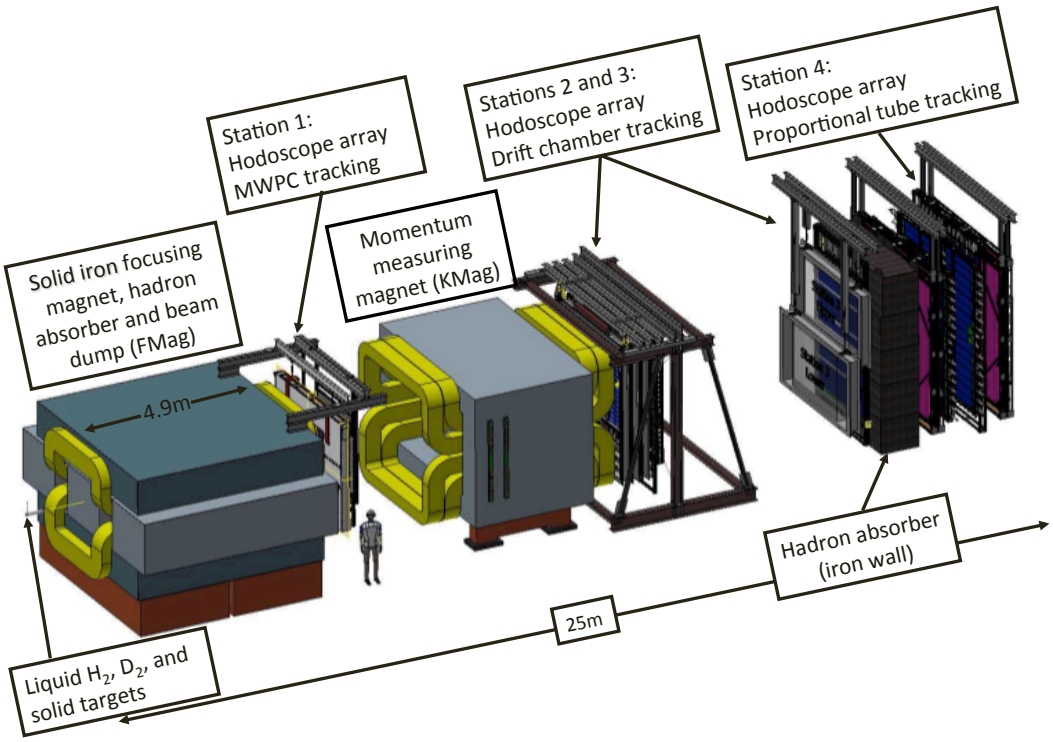

Figure 14: A detailed schematic representation of the SeaQuest spectrometer. The figure is taken from Ref. [3].

directing the light to the PMT. A readout board called QIE integrates and digitizes the signal received from the PMT. Since the protons in the RF bucket are synchronized, the readout system is synchronized with them. The counter has a short response time and measures the protons in each 53 MHz RF-bucket. It is also used to inhibit the triggers until the intensity falls to a reasonable level, which is about 65,000 and 95,000 protons per bucket. Located upstream of the Cherenkov counter, a Secondary Emission Monitor (SEM) is used for the normalization of the beam intensity. Integration of the SEM signal occurs over each spill.

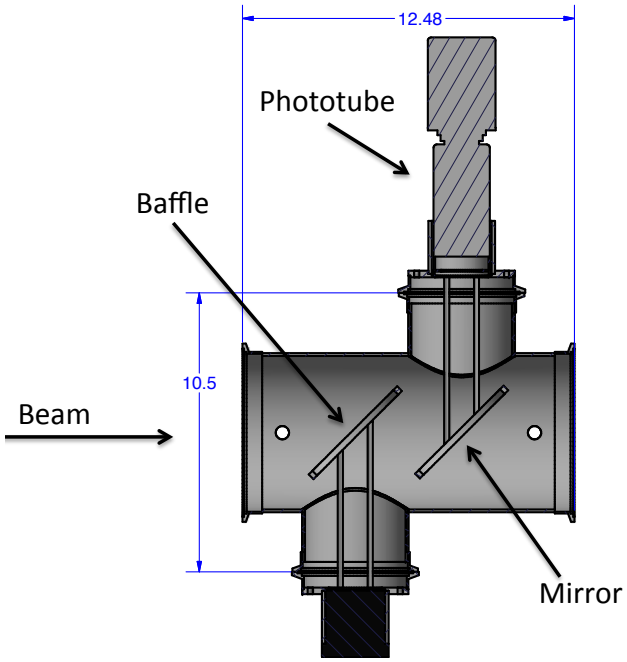

Figure 15: Beam Intensity Monitor (BIM) Cherenkov counter. The figure is taken from Ref. [3].

2.3 Targets

The target system includes two liquid targets (hydrogen and deuterium) and three solid targets (iron, carbon, and tungsten), all centered 130 cm upstream of the first spectrometer magnet known as FMag. The summary of the target system is listed in the table 4.

The liquid hydrogen was 99.999% pure. SeaQuest initially used gas for deuterium with a slight hydrogen contamination from ^{2}H and ^{1}H, where the mass spectroscopy was 95.8$\pm$0.2%. Later, SeaQuest switched to commercially available deuterium with 99.90% purity.

2.4 Magnet

There are two dipole magnets in SeaQuest, named FMag and KMag shown in the Fig. 14. FMag, also known as the beam dump or hadron absorber in station 1, upstream of

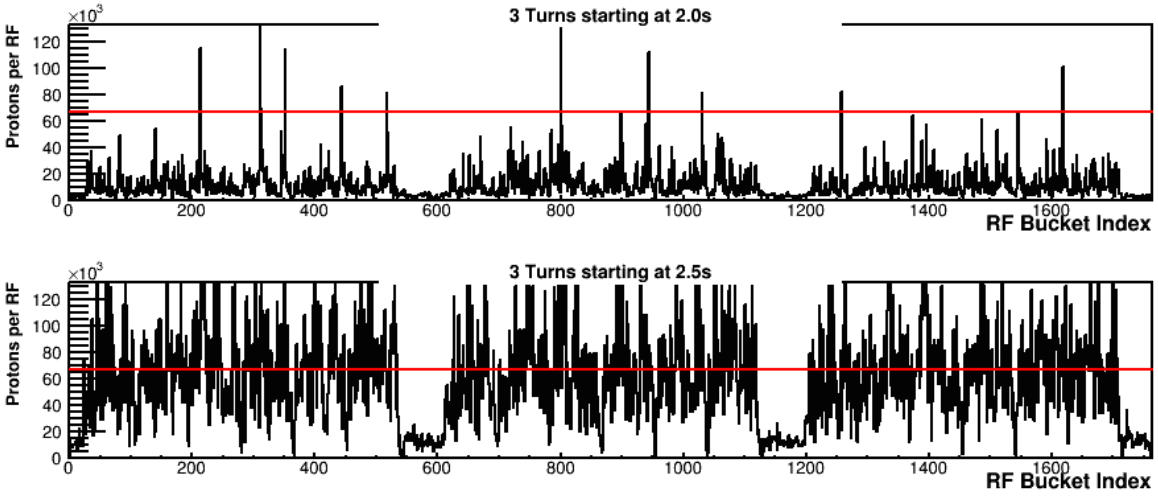

Figure 16: The figure shows the protons per RF bucket vs. RF Bucket Index, which were measured by the Beam DAQ Cerenkov counter. The red line indicates the threshold for trigger inhibition. No data will be recorded if the intensity exceeds the red line. However, the lower plot shows that the number is quite high. The figure is taken from Ref. [3].

the KMag, is made of iron slabs with dimensions of $43.2cm \times 160cm \times 503cm$. It has a 5cm (diameter) $\times 25cm$ hole. Low momentum muons don't get accepted in the SeaQuest spectrometer due to the high magnetic field strength. The 120 GeV protons that intended to interact with either the solid or liquid targets but did not interact, would interact within the central iron slab. Protons interacting with the iron target (FMag) can produce proton-induced Drell-Yan events, making FMag a suitable medium for studying this process with very high statistics. This thesis will analyze Drell-Yan dimuons originating from the iron dump target location. An optimized event selection, to be described in a later section 3.3, will isolate events originating from the dump location. The momentum-measuring magnet called KMag located between the station 1 and 2, is a 300 cm long iron rectangular magnet with a central air gap measuring 289 cm wide by 203 cm high. In FMag and KMag both,

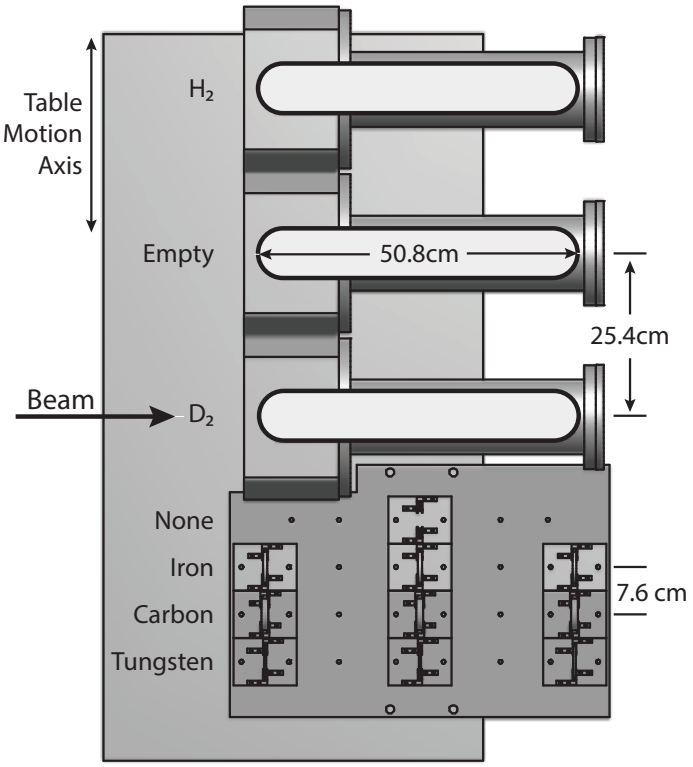

Figure 17: The figure presents a top-view diagram of the adjustable target table, illustrating the seven distinct positions. The figure is taken from Ref. [3].

Position	Material	Density (g/cm^3)	Thickness (cm)	Number of Interaction Lengths	Spills/ Cycle
1	H_2	0.071	50.8	0.069	10
2	Empty Flask	–	–	0.0016	2
3	D_2	0.163	50.8	0.120	5
4	No Target	–	–	0	2
5	Iron	7.87	1.905	0.114	1
6	Carbon	1.80	3.322	0.209	2
7	Tungsten	19.30	0.953	0.096	1

Table 4: SeaQuest target features. Taken from the Ref. [3].

the magnetic fields have been optimized based on the J/ψ resonance peak. The magnetic fields are vertically oriented, with the former data-taking runs aligned with +y and the latter with -y for this experiment. This thesis focuses only on analyzing trigger-road 67, where the magnetic field is directed along the -y axis.

Magnet	**Current (A)**	**Power (kW)**	**Voltage (V)**	**Field (T)**	**Origin**
FMag	2000	50	25	1.8	Columbia University Nevis Laboratory Cyclotron [46]
KMag	1600	430	270	0.4	University of Maryland Cyclotron (E799/KTeV collaboration [4])

Table 5: Summary of Spectrometer Magnet Configurations.

2.5 Hodoscopes

Hodoscopes in the SeaQuest spectrometer are made of plastic scintillators, serving as trigger detectors in four tracking stations. There are two kinds of hodoscope planes: 'X-planes,' measuring the x-position with vertically aligned paddles, and 'Y-planes,' measuring the y-position with horizontally aligned paddles. Stations 1, 2, and 4 have both X-planes and Y-planes, while Station 3 only has an X-plane. All the hodoscopes in Station 4 have PMTs on both ends of the scintillator bars, while in Stations 1, 2, and 3, hodoscope scintillators

have only one PMT on each of the scintillators. Each plane's scintillator bars in Station 4 are divided to create top/bottom pairs (for X hodoscope planes) or left/right pairs (for Y hodoscope planes). Figures 18, 19, 20, and 21 show the drawings of the hodoscopes, illustrating the geometry. The table 6 provides information regarding the number of hodoscope paddles in each station and their dimensions. Scintillator bars are connected to a readout photomultiplier tube (PMT) and sent to the hodoscope rack for discrimination using CAMAC-based modules. One additional feature of the module is that the current sum of each module, functioning like an 'OR' operation, is sent to the NIM trigger system. Using ribbon cables, channel-by-channel discriminated signals go to the DAQ and the FPGA trigger system. The PMTs are powered by LeCroy 1440 high-voltage supplies, where voltage can be monitored and controlled remotely. The 1443 Series of High Voltage Plug-in cards (16 channels) are used in the LeCroy 1440 high-voltage supplies, with each channel representing one of the PMTs. The hodoscope paddles are module-based, meaning each hodoscope paddle is separated. To compensate for this inefficiency, there are small overlaps between the paddles. This improves the efficiency of the triggers, but overlapping the bars also reduces the discriminating ability to identify background muon tracks. As the scintillators are very time-sensitive, all paddles are wrapped in black paper, so light leaks can be ignored. For the physics trigger, only x-measuring hodoscopes participate, while Y hodoscopes are involved in measuring the X-hodoscope efficiencies since the Y hodoscopes don't participate in the physics trigger. Stations 1 and 2, located very close to the target area, operate at high rates. The TDC time distributions from different hodoscope planes are shown in Figures 22, 23, 24, 25. In the figure it is shown how the RF in-time cut filters out the good hits, which eventually can be used as Hodoscope masking.

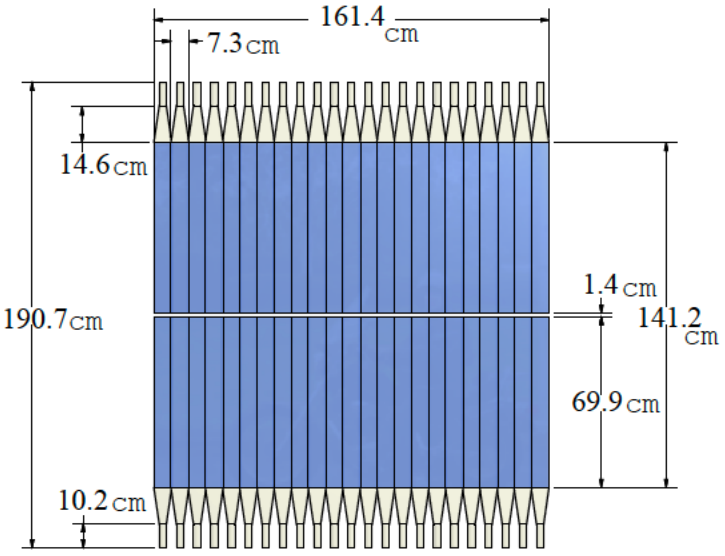

Hodoscope Array 1X

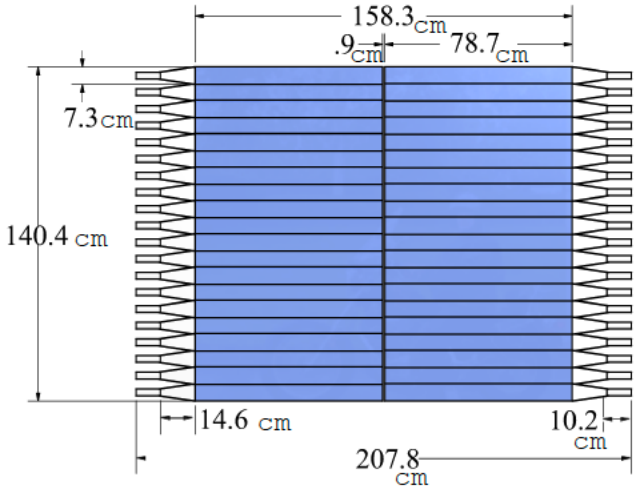

Hodoscope Array 1Y

Figure 18: The figure shows the scintillator hodoscopes for Station 1, denoted as H1X and H1Y. They are also known as the X and Y measuring hodoscopes. The figure is taken from Ref. [67].

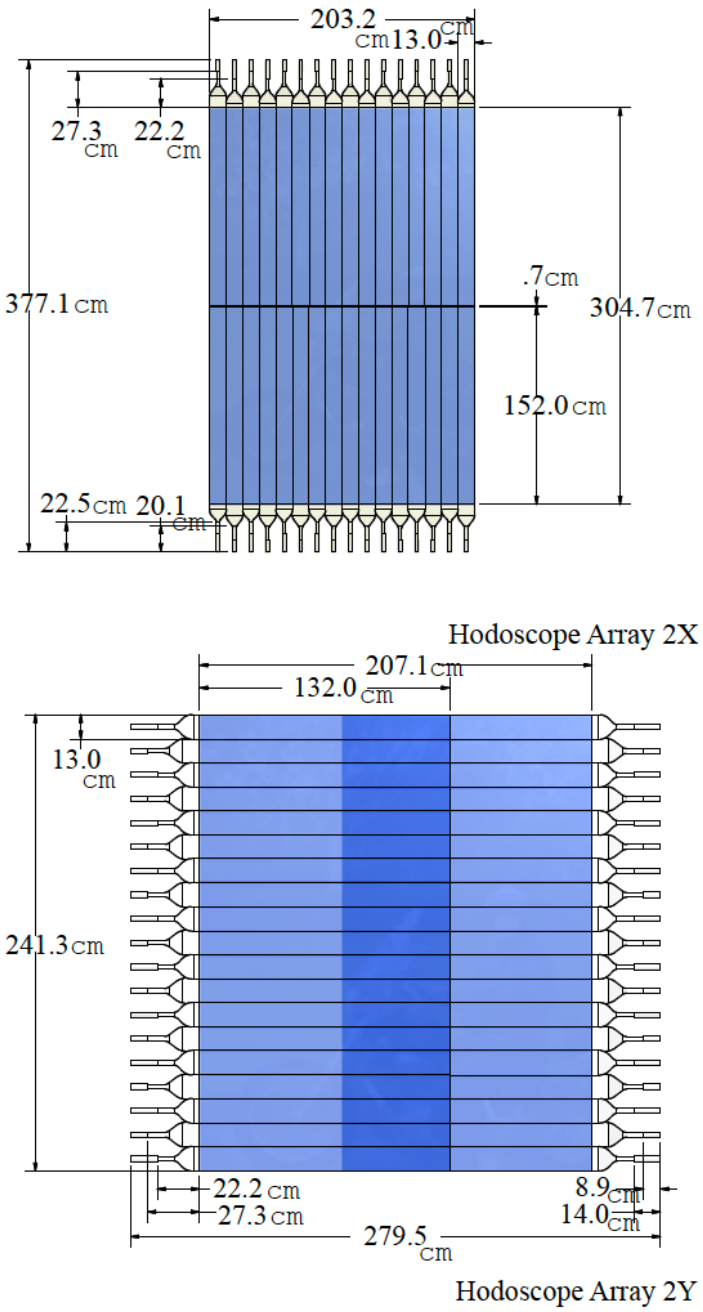

Figure 19: The figure shows the scintillator hodoscopes for Station 2, denoted as H2X and H2Y. The figure is taken from Ref. [67].

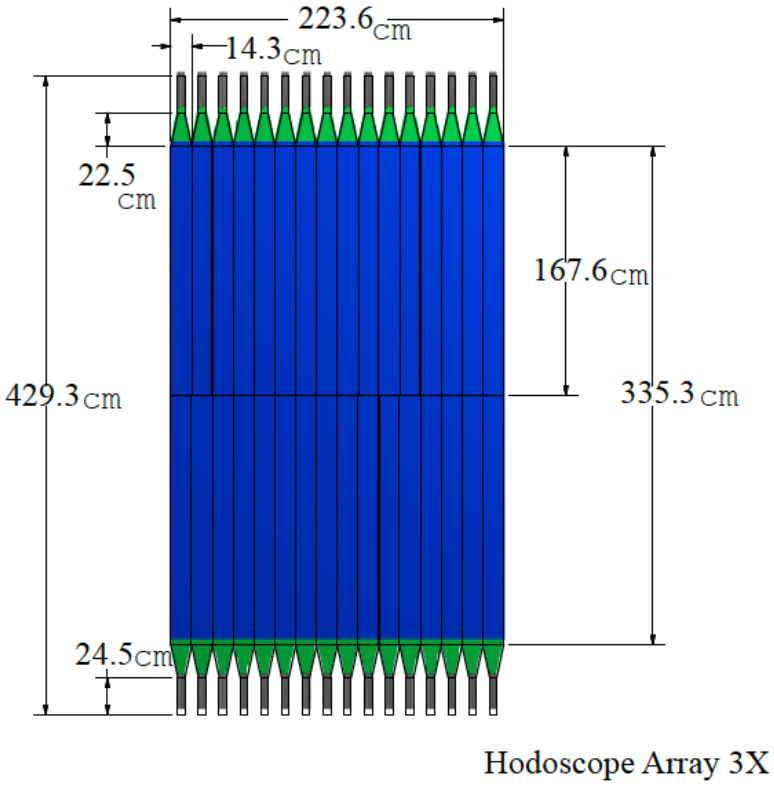

Figure 20: The figure shows the scintillator hodoscopes for Station 3, denoted as H3X. The figure is taken from Ref. [67].

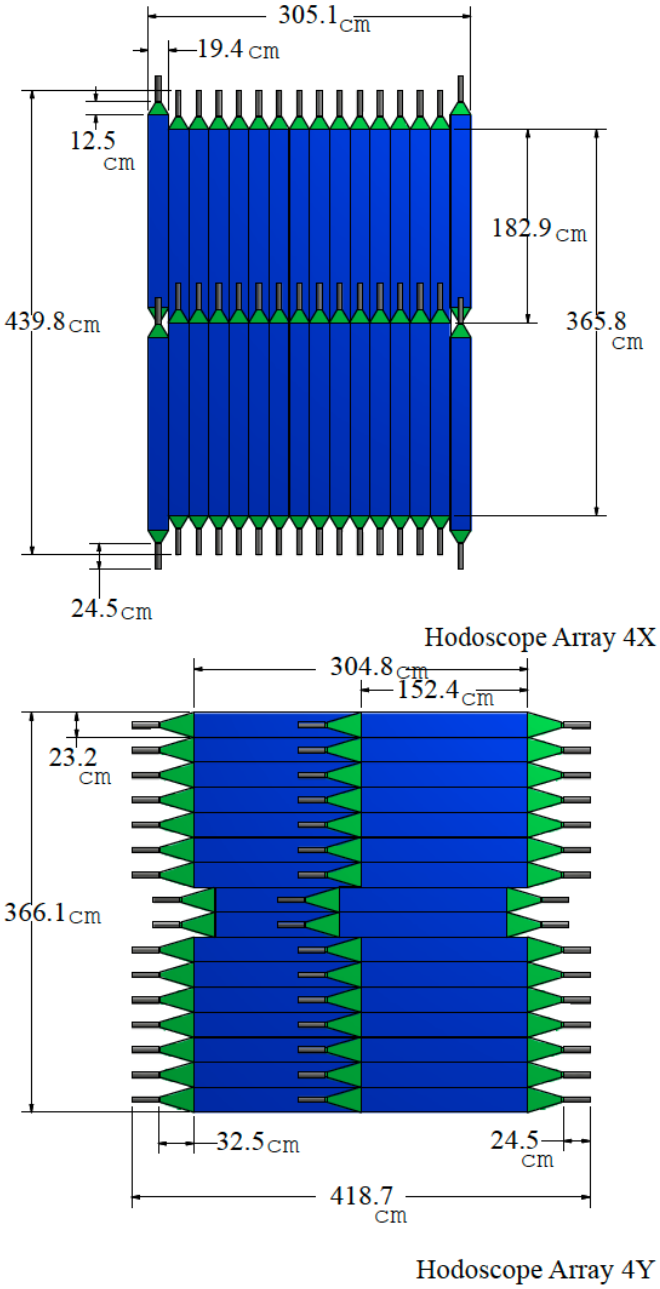

Figure 21: The figure shows the scintillator hodoscopes for Station 4, denoted as H4X and H4Y. The figure is taken from Ref. [67].

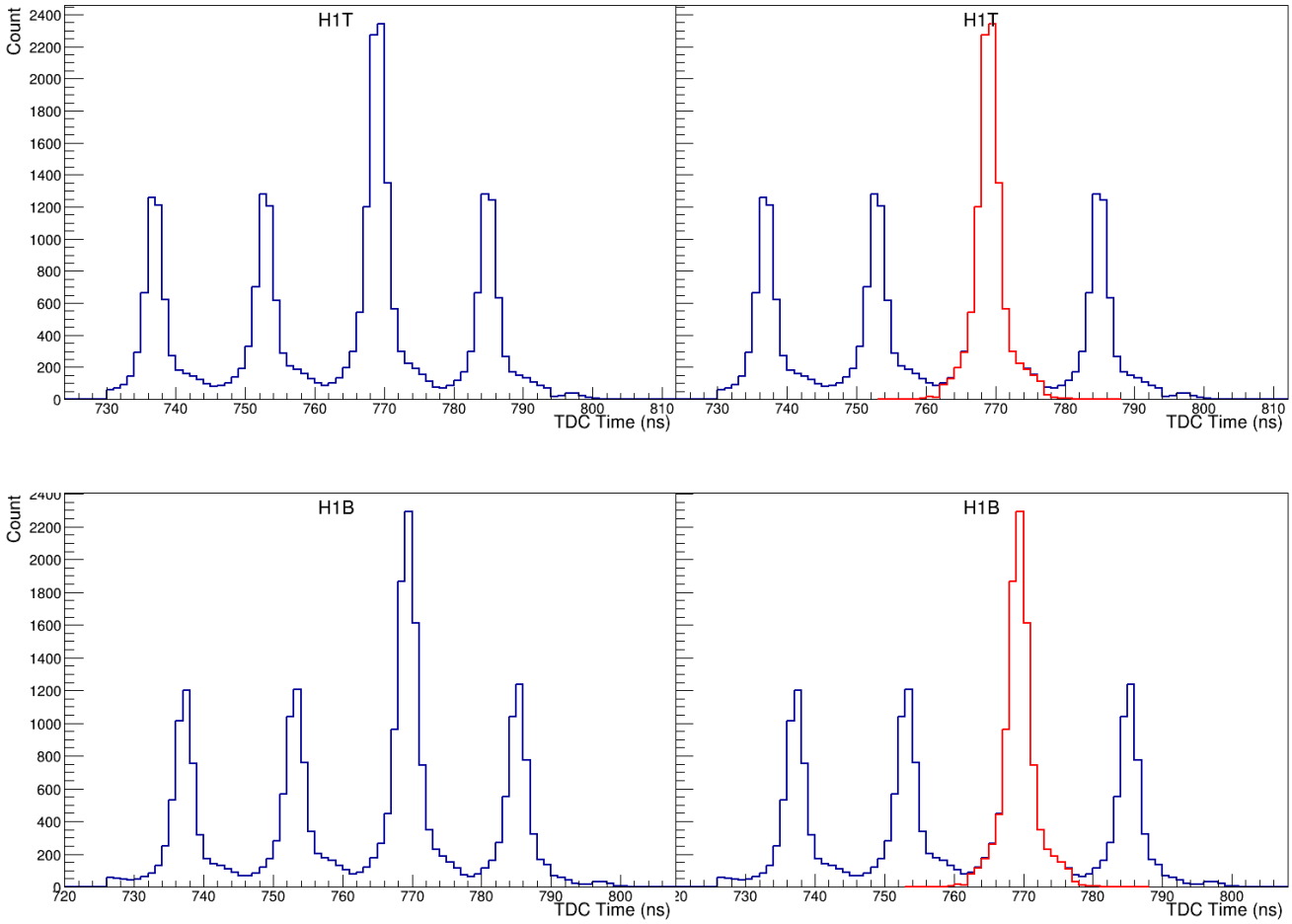

Figure 22: TDC time distributions of the top (H1T) and bottom (H1B) hodoscope planes. The left plot shows TCD time distributions for the FPGA trigger hits, and the right plot shows the Distributions (red) after applying the RF-based in-time cut.

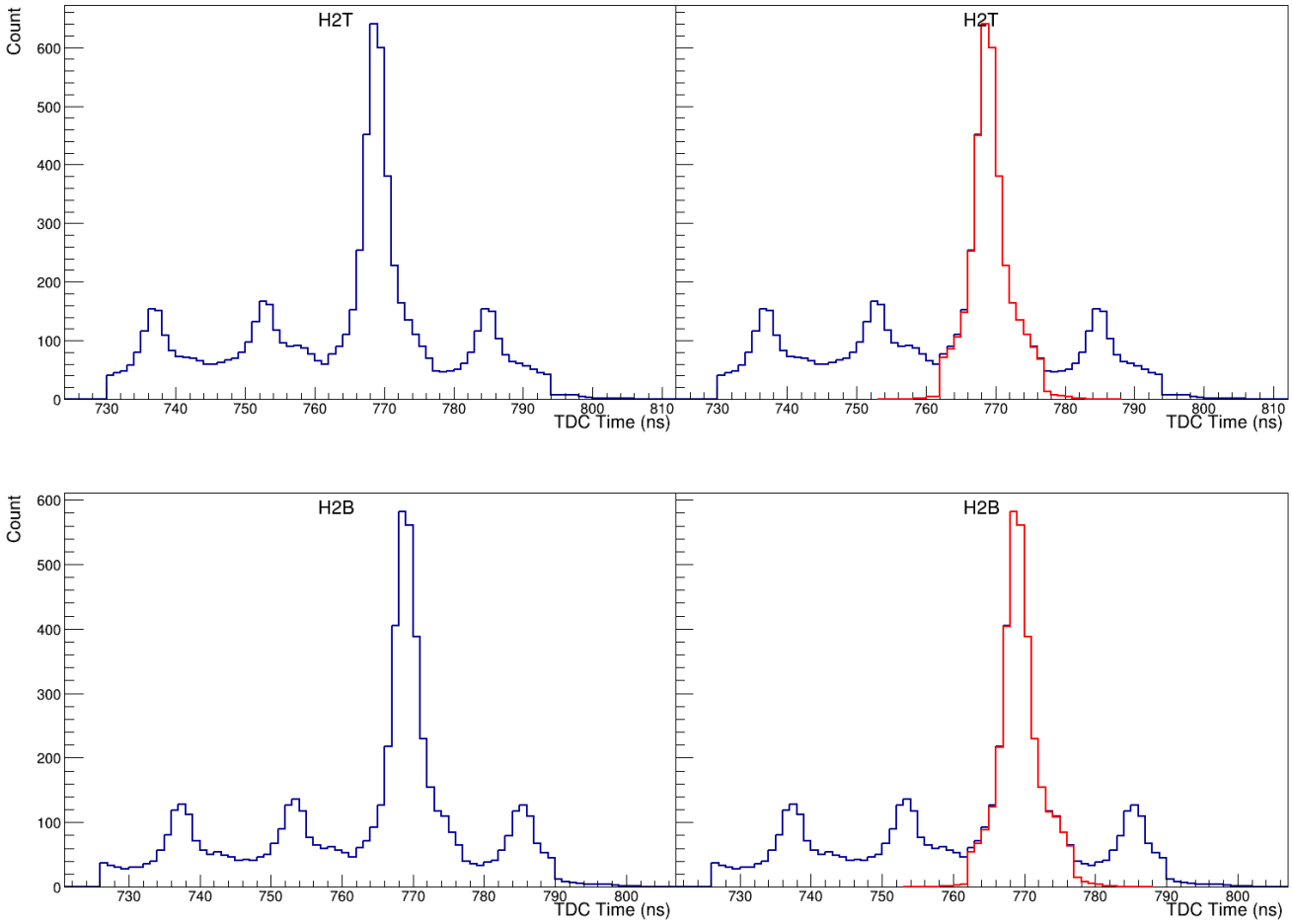

Figure 23: TDC time distributions of the top (H2T) and bottom (H2B) hodoscope planes. The left plot shows TCD time distributions for the FPGA trigger hits, and right plot shows the Distributions (red) after applying the RF-based in-time cut.

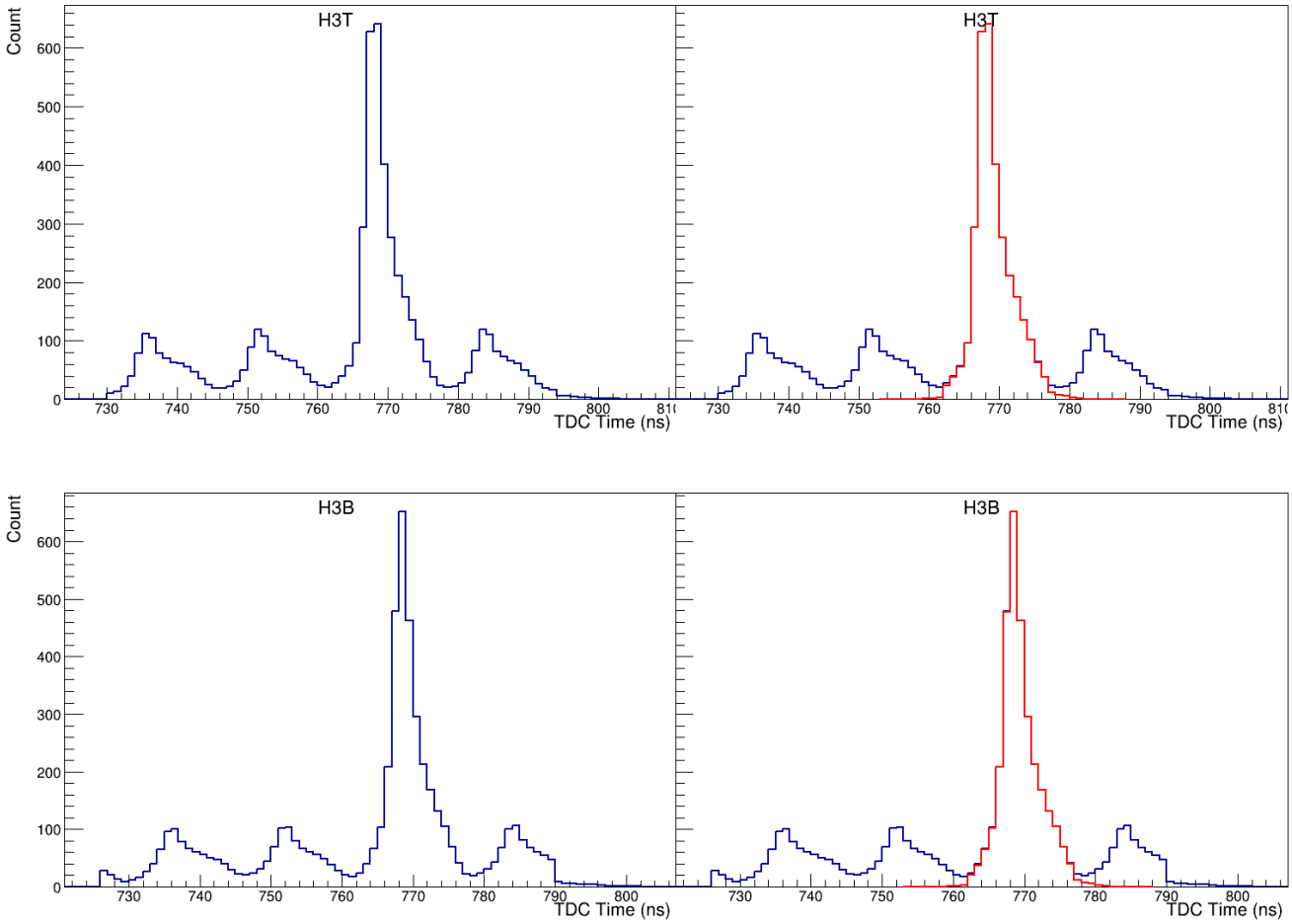

Figure 24: TDC time distributions of the top (H3T) and bottom (H3B) hodoscope planes. The left plot shows TCD time distributions for the FPGA trigger hits, and right plot shows the Distributions (red) after applying the RF-based in-time cut.

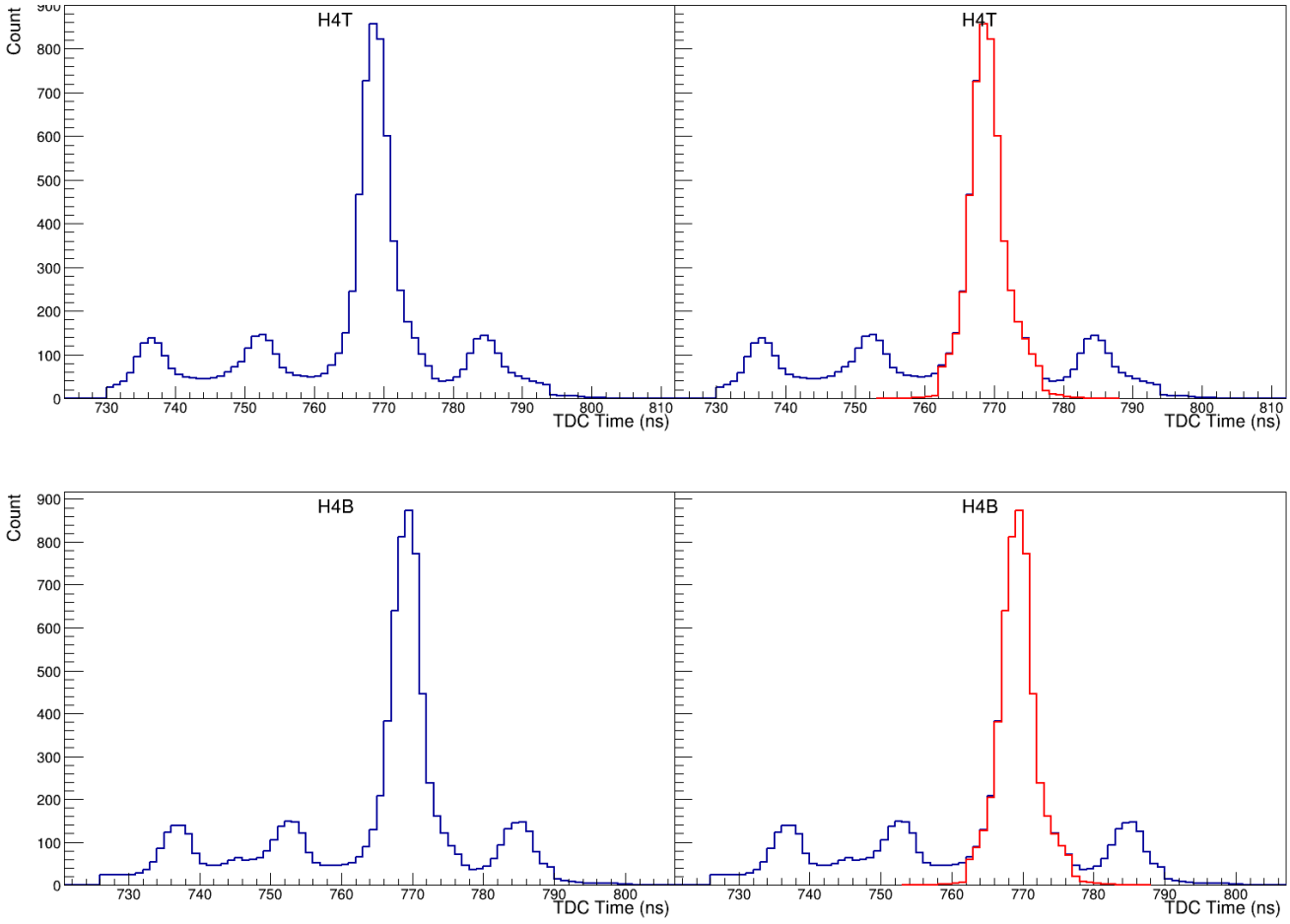

Figure 25: TDC time distributions of the top (H4T) and bottom (H4B) hodoscope planes. The left plot shows TCD time distributions for the FPGA trigger hits, and right plot shows the Distributions (red) after applying the RF-based in-time cut.

Plane	Number	Length (cm)	Width (cm)	Thickness (cm)	Array Width (cm)	Location (cm)	Ave. Eff.
1Y	20 × 2	78.7	7.32	0.64	140	663	
1X	23 × 2	69.9	7.32	0.64	161	653	0.978
2Y	19 × 2	132.0	13.0	0.64	241	1403	
2X	16 × 2	152.0	13.0	0.64	203	1421	0.989
3X	16 × 2	167.6	14.3	1.3	224	1958	0.959
4Y1	16 × 2	152.4	23.16	1.3	366	2130 (L) 2146 (R)	
4Y2	16 × 2	152.4	23.16	1.3	366	2200 (L) 2217 (R)	
4X	16 × 2	182.9	19.33	1.3	305	2240	0.979

Table 6: Details about the number and sizes of scintillators at each hodoscope plane are shown. Values in the table are taken from [3].

2.6 Tracking Chambers

The drift chambers are used to measure the positions of muons, as the position resolutions of the hodoscopes are large. The drift chambers are located at St1, St2, and St3. Each station has six planes: X, X', V, V', U, and U', as shown in Figures 27, 28, 29, and 30. Among these, two planes (X, X') are used for measuring x positions. UU' and VV' measure the stereo angles, tilted by only +14 and -14 degrees, respectively, from the vertical direction. The 'primed' planes play a role in the reconstruction process by helping to resolve the left-right ambiguity in track position with respect to a fired wire. The gas mixture used for the drift chambers is Ar:CH_4:CF_4 (88:8:4). Drift chambers at Stations 1 and 2 are referred to as D1 and D2, respectively, and were used in the previous Fermilab experiments E866 [53] and E605 [66]. The chamber at station 3 is separated into top and bottom halves, denoted as D3p and D3m, with D3p constructed in Japan and D3m constructed at Fermilab by the Japanese collaborators of SeaQuest. Table 7 summarizes the parameters of the drift chambers. Once a particular trigger is satisfied by the trigger module, known as the trigger supervisor, the signal from the drift chamber's sense wire is fed to the readout electronics called the ASDQ card [18]. The acronym "ASDQ" stands for amplification, shaping, discrimination, and charge integration, and these features are embedded in the "ASDQ chip". Each ASDQ card has 8 channels. The ASDQ card amplifies and discriminates the signal, with the discrimination threshold voltage set by the Level Shifter Board (LSB). The LSB board was developed at Fermilab for SeaQuest. It has 64 channels, thereby enabling each LSB to connect to 8 ASDQ cards. The LSB converts the differential signals from the ASDQs into standardized Low-Voltage Differential Signaling (LVDS); subsequently, the LVDS outputs are transmitted

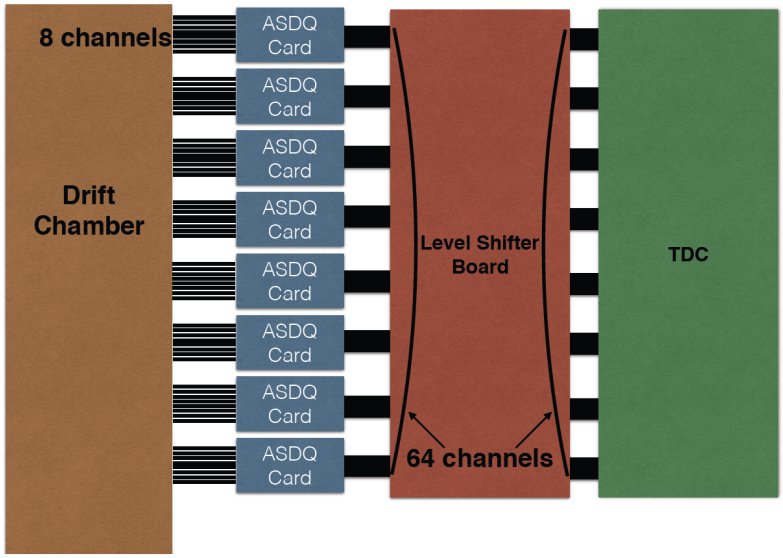

Figure 26: Drawing of the chamber readout electronics system. The figure is taken from Ref. [67].

via ribbon cables to the Time-to-Digital Converter (TDC) modules for readout. The drift chamber readout can be seen in the Figure 26.

The table 8 displays the detection efficiency and position resolution of various detector planes, where the efficiency was determined by measuring the likelihood of a track hitting the plane. The position resolution, as shown in Fig. 31, was calculated between the hit and the muon track.

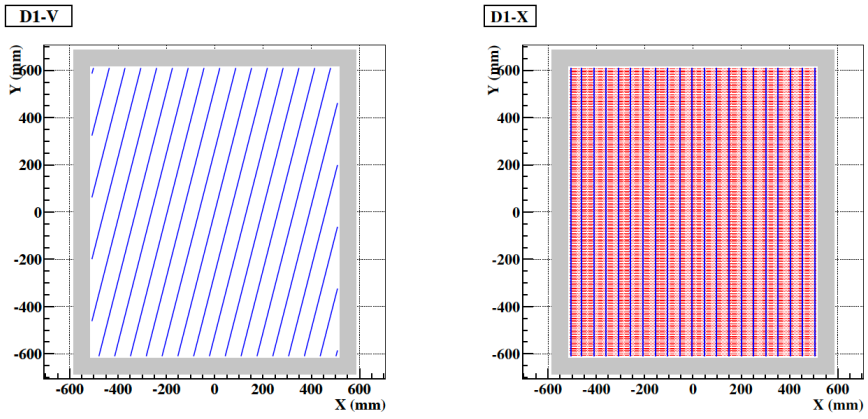

(a) V plane (b) X plane

Figure 27: Configuration of the St. 1 drift chamber is illustrated in (a) for the V plane, where the wires are tilted by approximately 14 degrees from the vertical direction. In (b), the X plane is shown with vertical wires. The figure is taken from Ref. [67].

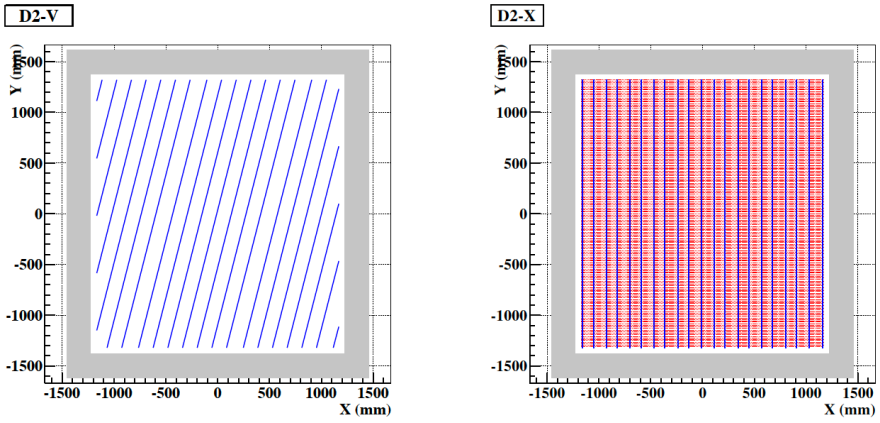

(a) V plane (b) X plane

Figure 28: Configuration of the St. 2 drift chamber is illustrated in (a) for the V plane, where the wires are tilted by approximately 14 degrees from the vertical direction. In (b), the X plane is shown with vertical wires. The figure is taken from Ref. [67].

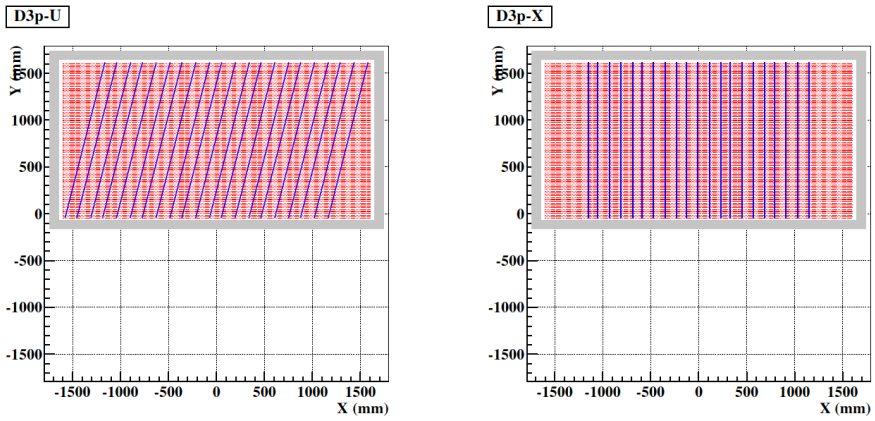

(a) U plane (b) X plane

Figure 29: Configuration of the St. 3+ drift chamber is illustrated in (a) for the V plane, where the wires are tilted by approximately 14 degrees from the vertical direction. In (b), the X plane is shown with vertical wires. The St. 3+ drift chamber covers upper half of St. 3. The figure is taken from Ref. [67].

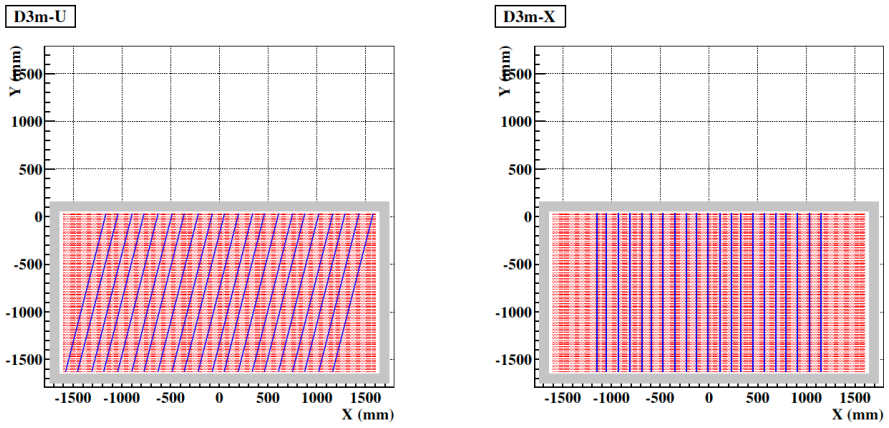

(a) U plane (b) X plane

Figure 30: Configuration of the St. 3- drift chamber is illustrated in (a) for the V plane, where the wires are tilted by approximately 14 degrees from the vertical direction. In (b), the X plane is shown with vertical wires. The St. 3+ drift chamber covers lower half of St. 3. The figure is taken from Ref. [67].

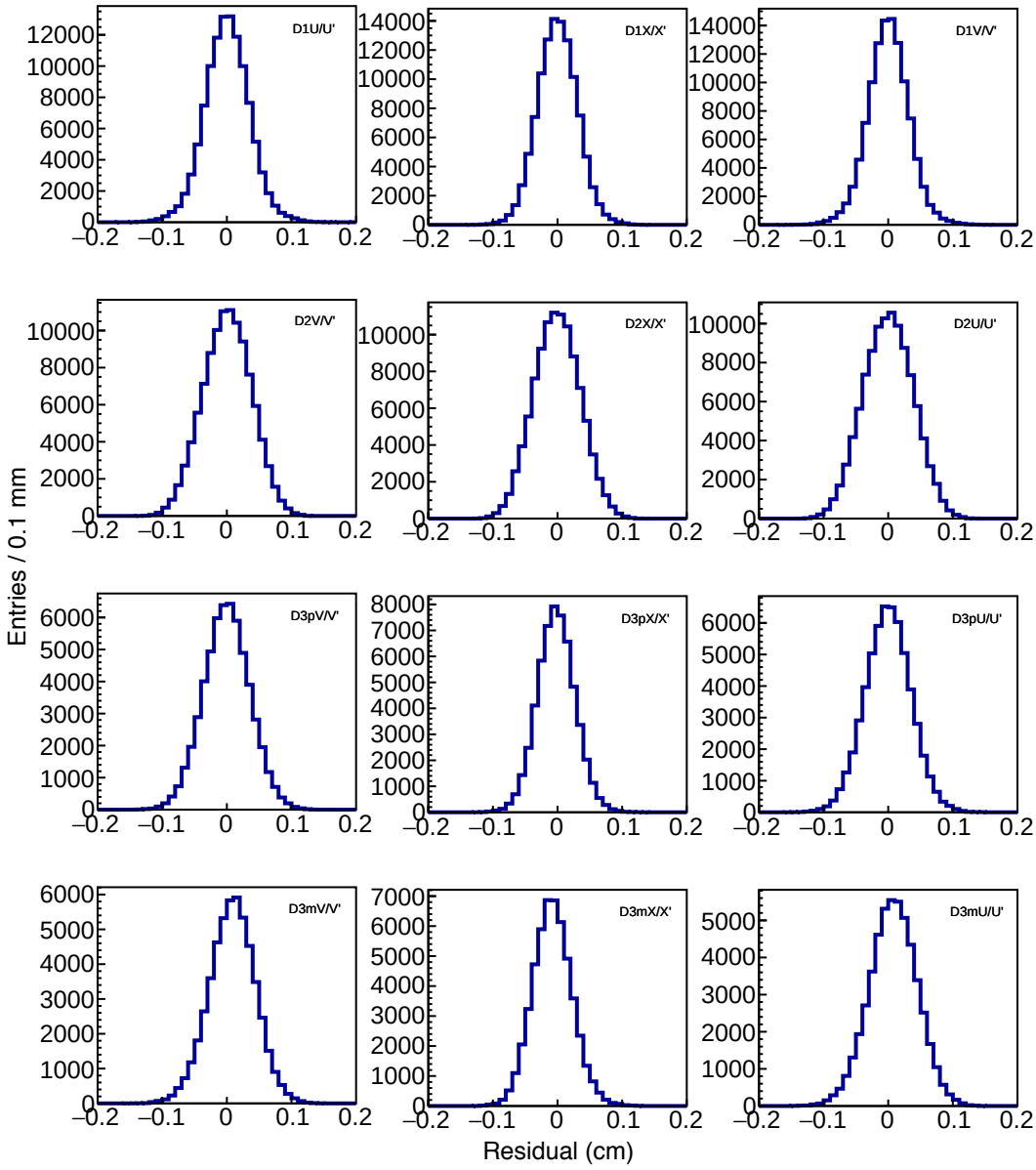

Figure 31: Drift Chamber Resolutions in Different Planes. The figure is taken from Ref. [3]

.

Table 7: Parameters of all chambers. The table is taken from [3].

Chamber	View	No. of wires	Cell width (cm)	Width × height (cm)	Position (cm)
DC1.1	x	160	0.64	102 × 122	616
	u, v	201	0.64	101 × 122	±20
DC1.2	x	320	0.50	153 × 137	691
	u, v	384	0.50	153 × 137	±1.2
DC2	x	112	2.1	233 × 264	1347
	u, v	128	2.0	233 × 264	±25
DC3p	x	116	2.0	232 × 166	1931
	u, v	134	2.0	268 × 166	±6
DC3m.1	x	176	1.0	179 × 168	1879
	u, v	208	1.0	171 × 163	±19
DC3m.2	x	116	2.0	232 × 166	1895
	u, v	134	2.0	268 × 166	±6

Table 8: Performance metrics for the drift chambers in the SeaQuest experiment (April 2014 - June 2015). The numbers are taken from [3].

Chamber	Max. drift (ns)	Pos. res. (μm)	Detection eff. (%) (min.-max.)
DC1.1	100	225	99-100
DC2	260	325	96-99
DC3p	220	240	95-98
DC3m.2	210	246	97-98

2.7 Muon Identification

The proportional tubes are used to identify final-state muons. They are located at station 4 downstream of the 1-meter thick iron wall. The layout is shown in Fig. 32. The proportional tubes are oriented horizontally and vertically to measure the y and x positions. Each tube is 3.66 meters in length, with a diameter of 5.08 centimeters and a wall thickness of 0.16 centimeters. Within the layers of proportional tube planes, there are nine modules, each containing 16 proportional tubes. The proportional tubes use the same gas mixtures as the drift chambers. These modules were developed by the Los Alamos National Laboratory [40]. High-energy muons can traverse two proportional tubes per plane, inducing hit signals by activating two anode wires. These signals, read out from groups of 16 anodes, can be transmitted via ribbon cables and sent to the main DAQ system using CAMAC modules. The typical drift time of proportional tubes is about 650 ns.

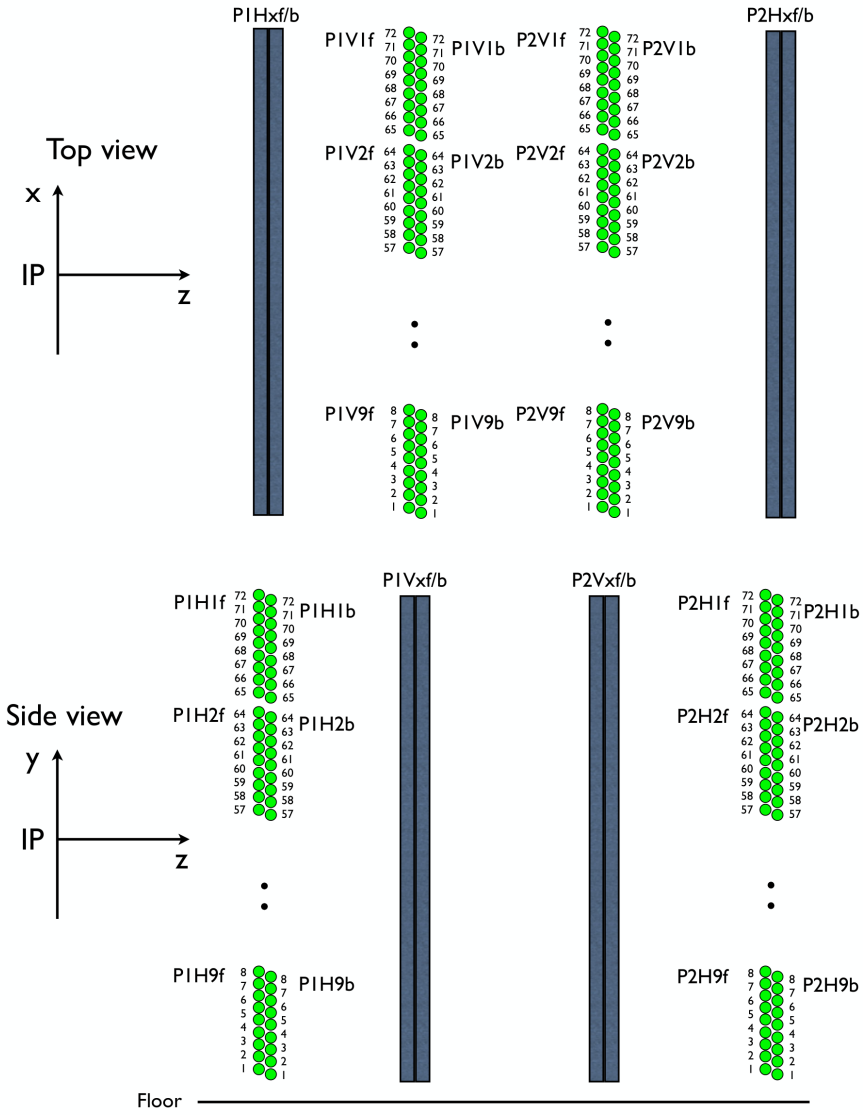

Figure 32: Layout of the proportional tubes showing the top (x-z) and side (y-z) views. [3]

Name	Side	Charge	p_x Req.	Notes	Prescale factor
FPGA 1	TB/BT	$+-/-+$	None	Main physics trigger	1
FPGA 2	TT/BB	$+-/-+$	None	Same-Side trigger	10000
FPGA 3	TB/BT	$++/--$	None	Like-Charge trigger	123
FPGA 4	T/B	$+/-$	None	All singles trigger	25461
FPGA 5	T/B	$+/-$	$p_x > 3$ GeV/c	High-p_T singles trigger	2427
NIM 1	Y coincidence	$+/-$	-	-	31991
NIM 2	X coincidence	$+/-$	-	-	-
NIM 3	Random RF	$+/-$	-	RF clock + 7.5 kHz clock	125

Table 9: Trigger configurations used in the SeaQuest experiment [3].

2.8 Trigger

To form the trigger, we have used the rapid signals from the trigger hodoscopes. For collecting physics data, the primary physics trigger is based on Field Programmable Gate Arrays (FPGAs), which have been optimized to detect high-mass (4-10 GeV/c^2) dimuons originating from the targets, thereby suppressing J/ψ events. In the primary DAQ system, 10 trigger bits are allocated for various trigger events, with five being FPGA-based, as listed in Table 9, and the remainder being NIM-based. All other triggers are heavily prescaled, except for FPGA 1, as given in Table 9. The pre-scale number used in the table is from Ref. [67].

2.8.1 NIM-Based Trigger

Before delivering the beam to the target, all detectors required thorough testing. NIM-based triggers were extensively used for this purpose. NIM triggers are based on NIM-based modules. To establish coincidence, long cable delays were necessary to adjust the timing between signals originating from different stations. Furthermore, additional cable delays were incorporated into the NIM trigger timing to synchronize with the FPGA-based trigger. NIM-1 trigger requires a coincidence signal of (H1T&&H2T&&H3T&&H4T) or (H1B&&H2B&&H3B&&H4B). It a coincidence between the 7.5 kHz pulse signal produced

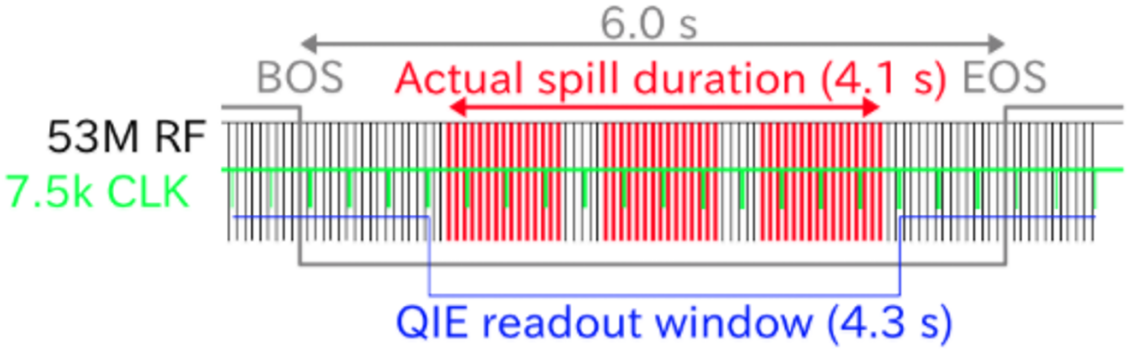

Figure 33: Schematic of NIM3 trigger [76].

by a gate generator and the RF clock provided by the Fermilab accelerator division. NIM 3 trigger is taken in random RF bucket. It requires a coincidence between the 7.5 kHz pulse signal generated by a gate generator and the RF clock supplied by the Fermilab accelerator division. This trigger is valuable for embedding chamber hits into simulated data. It is a crucial process for accurately accounting for reconstruction inefficiencies, as clean simulated data doesn't have chamber hit information based on beam intensity.

2.8.2 FPGA-Based Trigger

From the interactions between the beam and the target, numerous potential single tracks may traverse the detectors, originating from mesons such as π, K, D, and others. The role of the FPGA triggers is to discriminate between the signals and backgrounds effectively. The detailed implementation is discussed in the following article [42]. FPGA 1 serves as the main physics trigger, optimized for detecting high-mass regions such as Drell–Yan. The trigger operates in three steps, as shown in Fig. 35:

- **Level 0:** At this level, there are four V1495 modules, each corresponding to a "quadrant" of the hodoscopes.

  - **Production Mode:** In this mode, input signals are directly transmitted from the hodoscopes to the Level 1 modules.

  - **Pulser Mode:** In Pulser mode, the system looks for arbitrary hit patterns. It is used to verify the functionality of Level 1 and Level 2 triggers.

- **Level-1: Track Finder:** In this step, the V1495 modules receive signals from the Level 0 V1495 boards and are responsible for finding four hit track candidates. The track candidates are formed from hit patterns determined by Monte Carlo simulations of Drell–Yan and J/ψ. A "trigger-road" is denoted by a specific hit pattern used for triggering purposes; on the other hand, a "Roadset" is a collection of "trigger-roads". The Roadset is used in all FPGA-based triggers.

- **Level-2: Track Correlator:** Once Level-2 receives the trigger roadset information from Level-1, it forms all possible track candidates based on the firmware requirements. For instance, the FPGA-1 trigger requires to have both a top trigger-road and a bottom trigger-road. The FPGA-3 trigger is a like-sign dimuon trigger that requires two trigger roads with the same sign. This trigger serves the purpose of random background estimation. Conversely, FPGA-4 and FPGA-5 function as single muon triggers. Below are the trigger criteria:

  - **FPGA 1:** One is a top trigger-road and the other a bottom trigger-road.

  - **FPGA 2:** Both μ^+ and μ^- fire on the same side of the hodoscopes, either top and top or bottom and bottom. Events from this trigger have high dimuon transverse momentum.

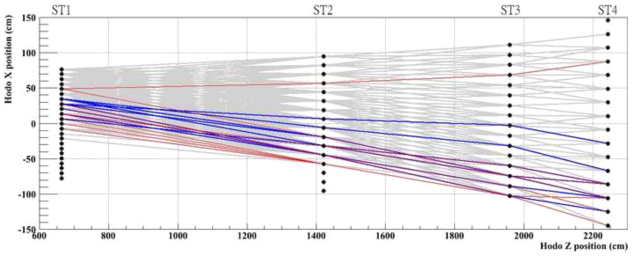

Figure 34: The hit patterns of positive muons on the X-hodoscopes are visualized here. In a top view, scintillator paddles are shown as black points. The red line highlights the 10 most frequently hit patterns, and the blue lines show the subsequent 10 most frequent patterns. All other patterns are represented in gray [42].

- **FPGA 3:** This trigger, known as the like-sign dimuon trigger, is used for background estimations, requiring the two tracks to have the same charges.
- **FPGA 4:** Accepts all single muon tracks regardless of their charges.
- **FPGA 5:** Accepts all single muon tracks regardless of their charges only with the road where $P_t > 3$ GeV/c.

In this thesis, the trigger dataset used is Roadset 67. Within this Roadset, hot trigger roads, which are noisy and highly likely to generate fake muon triggers, have been removed.

2.9 Data Acquisition Systems

There are three types of data acquisition systems based on the type of data, namely *Event DAQ*, *Scaler DAQ*, and *Beam DAQ*. The Event DAQ records information event by event of the triggers from all detectors, such as hodoscopes, drift chambers, and proportional tubes. The Scaler DAQ records scaler information on a 7.5 Hz clock and the Beam DAQ records proton beam information from the readout of the Cerenkov detector.

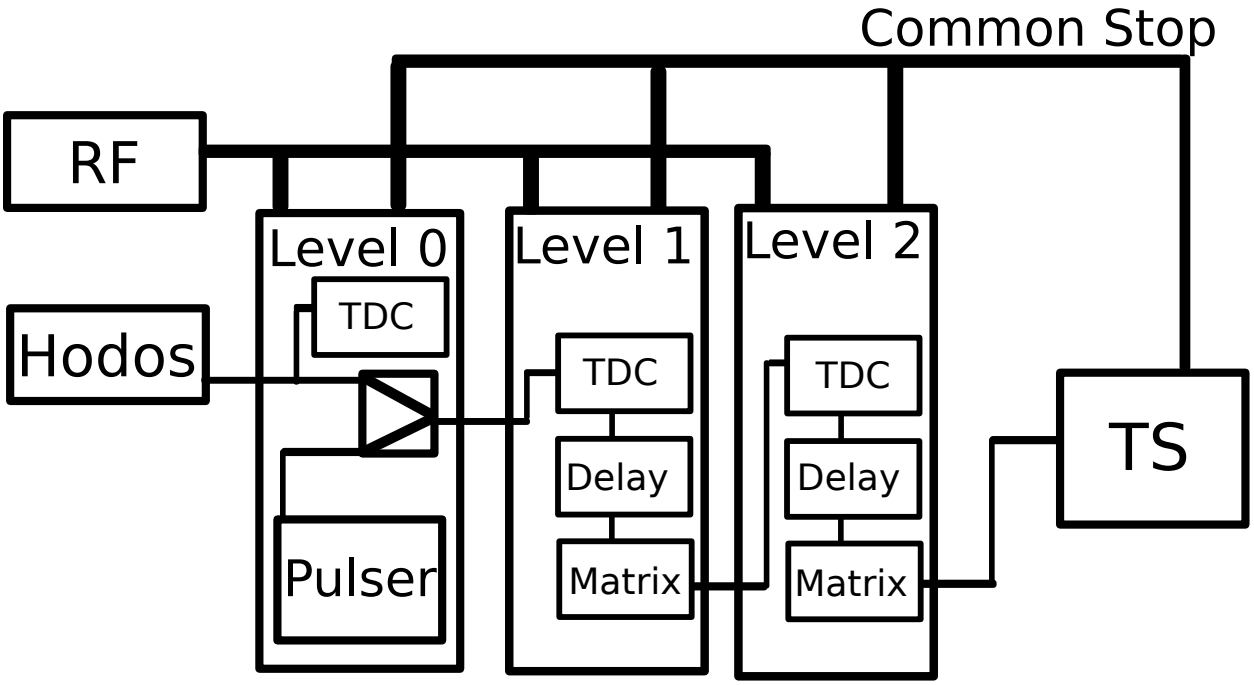

Figure 35: Trigger hardware schematic [63].

2.9.1 Event DAQ

The Event DAQ (also known as Main DAQ) reads data event by event, triggered by either FPGA-based or NIM-based triggers. The Event DAQ has 14 VME crates, where the 13 crates contain VME processors, Trigger Interface (TI), and Time-to-Digital Converters (TDCs), shown in figure 36. The other VME crate is called the "Trigger Supervisor (TS)" for more details see [56], which has 12 input trigger slots. Among them, 5 trigger bits are assigned for the FPGA-based triggers, and 3 bits are used for the NIM-based triggers (NIM-1 to NIM-3). The remaining triggers are reserved for the "BOS" (beginning of spill) and "EOS" (end of spill) signals, which are provided by the Fermilab Accelerator Division.

Upon receiving trigger signals from FPGA- or NIM-based systems, the Trigger Supervisor (TS) generates a common stop signal. This signal is then distributed to the trigger interface

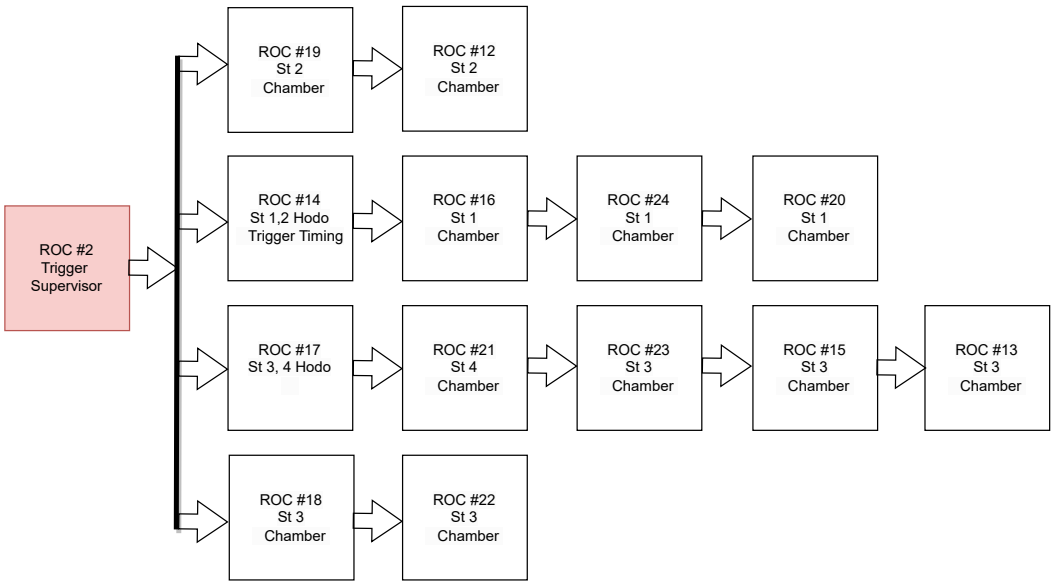

Figure 36: A chain of VME crates.

in each VME crate. Upon receiving the common stop signal, the trigger interface instructs the TDC modules and sends the hit information from all detectors to the DAQ host. The four FPGA triggers (MATRIX1-4) can be prescaled up to 24 bits, while the other four trigger bits (MATRIX5, NIM1-3) allow prescaling up to 16 bits. Triggers beyond these, such as NIM4, flush trigger, BOS, and EOS, cannot be prescaled.

2.9.2 Scaler DAQ

The Scaler DAQ system, also designed by the JLab CODA system, remains operational regardless of whether the Event DAQ is recording events. Its main purpose is to monitor spectrometer, trigger, and beam conditions. It consists of one VME crate which reads out to

the scalars. One of the channels of the Scaler DAQ forms the coincidence between a 7.5 kHz gate generator and beam spill signal. For each beam spill, the Scaler DAQ system registers the number of triggers fired in the Event DAQ, measures the beam intensity, and records the hit rate of the hodoscope arrays.

2.9.3 Beam DAQ

To read the 53 MHz beam structure with the Cherenkov counter, the Beam DAQ uses the QIE board. The duty factor of the proton beam is defined as $DF = \frac{<I>^2}{<I^2>}$, which describes the beam intensity with time, and the value 1 represents a very stable beam between the buckets in spills. The Beam DAQ collects:

Four types of data are recorded by the QIE board during the spill:

1. The intensity of each RF bucket.
2. The number of protons inhibited due to high instantaneous intensity for each inhibit generated.
3. The number of protons missed because the trigger system was busy during readout.
4. The sum of beam intensity I and the total of the squared beam intensity I in a spill.

3 Analysis Method

The goal of the analysis is to extract the angular distributions qualitatively and quantitatively and to understand the dependency of the parameters in different kinematics. This section will start with event selections, where we are going to use Figure of Merit to exclude the unphysical dimuon events. We will also review the method used to subtract the combinatorial background, and the event reweighting method to calibrate the MC events. After that, we construct the response matrix using MC data, and using the Bayesian Iterative Unfolding method, we unfold the reconstructed Drell-Yan events.

3.1 Data Set

In this analysis, we only use the signal events that come from the dump target (FMag) location, and therefore the dataset has been chosen accordingly. We have used only trigger roadset 67, where the run range is (12525 - 15789), the spill range is (484746 - 676223), the beam offset in the Y-axis is 1.6 cm, and the orientation of the B field is in the -Y direction. In the roadset, we only analyzed the data when a proton was hitting the LH_2 target. By applying the appropriate vertex cut, we have isolated the events originating from the dump, which we will discuss further in Section 3.3.

3.2 Event Reconstruction

Reconstructing a dimuon event involves many steps, beginning with the analysis of the chamber's hits to optimize the tracking process, and vertexing the μ^+ and μ^- tracks. There are three steps: Pre-tracking Analysis, single-track reconstruction, and vertex reconstruction, as shown in Figure 37. The program that performs track reconstruction and vertexing is called

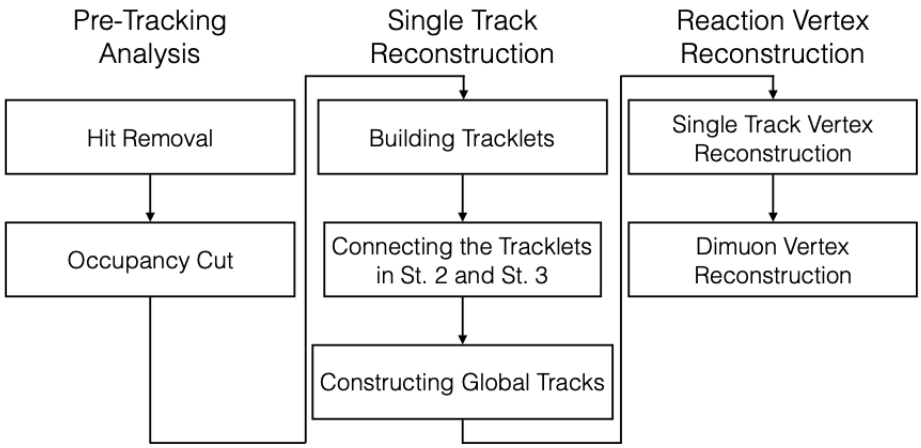

Figure 37: Procedure of the dimuon reconstruction based on the kTracker [67].

kTracker, primarily developed by Kun Liu, who is a scientist from the Los Alamos National Laboratory. A nice introduction is given in Ref. [61]. The details of track reconstruction and vertexing are given in the very well-written thesis [67].

3.2.1 Pre-tracking Analysis

Before we begin the track finding, there are some pre-tracking cuts applied. The pre-tracking analysis has two steps: hit removal and occupancy cuts.

3.2.1.1 Hit Removal

- **Out-of-time hits:** There could be some tails outside of the TDC time distributions from different detectors. This stage removes any hits that are outside a predefined time window.

- **Afterpulse Removal:** Due to noise and other backgrounds, additional pulses could be received after the first pulse, known as afterpulses. In this step, we only keep the first signal, which is most likely to be the true signal.

- **Random hits removal:** Based on the hodoscope hit positions, the random hits on the chambers can be identified and removed. This process is called hodoscope masking. By analyzing the chamber hit positions, we can determine if the neighboring hodoscope paddles are also fired. Any chamber hits with no corresponding hodoscope paddle hits are then removed.

- **Hit cluster removal:** As a particle traverses the chamber, it ionizes gas particles along its path. These ions induce signals in nearby wires, creating a cluster of hits likely originating from a single particle. Faulty electronics could also generate these kinds of clusters. The cluster size represents the total number of hits in the cluster, which are categorized into three types in the SeaQuest spectrometer. The first one is electronic noise, which may arise from either the noisy ASDQ card or the noise from the VME plane. Contiguous hits with an average time difference of less than 10 ns are removed. The second one is "edge hits", and they are generated when a muon traverses through the edge of the wires, resulting in hits in neighboring wires. The signal with the larger drift distance is discarded. The third scenario involves delta rays. If there are two or more contiguous hits in the cluster with a large average TDC-time difference, the cluster is considered to be generated by delta rays. To preserve the hit possibly produced by the muon, the two hits on the cluster's edges are kept, while the middle ones are rejected. More details on the hit removal can be found in the well-written Ref. [76].

3.2.1.2 Occupancy Cuts Even after performing hit removal, some events could be very noisy due to the numerous chamber hits. Including all chamber hits could be very time-

consuming in the track-building steps. Therefore, an occupancy window in each station is important. Occupancy is defined as the total number of chamber hits after the hit removal conditions are applied.

Table 10: Upper limits of the occupancy of each drift chamber. The numbers are taken from [67].

Detector	St. 1	St. 2	St. 3+	St. 3-
Occupancy	320	160	150	150
Number of total sense wires	1124	736	768	768

3.2.2 Track Reconstruction

As discussed in the Spectrometer section, each chamber comprises six planes: X, X', V, V', U, and U'. These hits construct the local track inside the chambers. Track finding in the chamber begins with the XX' planes. We search for hits on each of the X planes, and hit pairs are formed if the difference in element IDs of hits on X and X' is one or less. For given hits on the XX' plane, we search the hit pairs on the UU' planes within windows determined about $20cm$. We can call this doublet, and for the given doublet, we can find the hit pairs in the VV' plane within windows determined about $5cm$. After that, we perform the fit without drift distance. In this step, there could be multiple tracklets be formed from the same hits.

A tracklet can be rejected if any of the conditions listed below are not satisfied:

- $\chi^2 < 15$.
- $N_{hits} > 4$.
- The neighboring x hodoscopes are not fired.

The next step is to construct the back partial track by connecting tracklets in St2 and St3. The connected back partial track can be extrapolated to the proportional tubes. Having a valid track requires a hit on one of the proportional tubes; if no valid hit is found on the proportional tubes, the track can be discarded.

After constructing the back partial track, the global track is formed by projecting the back partial track in the chamber located in station 1 to pair with the appropriate tracklet constructed at the station 1 chamber. To find a valid tracklet in St1, there is a search window which determined using the Sagitta ratio. It is the ratio of the distance s_1 and s_2 as shown in Figure 38. The track has five parameters, which are: s/p_{xz}, t_{xz}, t_y, x_0, and y_0, where the parameters are defined for the back partial track within the track as follows:

- s: Charge of the track.
- p_{xz}: Denotes the momenta, where $p_{xz} = \sqrt{p_x^2 + p_z^2}$.
- t_{xz}: Slope in the X-Z plane.
- t_y: Slope in the Y-Z plane.
- x_0: Intersections in the X-Z plane.
- y_0: Intersections in the Y-Z plane.

The slopes and the intersections are calculated using the formulas:

$$t_x^{St1} = t_x + \frac{P_T^{kick} \cdot s}{p_{xz}}$$

$$x_0^{St1} = t_x \cdot z_{bend} + x_0 - t_x^{St1} \cdot z_{bend}$$

The P_T kick, provided by the KMAG and equal to 0.4016 GeV/c, along with z_{bend} =

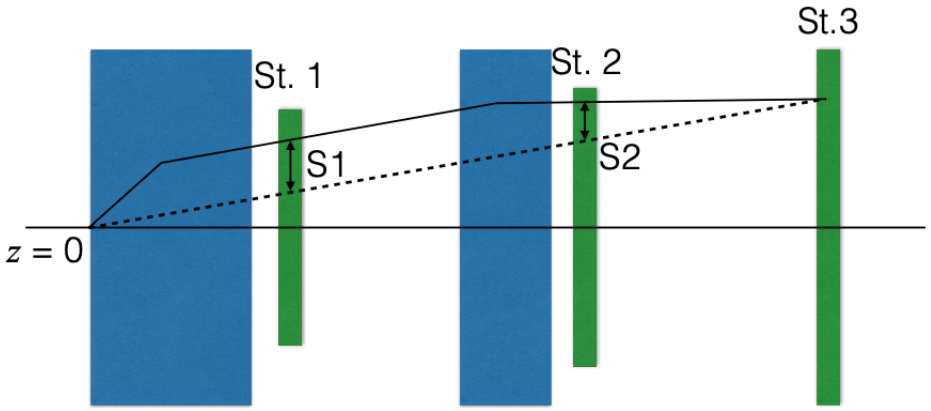

Figure 38: The global track reconstruction uses the sagitta ratio. The figure is taken from [67].

1064.26cm, the z position of the center of KMAG, are used in this process. An iterative procedure is used to clean out bad hits to reconstruct global tracks. After fitting a track candidate, any hit with a residual greater than three times the chamber resolution is discarded. The remaining hits are then subjected to a re-fit. The following sections must follow to have a valid global track:

- $N_{\text{hits}} > 14$
- $5\,\text{GeV} < P < 100\,\text{GeV}$
- $\chi^2 < 20$

3.2.3 Single Track Vertex Reconstruction

The track vertexing details can be found in the theses [76, 67], and I will give an overview of that. To understand the vertex finding, one needs to understand how muons traverse about 5m of Fe and are projected along the Z direction to the target regions. The FMag is divided into 100 slices, where each slice is divided into two steps. Accounting for the energy loss in

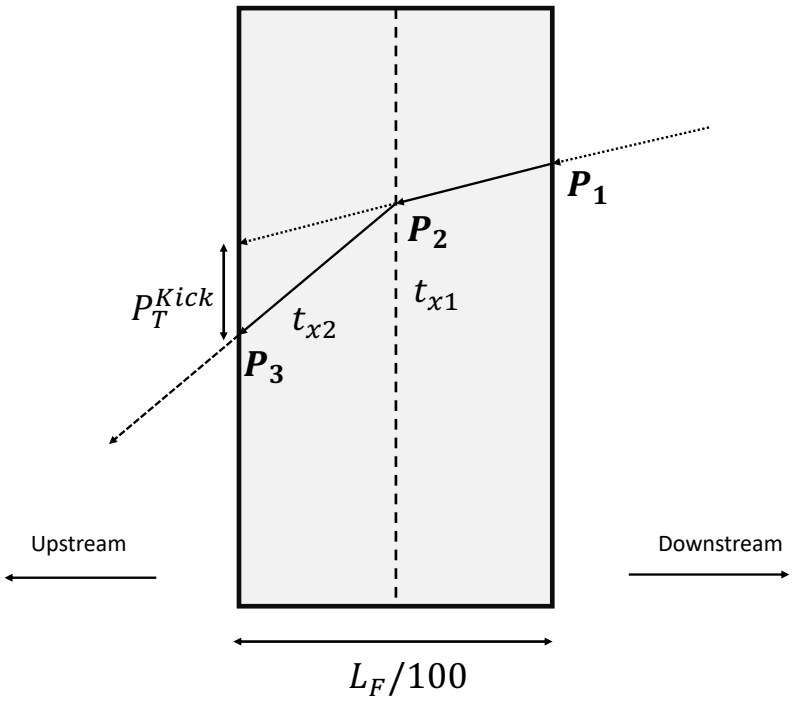

Figure 39: Vertex reconstruction at FMag slice is shown where the P_T^{Kick} is applied.

each two-step is followed by:

- The energy loss is applied in the first half of the step.
- P_T^{Kick} is applied at the center of the slice.
- Apply energy loss in the second half-step.

In two steps, t_{x1} and t_{x2}, denote the slopes before and after the muon receives the P_T^{Kick} at the center, as shown in the figure. The changed slope t_{x2} from t_{x1} can be determined from the following equation [67]:

$$t_{x2} = t_{x1} + s\frac{P_T^{\text{Kick}}}{L_{\text{FMag}}}\frac{L_{\text{FMag}}}{N_s}\frac{1}{\sqrt{P_{1x}^2 + P_{1z}^2}}. \tag{15}$$

In the equation (15), s denotes the charge of the track, while t_{x1} and t_{x2} represent the

track slopes in the X-Z plane at the downstream and upstream surfaces of the FMag slices, respectively. N_s represents the number of slices in the FMag. Subsequently, the 3-momentum at the center of the FMag slice, P_2, is calculated as follows:

$$|\mathbf{P}_2| = |\mathbf{P}_1| + \left(E_0 + |\mathbf{P}_1| \cdot E_1 + |\mathbf{P}_1|^2 \cdot E_2 + |\mathbf{P}_1|^3 \cdot E_3 + |\mathbf{P}_1|^4 \cdot E_4\right) \cdot \frac{1}{\mathrm{L}_{FMag}} \cdot \frac{1}{|\mathbf{T}_1|}$$

Where T_1 is the trajectory of the track at the former half of the FMag slice:

$$T_1 = \left(\frac{t_{x1} \cdot L_{FMAg}}{2N_s}, \frac{t_y \cdot L_{FMAg}}{2N_s}, \frac{L_{FMAg}}{2N_s}\right) \tag{16}$$

These constants, kick, E_0, E_1, E_2, E_3, and E_4, are determined with Monte-Carlo simulation, while the others are determined with detector survey.

Name	Value	Description
P_T^{Kick}	2.909	pT kick at FMag (GeV)
L_{hole}	27.94	Length of the FMag hole (cm)
R_{hole}	1.27	Radius of the FMag hole (cm)
L_{FMag}	502.92	Length of the FMag (cm)
Z_U	-500	Upstream end (cm)
Energy Parameters		
E_0	7.18274	Parameter for energy loss
E_1	0.0361447	
E_2	-0.000718127	
E_3	7.97312×10^{-6}	
E_4	-3.05481×10^{-8}	

Table 11: Vertex fitting parameters and variables.

Similarly, the upstream slice of the FMag would be :

$$|\mathbf{P}_3| = |\mathbf{P}_2| + \left(E_0 + |\mathbf{P}_2| \cdot E_1 + |\mathbf{P}_2|^2 \cdot E_2 + |\mathbf{P}_2|^3 \cdot E_3 + |\mathbf{P}_2|^4 \cdot E_4\right) \cdot \frac{1}{\mathrm{L}_{FMag}} \cdot \frac{1}{|\mathbf{T}_2|}$$

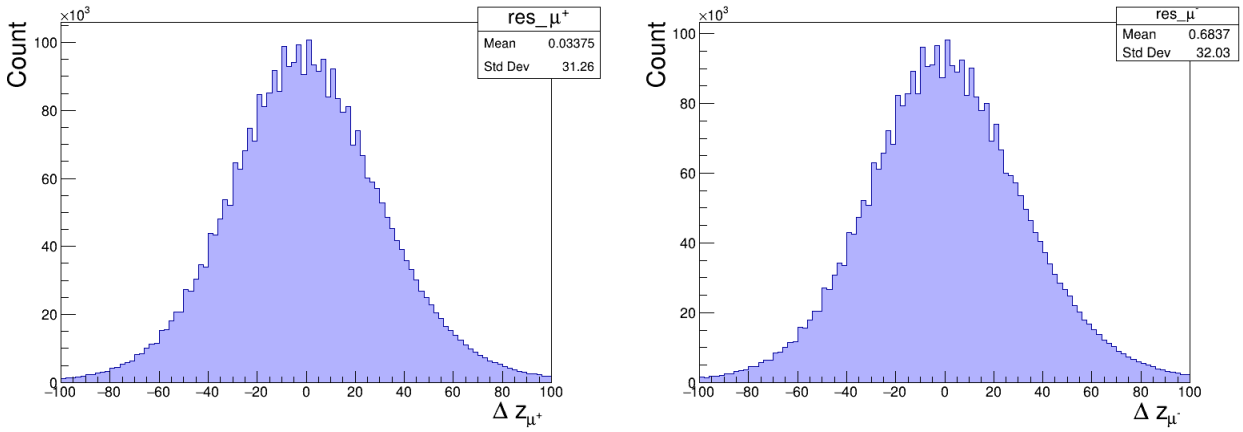

Figure 40: The resolutions of the μ^+ and μ^- tracks.

Where T_2 is the trajectory of the track at the downstream half of the FMag slice:

$$T_2 = \left(\frac{t_{x2} \cdot L_{FMag}}{2N_s}, \frac{t_y \cdot L_{FMag}}{2N_s}, \frac{L_{FMag}}{2N_s} \right) \tag{17}$$

This process continues until the muons traverse through the entire FMag, projecting the track to the target location to assess the vertex position, and the position of the single muon vertex is determined as the point closest to the beam line.

3.2.4 Dimuon Vertex Reconstruction

After completing track reconstruction, we select all possible single tracks and conduct dimuon vertexing using the Extended Kalman Filter procedure [51]. The vertex is represented by the state vector, which the Kalman filter estimates. This process involves iteratively updating the state vector until convergence, with the final measurement providing the optimal state vector after predefined iterations. The initial vertex position is set at $X = Y = 0$, with attempts made at two different Z positions, and the optimal Z position is selected from:

- The mean value of z_{μ^+} and z_{μ^-}.

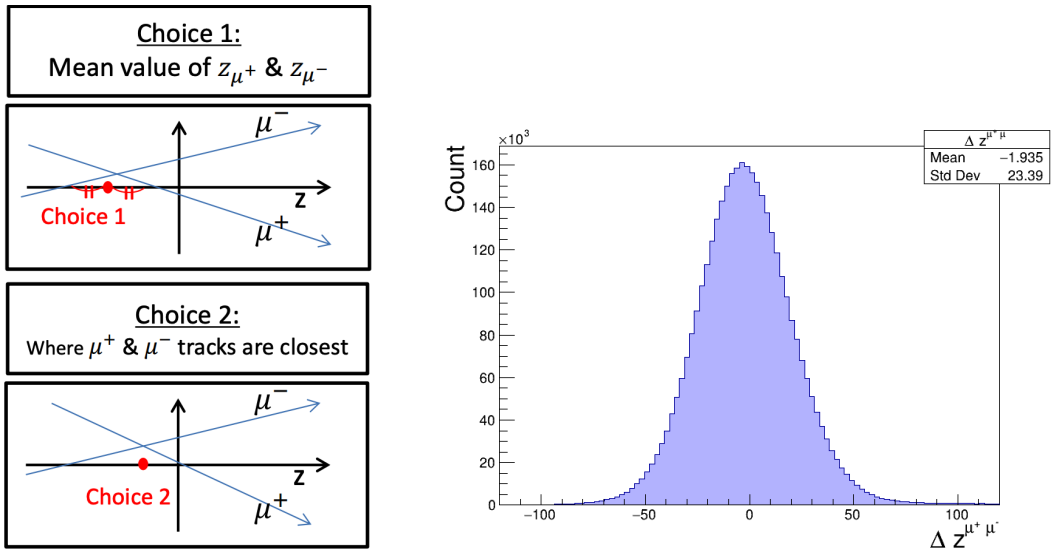

(a) label 1 (b) label 2

Figure 41: Vertex reconstructions method. The left figure is taken from [65].

- The position where μ^+ and μ^- are closest.

These two choices are illustrated in Figure 41. Additionally, the z-vertex distributions for the dimuons are shown. During the vertexing process, the method chosen will be the one that yields a better vertex-fitting χ^2.

3.2.5 Monte Carlo Simulation

In the SeaQuest experiment, we use Geant4-based Monte Carlo simulation, often referred to as GMC. We can generate many kinds of simulated events using it, for example, Drell–Yan, J/ψ, ψ', etc. The PDF parameterizations for generating the MC events are taken from CTEQ6 [41]. Once the events are generated, they are fed into the Geant4-based reconstructions, where magnetic fields and chamber efficiency are applied. The acceptance is defined when two muon tracks pass through each station's x-hodoscope array and drift chambers. Each event at the generator level has an associated weight, determined based on

the cross-section of the process.

There are two kinds of simulated events we use in the SeaQuest experiment: Clean MC and Messy MC. To match the "realistic" conditions like those in the GMC, hits are smeared in a Gaussian manner, and 6% are dropped in the Monte Carlo simulation to account for inefficiency. This process is referred to as "Realization." This realization is applied to both the Clean MC and Messy MC. The difference between the clean and the messy MC is that the Clean MC refers to the case where we did not apply any hit embedding to the simulated events, while Messy MC refers to hits from real data using the NIM 3 trigger. Here, NIM3 denotes the RF bucket trigger, and using that, we collect real data hits randomly.

In the context of the angular distributions study, the Monte Carlo events must have the same beam conditions as the real data, and by doing the hit embedding we make sure that. These are the generator dimuon variable ranges used in the simulation to generate the Drell–Yan events from the dump target:

- A flat distribution of x-Feynman is used: $-1.0 < x_F < 1.0$.
- True dimuon mass range is $M_{\mu^+\mu^-} > 4.0$ (GeV/c^2).
- True x_F range is $-1.0 < x_F < 1.0$.
- True Bjorken-x-Beam is $0.0 < x_B < 1.0$.
- True Bjorken-x-Target is $0.0 < x_T < 1.0$.
- True Dimuon $P_T^2 > 0.0(GeV/c)^2$.
- $-0.7 < True\ cos\theta < 0.7$.

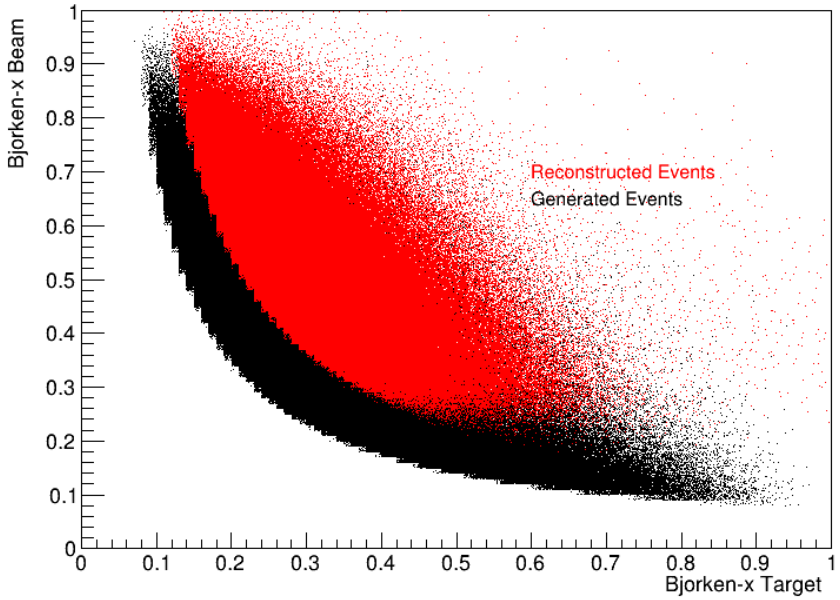

Figure 42: The plot shows the range of Bjorken-x-Beam versus Bjorken-x-Target for the beam dump target location using the Drell-Yan process. The black points represent the generated 4π GMC events, while the red points represent the reconstructed GMC.

3.3 Event Selections

A set of event selections was developed for selecting physical dimuon events by optimizing a figure of merit, defined as $\frac{S}{\sqrt{S+B}}$, where S represents the signal and B stands for the expected background within the signal region. Therefore, the figure of merit (FOM) quantifies the signal significance for a counting experiment.

$$F(\alpha) = \frac{S(\alpha)}{\sqrt{S(\alpha) + Bg(\alpha)}} = \frac{a \times Y_S^{MC}(\alpha)}{\sqrt{b \times Y_{Unmix-Mix}^{Data}(\alpha)}}$$

$$F(\alpha) = \frac{a}{\sqrt{b}} \frac{Y_S^{MC}(\alpha)}{\sqrt{Y_{Unmix-Mix}^{Data}(\alpha)}} \Rightarrow \; FOM(\alpha) = \frac{Y_S^{MC}(\alpha)}{\sqrt{Y_{Unmix-Mix}^{Data}(\alpha)}}$$

- a and b are the normalization constants, and $FOM(\alpha) = \frac{F(\alpha)}{\frac{a}{\sqrt{b}}}$

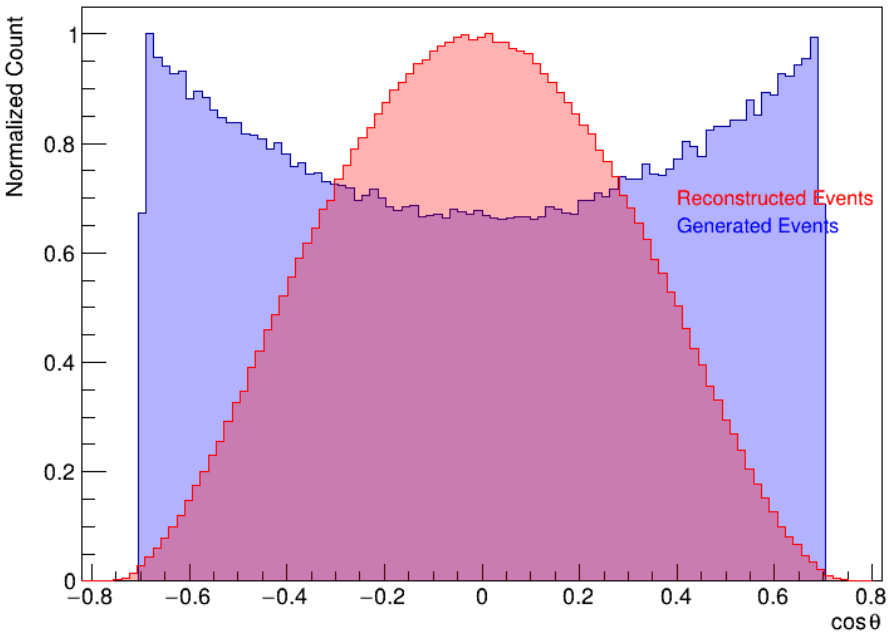

Figure 43: The plot illustrates the range of true $\cos\theta$ versus the reconstructed distribution for the beam dump target location using the Drell–Yan process. The blue histogram represents the generated 4π GMC events, while the red histogram represent the reconstructed GMC. Both histograms are scaled to $Y_{\max}$ yield of 1.

- For optimum upper and lower limit FOM:

$$Y_{up}(\alpha) = \sum_{i_{bin}=1}^{m} Y_{i_{bin}}(\alpha)\ ; \quad Y_{low}(\alpha) = \sum_{i_{bin}=m}^{n} Y_{i_{bin}}(\alpha)$$

- α is the cut variables that we need to find the optimum range. Y_i is the bin content in the i'th bin.

- m is the bin number where we look for the FOM, and n is the total bin number. Generally, we look for the optimum FOM value, where we get a greater proportion of the signals from the data.

The definitions of the used variables in the event selection lists are given below:

Any event that passes the track and dimuon level event selections mentioned in the following sections will be considered a successfully reconstructed event originating from the dump. Subsequently, further analysis can be conducted.

Variable Name	Description
$x^{\mu^+}_{\rm St1}$, $y^{\mu^+}_{\rm St1}$,$z^{\mu^+}_{\rm St1}$,	μ^- track positions at St1
$x^{\mu^+}_{\rm St3}$, $y^{\mu^+}_{\rm St3}$,$z^{\mu^+}_{\rm St3}$,	μ^- track positions at St3
$x^{\mu^+}_{\rm dump}$, $y^{\mu^+}_{\rm dump}$,$z^{\mu^+}_{\rm dump}$,	μ^+ track positions at dump
$x^{\mu^+}_{\rm target}$, $y^{\mu^+}_{\rm target}$,$z^{\mu^+}_{\rm target}$,	μ^+ track positions at target
$x^{\mu^-}_{\rm dump}$, $y^{\mu^-}_{\rm dump}$,$z^{\mu^-}_{\rm dump}$,	μ^+ track positions at dump
$x^{\mu^-}_{\rm target}$, $y^{\mu^-}_{\rm target}$, $z^{\mu^-}_{\rm target}$,	μ^- track positions at target
$P^{\mu^+}_{x,\rm vtx}$, $P^{\mu^+}_{y,\rm vtx}$, $P^{\mu^+}_{z,\rm vtx}$	μ^+ track momenta at vertex
$P^{\mu^-}_{x,\rm vtx}$, $P^{\mu^-}_{y,\rm vtx}$, $P^{\mu^-}_{z,\rm vtx}$	μ^- track momenta at vertex
$P^{\mu^+}_{x,\rm St1}$, $P^{\mu^+}_{y,\rm St1}$, $P^{\mu^+}_{z,\rm St1}$	μ^+ track momenta at station 1
$P^{\mu^-}_{x,\rm St3}$, $P^{\mu^-}_{y,\rm St3}$, $P^{\mu^-}_{z,\rm St3}$	μ^+ track momenta at station 3
$\chi^{\mu^+}_{\rm target,\ \mu^+}$, $\chi^{\mu^+}_{\rm dump,\ \mu^+}$	μ^+ track χ^2 at dump location
$\chi^{\mu^+}_{\rm target,\ \mu^+}$, $\chi^{\mu^+}_{\rm dump,\ \mu^+}$	μ^+ track χ^2 at target location
$\chi^{\mu^-}_{\rm target,\ \mu^+}$, $\chi^{\mu^-}_{\rm dump,\ \mu^-}$	μ^- track χ^2 at dump location
$\chi^{\mu^-}_{\rm target,\ \mu^-}$, $\chi^{\mu^+}_{\rm dump,\ \mu^-}$	μ^- track χ^2 at target location
px_1, py_1, pz_1	μ^+ track momenta at vertex
px_2, py_2, pz_2	μ^- track momenta at vertex
x_1, y_1, z_1	μ^+ track positions at vertex
x_2, y_2, z_2	μ^- track positions at vertex
dpx, dpy, dpz	Dimuon momenta at vertex
dx, dy, dz	Dimuon vertex positions
$x1_t, y1_t, x1_d, y1_d$	μ^+ positions at target and dump
$x2_t, y2_t, x2_d, y2_d$	μ^- positions at target and dump
nHits1, nHits2	Total reconstructed track hits
nHits1St1, nHits2St1	Reconstructed track hits in station 1
$chisq1_{target}$, $chisq1_{dump}$, $chisq1_{upstream}$	χ^2 for μ^+ track in target, dump, and upstream positions
$chisq2_{target}$, $chisq2_{dump}$, $chisq2_{upstream}$	χ^2 for μ^- track in target, dump, and upstream positions
$cos\theta$, ϕ	Polar and azimuthal angles in the Collins-Soper frame

Table 12: List of variables and descriptions.

3.3.1 Track Level Selections (μ^+)

- $1.086 < \text{atan}\left(\frac{y^{\mu^+}_{\text{St3}}}{y^{\mu^+}_{\text{St1}}}\right) < 1.562$
- $(x^{\mu+}_{\text{target}})^2 + (y^{\mu+}_{\text{target}} - 1.6)^2 < 1425.0\ cm^2$
- $(x^{\mu+}_{\text{dump}})^2 + (y^{\mu+}_{\text{dump}} - 1.6)^2 < 141.0\ cm^2$
- $0.413 < \left|P^{\mu^+}_{x,\text{St1}} - P^{\mu^+}_{x,\text{St3}}\right| < 0.420$
- $\left|P^{\mu^+}_{y,\text{St1}} - P^{\mu^+}_{y,\text{St3}}\right| < 0.005$
- $\left|P^{\mu^+}_{z,\text{St1}} - P^{\mu^+}_{z,\text{St3}}\right| < 0.074$
- $-2.5 > (\chi^2_{\text{target, }\mu^+} - \chi^2_{\text{dump, }\mu^+}) < 77.5$
- $10 < P^{\mu+}_{z} < 78$
- $\text{nHits}^{\mu+} > 13$
- $(y^{\mu+}_{St1} \cdot y^{\mu+}_{St3}) > 0$
- $\frac{\chi^2_{\text{dump},\mu+}}{\chi^2_{\text{upstream},\mu+}} < 0.165$
- $nHits^{\mu+}_{St1} > 4$
- $-45.0 < z^{\mu+}_{vtx} < 125.0$

3.3.2 Track Level Selections (μ^-)

- $0.666 < \text{atan}\left(\frac{y^{\mu^-}_{\text{St3}}}{y^{\mu^-}_{\text{St1}}}\right) < 1.506$
- $(x^{\mu-}_{\text{target}})^2 + (y^{\mu-}_{\text{target}} - 1.6)^2 < 1485.0\ cm^2$
- $(x^{\mu-}_{\text{dump}})^2 + (y^{\mu-}_{\text{dump}} - 1.6)^2 < 201.0\ cm^2$

- $0.414 < \left| P^{\mu^-}_{x,\mathrm{St1}} - P^{\mu^-}_{x,\mathrm{St3}} \right| < 0.420$
- $\left| P^{\mu^-}_{y,\mathrm{St1}} - P^{\mu^-}_{y,\mathrm{St3}} \right| < 0.005$
- $\left| P^{\mu^-}_{z,\mathrm{St1}} - P^{\mu^-}_{z,\mathrm{St3}} \right| < 0.05$
- $-2.5 > (\chi^2_{\mathrm{target},\,\mu^-} - \chi^2_{\mathrm{dump},\,\mu^-}) < 77.5$
- $9 < P^{\mu-}_z < 78$
- $\mathrm{nHits}^{\mu-} > 13$
- $(y^{\mu-}_{St1} \cdot y^{\mu-}_{St3}) > 0$
- $\frac{\chi^2_{\mathrm{dump},\mu-}}{\chi^2_{\mathrm{upstream},\mu-}} < 0.195$
- $nHits^{\mu-}_{St1} > 4$
- $-45.0 < z^{\mu-}_{vtx} < 135.0$

3.3.3 Dimuon Level Selections

- $\mathrm{abs}(x^{\mu^+}_{\mathrm{St1}} + y^{\mu^-}_{\mathrm{St1}}) < 30.0\,\mathrm{cm}$
- $0\,\mathrm{cm} < \mathrm{z}^{vtx}_{\mu^+\mu^-} < 100\,\mathrm{cm}$
- $|\mathrm{x}^{vtx}_{\mu^+\mu^-}| < 0.262\,\mathrm{cm}$
- $|\mathrm{y}^{vtx}_{\mu^+\mu^-} - 1.6| < 0.225$ cm
- $(\mathrm{x}^{\mathrm{vtx}}_{\mu^+\mu^-})^2 + (\mathrm{y}^{\mathrm{vtx}}_{\mu^+\mu^-} - 1.6)^2 < 0.105\ cm^2$
- $\mathrm{y}^{\mu^+}_{St1} \times \mathrm{y}^{\mu^+}_{St3} > 0\ cm^2$
- $|\mathrm{z}^{\mu^+}_{\mathrm{vertex}} - \mathrm{z}^{\mu^-}_{\mathrm{vertex}}| < 125\,\mathrm{cm}$

- $(P_{x,\mathrm{vtx}}^{\mu^+\mu^-})^2 + (P_{y,\mathrm{vtx}}^{\mu^+\mu^-})^2 < 5.3\ (\mathrm{GeV/c})^2$
- $40.0\ GeV/c\ < P_{z,\mathrm{vtx}}^{\mu^+\mu^-} < 114.0\ GeV/c$
- $|P_{x,\mathrm{vtx}}^{\mu^+\mu^-}| < 1.675\ GeV/c$
- $|P_{y,\mathrm{vtx}}^{\mu^+\mu^-}| < 2.4\ GeV/c$
- $\mathrm{nHits}_{St1} + \mathrm{nHits}_{St2} > 30$
- $\mathrm{nHits}_{St1}^{\mu+} + \mathrm{nHits}_{St1}^{\mu-} > 9$
- $\chi^2_{\mu^+\mu^-} < 11.5$
- $\chi^2_{\mu^+\mu^-} < 11.5$
- $D1 < 400\ and\ D2 < 400\ and\ D3 < 400$
- $-0.18 < x_F < 0.94$
- $0.007 < x_T < 0.54$
- $5.0\,\mathrm{GeV/c^2} < M_{\mu^+\mu^-} < 8.0\,\mathrm{GeV/c^2}$
- $0.0\,\mathrm{GeV/c} < P_T^{\mu^+\mu^-} < 2.0\,\mathrm{GeV/c}$

3.4 Estimation of Combinatoric Background

In the reconstructed real data, many dimuon events contain multiple single muon tracks with opposite charges. We combine all possible combinations of the opposite-charged tracks to form the four-vector of dimuons. However, in many events, not all tracks originate from the same physics vertex. Therefore, any combination of uncorrelated tracks, whether with other uncorrelated or correlated tracks, results in background events. This is known as combinatorial background, and it impacts the reconstructed distributions. For an accurate interpretation of experimental results, it is crucial to subtract this type of background from the total reconstructed data. This subtraction is necessary for calculating the cross-section, properly accounting for the acceptance effect, etc. Combinatorial background estimation can be achieved by randomly combining single tracks from uncorrelated single muon tracks and calculating a scaling factor through a dimuons mass component fit, which determines the yield of the background. Failure to correctly estimate the combinatorial background can lead to larger systematic uncertainties and unreliable results when determining physics parameters or cross-section values from the signal events, which are obtained after subtracting the background from the total data. Therefore, careful consideration and accurate estimation of combinatorial background are essential for the robustness of high-energy physics experiments. In this review, we will summarize techniques that estimate the background without the need for any additional scaling factor, as extensively discussed in the paper [70]. We will also address the considerations that an analyzer needs to make before using this event-mixing method in any particular experiment.

3.4.1 Tracks Types in SeaQuest

Since many reconstructed events will have uncorrelated reconstructed tracks that come from different physics vertices, it could be extremely difficult to identify them from the data stream. They also have very similar beam conditions, corresponding to similar proton beam buckets. When we sample these tracks along with the tracks from the physics vertex of interest, we get the background events as well as the signal events. Since the uncorrelated tracks mostly originate from a similar beam-like environment, it is important to ensure that the tracks we mix to create background events mostly represent the data's beam-like environment. This motivates us to sample tracks from similar beam-like events. To achieve this, we sort the tracks according to drift chamber D1 occupancy (like from low to high counts). The track multiplicities (positive and negative) for different occupancy regions are shown in 44. The number of tracks per event increases with increasing occupancy. Here are the kinds of tracks we have in the SeaQuest events data stream:

- **Reconstructed Tracks in Events:**
  - Events may have multiple tracks, these tracks are categorized into two groups: *Signal Tracks* and *Background Tracks*.
    - Signal Tracks: Produced by a muon from J/ψ, ψ', or Drell–Yan decay, these form pairs of one positive and one negative track.
    - Background Tracks: Does not have any physics vertex. It may come from a physics vertex, but if both of them don't get reconstructed, we still consider the single track as a background track.

- **Empty track events**

  – Some events may not have any reconstructed single tracks. We also keep these events in our data stream. The majority of top/bottom-triggered events do not have a valid reconstructed track.

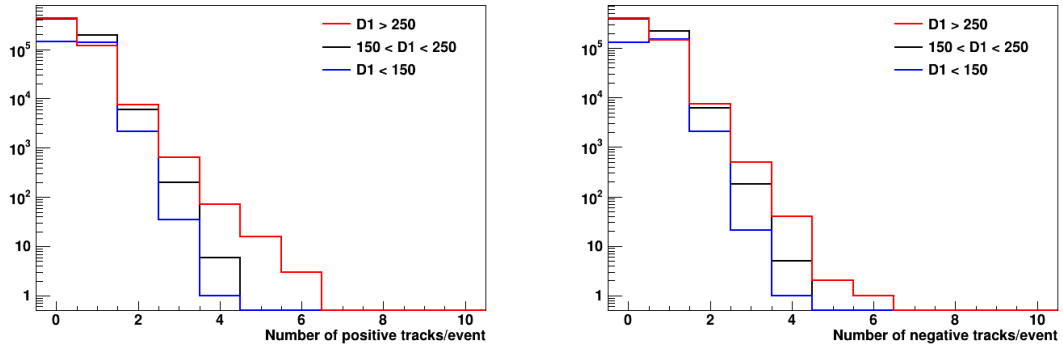

Figure 44: This figure shows the track multiplicities for positive (left) and negative (right) tracks across various D1 occupancies. The color coding is as follows: blue represents low occupancy, black denotes medium occupancy, and red indicates high occupancy. Generally, there are more positive tracks than negative tracks, which can be attributed to the higher production of positive pions compared to negative pions in proton-nucleus collisions. The plot is taken from Ref. [70].

3.4.2 Event Mixing Steps

Event mixing has three basic steps: sorting events according to occupancy, mixing opposite tracks from adjacent events, and vertexing.

- **Sorting the track**

  – If we randomly mix the tracks without considering the beam intensity or chamber occupancy, we won't consistently maintain the beam-like conditions for the tracks

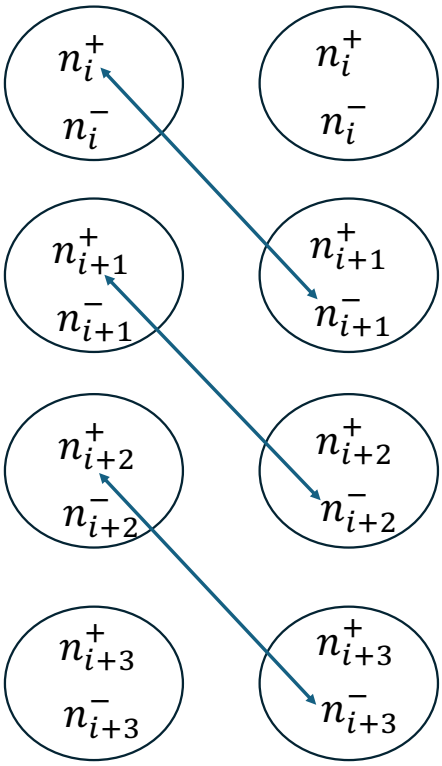

Figure 45: All positive tracks from event i and all negative tracks from event $i+1$ are combined into a new mixed event. This combination assumes that event sorting based on occupancy has already been done.

we are mixing. To ensure this, we first sort the events in the station 1 chamber occupancy from low to high. This ensures that adjacent events are likely to have similar beam conditions based on comparable chamber occupancy.

- **Mixing the single tracks**
  - Once the events are sorted according to the chamber occupancy, we combine all positive tracks from event i and all negative tracks from event $i+1$ into a new mixed event, showed in the cartoon 45. This is implemented for all events, including the empty-track events. These mixed events are saved into a new tree, referred to as the "mixed run."

- We also want to make sure that each track is used only once. This is done to make sure how the physics dimuon is also formed.

- **Passing through the veretxing**

  - Once we combine the positive and negative muon combinations and save them into a new file called "mixed run," we run the vertexing through the track pairs. In addition to this, the track pairs for real data or combinatorial events face the same trigger condition, known as top/bottom-trigger.

3.4.3 Mixing Method: Mathematical Argument for Normalization and Approximation

In this section, we review that under a certain approximation, the shape of the combinatorial background can be determined without introducing any additional scaling factor. This is extensively discussed in the paper [70] with more details.

- Track multiplicity:

  - s_i^+: positive signal tracks (0 or 1).

  - s_i^-: negative signal tracks (0 or 1).

  - b_i^+: positive background tracks (0, 1, 2, ...).

  - b_i^-: negative background tracks (0, 1, 2, ...).

- N_E: total number of events in each run.

- N_P: total number of unlike-sign track pairs.

$$N_P = \sum_{i=1}^{N_E} \left(s_i^+ s_i^- + s_i^+ b_i^- + b_i^+ s_i^- + b_i^+ b_i^- \right).$$

The first term, denoted as $N_S = \sum_{i=1}^{N_E} s_i^+ s_i^-$, represents the total number of signal dimuon pairs in this run, while the remaining terms contribute to the combinatoric background, which is denoted as N_C, and can be written below:

$$N_C = \sum_{i=1}^{N_E} \left(s_i^+ b_i^- + b_i^+ s_i^- + b_i^+ b_i^- \right).$$

$$N_C = \sum_{\omega=0}^{\omega_{\max}} \sum_{i=1}^{N_\omega} \left(s_i^+ b_i^- + b_i^+ s_i^- + b_i^+ b_i^- \right) \quad \text{[Sorting events by D1 chamber occupancy, } \omega\text{]}$$

$$N_C = \sum_{\omega=0}^{\omega_{\max}} N_\omega \left(\left\langle s^+ b^- \right\rangle_\omega + \left\langle b^+ s^- \right\rangle_\omega + \left\langle b^+ b^- \right\rangle_\omega \right) \quad \text{[Sum over events with the same occupancy]}$$

The total number of pairs in the run is given by:

$$N_P = N_S + N_C.$$

For mixed run's case:

$$N'_P = \sum_{i=1}^{N_E} \left(s_i^+ s_{i+1}^- + s_i^+ b_{i+1}^- + b_i^+ s_{i+1}^- + b_i^+ b_{i+1}^- \right)$$

The term representing adjacent signals, $s_i^+ s_{i+1}^-$, in the above equation is very small in SeaQuest. Therefore, we consider

$$N_{\text{AS}} = \sum_{i=1}^{N_E} s_i^+ s_{i+1}^- \approx 0.$$

The remaining three terms can be handled in the same way as in the normal run.

$$N'_C = \sum_{\omega=0}^{\omega_{\max}} N_\omega \left(\left\langle s^+ b^- \right\rangle_\omega + \left\langle b^+ s^- \right\rangle_\omega + \left\langle b^+ b^- \right\rangle_\omega \right).$$

In cases of large statistics, the sums N_C (normal run) and N'_C (mixed run) are equal. As the statistics decrease, the equality $N_C \approx N'_C$ continues to hold within statistical uncertainties. This observation is validated by the expression:

$$N_P - N'_P = (N_S + N_C) - N'_C \approx N_S,$$

which implies that $N_C \approx N'_C$ remains accurate within the uncertainties.

The adjacent term approximation is valid when the signal rates in the data stream are very low. In the next section, we will quantitatively explain the systematic effect coming from the adjacent term.

3.4.4 Method Validation with Simulated Event

As we already learned the normalization of the event mixing method is true under the approximation that the adjacent signals in SeaQuest is very small. The motivation for this study is to embed the simulated reconstructed signals into the real/background data. Using the mixing method, we want to check whether we can recover the embedded signals using the event mixing method within the statistical uncertainty. There are two simulation type test is described in the paper [70], and we will go through them both.

3.4.4.1 Type I Test The steps of the Type I test have been shown in Figure 46.

- It has been shown that we take the SeaQuest normal run containing the signal and background tracks, or no tracks in some events. We sort the events and form the combinatoric background, and we call this the "mixed run".
- In a separate analysis, we take the "mixed run" and embed signals from simulated

events into every n'th (about 5%) interval. We form the combinatorial background and call it the "new mixed run".

- We run the vertexing through both the "mixed run" and the "new mixed run" and obtain the mass spectra for both cases. The differences would be the signal we embedded from the simulation within the statistical uncertainty.

To exercise the test, we have used a continuous Drell–Yan simulated reconstructed events, which are considered as our embedded signals to SeaQuest real data called (normal run), to conduct the Type I test. The combinatorial background from the normal run, known as "mixed run" is illustrated in the left plot of Figure 47, while the right plot shows the simulated events intended for embedding. Figure 48 on the left displays the combinatorial background from the "mixed run" (green), alongside the the embedded one (black). The right plot shows the recovered signals after we take the subtraction between "mixed run" and "new mixed run". The comparison between embedded simulated signals and recovered ones is shown in Fig. 49.

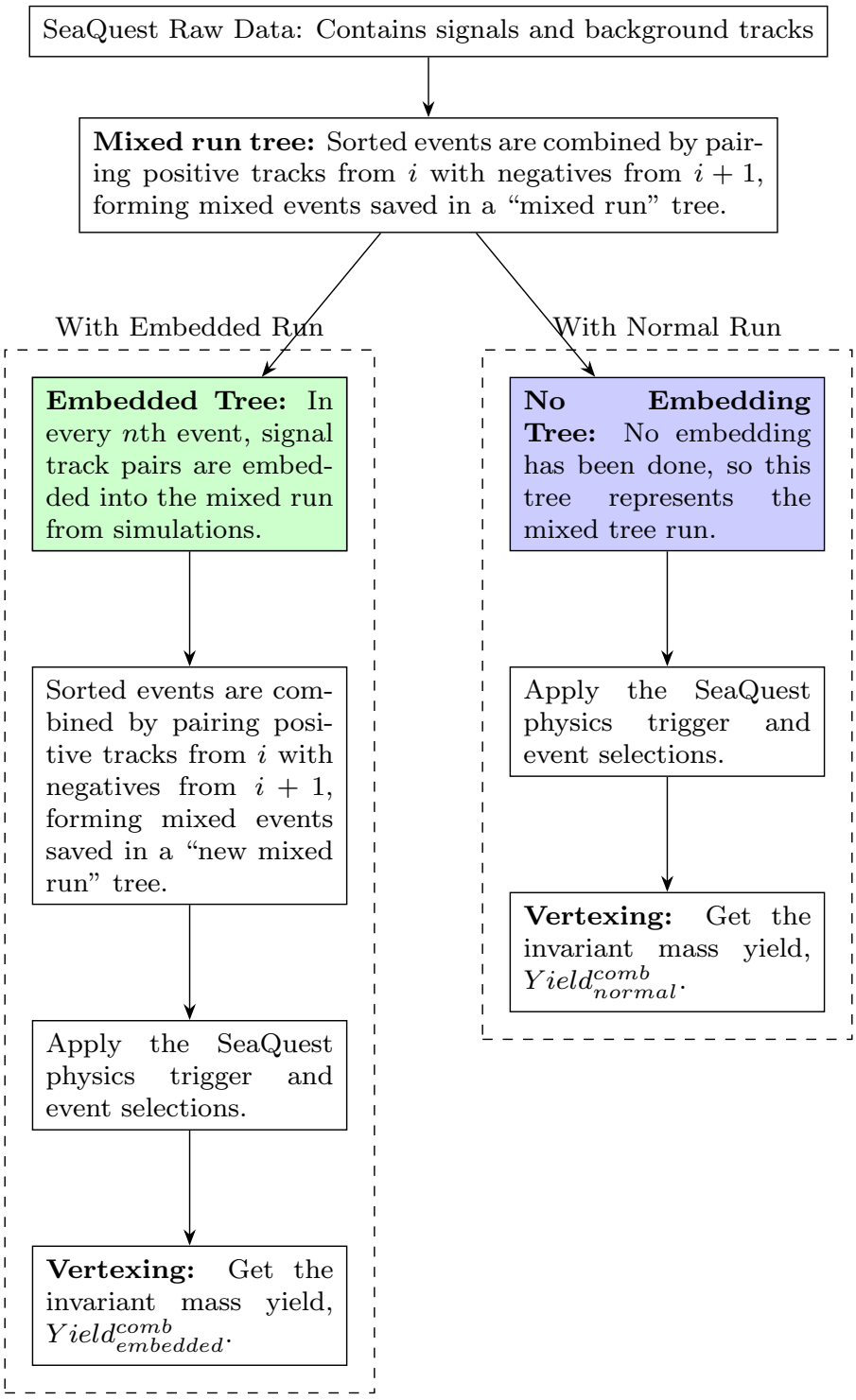

Figure 46: The steps show the Type I test, and at the end of the steps, the recovered signals can be obtained by taking the subtraction between the yields of $Yield^{\text{comb}}_{\text{embed}}$ and $Yield^{\text{comb}}_{\text{normal}}$.

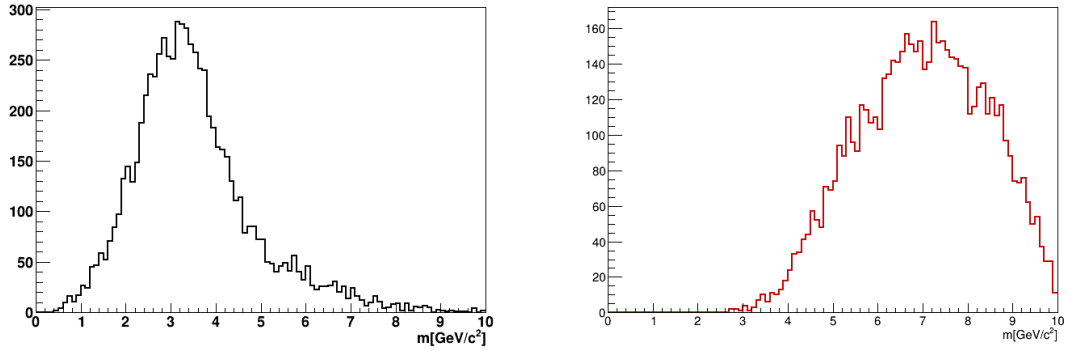

Figure 47: The left histogram shows mixing events from real data, whereas the right histogram shows simulated signals intended for embedding in those mixing events. This figure comes from Ref. [70].

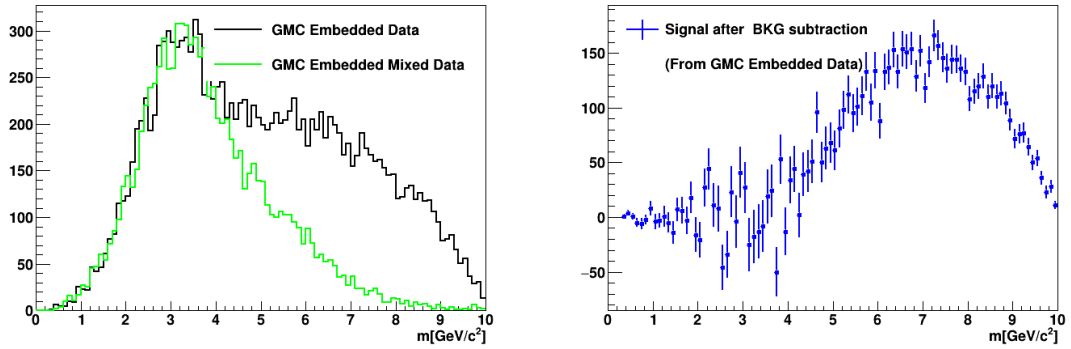

Figure 48: The left black and green histograms represent the sum of embedded simulated events and mixed events, respectively, while the right blue histogram shows the signal events obtained by subtracting the mixed events from the GMC embedded data. This figure is taken from Ref. [70].

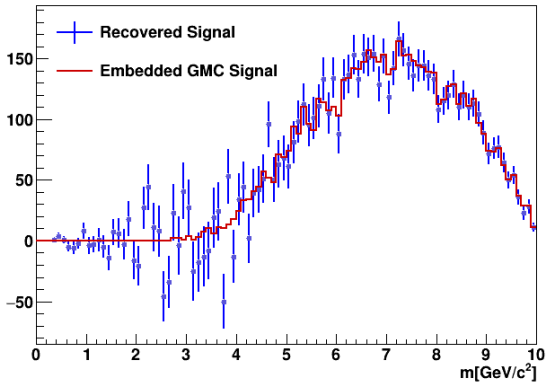

Figure 49: The blue histogram represents the signal recovered using the mixing method, as shown in Fig. 48 (right), and the red histogram displays the embedded simulated events, as shown in Fig. 47 (right). This figure is taken from Ref. [70].

3.4.4.2 Type II Test The steps of the Type II test have been illustrated in Figure 50.

- We first consider the SeaQuest normal run containing both signal and background, or no tracks in some events.
- Similar to the Type I test, we embed signals from simulated events into every nth (about 5%) interval. This becomes our "embedded run".
- **With normal run:** We calculate the yield, referred to as "Yield1", and then compute "Comb1" from the corresponding combinatoric background events. The signal events are given by: Signal1 = Yield1 − Comb1.
- **With embedded run:** Starting with the "embedded run," we calculate the yield, referred to as "Yield2", and then compute "Comb2" from the corresponding combinatoric background events. The signal events are given by: Signal2 = Yield2 − Comb2.
- Now, the difference between Signal1 and Signal2 is the embedded simulated signals.

To conduct the Type II test, we use 10 normal SeaQuest run data and embed simulated resonance signals with a mass of $6\,\mathrm{GeV/c^2}$. The process follows the steps outlined in the flowchart 50. Embedding will be performed with a fixed interval in 5% events in the 10 runs, which means the adjacent term (N_{AS}) will be zero. We will also use various normalization factors to demonstrate that the mixing method does not require an additional scaling factor. From Figure 51, the black plot shows the normal data of 10 runs, while the green one shows the corresponding combinatorial background events. The right plot shows the signals obtained after subtracting the combinatorial background events from the normal data. Figure 52 shows the resonance data that will be embedded into the normal data for the Type II test,

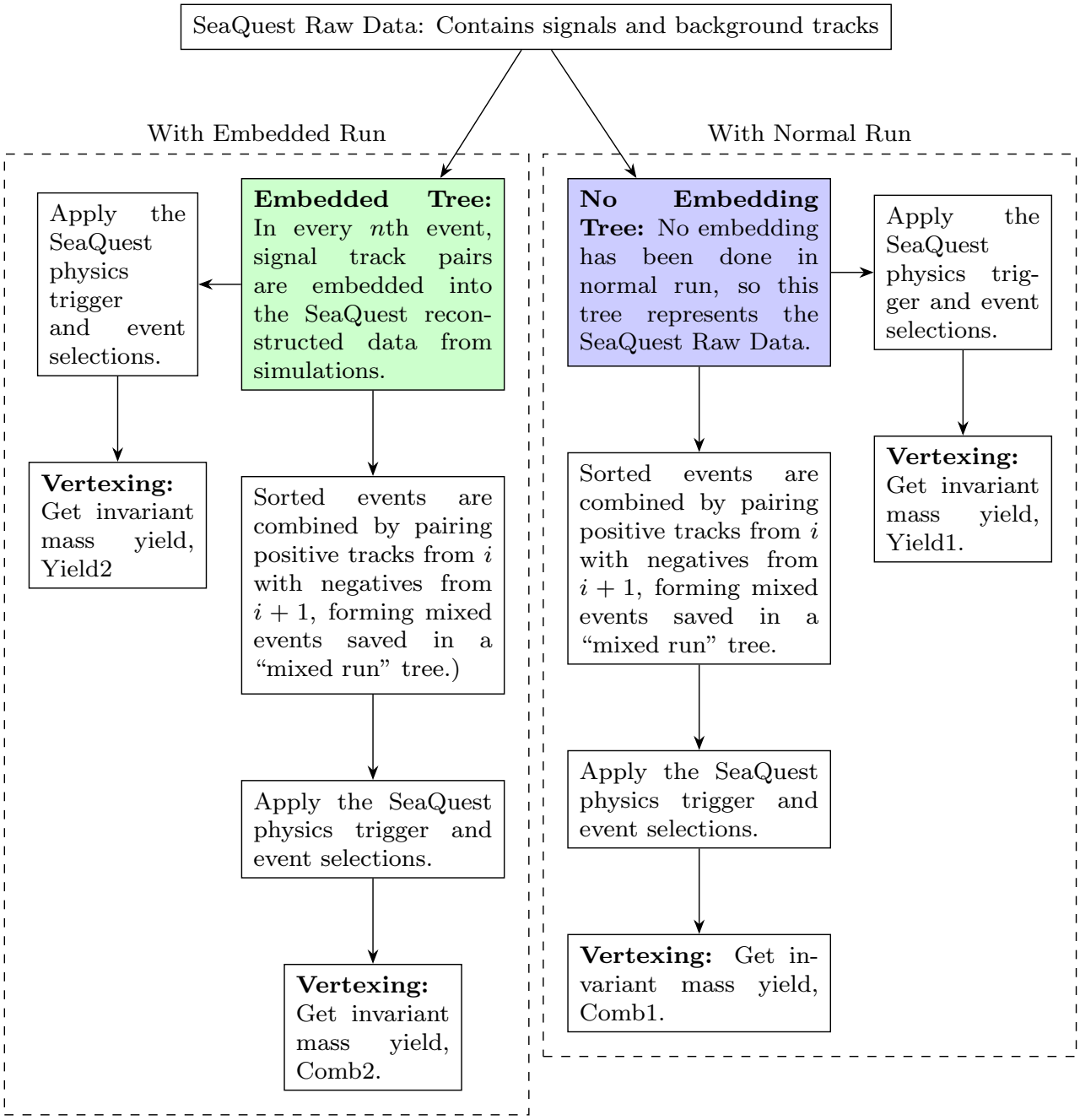

Figure 50: The steps show the Type II test, and at the end of the steps, the recovered signals can be obtained by taking the subtraction between the yields of Signal1 and Signal2.

while Figure 53 shows the normal data after the embedding, represented by the black color histogram. The green histogram shows the corresponding combinatorial background. The right plot shows the signal after subtracting the combinatorial background. The table shows the integrated event counts under different normalization scaling. The difference is shown as the blue points on the right-hand side of Fig. The left side of Fig. 54 shows the various signals, as discussed earlier, along with the red signal histogram. The right figure shows that the recovered distributions and the embedded simulated signal are in good agreement.

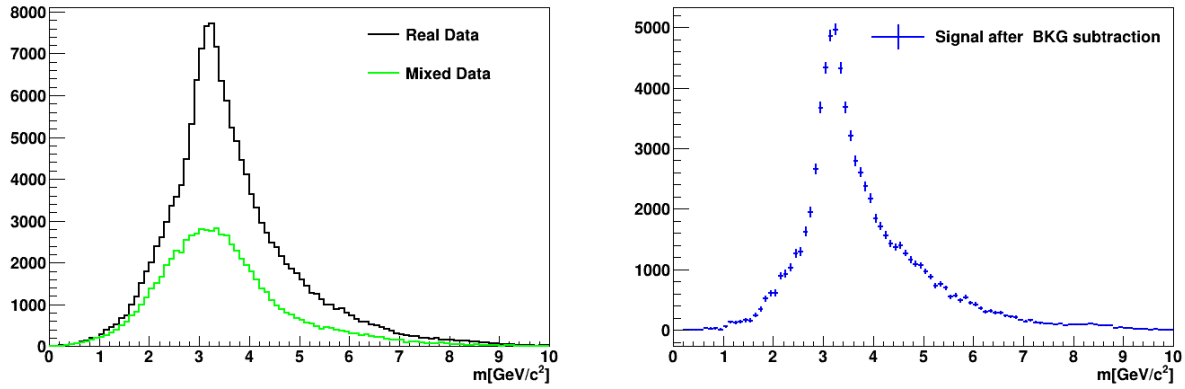

Figure 51: The left histogram displays the dimuon mass distributions for normal data (shown in black) and mixed data (shown in green) from 10 runs. The right histogram presents the signal, obtained by subtracting the mixed data from the normal data. This figure comes from Ref. [70].

Normalization	0.6	0.8	1.0	1.2	1.4
Area	-3610 ± 118	-1876 ± 125	-143 ± 132	1590 ± 138	3324 ± 145

Table 13: Area of each histogram in Figs. 55 and 56 as a function of the normalization factor NM.

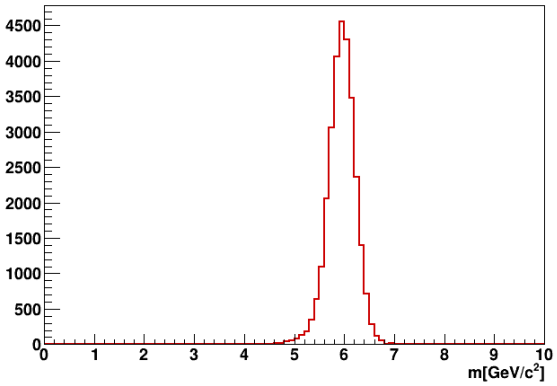

Figure 52: The figure shows a simulated resonance signal peaking at 6 GeV/c^2, which will be embedded into the data shown in Fig. 51. This figure comes from Ref. [70].

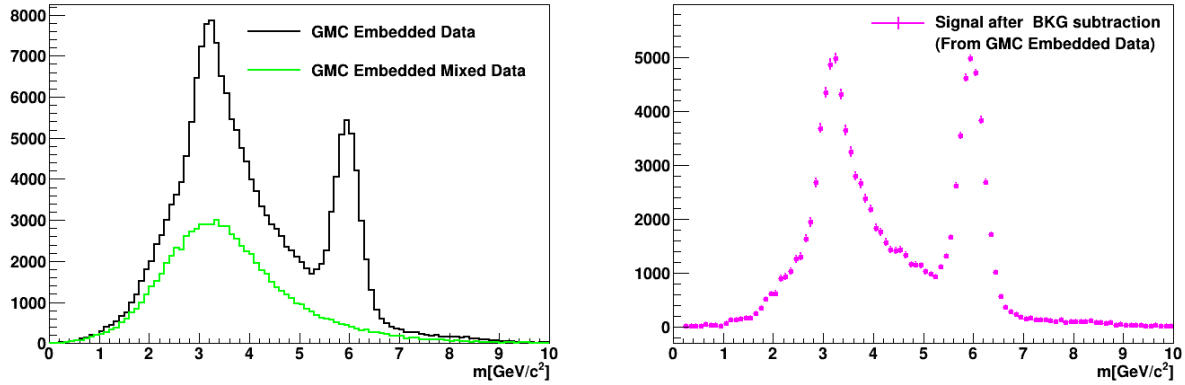

Figure 53: The left black histogram shows the dimuon distribution after embedding the simulated signals from Fig. 52 into the data from Fig. 51. The green histogram represents the corresponding combinatorial background. The right magenta histogram represents the signal obtained by subtracting the combinatorial background (green) from the total data (black). This figure is taken from Ref. [70].

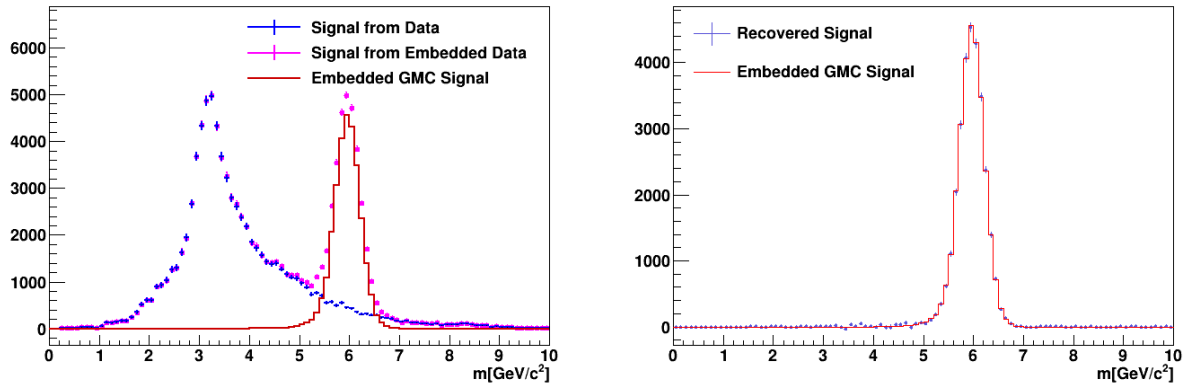

Figure 54: The figure shows a comparison of signals from different analysis stages. On the left, the blue histogram represents the signal (Signal1) from the 10 normal runs, and the magenta histogram represents the signal from the simulated data (Signal 2). Both of these were obtained after combinatorial background subtraction. The red histogram represents the embedded simulated signal, same as Fig. 52. The right histogram shows the difference (Signal2 - Signal1). This figure comes from Ref. [70].

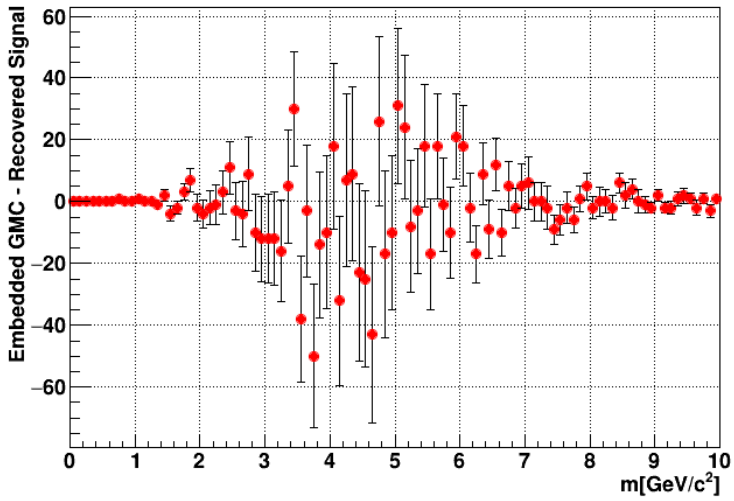

Figure 55: From the right side of Fig. 54, this figure illustrates the difference between the embedded GMC and the recovered simulated signal. This figure comes from Ref. [70].

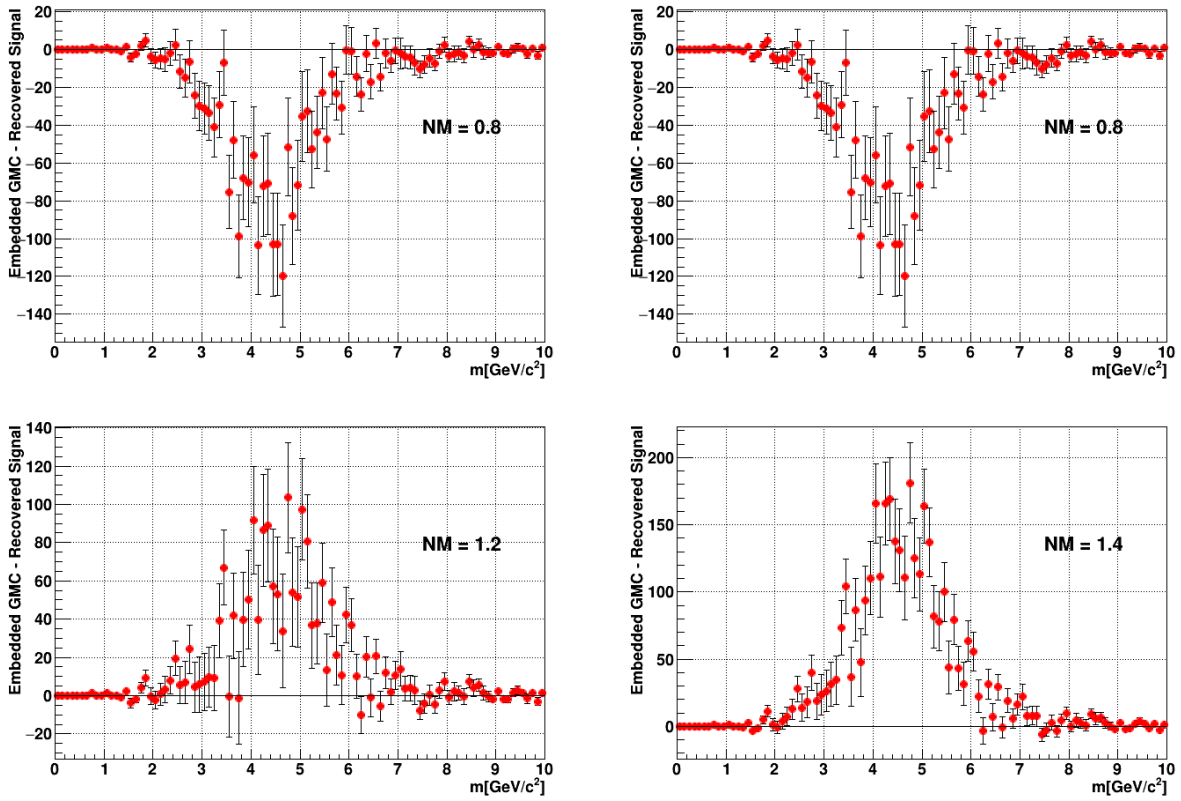

Figure 56: From the right side of Fig. 54, this figure illustrates the difference between the embedded GMC and the recovered simulated signal with different normalization factors (NM). This figure comes from Ref. [70].

3.4.5 Validity of the Event Mixing method for the SeaQuest experiment

In Section 3.4.4.2, we embedded events by turning off adjacent signal N_{AS}. Here, we want to estimate the systematic effect resulting from fixed interval embedding. Random event embedding is similar to the Type II fixed interval process we have done, with the difference that the embedded simulated events will be random. From the table, we observe that the residual signal in fixed interval embedding, obtained by integrating the recovered simulated signal from the Type II testing, fluctuates around zero. However, with random embedding, the residual signal is influenced by the adjacent signal term, leading to a net positive residual signal. Therefore, N_{AS} sets the upper limit for residual signals, and depending on the signal rates in total reconstructed data, the residuals could vary in a particular experiment.

Run Number	Fixed Embedding	Random Embedding
12525	143 ± 137.7	90 ± 138.1
12527	-43 ± 146.4	206 ± 147.3
12528	1 ± 143.3	225 ± 144.4
12529	-14 ± 109.6	148 ± 109.9
12530	84 ± 139.4	188 ± 140.4
12531	-22 ± 147.5	42 ± 148.1
12532	37 ± 91.3	160 ± 92.3
12533	-174 ± 146.8	119 ± 147.6
12534	150 ± 149.7	487 ± 150.1
12535	182 ± 145.0	364 ± 145.2
Weighted Average	33.1 ± 41.3	192.6 ± 41.5

Table 14: A list of residual signals is provided for the fixed embedding and for the random embedding using the Type I test. This Table is taken from Ref. [70].

3.5 Unfolding

In particle physics experiments, tracking detectors have finite resolutions, and due to that, we measure the noisy version of the true physics distributions. Additionally, the measurement techniques from the detectors could also differ. This introduces smearing to the reconstructed events, and as a result, there might be a nonzero probability of the reconstructed events being placed in different bins than the true variables—known as bin migration. In addition to the smearing effect, due to the detector-acceptance and reconstruction inefficiency, the reconstructed distributions could get further distorted. The goal of the physicists is to infer the true distributions from the measured (reconstructed) ones. To achieve this, it becomes essential to mitigate these systematic effects through a process known as unfolding or deconvolution.

SeaQuest, as a fixed-target experiment, has a narrow dimuon acceptance in the $\cos\theta_{CS}$, where the polar angle θ_{CS} is measured in the dimuon rest frame. For example, the true physics distribution in Figure 3.5 exhibits a $1 + \cos^2\theta_{CS}$ shape represented by the solid blue histogram. The reconstructed distributions, which have lower counts in the larger $|\cos\theta_{CS}|$ ranges, are shown by the shaded blue histogram. The goal of the unfolding process is to recover the true physics distributions from the reconstructed variables. The unfolded distribution is shown by the shaded red histogram. Depending on the physics, one could compare the yields or physics parameters between the true and unfolded histograms to check for the validity of the unfolding.

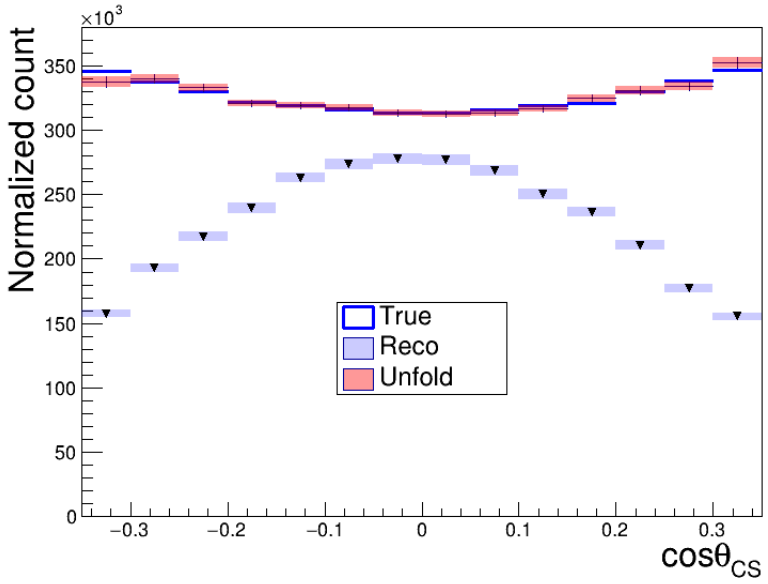

Figure 57: In the figure, we can see three kinds of distributions for the $cos\theta_{CS}$ in the Collins-Soper frame. It displays the true, reconstructed, and unfolded distributions.

Although unfolding is a very powerful method for retrieving physics information from reconstructed variables, depending on the unfolding method, there could be potential bias due to the regularization parameter used in the method. It's important to carefully review the method to ensure it works reliably well for the particular experiment.

3.5.1 Building Response Matrix

The motivation of the unfolding is to connect the mapping between true and reconstructed distributions, which can be expressed in terms of the response function $R(x|y)$:

$$f_{\text{reco}}(x) = \int R(x|y) \cdot f_{\text{true}}(y)\, dy.$$

Now, if the measurements are discrete, represented by histograms, we can express the equation as:

$$x_i = \sum_{j=1}^{N} R_{ij} \cdot y_j,$$

where:

- R_{ij}: Probability of an event that is reconstructed in bin i given the true value is in bin j.
- x_i represents the reconstructed distribution (histogram) at the detector level.
- y_j represents the true distribution (histogram) at the particle level.
- N denotes the number of bins in the distribution of the true quantity y.

Using the true and reconstructed distributions of the simulated data, the response matrices can be constructed. As an example, the response matrices for ϕ and $\cos\theta$ in the dimuon rest frame are shown in Figure 58

It's possible to recover the true distributions by inverting the response matrix, but one has to ensure that it doesn't yield any unphysical results. In our analysis, we will use an approach called Bayesian Iterative Unfolding, motivated by Bayesian statistics and proposed by G. D'Agostini [37]. The method iteratively retrieves the true distributions without inverting the response matrix.

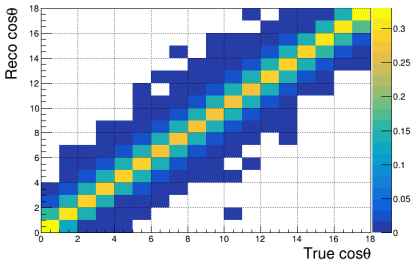

(a) $P_T \in (0.0, 2.0)$ GeV/c

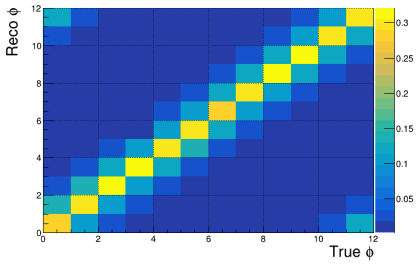

(b) $P_T \in (0.0, 2.0)$ GeV/c

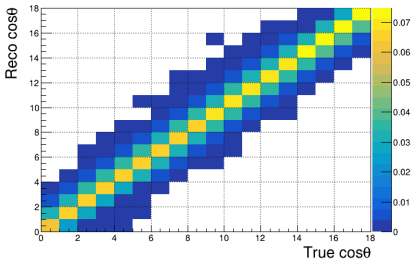

(c) $P_T \in (0.5, 1.0)$ GeV/c

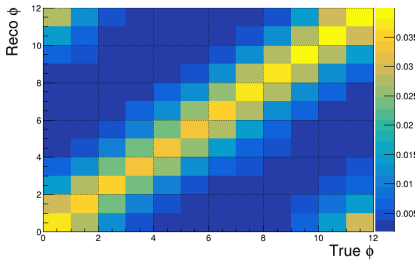

(d) $P_T \in (0.5, 1.0)$ GeV/c

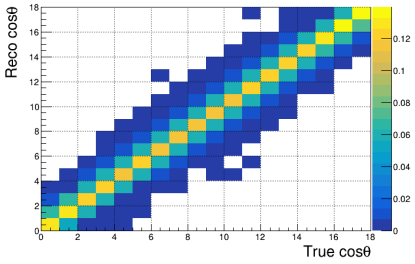

(e) $P_T \in (0.5, 1.0)$ GeV/c

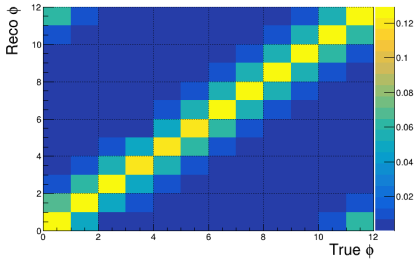

(f) $P_T \in (0.5, 1.0)$ GeV/c

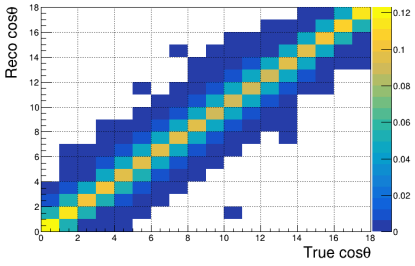

(g) $P_T \in (1.0, 2.0)$ GeV/c

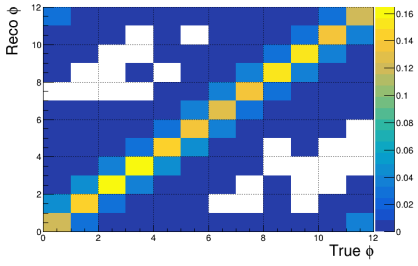

(h) $P_T \in (1.0, 2.0)$ GeV/c

Figure 58: Using the Monte Carlo events, the response matrix plots show bin-to-bin migration probabilities in 2D. The reconstructed dimuon mass chosen for this case ranges from 5 GeV/c^2 to 8 GeV/c^2. All the participated events went through the reconstructed cuts, so we don't have any inefficient events included in the response matrix.

3.5.2 The Unfolding Procedure in Analysis

In my analysis, I will unfold the angular distributions from the Drell–Yan events. To accomplish this, I will construct 2D histograms of reconstructed ϕ-$\cos\theta$ distributions across various kinematic variable ranges. Therefore, the response matrix should vary based on the chosen kinematics. The concept is that the conditions for reconstructed events in the response matrix should remain the same as those applied to the test histograms. The resolutions of the ϕ, and $cos\theta$ that participate in the response matrices are shown in Figure 59.

Before performing unfolding in an analysis, one should consider several aspects:

- Defining the variables that need to be unfolded (corrected). In our case, we correct in two dimensions using ϕ and $\cos\theta$ variables.
- Building the response matrix with specific bin combinations. In our case, we flatten the 2D histogram into a 1D array to construct the response matrix. We have chosen 12 bins for ϕ and 18 bins for $\cos\theta$.
- Choosing the method based on performance considerations. In our case, we used the Bayesian Iterative Unfolding Method.

The response matrix can be constructed using true and reconstructed events, where the diagonal elements represent the probability of correctly reconstructing a particular simulated variable, and the off-diagonal elements indicate the probability that a value reconstructed in bin j originated from the true bin i. An example of the detector response matrix is shown in Figure 60. Inefficient or missed events are not shown in the response matrix, but in the final analysis, these missed events will be accounted for to build the response matrix.

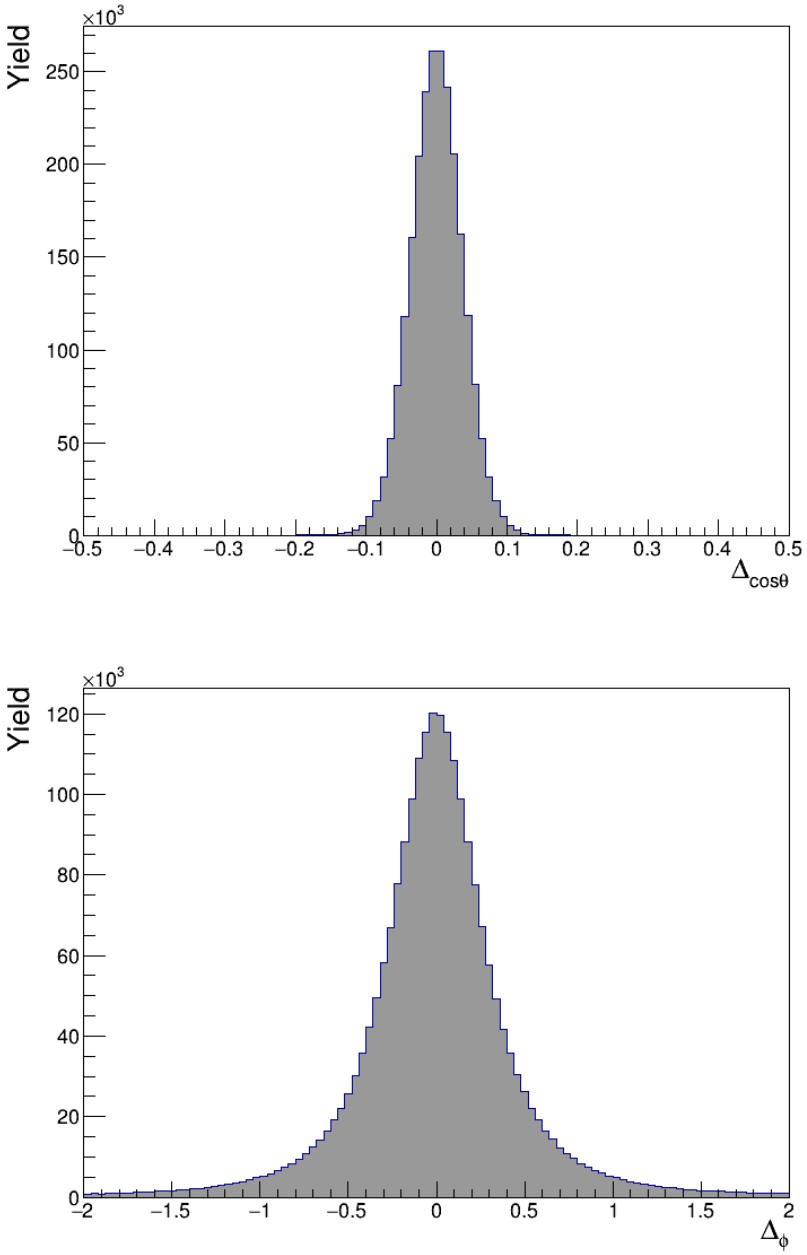

Figure 59: Resolution plots of ϕ and $\cos\theta$ in the Collins-Soper frame for the Drell–Yan dimuon P_T range of (0.0, 2.0) GeV/c and in the mass range of (5.0, 8.0) GeV/c^2.

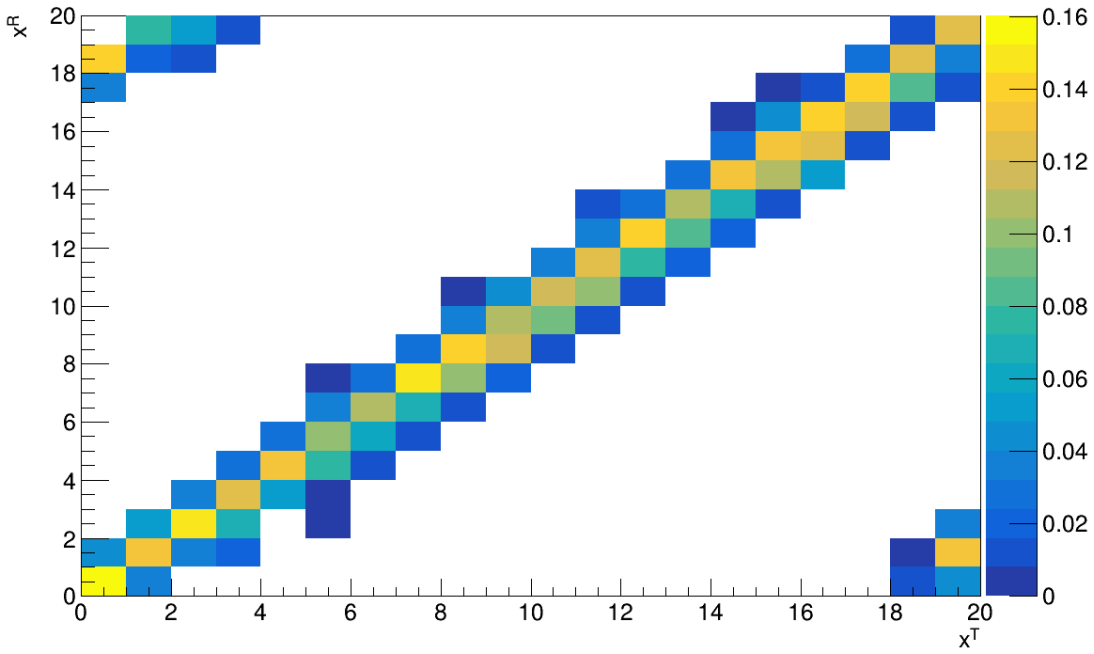

Figure 60: In this response matrix plot, the 2D bins represent the bin-to-bin migration probabilities without considering the inefficiency. x^T and x^R represent the true and reconstructed first 20×20 bin combinations from the two-dimensional variable response matrix $\phi \times \cos\theta$.

3.5.3 Interative Bayesian Unfolding

D'Agostini developed an iterative unfolding method based on Bayes' theorem, extensively outlined in Ref. [37, 38]. We will closely review the article Ref. [38]. A probabilistic approach has been used to obtain the true distributions from the reconstructed (or measured) ones. In the context of Bayesian unfolding, we can connect these relationships as "cause (C)" and "effects, (E)". The causes correspond to the true values before undergoing smearing, while the effects correspond to the values after smearing. Each cause can have multiple effects.

Let's assume many different causes $(C_1, C_2, C_3...C_{n_C})$ produce one effect, E. Then the Bayesian formula can be written as:

$$P(C_i \mid E) = \frac{P(E \mid C_i) \cdot P(C_i)}{\sum_l P(E \mid C_l) P(C_l)}. \tag{18}$$

- $P(C_i)$ is the initial probability of the i-th cause.
- $P(E \mid C_i)$ represents the conditional probability that the observed effect E was caused by the i-th cause C_i.
- $P(C_i \mid E)$ represents the conditional probability of the i-th cause given the effect E.

If we start with a prior, which could be uniform, or from MC true distributions, we can update the knowledge of $P(C_i)$ just by repeating the observations. $P(E \mid C_i)$ can be calculated from the Monte Carlo methods.

Now we can extend the equation (18) for multiple effects:

$$P(C_i \mid E_j) = \frac{P(E_j \mid C_i) \cdot P(C_i)}{\sum_l P(E_j \mid C_l) P(C_l)}. \tag{19}$$

Now summing over all the effects:

$$\hat{n}(C_i) = \sum_j n(E_j) \cdot P(C_i \mid E_j), \tag{20}$$

where,

- $\hat{n}(C_i)$ is the expected number of events in the cause bin i.
- $n(E_j)$ is the number of events in the effect bin j.

Considering the efficiency, we obtain the truth distribution as:

$$\hat{n}(C_i) = \frac{1}{\epsilon_i} \sum_j n(E_j) \cdot P(C_i \mid E_j) \quad ; \epsilon \neq 0. \tag{21}$$

Efficiency is defined as $\epsilon_i = \sum_j P(E_j \mid C_i)$, the probability that an event in bin 'i' of the true distribution has a partner in any bin of the reconstructed distribution.

The final value of $\hat{n}(C_i)$ is derived iteratively using equation (21), starting with the initial distributions $P(C_i)$ (the prior), as expressed in (19). The initial distributions can be obtained from simulations, and in our case, they are represented by 2-dimensional $\phi - \cos\theta$ histograms. These histograms must have the same binning as the response matrix $P(E_j \mid C_i)$, which is constructed using simulated data. This process is repeated until the output converges with the actual data distributions. This approach is the motivation for the Bayesian Iterative

Method, which operates similarly to a "for" loop, allowing us to iteratively improve the unfolded distributions. To ensure that the unfolded physics results are unbiased, the outcomes of the current and previous iterations are compared. It should be noted that excessive iterations may lead to an increase in statistical noise within the unfolded data; thus, they should be minimized. The unfolding process, using RooUnfoldBayes [1] in our analysis, takes the training truth as its initial prior.

3.5.4 Retraining the Response Matrix

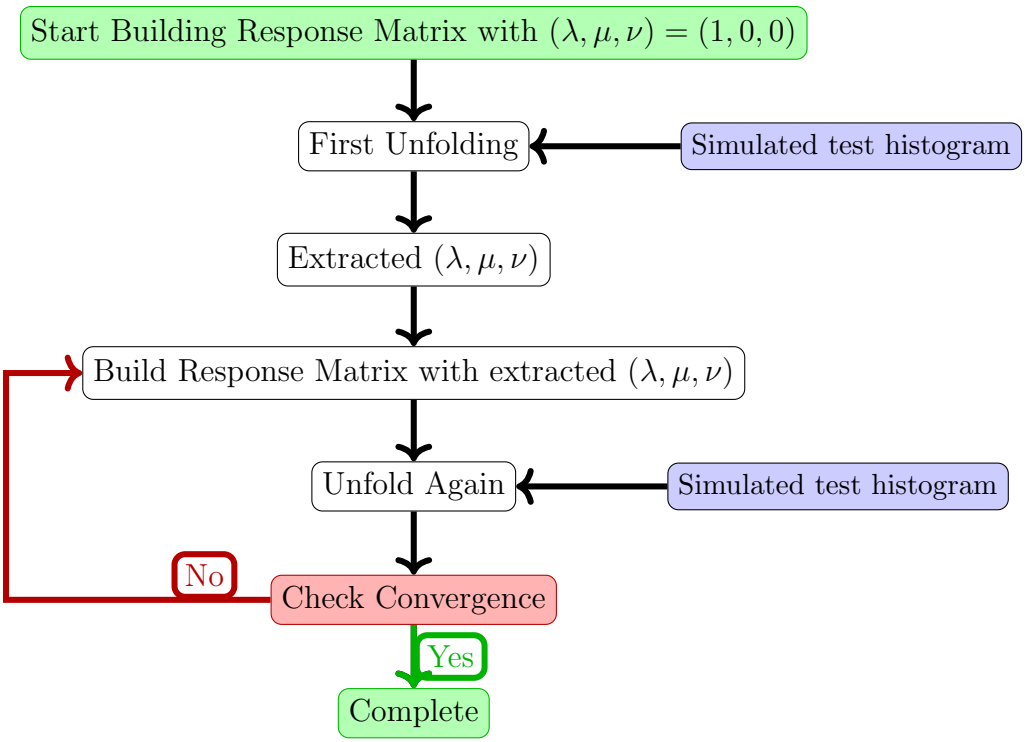

Figure 61: A flowchart of the Bayesian Iterative Unfolding method with iterative retraining of the response matrix.

In Bayesian Iterative Unfolding, the output distributions from the unfolding process may exhibit sensitivity to the regularization iterations. Increasing the regularization parameter

can result in increased uncertainty in the extracted parameters. In general, it is expected that the unfolding process iteratively retrieves the distribution to converge with the true data distribution. However, a large number of iterations does not guarantee convergence, and also not all unfolding models may work for a particular experiment. In our unfolding test, we do not check only the yield of the measured distributions, as the unfolded physics parameters are very sensitive to even small changes in the unfolded distribution yield. Therefore, we would like to check the difference between the injected physics parameters in the test histograms and the recovered ones. We will use many independent test datasets to check the reliability of the results as well. We can assume that many independent test datasets work like each independent experiment. To ensure an unbiased study, we also need to ensure that the unfolded distributions remain independent of the specific combinations of the parameters used to produce the simulated data. For example, in the simulated Drell–Yan data, we can have a specific set of values for angular distribution parameters (λ, μ, ν), and it's important to make sure that unfolded results don't depend on the particular physics parameters used to generate the simulated data. And, to effectively manage the large uncertainties and determine the appropriate stopping point for the iteration, it becomes necessary to retrain the response matrix to achieve highly stable unfolded results. Fig. 61 illustrates the steps involved in retraining the response matrix and utilizing the Bayesian iterative method to unfold the measured distributions.

To inject different parameters into the simulations, the following equation has been used:

$$R(\phi, \cos\theta) = \frac{1 + \lambda_{\text{inject}} \cos^2\theta + \mu_{\text{inject}} \sin 2\theta \cos\phi + \frac{1}{2}\nu_{\text{inject}} \sin^2\theta \cos 2\phi}{1 + \cos^2\theta}.$$

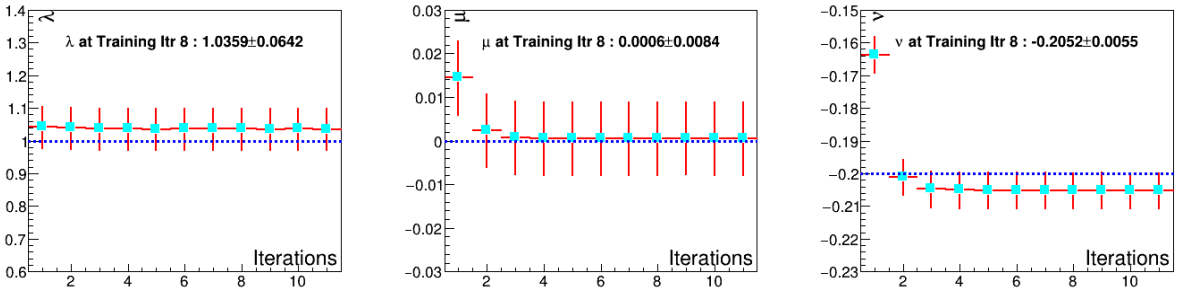

(a) Building the response matrix with (λ, μ, ν)= (1, 0, 0).

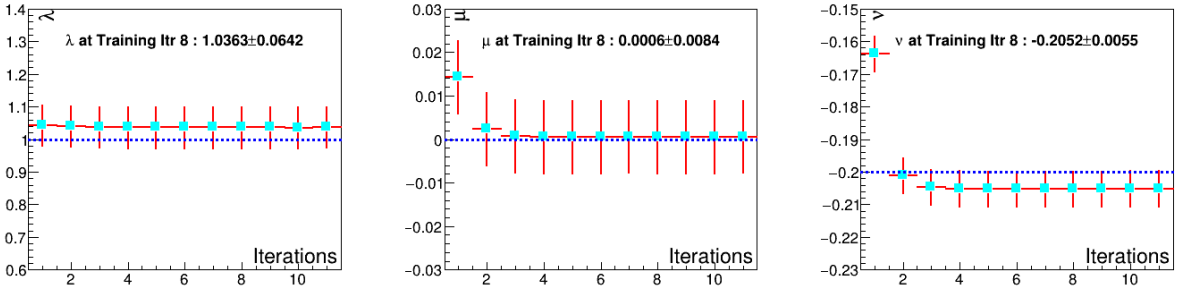

(b) Building the response matrix with (λ, μ, ν)= (0, 0, 0.2).

Figure 62: (λ, μ, ν) were extracted in the p_T range of (0.0, 2.0) GeV/c from a simulated test dataset using Bayesian Unfolding with unfolding regularization iteration 2.

In the initial training of the response matrix, we set an arbitrary combination of (λ, μ, ν), and in the subsequent iteration, as indicated by the reference to the flowchart (61), the (λ, μ, ν) values are obtained from the fit results of the unfolded distributions.

Fig. 62 demonstrates the validity of the flowchart shown in Fig. 61, indicating that we could recover the injected parameter from the test data within the statistical uncertainty regardless of the initial parameter combination used in the response matrix. Based on many simulation tests like this, we have determined that we will retrain 5 times to achieve better convergence of the unfolding process.

3.6 Event Reweighting Overview

Due to the limitation of the detector modeling in simulation and for not considering some effects, upon applying the event selections to both reconstructed events in the data and the Monte Carlo (MC) simulations, it's possible for discrepancies to arise between the real data and the MC. To align the MC with the data, a boosted decision tree-based method reweighting has been adopted to accomplish this calibration.

The details of the reweighting process using **Gradient Boosted Reweighter** can be found in the paper [74], but here are the few reweighting implementation steps summarized from the paper:

1. The input features of the Gradient Boosted Reweighter: `mass`, P_T, x_F, `D1`, $x^{\mu^+}_{st1}$, $x^{\mu^-}_{st1}$,$y^{\mu^+}_{st1}$, $y^{\mu^-}_{st1}$, $P^{\mu^+}_{x,st1}$, $P^{\mu^-}_{x,st1}$, $P^{\mu^+}_{y,st1}$, $P^{\mu^-}_{y,st1}$, `dpx`, `dpy`, `dpz`, `dx` , `dy`, `dz`. The naming conventions can be found in table 12.

2. The GB reweighter splits the input features into a couple of new regions and builds a shallow decision tree that aims to maximize the χ^2 metric:

$$\chi^2 = \sum_{\text{leaf}} \frac{(w_{\text{leaf, MC}} - w_{\text{leaf, RD}})^2}{w_{\text{leaf, MC}} + w_{\text{leaf, RD}}}. \tag{22}$$

   The symmetrized χ^2 metric measures the discrepancy between the Monte Carlo (MC) and real data (RD) distributions in different regions (leafs) of the decision tree. It guides the construction of decision trees by prioritizing the regions where the MC and RD distributions differ the most. The goal is to minimize this discrepancy by assigning appropriate weights to the MC events in those regions. It does not need reweighting if the weights of the original and target distribution are equal. If the sum is high,

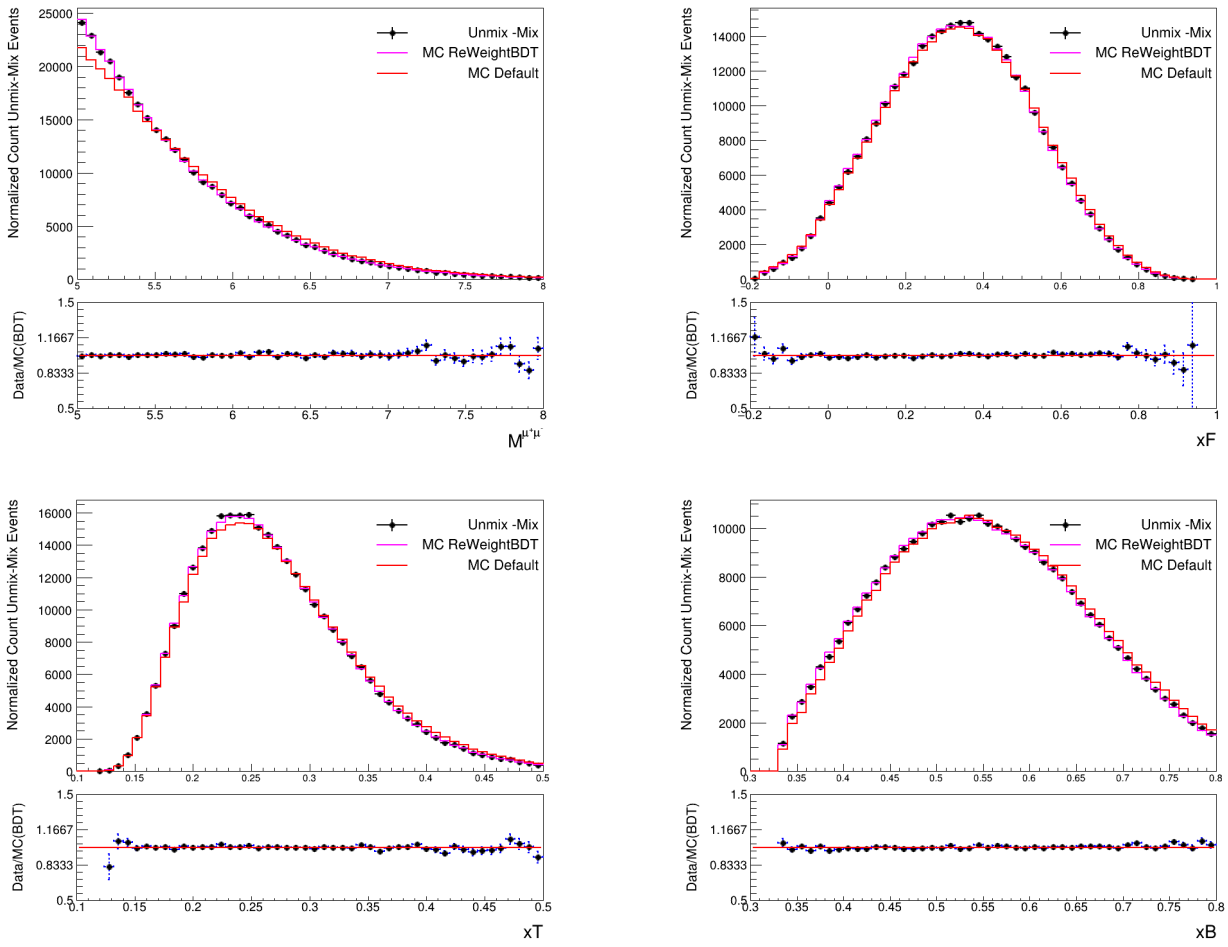

Figure 63: Illustration of the reweighting of dimuon mass, Feynman-x (x_F), Bjorken target (x_T) and Bjorken beam (x_B) variables. The MC default (red) and the reweighted MC (magenta) distributions are scaled to match the total counts of the signal (black) events. The signal events are obtained after subtracting the combinatorial events from all the data, which is represented by "Unmix-Mix" events.

reweighting in that leaf is needed.

3. The weight is computed in each leaf as:

$$w \times e^{\text{pred}}; \quad \text{where leaf\_pred} = \log \frac{w_{\text{leaf, MC}}}{w_{\text{leaf, RD}}}$$

For each event, "pred" is equal to the prediction of the leaf containing that event. In the BDT GB reweighter, each tree in the sequence attempts to address the discrepancies not resolved in previous iterations.

3.6.1 Event Reweighting in SeaQuest dump MC

We have discussed the optimal event selection in Section 3.3. The data events are compared with the MC distributions after event selections and after accounting for background subtraction [70]. Reweighted distributions for dimuon mass, Feynman-x (x_F), Bjorken target (x_T), and Bjorken beam (x_B) variables are shown in Figure 63. Before calculating the ratio, the MC events are scaled to match the events (Data = Unmix - Mix), where "Unmix - Mix" represents the signal events.

The following hyperparameters are used in the training of the Gradient Boosted Reweigter:

- n_estimators: 40
- learning_rate: 0.2
- min_samples_leaf: 200

3.6.2 Preserving the Statistical Uncertainty after Reweighting

After completing the reweighting process, we examined the unfolded distributions using both the reweighted events and the default weights, shown in Figure 64. By comparing the central

values and uncertainties of the unfolded parameter distributions, we conclude that we have preserved the statistical uncertainty without distorting the detector acceptance.

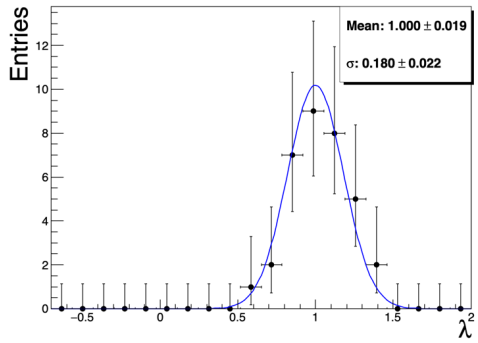

(a) Unfolded λ.

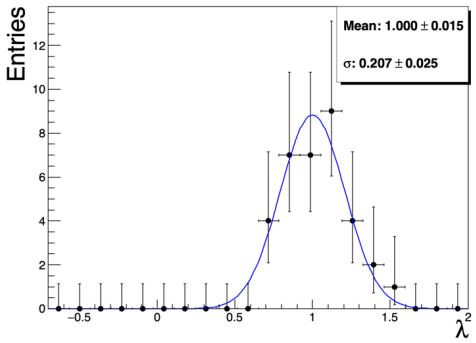

(b) Unfolded λ with reweight.

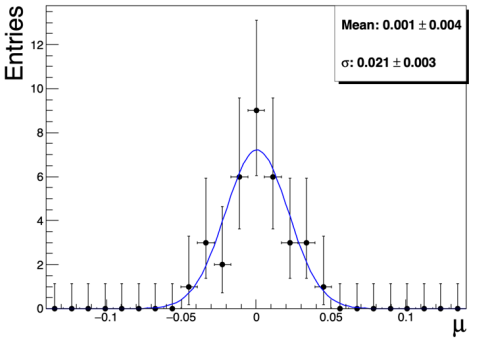

(c) Unfolded μ.

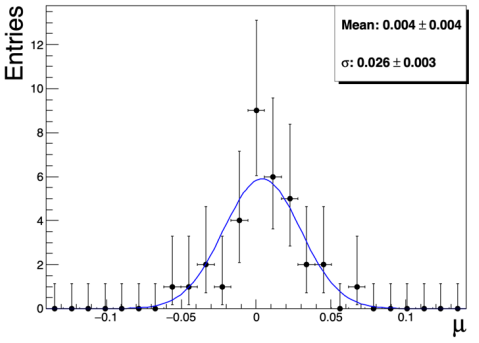

(d) Unfolded μ with reweight.

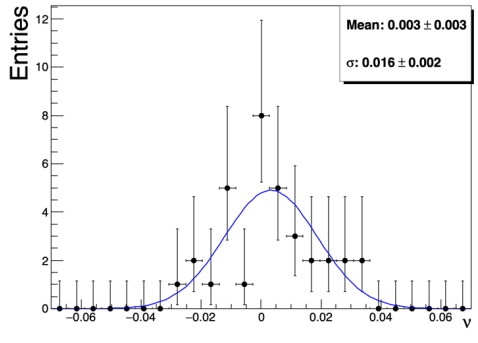

(e) Unfolded ν.

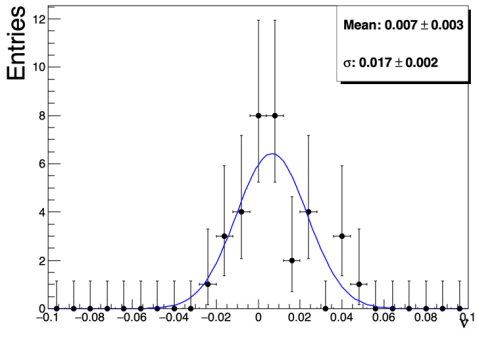

(f) Unfolded ν with reweight.

Figure 64: (λ, μ, ν) were extracted in the P_T range of (0.0, 2.0) GeV/c from independent test MC datasets. The injected values of (λ, μ, ν) into the MC test dataset were (1.0, 0.0, 0.0). The total data size in each MC test dataset was 50k events. The left column shows the unfolded (λ, μ, ν) extractions in the $\cos\theta$ range (-0.325, 0.325) with no additional weight, while the right column shows the same extraction with reweighted events.

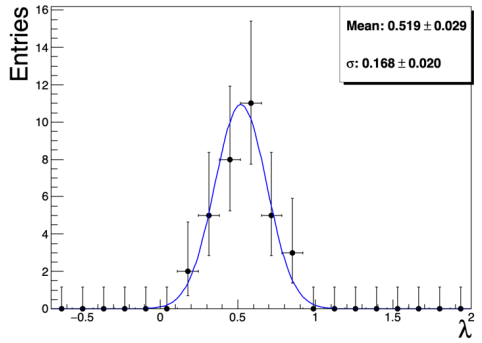

(a) Unfolded λ.

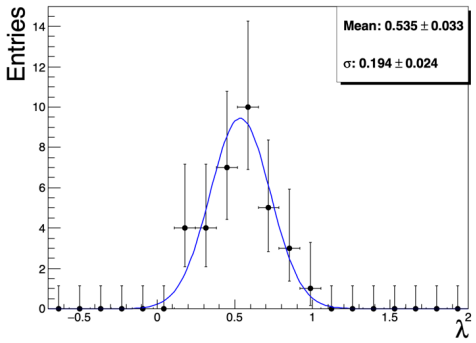

(b) Unfolded λ with reweight.

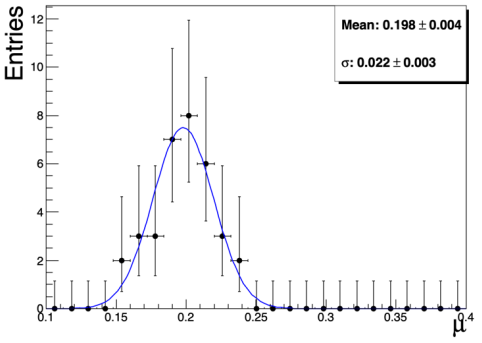

(c) Unfolded μ.

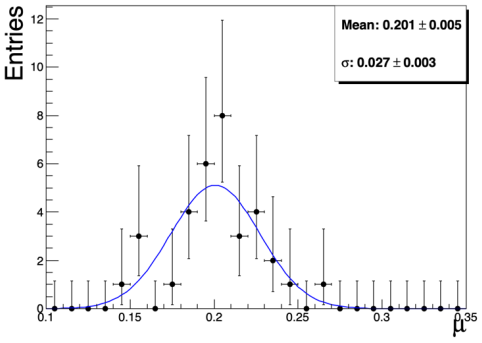

(d) Unfolded μ with reweight.

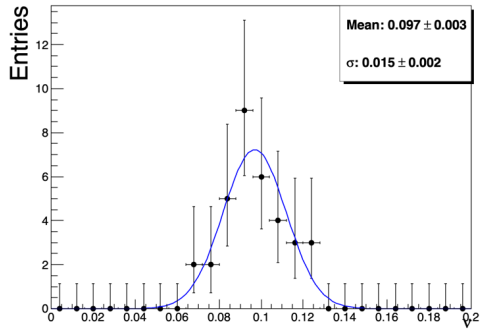

(e) Unfolded ν.

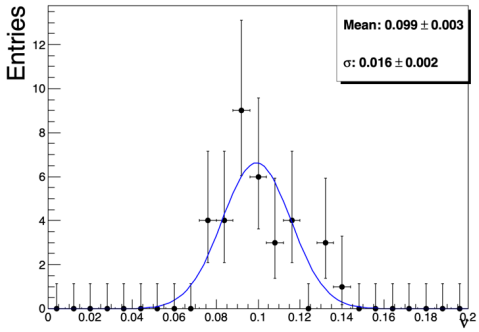

(f) Unfolded ν with reweight.

Figure 65: (λ, μ, ν) were extracted in the P_T range of (0.0, 2.0) GeV/c from independent test MC datasets. The injected values of (λ, μ, ν) into the MC test dataset were (0.5, 0.2, 0.1). The total data size in each MC test dataset was 50k events. The left column shows the unfolded (λ, μ, ν) extractions in the $\cos\theta$ range (-0.325, 0.325) with no additional weight, while the right column shows the same extraction with reweighted events.

3.7 Systematic Uncertainties

In addition to the statistical uncertainties, that arise from the fit results to the unfolded distributions, it's also important to estimate all possible systematic uncertainties or biases in the results. In this section, we will list all the systematic studies that we estimate using the simulated data.

3.7.1 Monte Carlo Closure Test

Closure tests will validate the Unfolding software by assessing its ability to account for acceptance and handle bin migration effectively. This will involve injecting various combinations of angular distribution parameters into independent Monte Carlo (MC) test data and examining whether the Bayesian Iterative Unfolding method, using the response matrix constructed from the true and reconstructed distributions, can accurately recover the true distribution parameters within the statistical uncertainties. If we take many independent test datasets, the mean value of the extracted distribution should match the injected parameter. Any difference will cause systematic bias. We will be extracting the values of λ, μ, and ν in different kinematic ranges.

Here are the findings from the Unfolded distributions shown in the Figures 66, 67, 68:

- In each of the test histograms, independent events are used to construct the histograms, where different sets of (λ, μ, ν) are used in different kinematics, and the validity of the unfolding method depends on its ability to recover the injected parameters from the test histograms.

- The kinematic ranges are used based on the ranges we have chosen to publish our final

results, and therefore each of the kinematic bins needs to be understood well if the Unfolding method could retrieve the angular distribution parameters. The event size in the test histograms is used the same as the total number of signal events we use in the final extraction steps. Once we unfold the histograms, we use the fit equation (23) to obtain the angular distribution parameters.

- Any difference between the injected parameters in the test histograms and the mean parameter value of the unfolded test histograms will be assigned as the systematic bias for the particular kinematic bin due to the unfolding method; let's denote this as σ_{unfold}. For example, in Figure 66, in the kinematic variable $P_T \in (0.1, 0.5)$ [1], we have injected a set of $(\lambda, \mu, \nu) = (0.862, 0.0511, 0.0256)$, and the mean value of the unfolded distributions in the left plot shows the quality of the unfolding process. We can observe a small difference between the injected (λ, μ, ν) values and the unfolded values, and these differences are shown in blue in the left plots, which are $(\sigma^{\lambda}_{unfold}, \sigma^{\mu}_{unfold}, \sigma^{\nu}_{unfold}) = (0.019, 0.00, 0.021)$. Similarly, we can observe the unfolding bias in the figures: 66, 67, 68, 69, 71, 73, 75.

3.7.2 Acceptance Effect

In SeaQuest, we have a narrow acceptance range for $\cos\theta$. The reconstructed range can be seen in figure 43. Due to this limitation, we have chosen a narrow window for $\cos\theta$. This ensures that the unfolding extraction process is more reliable, as we have a higher statistical precision within that window. Nevertheless, we need to assess the sensitivity of extracting the λ, μ, and ν parameters in different $\cos\theta_{CS}$ ranges. We have selected two ranges: one

[1] The low dimuon transverse momentum P_T between 0.0 and 0.1 GeV/c is excluded from the reconstructed events due to poor reconstruction around $P_T \approx 0$ GeV/c.

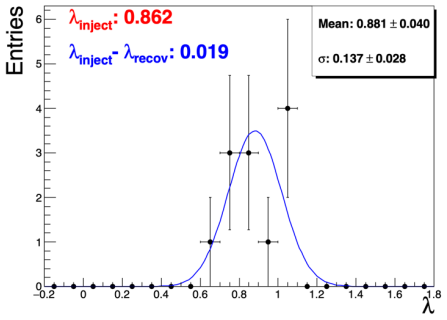

(a) Unfolded λ.

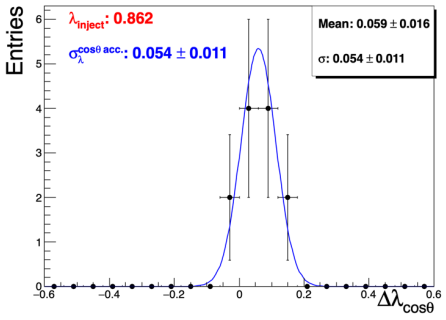

(b) Unfolded $\Delta\lambda_{cos\theta}$.

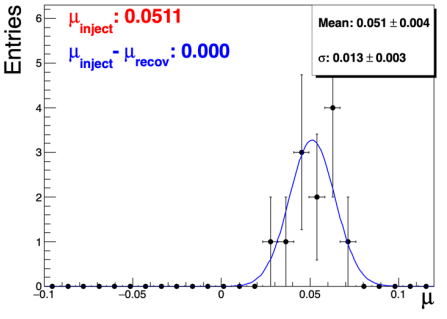

(c) Unfolded μ.

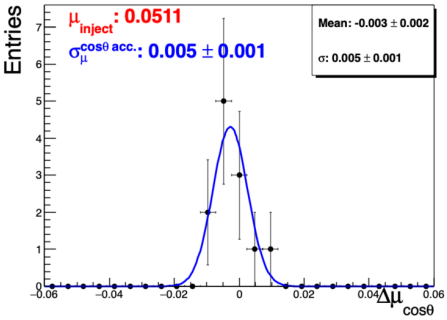

(d) Unfolded $\Delta\mu_{cos\theta}$.

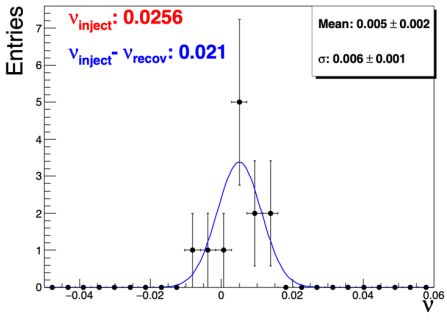

(e) Unfolded ν.

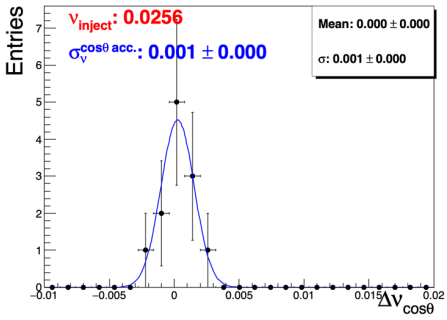

(f) Unfolded $\Delta\nu_{cos\theta}$.

Figure 66: The y-axis shows the total number of independent test unfolded histograms in the p_T range of (0.1, 0.5) GeV/c. The injected (λ, μ, ν) into the MC test dataset were (0.862, 0.0511, 0.0256). The total event size in each MC test unfolded histogram is about $80k$ for each histogram, and listed in the table 15. The left column shows the unfolded (λ, μ, ν) extractions in the $\cos\theta_{CS}$ range (-0.325, 0.325), and the right column shows the difference of the unfolded parameters between the two $\cos\theta_{CS}$ ranges (-0.325, 0.325) and (-0.275, 0.275).

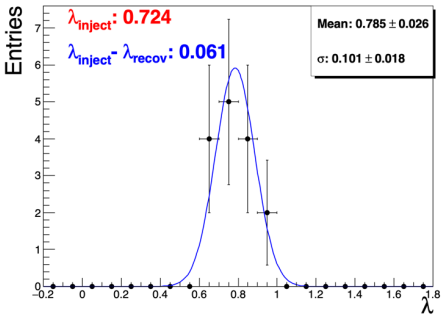

(a) Unfolded λ.

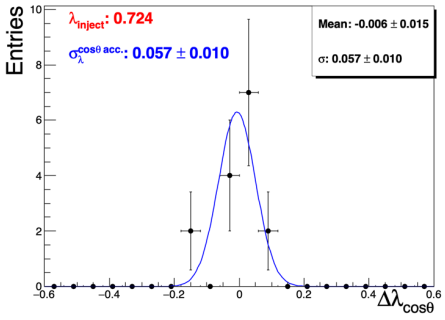

(b) Unfolded $\Delta\lambda_{cos\theta}$.

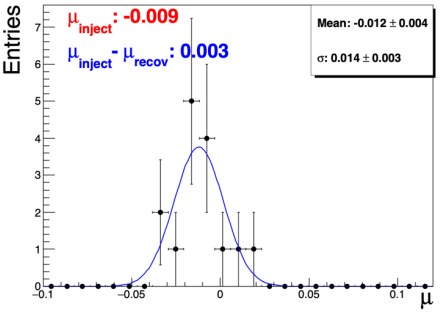

(c) Unfolded μ.

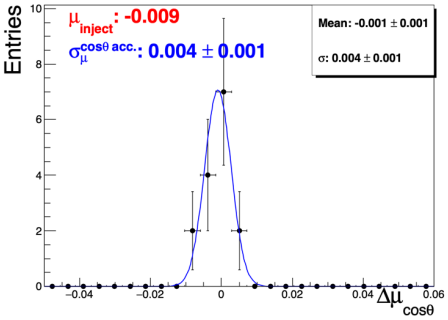

(d) Unfolded $\Delta\mu_{cos\theta}$.

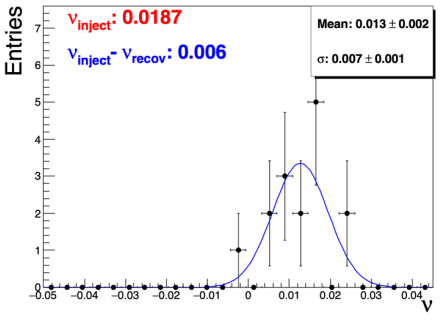

(e) Unfolded ν.

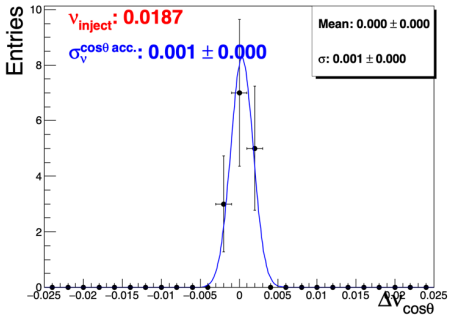

(f) Unfolded $\Delta\nu_{cos\theta}$.

Figure 67: The y-axis shows the total number of independent test unfolded histograms in the p_T range of (0.5, 1.0) GeV/c. The injected (λ, μ, ν) into the MC test dataset were (0.724, -0.009, 0.0187). The total event size in each MC test unfolded histogram is about $130k$ for each histogram, and listed in the table 15. The left column shows the unfolded (λ, μ, ν) extractions in the $\cos\theta_{CS}$ range (-0.325, 0.325), and the right column shows the difference of the unfolded parameters between the two $\cos\theta_{CS}$ ranges (-0.325, 0.325) and (-0.275, 0.275).

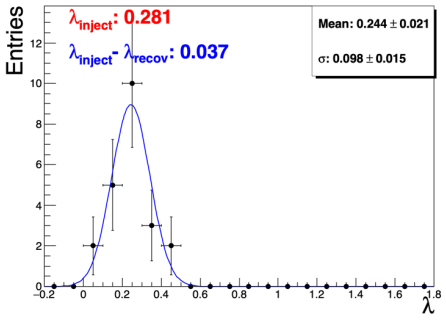

(a) Unfolded λ.

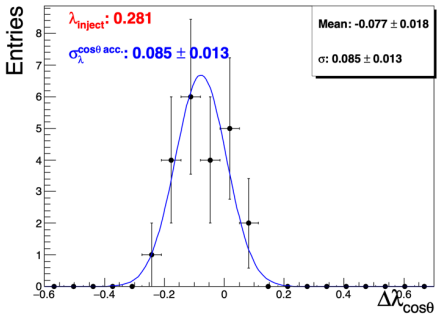

(b) Unfolded $\Delta\lambda_{cos\theta}$.

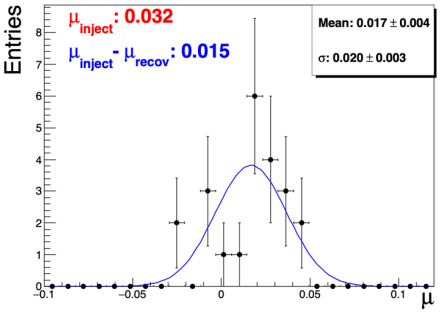

(c) Unfolded μ.

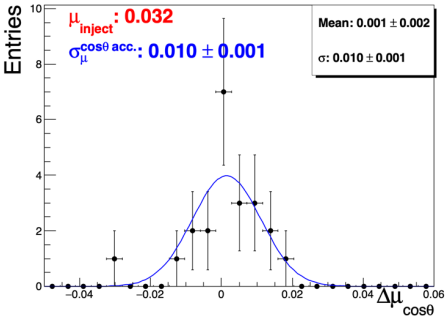

(d) Unfolded $\Delta\mu_{cos\theta}$.

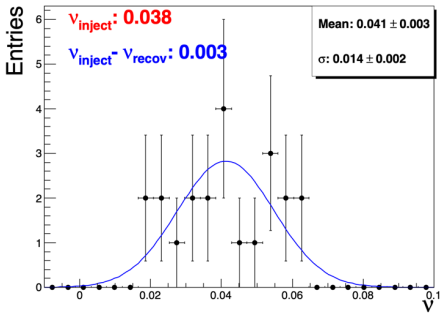

(e) Unfolded ν.

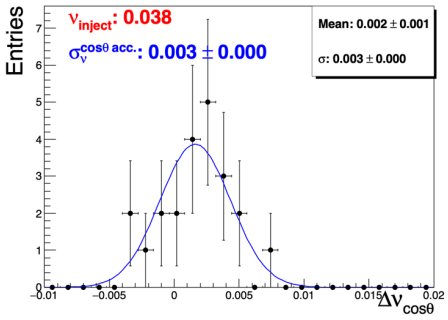

(f) Unfolded $\Delta\nu_{cos\theta}$.

Figure 68: The y-axis shows the total number of independent test unfolded histograms in the p_T range of (1.0, 2.0) GeV/c. The injected (λ, μ, ν) into the MC test dataset were (0.281, 0.032, 0.038). The total event size in each MC test unfolded histogram is about $70k$ for each histogram, and listed in the table 15. The left column shows the unfolded (λ, μ, ν) extractions in the $\cos\theta_{CS}$ range (-0.325, 0.325), and the right column shows the difference of the unfolded parameters between the two $\cos\theta_{CS}$ ranges (-0.325, 0.325) and (-0.275, 0.275).

is (-0.275, 0.275), and the other is (-0.325, 0.325). The standard deviation of the difference between the parameter values in the two $\cos\theta_{CS}$ ranges will contribute to another source of systematic uncertainty, let's call this σ_{acc}. The right column of Figures 66, 67, 68 show the sensitivity of the (λ, μ, ν) parameter extractions in two different $\cos\theta_{CS}$ ranges.

3.7.3 Kinematic Dependence of ν

Like the sections [3.7.1,3.7.2], we are going to study the systematic effects in extracting the ν parameters in the kinematic variables: mass, x_F, x_T, and x_B. We particularly examine this systematic effect because we focus on the extraction of the ν variable, which provides insights into the Boer-Mulder function and QCD contributions. We will look for systematic biases coming from the Bayesian Iterative Unfolding method, as well as the systematic uncertainty coming from the $\cos\theta$ acceptance. In Figures [69, 71, 73, 75], we show the systematic bias, which is defined by the difference between the injected ν parameter and the unfolded distributions' mean in the corresponding kinematic variable. Any nonzero value will represent the bias in each of the corresponding kinematic bins. On the other hand, Figures [70, 72, 74, 76] show the systematic uncertainty calculated by the standard deviation of the distribution, where the variable in the distributions are defined as the difference of the unfolded ν in the two different $\cos\theta_{CS}$ ranges (-0.325, 0.325) and (-0.275, 0.275) respectively.

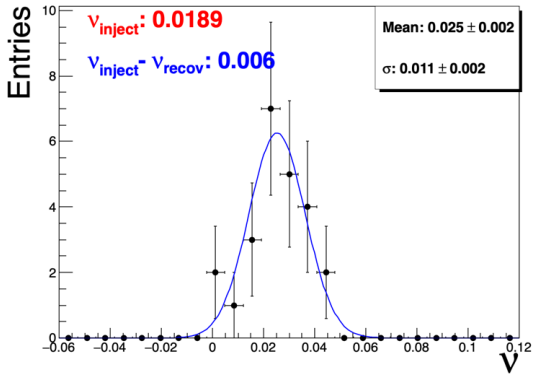

(a) mass is in $(5.0, 5.5) GeV/c^2$ with 90k events per histogram.

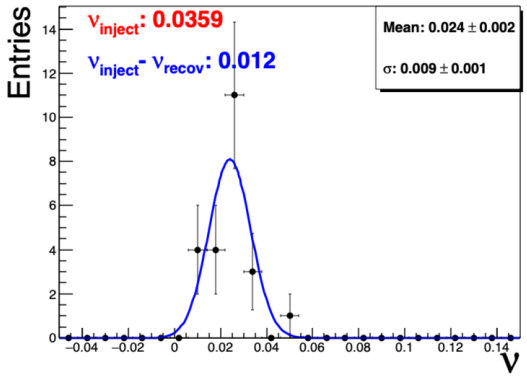

(b) mass is in $(5.5, 5.5) GeV/c^2$ with 50k events per histogram.

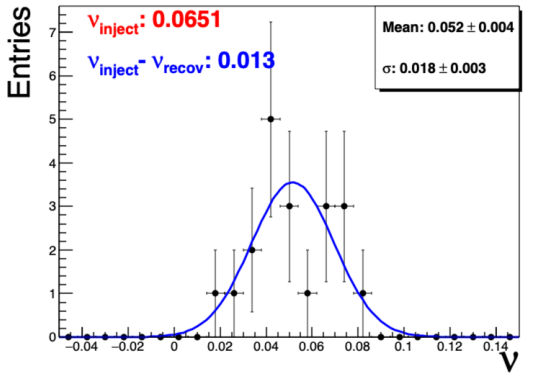

(c) mass is in $(6.0, 6.5) GeV/c^2$ with 30k events per histogram.

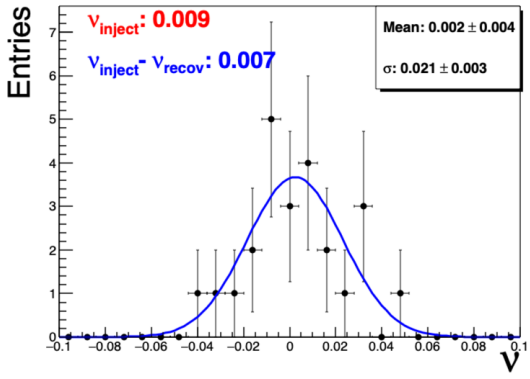

(d) mass is in $(6.5, 8.0) GeV/c^2$ with 20k events per histogram.

Figure 69: In each figure, ν values were extracted in the p_T range of (0.0, 2.0) GeV/c from independent test MC datasets using Bayesian Iterative Unfolding with 2 unfolding regularization iterations. The difference between the injected ν parameter and the mean of the unfolded distribution is used as the systematic bias coming from the unfolding method.

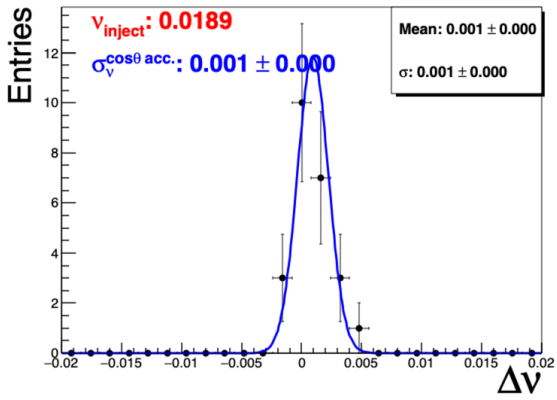

(a) mass is in $(5.0, 5.5) GeV/c^2$ with 45k events per histogram.

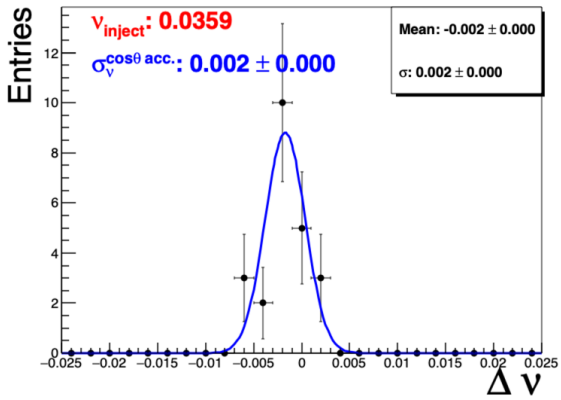

(b) mass is in $(5.5, 6.0) GeV/c^2$ with 45k events per histogram.

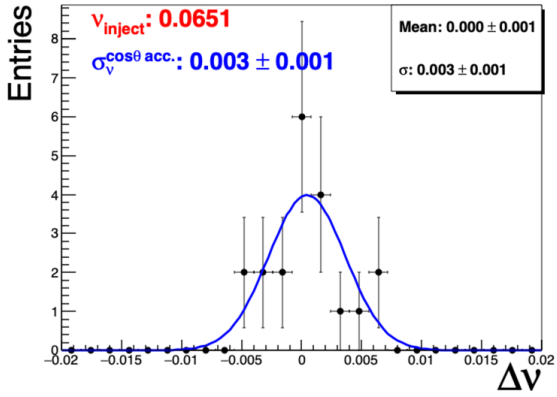

(c) mass is in $(6.0, 6.5) GeV/c^2$ with 45k events per histogram.

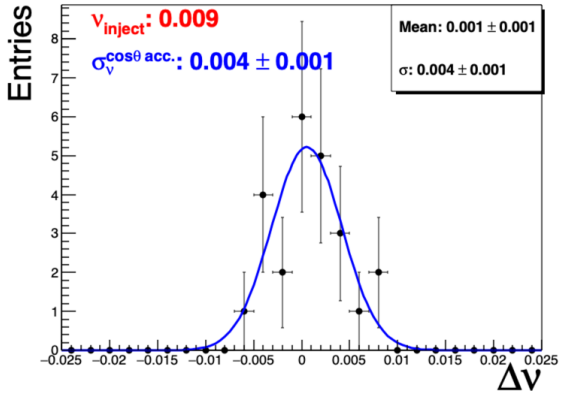

(d) mass is in $(6.5, 8.0) GeV/c^2$ with 45k events per histogram.

Figure 70: In each figure, ν values were extracted in the p_T range of (0.0, 2.0) GeV/c from independent test MC datasets using Bayesian Iterative Unfolding with 2 unfolding regularization iterations. Each plot shows the difference between the extracted ν parameters using two $\cos\theta$ fit ranges, namely (-0.325, 0.325) and (-0.275, 0.275).

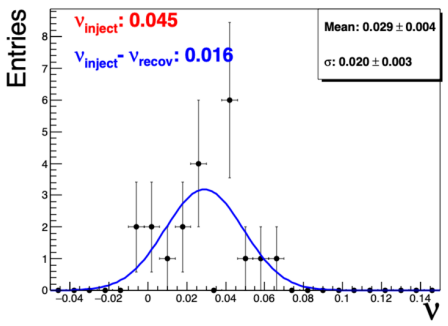

(a) $x_F \in (-0.18, 0.1)$, 30k events/hist.

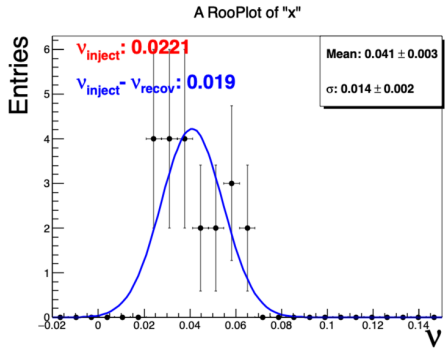

(b) $x_F \in (0.1, 0.25)$, 50k events/hist.

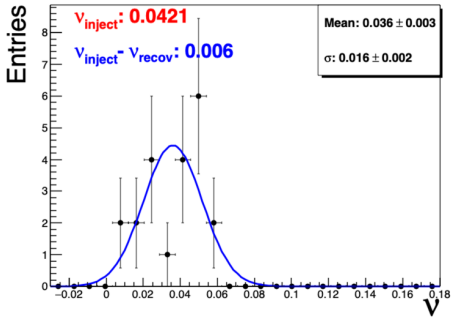

(c) $x_F \in (0.25, 0.35)$, 45k events/hist.

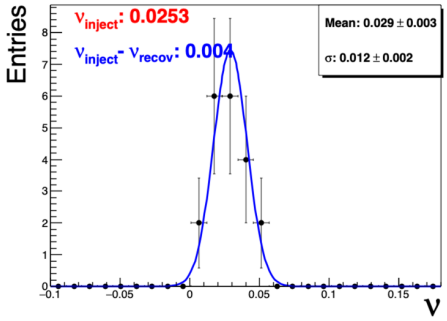

(d) $x_F \in (0.35, 0.45)$, 50k events/hist.

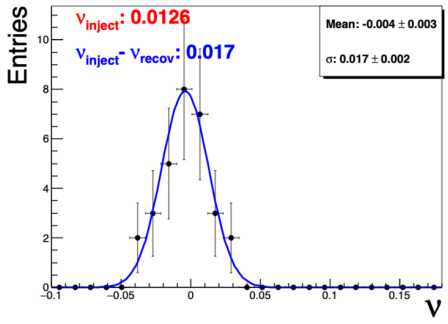

(e) $x_F \in (0.45, 0.9)$, 50k events/hist.

Figure 71: In each figure, ν values were extracted in the p_T range of (0.0, 2.0) GeV/c from independent test MC datasets using Bayesian Iterative Unfolding with 2 unfolding regularization iterations. The difference between the injected ν parameter and the mean of the unfolded distribution is used as the systematic bias coming from the unfolding method.

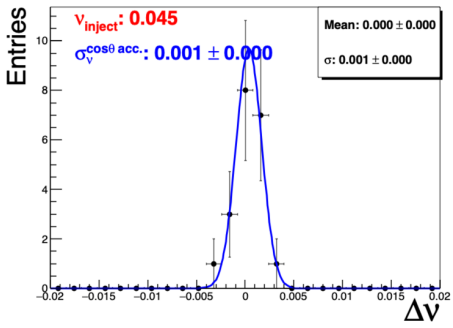

(a) $x_F \in (-0.18, 0.1)$, 30k events/hist.

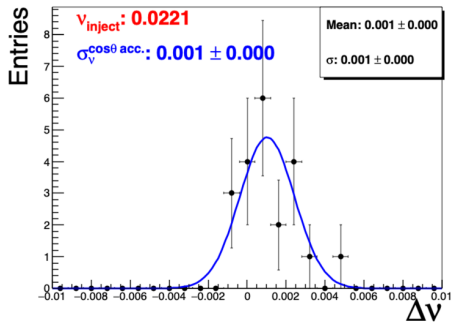

(b) $x_F \in (0.1, 0.25)$, 50k events/hist.

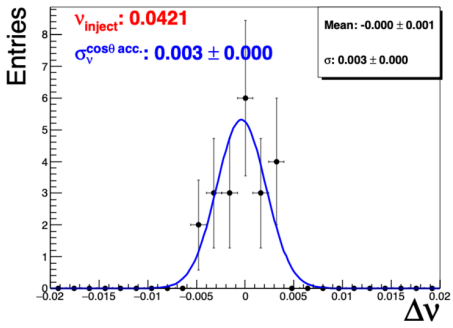

(c) $x_F \in (0.25, 0.35)$, 45k events/hist.

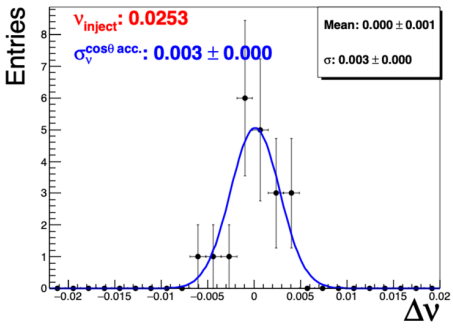

(d) $x_F \in (0.35, 0.45)$, 50k events/hist.

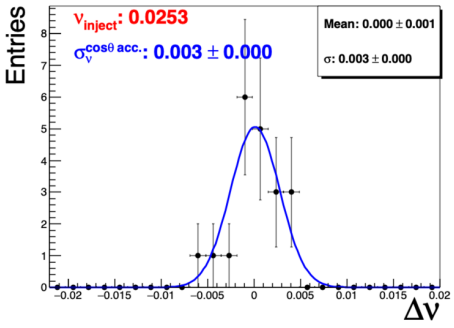

(e) $x_F \in (0.45, 0.9)$, 50k events/hist.

Figure 72: In each figure, ν values were extracted in the p_T range of (0.0, 2.0) GeV/c from independent test MC datasets using Bayesian Iterative Unfolding with 2 unfolding regularization iterations. Each plot shows the difference between the extracted ν parameters using two $\cos\theta$ fit ranges, namely (-0.325, 0.325) and (-0.275, 0.275).

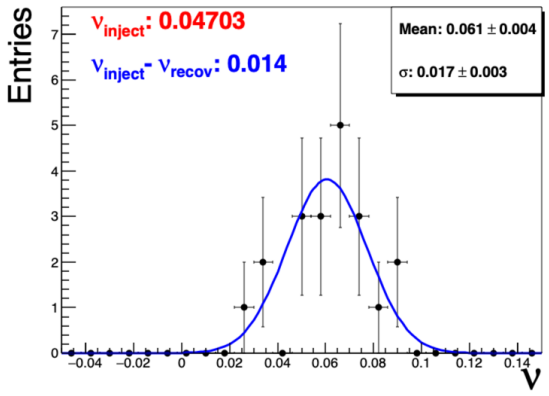

(a) x_B is in (0.3, 0.45) with 45k events per histogram.

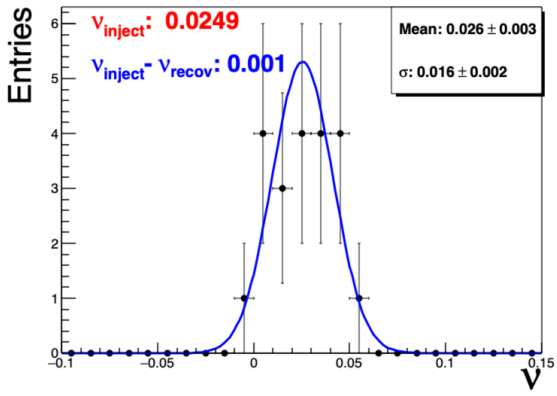

(b) x_B is in (0.45, 0.55) with 75k events per histogram.

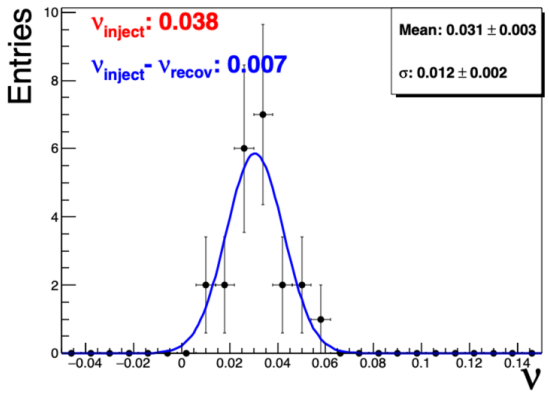

(c) x_B is in (0.55, 0.65) with 65k events per histogram.

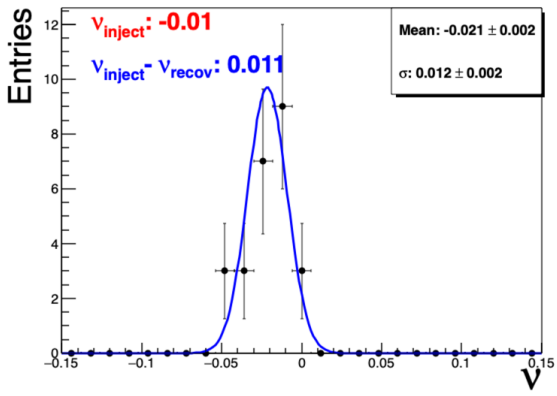

(d) x_B is in (0.65, 1.0) with 45k events per histogram.

Figure 73: In each figure, ν values were extracted in the p_T range of (0.0, 2.0) GeV/c from independent test MC datasets using Bayesian Iterative Unfolding with 2 unfolding regularization iterations. The difference between the injected ν parameter and the mean of the unfolded distribution is used as the systematic bias coming from the unfolding method.

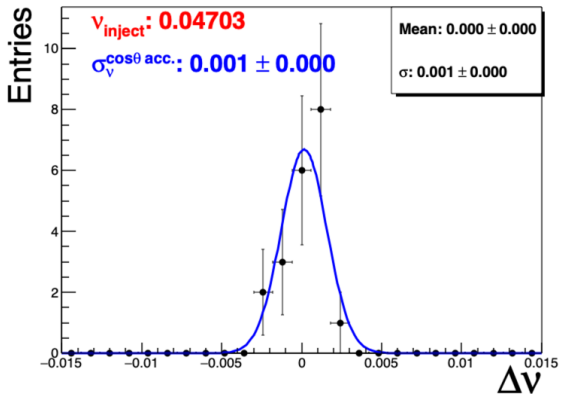

(a) x_B is in (0.3, 0.45) with 45k events per histogram.

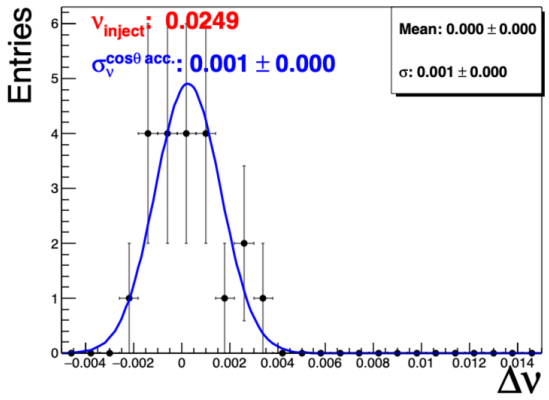

(b) x_B is in (0.45, 0.55) with 75k events per histogram.

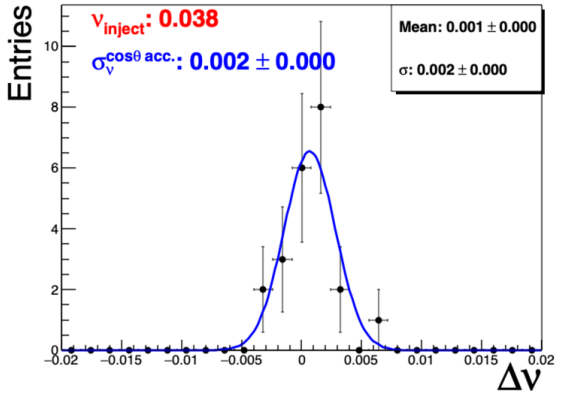

(c) x_B is in (0.55, 0.65) with 65k events per histogram.

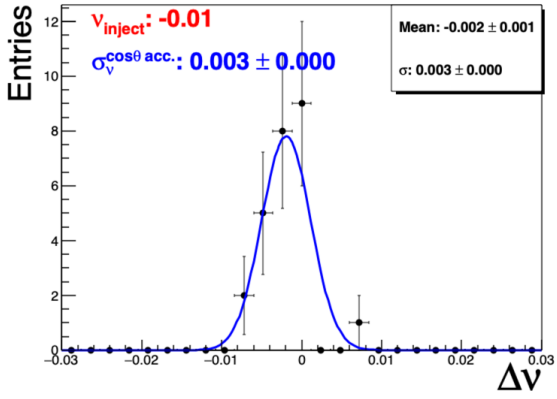

(d) x_B is in (0.65, 1.0) with 45k events per histogram.

Figure 74: In each figure, ν values were extracted in the p_T range of (0.0, 2.0) GeV/c from independent test MC datasets using Bayesian Iterative Unfolding with 2 unfolding regularization iterations. Each plot shows the difference between the extracted ν parameters using two $\cos\theta$ fit ranges, namely (-0.325, 0.325) and (-0.275, 0.275).

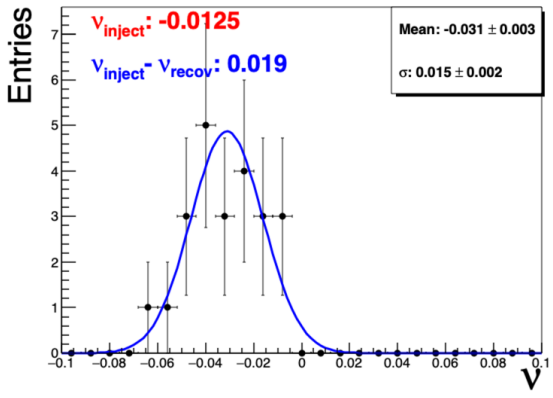

(a) x_T is in (0.1, 0.2) with 45k events per histogram.

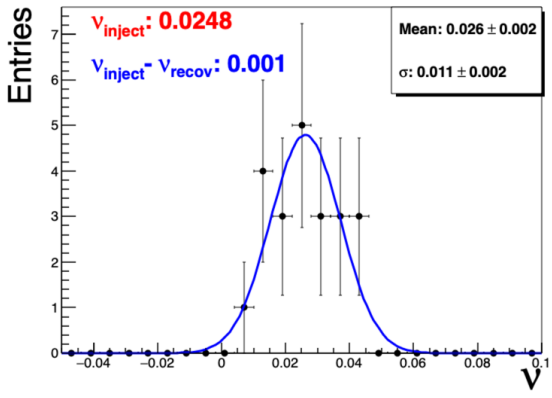

(b) x_T is in (0.2, 0.25) with 45k events per histogram.

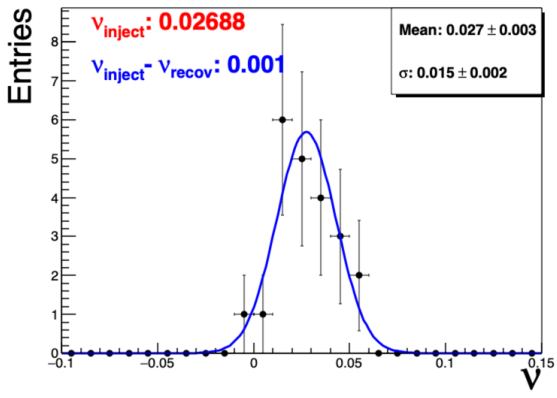

(c) x_T is in (0.25, 0.30) with 45k events per histogram.

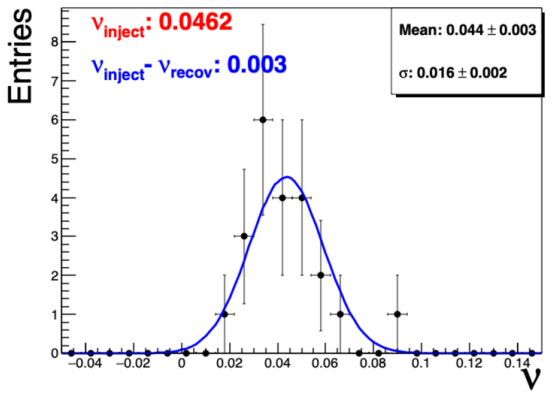

(d) x_T is in (0.3, 0.60) with 45k events per histogram.

Figure 75: In each figure, ν values were extracted in the p_T range of (0.0, 2.0) GeV/c from independent test MC datasets using Bayesian Iterative Unfolding with 2 unfolding regularization iterations. The difference between the injected ν parameter and the mean of the unfolded distribution is used as the systematic bias coming from the unfolding method.

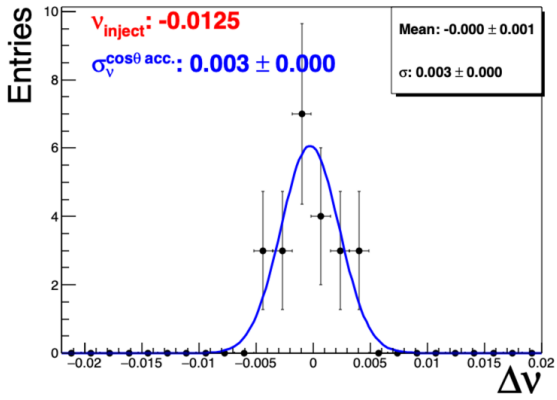

(a) x_T is in (0.1, 0.2) with 45k events per histogram.

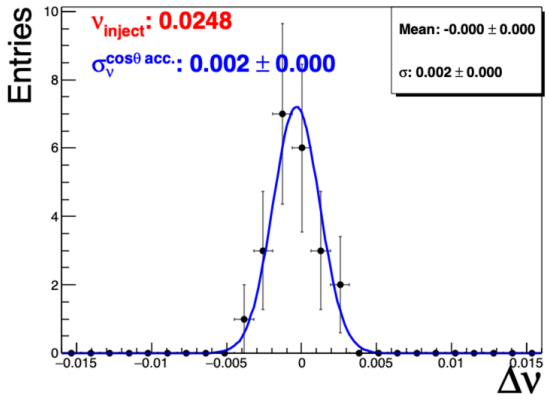

(b) x_T is in (0.2, 0.25) with 45k events per histogram.

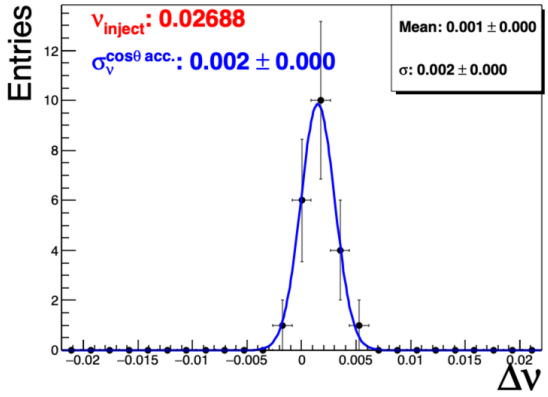

(c) x_T is in (0.25, 0.30) with 45k events per histogram.

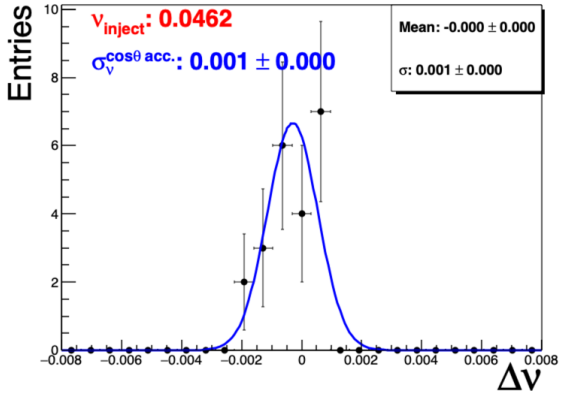

(d) x_T is in (0.3, 0.60) with 45k events per histogram.

Figure 76: In each figure, ν values were extracted in the p_T range of (0.0, 2.0) GeV/c from independent test MC datasets using Bayesian Iterative Unfolding with 2 unfolding regularization iterations. Each plot shows the difference between the extracted ν parameters using two $\cos\theta$ fit ranges, namely (-0.325, 0.325) and (-0.275, 0.275).

3.7.4 Secondary Beam Effect

In SeaQuest terminology, primary particles are created by the generators and subsequently fed into the Geant4 simulation as input information. By default, the Geant4 only simulates dimuons in the spectrometer, with the assumption that the primary beam proton hits the target along the laboratory z-direction. The z-vertex of each dimuon is selected at random with a probability, $P(z) \propto \exp(-z/L_{Fe})$. In this study, we will focus on hadronic interactions and examine the state of the beam protons after these interactions. We will also investigate whether significant secondary hadrons are observed from proton and Fe target interactions. Additionally, we will estimate the transverse momentum of these secondary hadrons.

3.7.4.1 Yield Estimation of Secondary Beam P_T Hadrons This hadronic study has been conducted independently, and it means that we have not simulated the dimuons resulting from the secondary hadrons through Geant4 simulations. However, a similar geometry has been used, which was used in the real data analysis, so we can use the findings of the study to examine the systematic effects for dimuon angular distributions. The z-position vertex condition for the beam dump analysis is that dimuons are selected within the range of $0 < z < 100$ cm in simulated data (GMC). To replicate the setup used in the simulated events for the beam dump analysis, we incorporate these settings into the Geant4 standalone simulations.

Geant4 Simulation Configuration	
Geant4 Version	10.01.03
Reference module	Official example, "Hadr01"
Physics list	QBBC, FTFP_BERT, and QGSP_BERT (The elastic & quasielastic scatterings are enabled)
Target	
Material	Fe
Radius	20 cm
Length	80 cm $\sim$ 5 interaction lengths
NumberDivZ	80
Magnetic Field	No
Beam	
Particle	proton
Energy	120 GeV
beamOn	10000

A more comprehensive study has been done in the following document [68]. The summaries, using different Geant4 physics lists, of the findings from Figures 77, 78, and 79 are as follows:

- QBBC: The mean P_T is 0.3 GeV/c within $P_z^{beam}(110, 120)$ GeV/c. The total yield of the secondary beam protons is 10% of the total incident beam.
- FTFP_BERT: The mean P_T is 0.31 GeV/c within $P_z^{beam}(110, 120)$ GeV/c. The total yield of the secondary beam protons is 11% of the total incident beam.
- QGSP_BERT: The mean P_T is 0.5 GeV/c within $P_z^{beam}(110, 120)$ GeV/c. The total yield of the secondary beam protons is 7.5% of the total incident beam.

Other secondary hadrons, such as pions and neutrons, are insignificant and therefore do not need to be included in the contribution to the angular distribution analysis. In the next section, we will smear the dimuon P_T to estimate the effect of hadronic interactions on the unfolded distributions, based on the estimated secondary beam P_T.

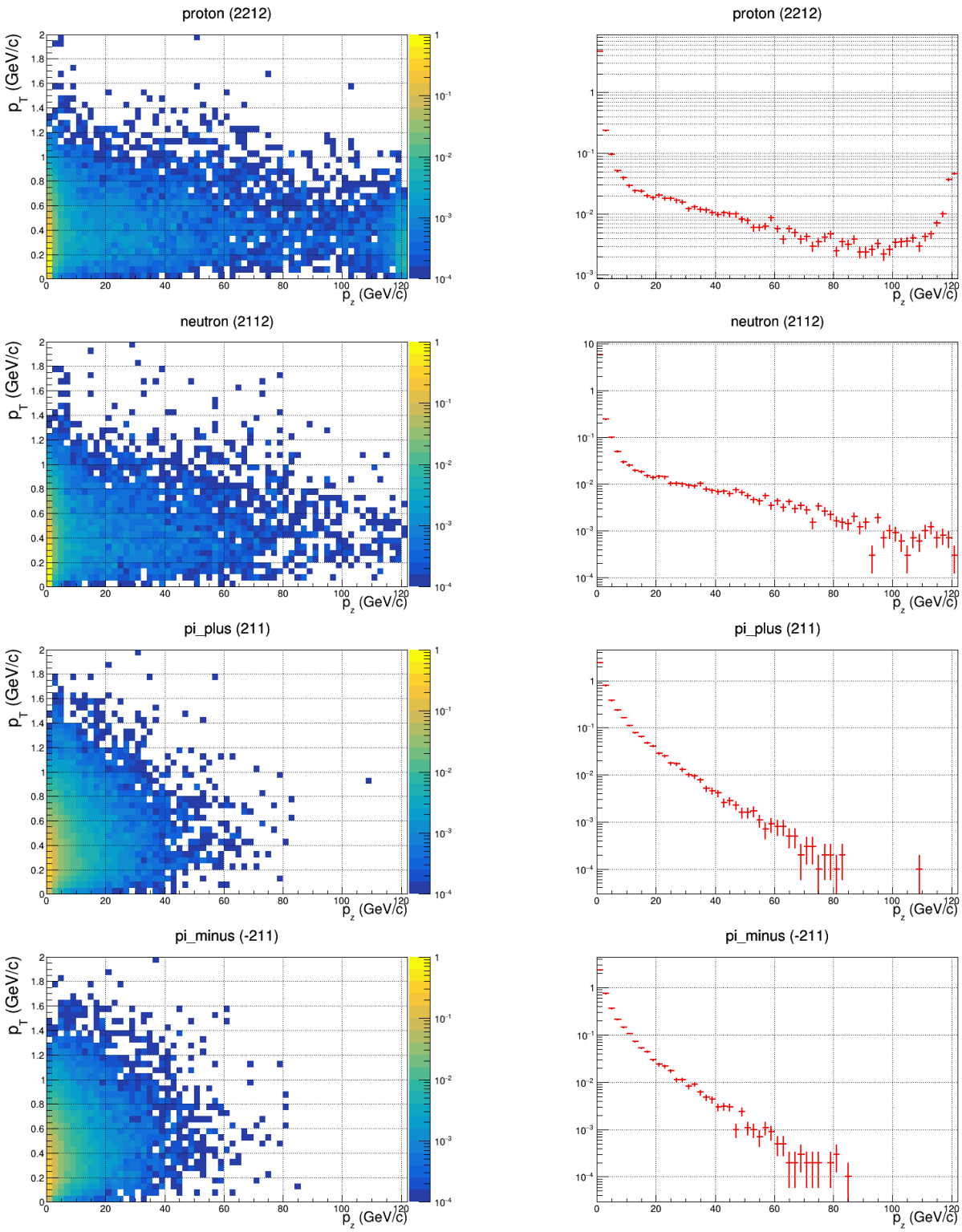

Figure 77: The left plots show the P_T vs. P_z distributions of direct secondary protons, neutrons, π^+, and π^-. The right plots represent the corresponding 1D projections, displaying the P_z distributions. The total count of the P_z distributions is scaled by 1/10,000. The Geant4 physics list used was QBBC.

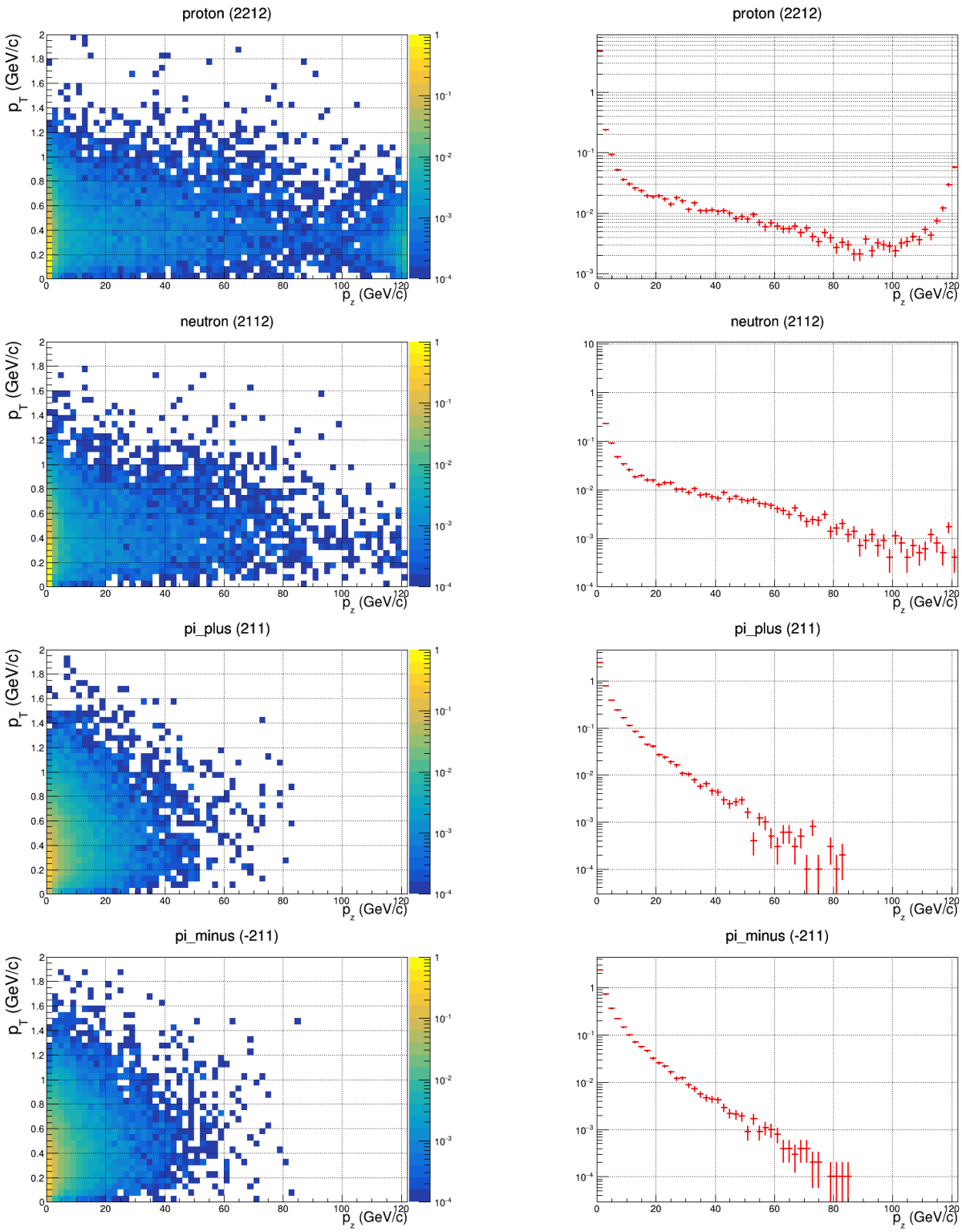

Figure 78: The left plots show the P_T vs. P_z distributions of direct secondary protons, neutrons, π^+, and π^-. The right plots represent the corresponding 1D projections, displaying the P_z distributions. The total count of the P_z distributions is scaled by 1/10,000. The Geant4 physics list used was FTFP_BERT.

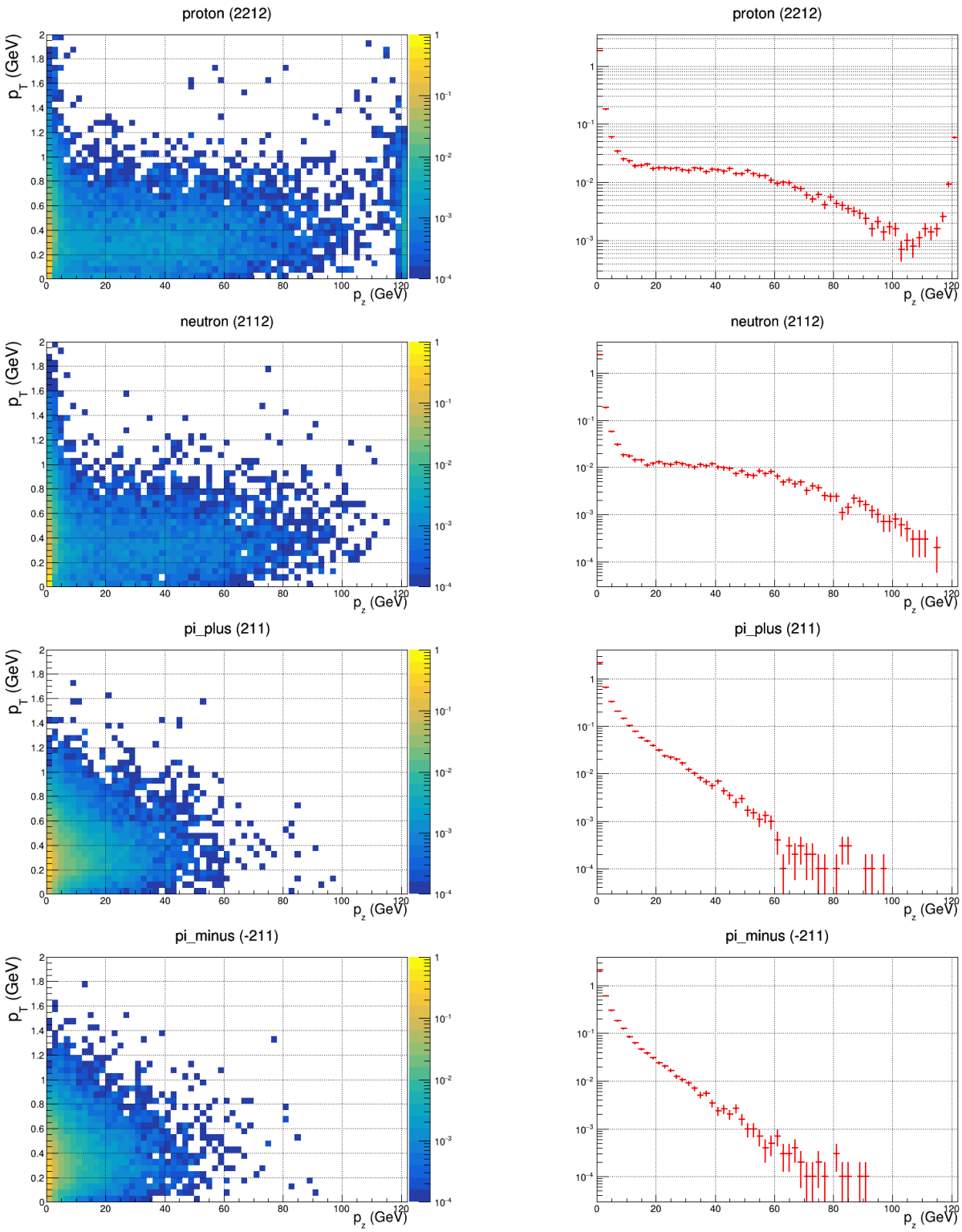

Figure 79: The left plots show the P_T vs. P_z distributions of direct secondary protons, neutrons, π^+, and π^-. The right plots represent the corresponding 1D projections, displaying the P_z distributions. The total count of the P_z distributions is scaled by 1/10,000. The Geant4 physics list used was QGSP_BERT.

3.7.4.2 (λ, μ, ν) extractions To estimate the effect from the nonzero transverse momentum of the secondary beam hadron, we would like to smear the dimuon momentum accordingly. Here are the considerations:

- The smeared transverse momentum of the dimuon $\vec{p}_{T_{\text{smeared}}} = x_B \times p_T^{\text{beam}} \Big(\cos\phi^{beam}\hat{x} + \sin\phi^{beam}\hat{y} \Big)$.
- the x_B is the beam Bjorken variable.
- p_T^{beam} follows a uniform distribution from (0.0, 0.5) or (0.0, 1.0) based on the Geant4 physics list, and ϕ^{beam} follows a uniform distribution from $(-\pi, \pi)$.
- The $\vec{p}_{T_{\text{smeared}}}$ is calculated for the test MC data only where we randomly picked 10% of the reconstructed events.
- For the training response matrix, we did not apply any $\vec{p}_{T_{\text{smeared}}}$.
- For calculating the smeared ϕ and $cos\theta$ in the CS frame, we have added the smeared dimuon momenta to the reconstructed dimuon P_T to get the resultant new dimuon $\vec{P}_T$.

Figure 80 shows the 2D histograms of ϕ and $\cos\theta$ with and without the 10% beam P_T smearing effect. From Figure 81, we see that the effect is insignificant, as all $\phi - \cos\theta$ bin combinations are very close to 1.0. Nevertheless, we will estimate the quantitative number by using the smeared events in the reconstructed test histograms, where the trained simulated (GMC) events will not have this smearing effect. Any deviation can be assigned as a systematic uncertainty.

Now we want to inject a set of (λ, μ, ν) into the reconstructed test data with multiple independent test datasets. Figure 82 shows the smearing effect on the unfolded distributions

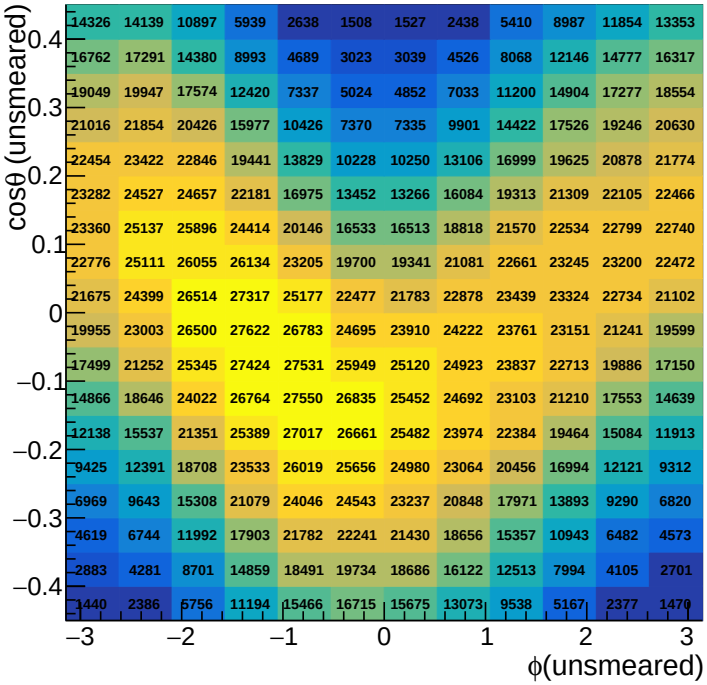

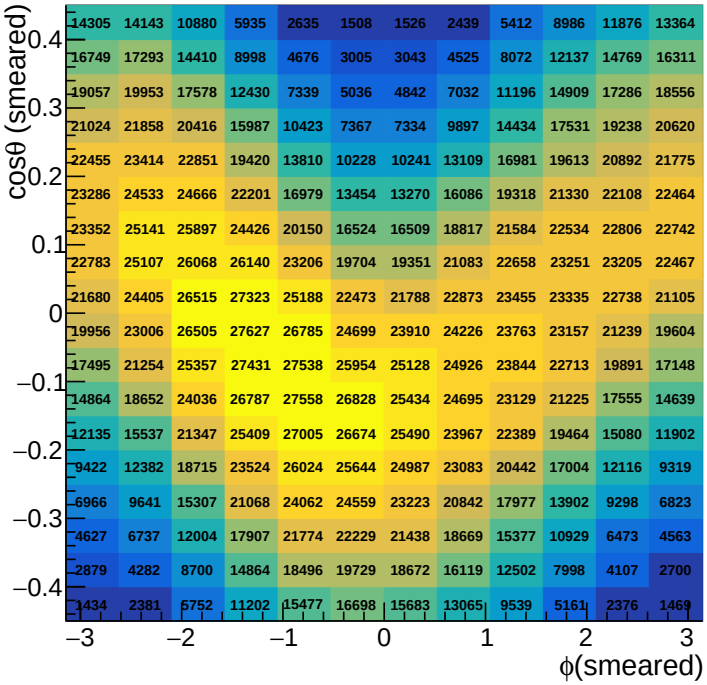

Figure 80: This shows the ratio between the 2D ϕ-$\cos\theta$ histograms for unsmeared and smeared ones.

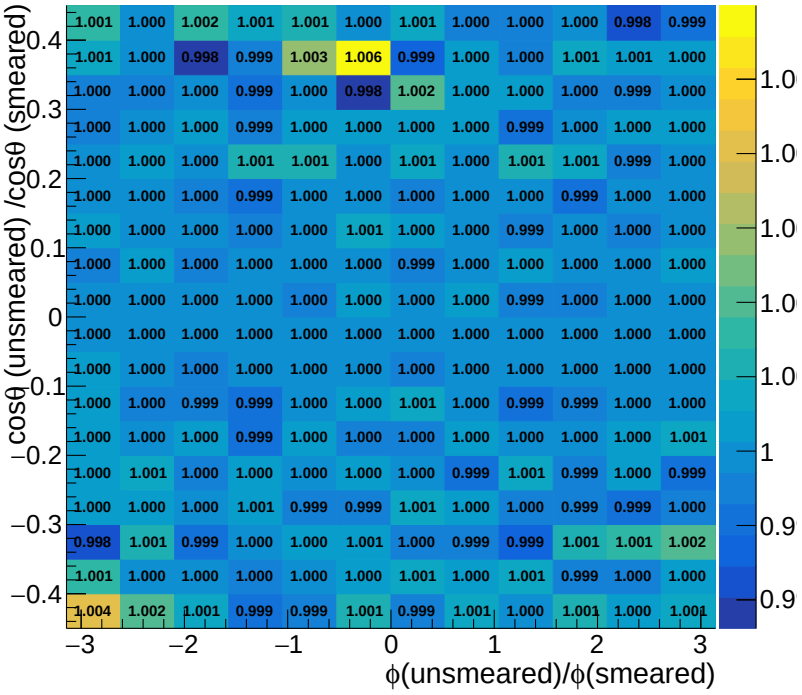

Figure 81: This shows the ratio between the 2D ϕ-$\cos\theta$ histograms for unsmeared and smeared ones.

when the beam P_T was taken in the range (0.0, 0.5) GeV/c, and in Figure 83, the beam P_T was taken in the range (0.0, 1.0) GeV/c. In both cases, the mean differences of the unfolded distributions with smearing and without smearing are very small, so we can ignore the effect of the secondary beam P_T as part of the systematic uncertainties.

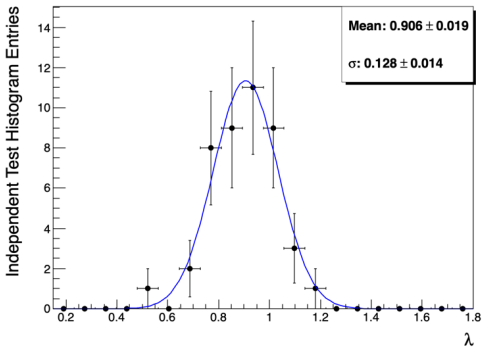

(a) Unfolded unsmeared λ.

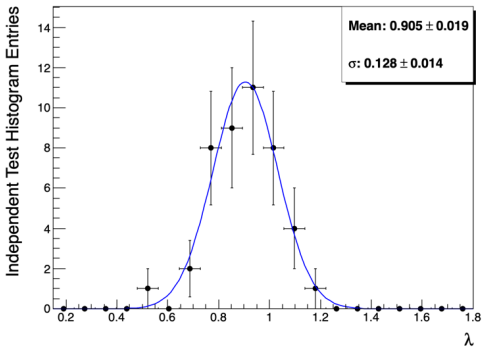

(b) Unfolded smeared λ.

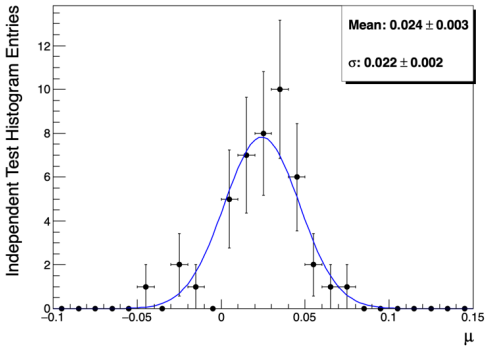

(c) Unfolded unsmeared μ.

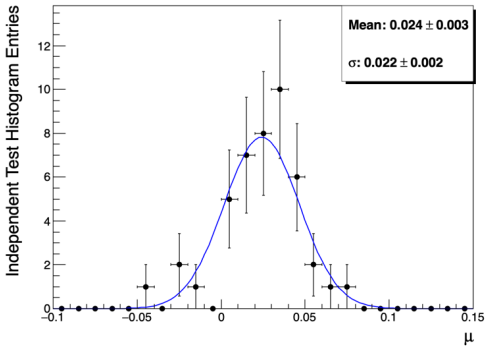

(d) Unfolded smeared μ.

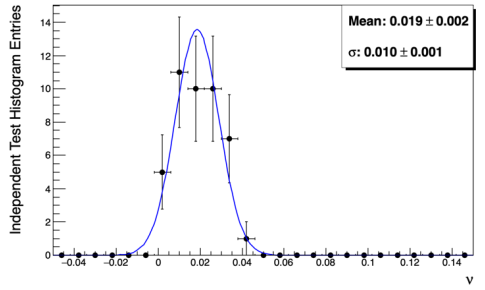

(e) Unfolded unsmeared ν.

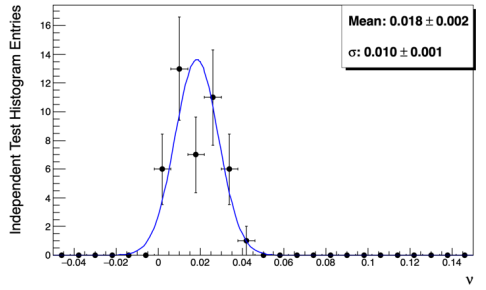

(f) Unfolded smeared ν.

Figure 82: (λ, μ, ν) were extracted in the P_T range of (0.0, 2.0) GeV/c from independent test MC datasets. The injected values of (λ, μ, ν) into the MC test dataset were (0.95, 0.03, 0.02). The total data size in each MC test dataset was 90k events. The left column shows the unfolded (λ, μ, ν) extractions in the $\cos\theta$ range (-0.325, 0.325) with no P_T^{beam} smearing, while the right column shows the same extraction with P_T^{beam} smeared events. The P_T^{beam} distributions were uniformly taken in the range (0.0, 0.5).

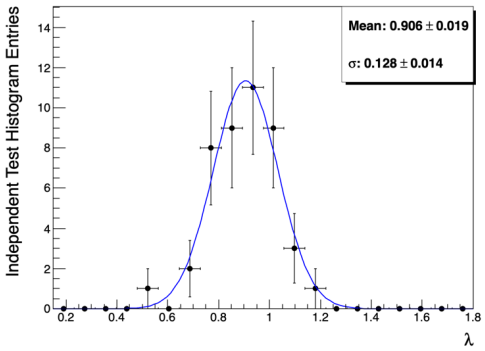

(a) Unfolded unsmeared λ.

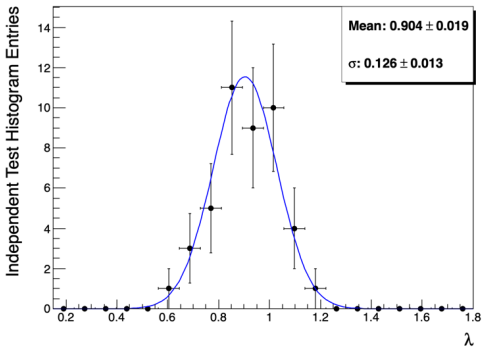

(b) Unfolded smeared λ.

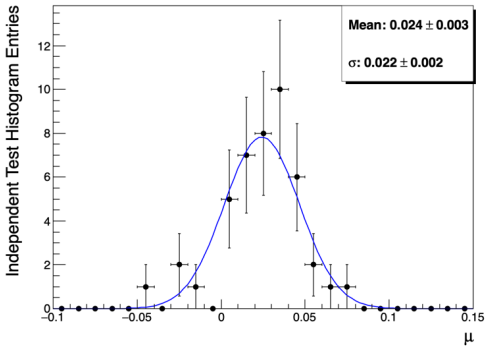

(c) Unfolded unsmeared μ.

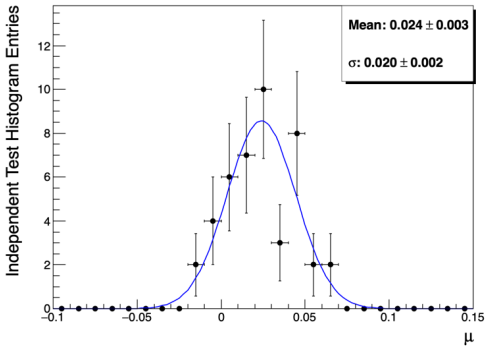

(d) Unfolded smeared μ.

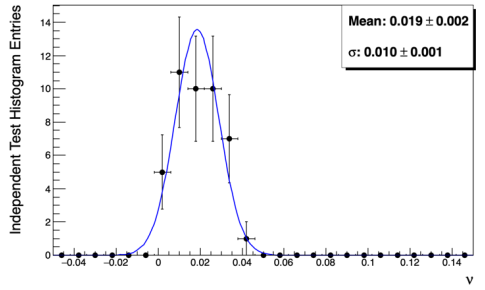

(e) Unfolded unsmeared ν.

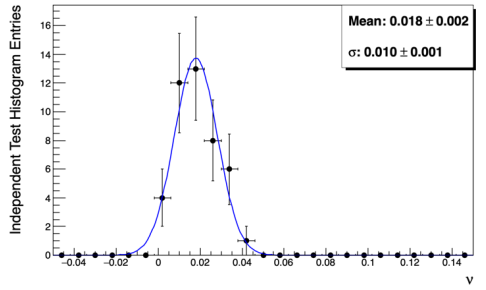

(f) Unfolded smeared ν.

Figure 83: (λ, μ, ν) were extracted in the P_T range of (0.0, 2.0) GeV/c from independent test MC datasets. The injected values of (λ, μ, ν) into the MC test dataset were (0.95, 0.03, 0.02). The total data size in each MC test dataset was 90k events. The left column shows the unfolded (λ, μ, ν) extractions in the $\cos\theta$ range (-0.325, 0.325) with no P_T^{beam} smearing, while the right column shows the same extraction with P_T^{beam} smeared events. The P_T^{beam} distributions were uniformly taken in the range (0.0, 1.0).

3.8 Combinatorial Background Subtraction

In real data, unlike Monte Carlo events, we encounter contributions from combinatorial backgrounds. To subtract this background, we have used the event mixing method [70]. Figures 84, 85, 86, and 87 show the 2D distributions for $p_T \in (0.1, 2.0)$ GeV/c, $p_T \in (0.1, 0.5)$ GeV/c, $p_T \in (0.5, 1.0)$ GeV/c, and $p_T \in (1.0, 2.0)$ GeV/c respectively, using SeaQuest roadset-67 data after applying the event selections described below:

- Track Level Selections for μ^+, details in Section 3.3.1.
- Track Level Selections for μ^-, details in Section 3.3.2.
- Dimuon Level Selections, details in Section 3.3.3.

Similarly, we have tabulated the SeaQuest roadset-67 data, combinatorial background events, and signal events in Table 15 for all the kinematic ranges used in the unfolding process. The category 'All events' in the table represents the roadset-67 data, which includes both signal and background. The number of signal events in the table is equal to the total number of 'All events' minus the combinatorial background (comb events) events. The signal events will be used to construct the 2D $\cos\theta - \phi$ histograms in various kinematic ranges for the unfolding process.

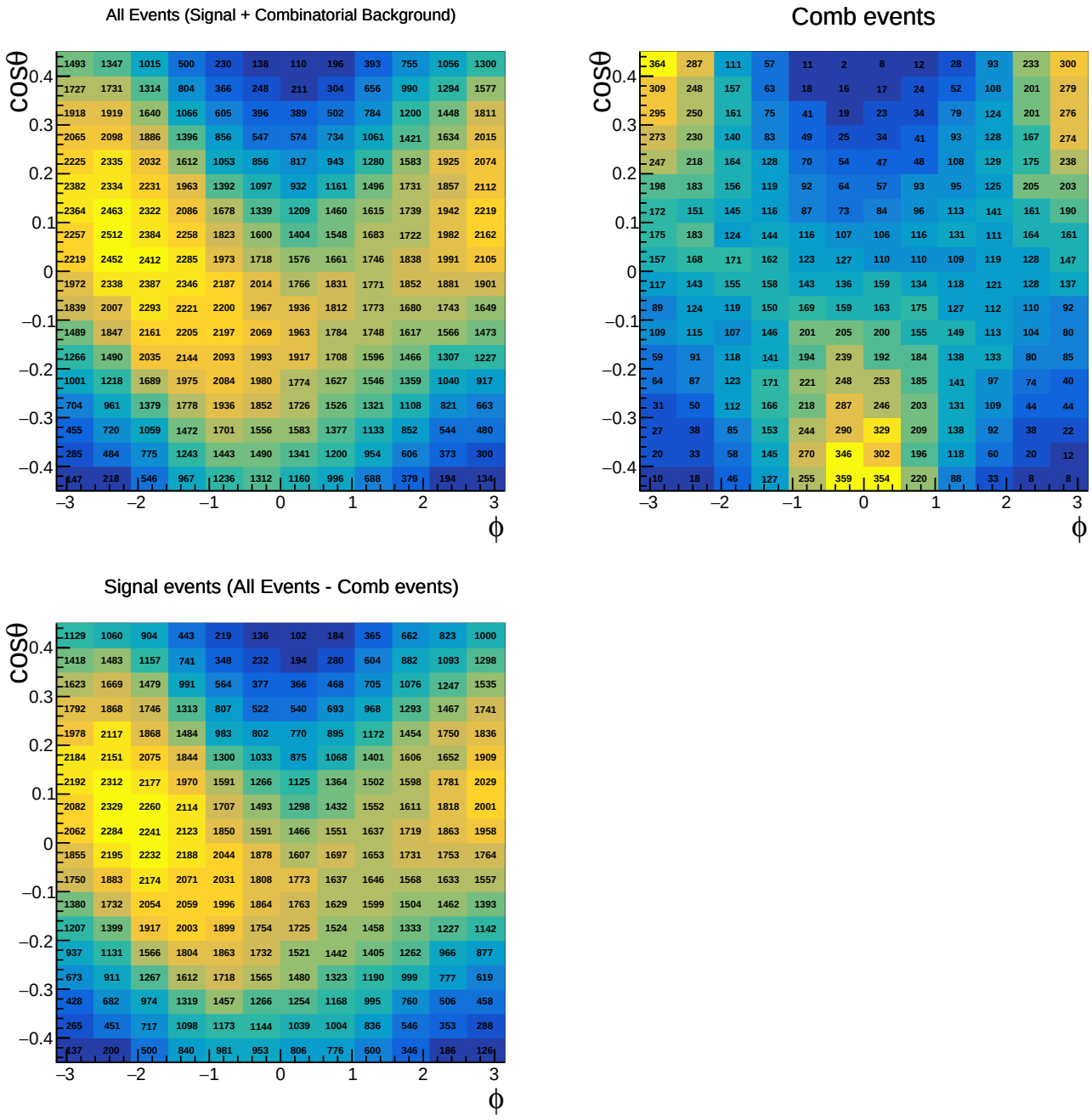

Figure 84: We show here the 2D histogram of $\cos\theta - \phi$ after applying the event conditions outlined in Section 3.3 for the p_T range of (0.1, 2.0) GeV/c.

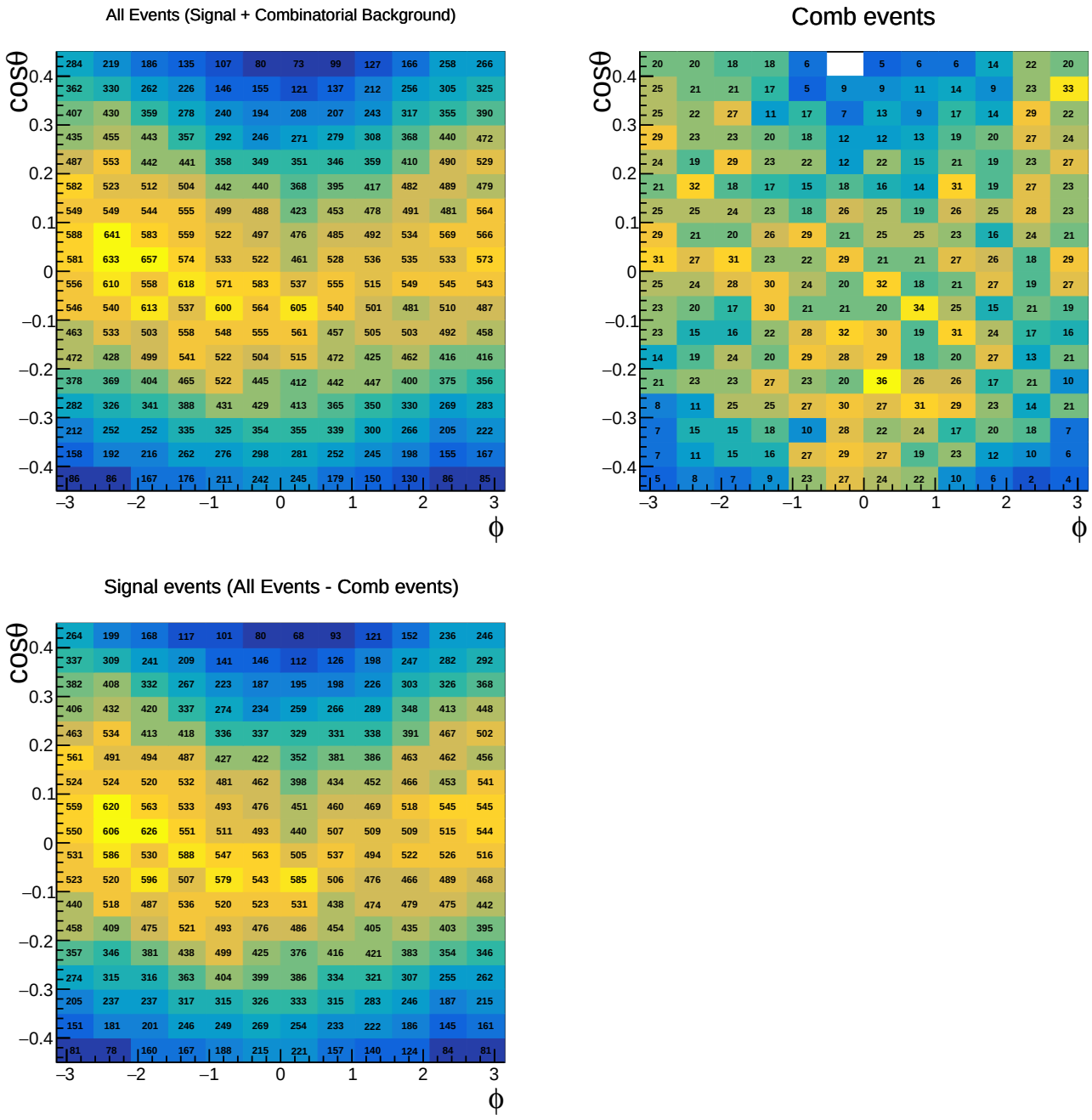

Figure 85: We show here the 2D histogram of $\cos\theta - \phi$ after applying the event conditions outlined in Section 3.3 for the p_T range of (0.1, 0.5) GeV/c.

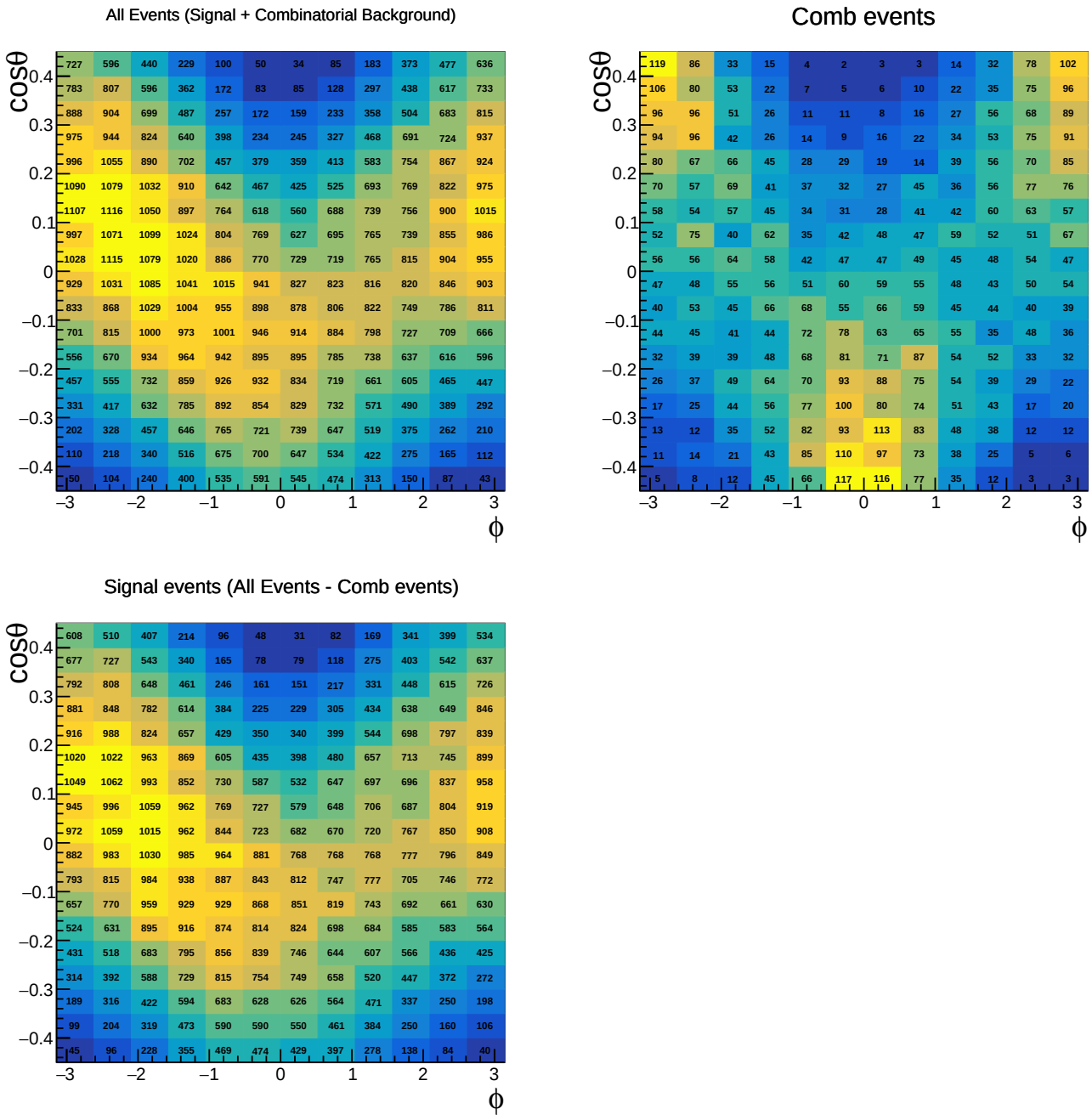

Figure 86: We show here the 2D histogram of $\cos\theta - \phi$ after applying the event conditions outlined in Section 3.3 for the p_T range of (0.5, 1.0) GeV/c.

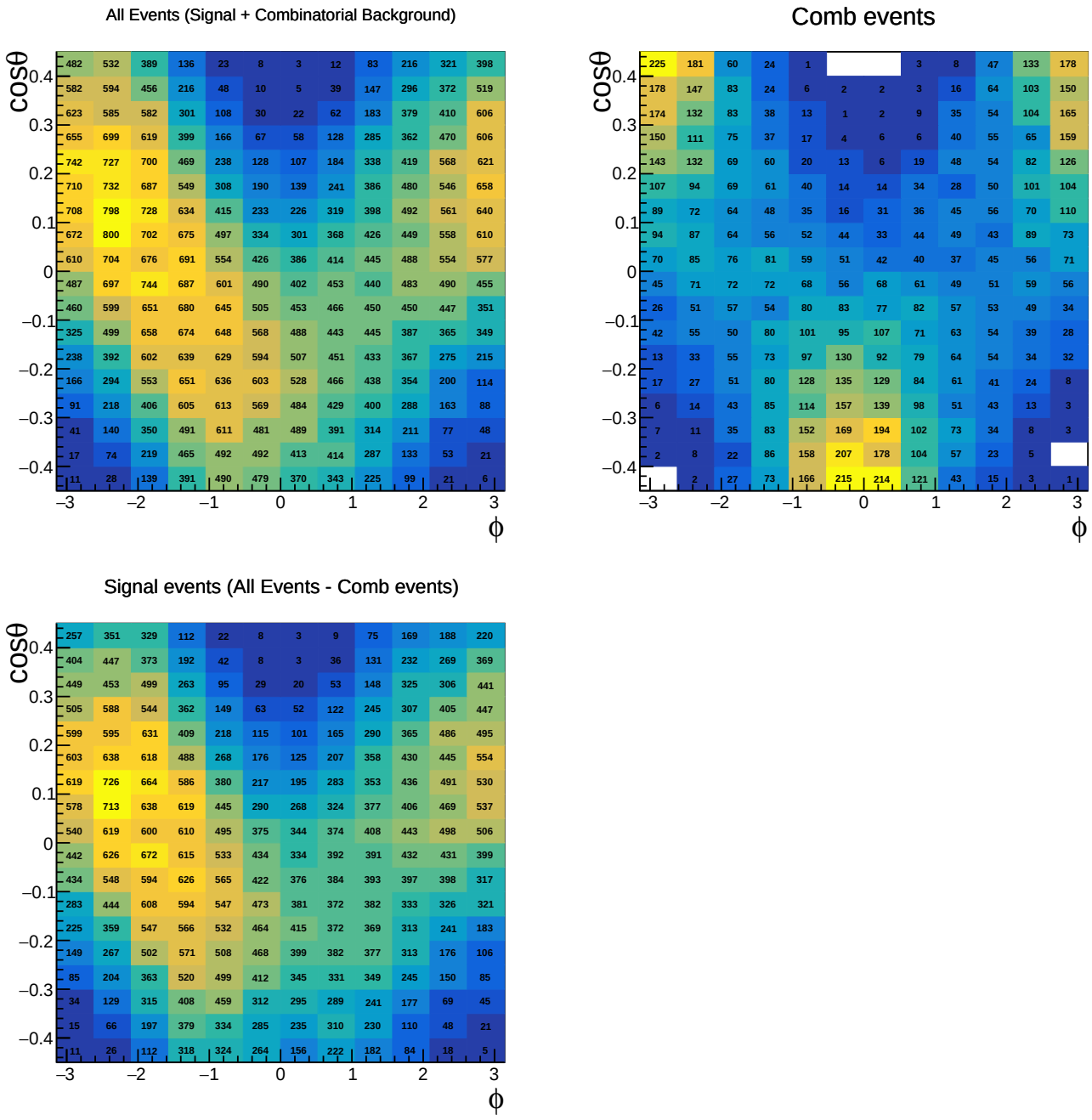

Figure 87: We show here the 2D histogram of $\cos\theta - \phi$ after applying the event conditions outlined in Section 3.3 for the p_T range of (1.0, 2.0) GeV/c.

p_T range	mass range	x_F range	x_B range	x_T range	All events	Comb events	Signal events
$P_T \in (0.1, 2.0)$	$M \in (5.0, 8.0)$	$x_F \in (-0.18, 0.94)$	$x_B \in (0.3, 1.0)$	$x_T \in (0.1, 0.6)$	314005	28819	285186
$P_T \in (0.1, 0.5)$	$M \in (5.0, 8.0)$	$x_F \in (-0.18, 0.94)$	$x_B \in (0.3, 1.0)$	$x_T \in (0.1, 0.6)$	85085	4374	80711
$P_T \in (0.5, 1.0)$	$M \in (5.0, 8.0)$	$x_F \in (-0.18, 0.94)$	$x_B \in (0.3, 1.0)$	$x_T \in (0.1, 0.6)$	142232	10547	131685
$P_T \in (1.0, 2.0)$	$M \in (5.0, 8.0)$	$x_F \in (-0.18, 0.94)$	$x_B \in (0.3, 1.0)$	$x_T \in (0.1, 0.6)$	86688	13898	72790
$P_T \in (0.1, 2.0)$	$M \in (5.0, 5.5)$	$x_F \in (-0.18, 0.94)$	$x_B \in (0.3, 1.0)$	$x_T \in (0.1, 0.6)$	167668	21346	146322
$P_T \in (0.1, 2.0)$	$M \in (5.5, 6.0)$	$x_F \in (-0.18, 0.94)$	$x_B \in (0.3, 1.0)$	$x_T \in (0.1, 0.6)$	84043	5792	78251
$P_T \in (0.1, 2.0)$	$M \in (6.0, 6.5)$	$x_F \in (-0.18, 0.94)$	$x_B \in (0.3, 1.0)$	$x_T \in (0.1, 0.6)$	38364	1311	37053
$P_T \in (0.1, 2.0)$	$M \in (6.5, 8.0)$	$x_F \in (-0.18, 0.94)$	$x_B \in (0.3, 1.0)$	$x_T \in (0.1, 0.6)$	23930	370	23560
$P_T \in (0.1, 2.0)$	$M \in (5.0, 8.0)$	$x_F \in (-0.18, 0.25)$	$x_B \in (0.3, 1.0)$	$x_T \in (0.1, 0.6)$	112694	11380	101314
$P_T \in (0.1, 2.0)$	$M \in (5.0, 8.0)$	$x_F \in (0.25, 0.35)$	$x_B \in (0.3, 1.0)$	$x_T \in (0.1, 0.6)$	60753	5870	54883
$P_T \in (0.1, 2.0)$	$M \in (5.0, 8.0)$	$x_F \in (0.35, 0.45)$	$x_B \in (0.3, 1.0)$	$x_T \in (0.1, 0.6)$	57176	4919	52257
$P_T \in (0.1, 2.0)$	$M \in (5.0, 8.0)$	$x_F \in (0.45, 0.55)$	$x_B \in (0.3, 1.0)$	$x_T \in (0.1, 0.6)$	43405	3379	40026
$P_T \in (0.1, 2.0)$	$M \in (5.0, 8.0)$	$x_F \in (0.55, 0.90)$	$x_B \in (0.3, 1.0)$	$x_T \in (0.1, 0.6)$	39905	3246	36659
$P_T \in (0.1, 2.0)$	$M \in (5.0, 8.0)$	$x_F \in (-0.18, 0.94)$	$x_B \in (0.3, 0.45)$	$x_T \in (0.1, 0.6)$	65294	7543	57751
$P_T \in (0.1, 2.0)$	$M \in (5.0, 8.0)$	$x_F \in (-0.18, 0.94)$	$x_B \in (0.45, 0.55)$	$x_T \in (0.1, 0.6)$	102232	10109	92123
$P_T \in (0.1, 2.0)$	$M \in (5.0, 8.0)$	$x_F \in (-0.18, 0.94)$	$x_B \in (0.55, 0.65)$	$x_T \in (0.1, 0.6)$	87243	6772	80471
$P_T \in (0.1, 2.0)$	$M \in (5.0, 8.0)$	$x_F \in (-0.18, 0.94)$	$x_B \in (0.65, 1.0)$	$x_T \in (0.1, 0.6)$	59236	4395	54841
$P_T \in (0.1, 2.0)$	$M \in (5.0, 8.0)$	$x_F \in (-0.18, 0.94)$	$x_B \in (0.3, 1.0)$	$x_T \in (0.1, 0.2)$	43161	4376	38785
$P_T \in (0.1, 2.0)$	$M \in (5.0, 8.0)$	$x_F \in (-0.18, 0.94)$	$x_B \in (0.3, 1.0)$	$x_T \in (0.2, 0.25)$	92909	9160	83749
$P_T \in (0.1, 2.0)$	$M \in (5.0, 8.0)$	$x_F \in (-0.18, 0.94)$	$x_B \in (0.3, 1.0)$	$x_T \in (0.25, 0.30)$	85206	8561	76645
$P_T \in (0.1, 2.0)$	$M \in (5.0, 8.0)$	$x_F \in (-0.18, 0.94)$	$x_B \in (0.3, 1.0)$	$x_T \in (0.3, 0.6)$	92729	6722	86007

Table 15: After event selection, all data events, combinatorial background events, and signal events are listed.

4 Results

The final step is to extract the angular distributions in the different kinematic regions from the SeaQuest data, as described earlier. We have used only the trigger Roadset-67 data. The real data undergoes the same event selections (discussed in Section 3.3) and unfolding extraction process (discussed in Section 3.5.2), with the exception that background subtraction is required for the real data, as discussed in Section 3.8.

4.1 Steps to Extract the (λ, μ, ν) from Fe (dump) Data

Below are the summarized steps provided for extracting the (λ, μ, ν), as previously mentioned:

- Event selections in the MC events and data events are applied using the selections mentioned in section 3.3.
- Unlike in the MC studies, real data has the combinational background, and it needs to be subtracted from data before unfolding. The subtraction method is given details in section 3.8.
- Reweighted MC is used to build the response matrix. Then, we unfold the 2D $\cos\theta - \phi$ distributions using doubly-iterative Bayesian unfolding. The total retraining of the response matrix is 5, the same as what we did in the simulation study. The total regularization iteration used is 2 (see section 3.5.2).
- Perform the fit using the equation:

$$\frac{dN}{d\Omega} \propto \left[1 + \lambda \cos^2\theta + \mu \sin 2\theta \cos\phi + \frac{\nu}{2} \sin^2\theta \cos 2\phi\right], \tag{23}$$

where we use the fit range for $\cos\theta \in (-0.325, 0.325)$, and full coverage of ϕ. The total number of ϕ and $\cos\theta$ bins are 12 and 18, respectively, the same as what we used in the simulation study.

4.2 Source of Uncertainties in Extracted Parameters

We have conducted numerous systematic studies to address the total uncertainties in the extracted angular distribution parameters. The statistical uncertainty arises from the fit performed using the equation (23), and we denote this by σ_{stat}. Least squares method [21] has been used in the fitting.

These are the possible systematic effects that could affect the unfolded distributions, as discussed previously:

1. MC closure test (see Section 3.7.1): σ_{unfold}.
2. Narrow acceptance of $\cos\theta$ (see Section 3.7.2): σ_{acc}.
3. Secondary beam effects (see Section 3.7.4).
    - Since the contribution of this systematic effect to the unfolded distributions is insignificant, we have not included it in the calculation of the systematic uncertainty.
4. Poor reconstruction around $P_T \approx 0\,\text{GeV}/c$.
    - We have applied a minimum dimuon transverse momentum cut at 0.1 GeV/c. Therefore, we do not need to consider the systematic effect resulting from poor reconstruction at very low transverse momenta.

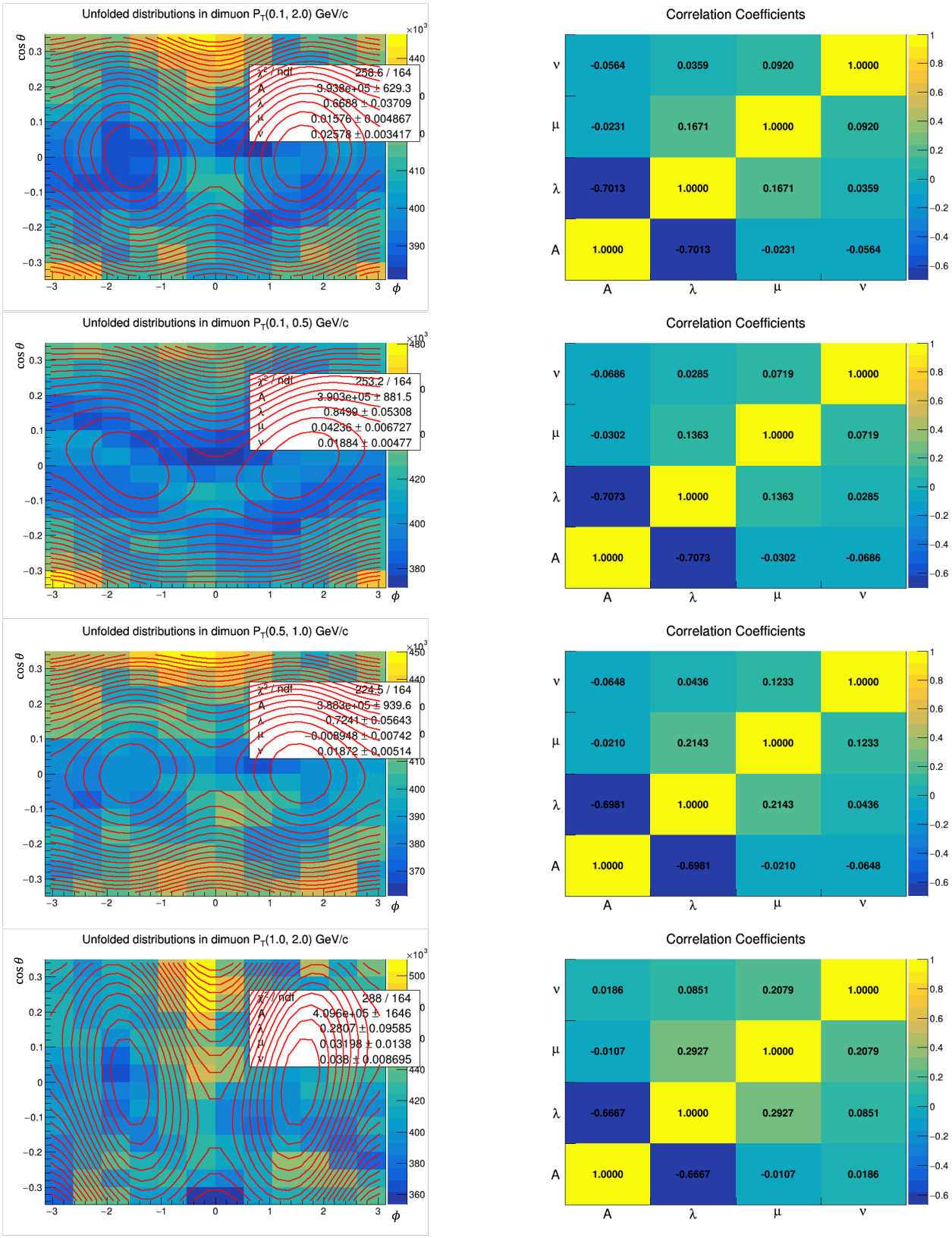

Figure 88: Unfolded Results: The left columns represent the unfolded results in different pT ranges, while the right columns are the corresponding correlation coefficients between the unfolded parameters

Therefore, the the total uncertainty (σ_{tot}) is calculated as follows:

$$\sigma_{\text{tot}} = \sqrt{\sigma^2_{\text{stat}} + (\sigma^2_{\text{unfold}} + \sigma^2_{\text{acc}})}, \tag{24}$$

where:

- σ_{unfold} represents the systematic bias (or uncertainty) from the MC closure test.
- σ_{acc} represents the systematic uncertainty due to the sensitivity of the $cos\theta$ acceptance.

After the unfolding process is completed and a fit is performed, we obtain the extracted parameters along with their statistical uncertainties, which are listed in Figure 88. The results are also tabulated in Table 16 for the central values, statistical uncertainties, and the systematic uncertainties in Table 17.

P_T Range	P_T mean	λ	μ	ν	χ^2/ndf
0.1–0.5	0.32	0.8499 ± 0.0530	0.0424 ± 0.0067	0.0188 ± 0.0048	1.54
0.5–1.0	0.74	0.7241 ± 0.0774	-0.0089 ± 0.0074	0.0187 ± 0.0051	1.37
1.0–2.0	1.30	0.2807 ± 0.0958	0.0320 ± 0.0138	0.0380 ± 0.0087	1.76

Table 16: SeaQuest results for angular coefficients from a two-dimensional fit of $\cos\theta$ vs. ϕ for $p + Fe$ Drell-Yan in the Collins-Soper frame. Uncertainties are statistical only. The response matrix was built within $\cos\theta \in (-0.425, 0.425)$, and the fit was performed within the range $cos\theta \in (-0.325, 0.325)$.

P_T Range	P_T mean	λ		μ		ν	
		σ_{unfold}	σ_{acc}	σ_{unfold}	σ_{acc}	σ_{unfold}	σ_{acc}
0.1–0.5	0.32	0.019	0.054	0.0	0.005	0.021	0.001
0.5–1.0	0.74	0.061	0.057	0.003	0.004	0.006	0.001
1.0–2.0	1.30	0.037	0.085	0.015	0.010	0.003	0.003

Table 17: The systematic uncertainties are taken from the sections 3.7.1, 3.7.2.

4.3 The Lam-Tung (LT) Quantity in SeaQuest

The Lam-Tung quantity can be written as:

$$f(\nu, \lambda) = 2\nu - (1 - \lambda). \tag{25}$$

If $2\nu - (1 - \lambda) = 0$, then the relationship holds, which is also discussed in Section 1.4. Statistical uncertainty for $f(\nu, \lambda)$:

$$\sigma^2_{\text{stat}}(f) = \left(\frac{\partial f}{\partial \nu}\sigma_\nu\right)^2 + \left(\frac{\partial f}{\partial \lambda}\sigma_\lambda\right)^2 + 2\left(\frac{\partial f}{\partial \nu}\sigma_\nu\right)\left(\frac{\partial f}{\partial \lambda}\sigma_\lambda\right)\sigma_{\lambda,\nu}, \tag{26}$$

$$\sigma_{\text{stat}}(f) = \sqrt{4\sigma^2_\nu + \sigma^2_\lambda + 4\sigma_\nu\sigma_\lambda\sigma_{\lambda,\nu}}, \tag{27}$$

where $\sigma_{\lambda,\nu}$ in the above equation represents the covariance between σ_λ, and σ_ν.

Systematic error for $f(\nu, \lambda)$:

$$\sigma_{\text{sys}}(f) = \sqrt{4\sigma^2_\nu + \sigma^2_\lambda}. \tag{28}$$

Using the uncertainties from σ_{unfold} and σ_{acc} from table 17, we calculate the two systematic uncertainties $\sigma_{\text{unfold}}(f)$ and $\sigma_{\text{acc}}(f)$.

The total uncertainty of the LT quantity would be:

$$\sigma_{\text{total}} = \sqrt{\sigma^2_{\text{stat}}(f) + \sigma^2_{\text{unfold}}(f) + \sigma^2_{\text{acc}}(f)}. \tag{29}$$

From the fit results to the unfolded distributions, shown in Figure 88, we have access to the correlation matrix between the parameters (λ, μ, ν), which will be used to calculate the uncertainties for the LT quantity.

From the fit results, we obtain the full covariance matrix for the p_T range $0.1 < p_T < 0.5$ GeV/c.

	A	λ	μ	ν
A	7.628×10^5	-32.34	-0.1767	-0.2838
λ	-32.34	0.002741	4.782×10^{-5}	7.056×10^{-6}
μ	-0.1767	4.782×10^{-5}	4.491×10^{-5}	2.281×10^{-6}
ν	-0.2838	7.056×10^{-6}	2.281×10^{-6}	2.243×10^{-5}

Full covariance matrix in $0.5 < p_T < 1.0$ GeV/c:

	A	λ	μ	ν
A	8.828×10^5	-37.01	-0.1461	-0.313
λ	-37.01	0.003185	8.974×10^{-5}	1.266×10^{-5}
μ	-0.1461	8.974×10^{-5}	5.506×10^{-5}	4.702×10^{-6}
ν	-0.313	1.266×10^{-5}	4.702×10^{-6}	2.642×10^{-5}

Full covariance matrix in $1.0 < p_T < 2.0$ GeV/c:

	A	λ	μ	ν
A	2.71×10^6	-105.2	-0.244	0.2657
λ	-105.2	0.009187	0.0003873	7.092×10^{-5}
μ	-0.244	0.0003873	0.0001905	2.495×10^{-5}
ν	0.2657	7.092×10^{-5}	2.495×10^{-5}	7.56×10^{-5}

Using the Equations (25) to (29), we have extracted Lam-Tung quantity and shown in the Figure 89. The value of the Lam-Tung quantity in the p_T bins:

p_T Range	p_T mean	$2\nu - (1 - \lambda)$		
		Central Value	σ_{stat}	σ_{sys}
0.1–0.5	0.32	-0.113	0.054	0.059
0.5–1.0	0.74	-0.239	0.078	0.084
1.0–2.0	1.30	-0.643	0.097	0.093

Table 18: The central and systematic values are given for the Lam-Tung quantity $2\nu-(1-\lambda)$.

4.4 Extracting ν in different kinematics

Similar to the parameter extraction as a function of P_T, we have also extracted the ν parameter for different kinematic variables. This is to understand how sensitive the $\cos 2\phi$

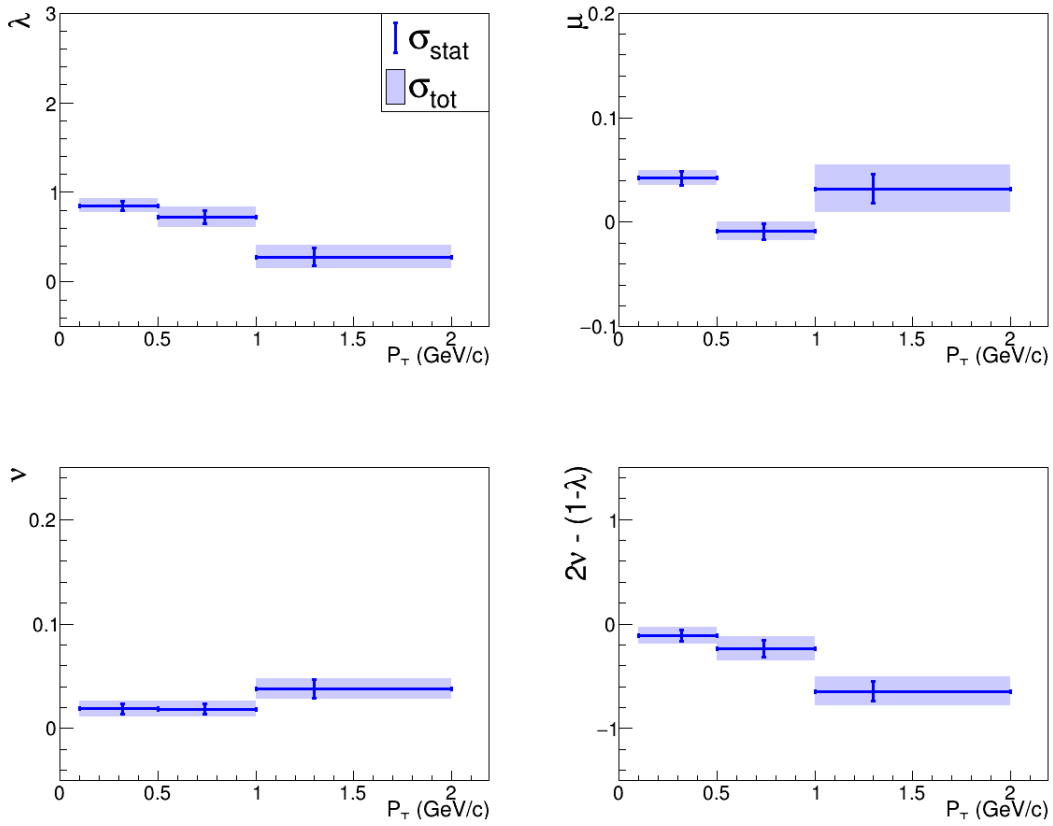

Figure 89: Parameters λ, μ, and ν, and the Lam-Tung quantity $2\nu - (1 - \lambda)$ versus p_T in the Collins-Soper frame. The blue line represents results from SeaQuest $p + Fe$ (Dump target) at 120 GeV when the (LH_2) target was present. The vertical blue error bars are statistical only, and the shaded blue area represents the combination of statistical uncertainty (σ_{stat}) and systematic uncertainties (σ_{unfold}, σ_{acc}).

modulations are in different kinematic regions. To accomplish this, we performed the unfolding process and accounted for all systematic effects. The detailed study is presented in 3.7, where we list these uncertainties in Table 19, including the central value of ν and the statistical uncertainty from the fit results. Parameter ν versus $M_{\mu^+\mu^-}, x_F, x_B$, and x_T in the Collins-Soper frame has been shown in the Figure 90. The blue line represents results from SeaQuest p+Fe(Dump target) at 120 GeV when the (LH_2) target was present. From the ν parameters we can see that, we don't see a strong dependency on different kinematic variables.

All Data	Data Mean	Center Value	σ_{stat}	σ_{unfold}	σ_{acc}
$x_F \in (-0.18, 0.25)$	0.13	**0.025**	0.005	0.000	0.001
$x_F \in (0.25, 0.35)$	0.28	**0.043**	0.008	0.006	0.003
$x_F \in (0.35, 0.45)$	0.40	**0.024**	0.007	0.004	0.003
$x_F \in (0.45, 0.55)$	0.50	**0.033**	0.010	0.017	0.003
$x_F \in (0.55, 0.90)$	0.64	**-0.021**	0.010	0.008	0.002
$M_{\mu^+\mu^-} \in (5.0, 5.5)$	5.22	**0.014**	0.005	0.006	0.004
$M_{\mu^+\mu^-} \in (5.5, 6.0)$	5.71	**0.031**	0.006	0.012	0.002
$M_{\mu^+\mu^-} \in (6.0, 6.5)$	6.21	**0.067**	0.010	0.013	0.003
$M_{\mu^+\mu^-} \in (6.5, 8.0)$	6.90	**0.015**	0.010	0.007	0.001
$x_B \in (0.3, 0.45)$	0.40	**0.041**	0.007	0.013	0.001
$x_B \in (0.45, 0.55)$	0.50	**0.025**	0.005	0.003	0.001
$x_B \in (0.55, 0.65)$	0.60	**0.036**	0.007	0.007	0.002
$x_B \in (0.65, 1.0)$	0.72	**-0.013**	0.008	0.011	0.003
$x_T \in (0.10, 0.20)$	0.18	**-0.017**	0.009	0.019	0.003
$x_T \in (0.20, 0.25)$	0.22	**0.020**	0.006	0.002	0.002
$x_T \in (0.25, 0.30)$	0.27	**0.025**	0.007	0.003	0.002
$x_T \in (0.30, 0.60)$	0.35	**0.044**	0.006	0.003	0.001

Table 19: Uncertainties for different kinematic variables.

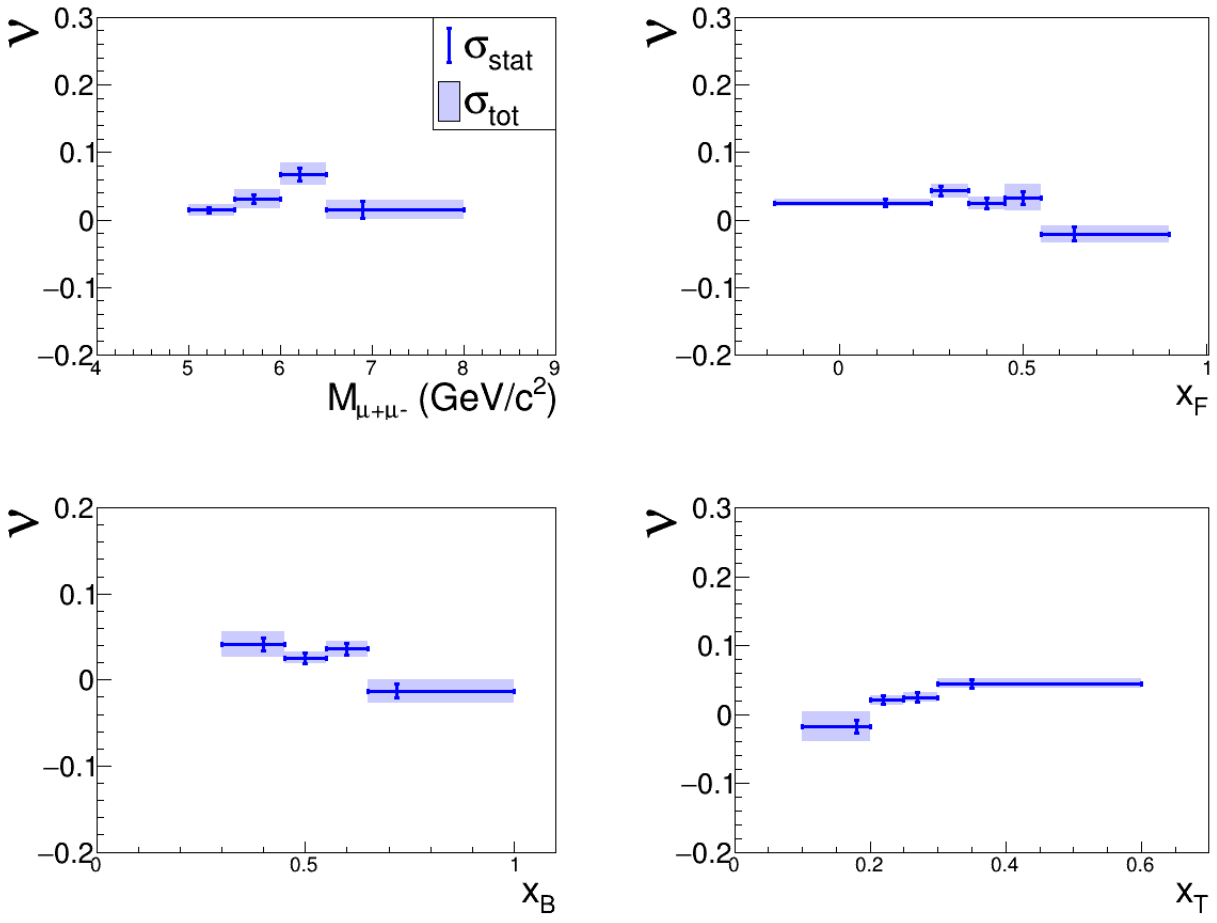

Figure 90: Parameter ν versus $M_{\mu^+\mu^-}, x_F, x_B,$ and x_T in the Collins-Soper frame. The blue line represents results from SeaQuest $p + Fe$ (Dump target) at 120 GeV when the (LH_2) target was present. The vertical blue error bars are statistical only, and the shaded blue area represents the combination of statistical uncertainty (σ_{stat}) and systematic uncertainties (σ_{sys1}, σ_{sys2}).

5 Discussion & Conclusion

5.1 Comparing E906/SeaQuest Proton-induced Drell-Yan Angular Distributions with E866/NuSea

- The extraction of λ from the E906/SeaQuest Drell-Yan $p + \text{Fe}$ angular distributions follows the upper bound of the λ [58, 60]. If $\lambda = 1$, it signifies that the virtual photon is transversely polarized in the rest frame, known as the Collins-Soper frame. The values of λ are as follows:

P_T (GeV/c)	$\lambda \pm$ (stat.) $\pm$ (syst.)
$P_T \in (0.1, 0.5)$	$0.8499 \pm 0.0530 \pm 0.0572$
$P_T \in (0.5, 1.0)$	$0.7241 \pm 0.0774 \pm 0.0835$
$P_T \in (1.0, 2.0)$	$0.2807 \pm 0.0958 \pm 0.0927$

  At low transverse momentum (P_T), λ is close to 1. We also observe as P_T increases, λ decreases. This trend is also predicted by NNLO perturbative QCD [43, 24, 23]. However, for E906/SeaQuest, the rate of decrease in λ value is higher than the predicted values, as shown in Figure 91. Beyond the QCD effect, it is crucial to explore other potential factors, such as nuclear effects, quark energy loss, or any underlying systematic uncertainties that might account for this behavior. The NuSea/E866 experiments shows a similar trend, although in their first P_T bin, λ is slightly larger than the upper bound limit $\lambda < 1.0$.

- From E906/SeaQuest data, the ν parameter is fairly consistent with the E866/NuSea result within the dimuon transverse momentum ($P_T < 2.0$ GeV/c); this means that, like E866/NuSea, E906/SeaQuest does not exhibit a strong $\cos 2\phi$ dependency. The values of ν are as follows:

P_T (GeV/c)	$\nu \pm$ (stat.) $\pm$ (syst.)
$P_T \in (0.1,\ 0.5)$	$0.0188 \pm 0.0048 \pm 0.0061$
$P_T \in (0.5,\ 1.0)$	$0.0187 \pm 0.0051 \pm 0.0061$
$P_T \in (1.0,\ 2.0)$	$0.0380 \pm 0.0087 \pm 0.0040$

Particularly at high x_F, or the higher Bjorken x-Beam (x_B), the Fe data from SeaQuest has $x_F \in (0.55, 0.9)$, ν is $-0.021 \pm 0.010\,(\text{stat.}) \pm 0.008\,(\text{syst.})$, which exhibits a similar trend to the $p+d$ data from E866/NuSea [79], as illustrated in Figure 92. In addition to that, E906/SeaQuest data does not have a strong dependency of ν on the kinematic variables $M_{\mu^+\mu^-}, x_F, x_B$, and x_T. The extracted ν in these kinematics are also consistent with the NNLO perturbative QCD predicted values, as shown in Figure 92. However, at larger P_T, $1.0 < P_T < 2.0$ GeV/c, the ν value from E906/SeaQuest showed a weak dependency, whereas the perturbative NNLO QCD predicted value exhibited a stronger dependency, as shown in Figure 91. Since quark energy loss is significant at higher x_F, as suggested by Ref. [48], the high x_F dimuon yield could be affected by the quark energy loss. An ongoing study in E906/SeaQuest is currently investigating quark energy loss for the Fe target. We may gain a better understanding of the effect once the results are published.

- As we already understand that at larger P_T, ν could be strongly dependent on P_T, it would be very interesting to have more data points of ν at larger P_T. In E906/SeaQuest, the high transverse momentum-based trigger, also known as Trigger FPGA-2, requires the dimuons to be detected in either the top or bottom half of the hodoscope planes. The trigger is heavily prescaled, as shown in the table 9, and therefore we do not have a significant number of events to analyze at transverse momenta larger than 2 GeV/c. Moreover, in the high P_T regions, we have a more combinatorial background than the

low mass regions, requiring special consideration to mitigate any strong systematic effects arising from the background. Additional data points would enhance the understanding of angular distribution trends at high P_T, especially to investigate whether the ν parameter shows strong dependence on $\cos 2\phi$ modulations at high P_T.

- In Figure 91, the NNLO perturbative QCD shows a strong dependence on the $\cos 2\phi$ modulations at large P_T. On the other hand, from the E906/SeaQuest data, we observe a weak $\cos 2\phi$ dependency at low P_T, even around $\approx 2\text{GeV}/c$, suggesting that the Boer-Mulders function could play a role and make the ν parameters show less dependency on high P_T [25]. This perturbative QCD effect should be considered before extracting the Boer-Mulders function. Another important feature of the ν asymmetry is that both E906/SeaQuest and E866/NuSea exhibit smaller ν asymmetry than predicted by QCD, as shown in Figure 91.

- The Lam-Tung relationship is very mildly violated in the dimuon $P_T < 1.0$ GeV/c, but for large P_T, the violation becomes more significant, as shown in Figure 91 and listed below:

P_T (GeV/c)	$(2\nu - (1-\lambda)) \pm$ (stat.) $\pm$ (syst.)
$P_T \in (0.1, 0.5)$	$-0.113 \pm 0.054 \pm 0.059$
$P_T \in (0.5, 1.0)$	$-0.239 \pm 0.078 \pm 0.084$
$P_T \in (1.0, 2.0)$	$-0.643 \pm 0.097 \pm 0.093$

To satisfy the Lam-Tung relationship, the quantity $2\nu - (1-\lambda)$ should equal zero even at higher P_T; however, it does not exhibit this behavior at high P_T. The discrepancy between the NNLO order QCD prediction and the observed Lam-Tung quantity increases at higher P_T, although only a small violation is allowed[5, 64]. This difference

in the data is mainly caused by the ν value not increasing as the λ decreases more rapidly at higher transverse momentum.

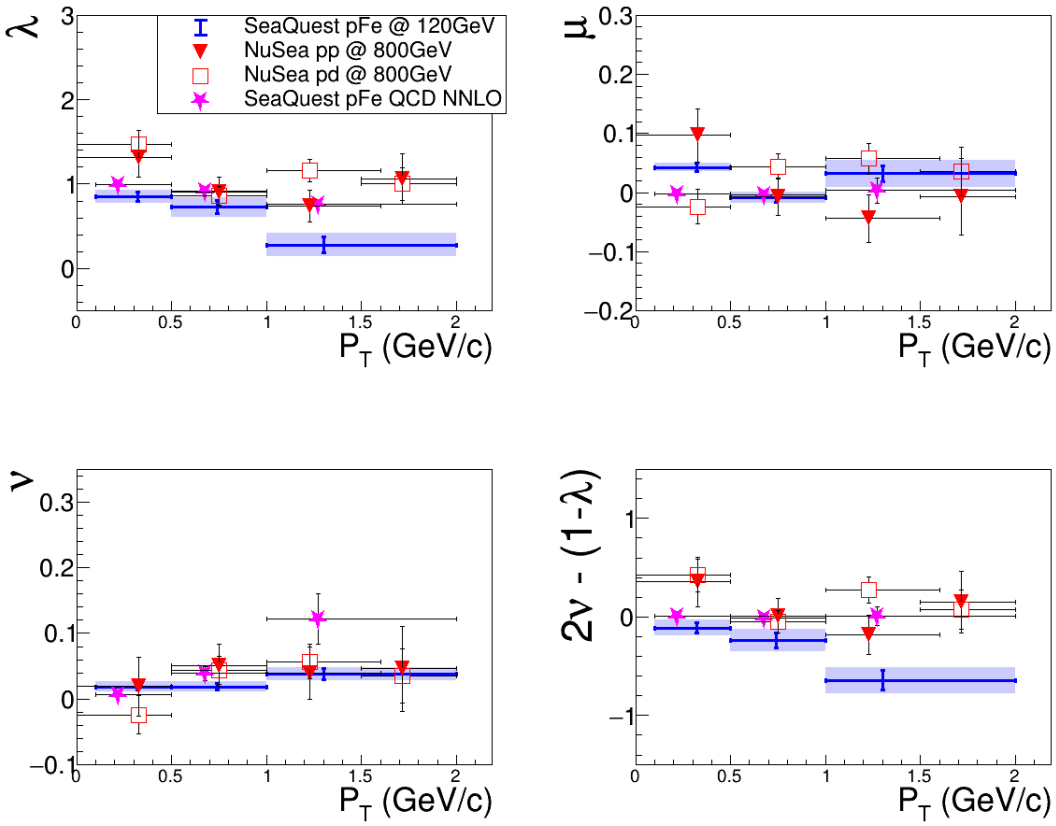

Figure 91: Parameters λ, μ, and ν, and the Lam-Tung quantity $2\nu - (1 - \lambda)$ versus P_T in the Collins-Soper frame. The blue line represents results from SeaQuest $p + Fe$ (dump target) at 120 GeV when the (LH_2) target was present. The vertical blue error bars are statistical only, and the shaded blue area represents the combination of statistical uncertainty (σ_{stat}) and systematic uncertainties (σ_{unfold}, σ_{acc}). The magenta-colored data points represent the NNLO perturbative QCD predicted values of λ, μ, and ν as a function of P_T [43]. The results from the E866 experiments [79, 80] in the $P_T \in (0.0, 2.0) GeV/c$ are also added for comparison.

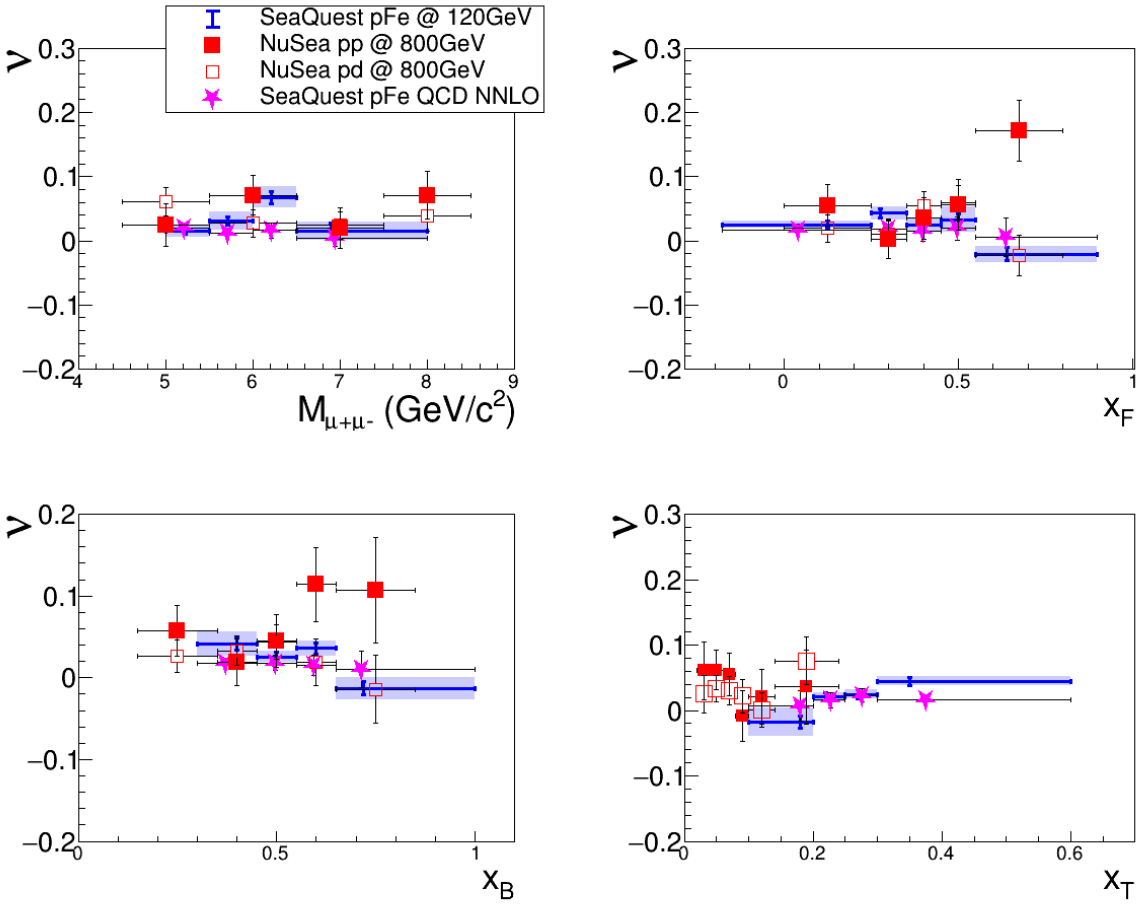

Figure 92: Parameter ν versus $M_{\mu^+\mu^-}, x_F, x_B$, and x_T in the Collins-Soper frame. The blue line represents results from E906/SeaQuest $p + Fe$ (dump target) at 120 GeV when the (LH_2) target was present. The vertical blue error bars are statistical only, and the shaded blue area represents the combination of statistical uncertainty (σ_{stat}) and systematic uncertainties (σ_{sys1}, σ_{sys2}). The magenta-colored data points represent the NNLO perturbative QCD predicted values [43]. The results from the E866 experiments [79, 80] in the $P_T \in (0.0, 2.0) GeV/c$ are also added for comparison.

5.2 Conclusion

E906/SeaQuest is a nuclear physics fixed-target dimuon experiment at Fermilab. In addition to exploring the quark and antiquark structure [35], the experiment has a keen interest in understanding the angular distributions from the proton-induced Drell-Yan process. By measuring the angular distributions from the Drell-Yan process using the nuclear target Fe, we have extended the understanding of the angular distributions. We have extensively studied numerous systematic effects using the Bayesian Iterative Unfolding method to ensure robust measurements. For example, to ensure the RooUnfolding software [21] accurately unfolds angular distributions, we injected various signals into independent Monte Carlo test data. We then verified that the software recovered the injected signals by correcting the detector inefficiency and bin migration. We also have examined the effects of secondary beam hadrons in Drell-Yan dimuon production and their impact on angular distributions. We investigated the effect of narrow detector acceptance by varying the fit ranges in $\cos\theta$. Additionally, we developed a novel method for subtracting combinatorial background, eliminating the need for any fits or floating normalization for background subtraction.

Even though we effectively corrected for detector acceptance and bin migration by constructing robust response matrices, the narrow detector acceptance for $\cos\theta$ introduced a systematic error, which is the largest, approximately $\sigma^{\lambda}_{\text{acc}} \approx (0.05 \text{ to } 0.08)$, as listed in Tables 17. If we can mitigate the significant systematic effects, especially those arising from detector acceptance, it would be worthwhile to add more events from other datasets to enhance the significance of the λ parameter.

We have provided the first complete measurement of Drell-Yan angular distribution using

an unpolarized proton beam and a heavy nuclear target, Fe. We observed very weak $\cos 2\phi$ modulations as a function of the transverse momentum of the dimuon $P_T < 2.0\ GeV/c$, and the results are listed in Table 16. We compared the kinematic dependence to $\cos 2\phi$ modulations, which were found to be weak, plotted in Figure 92, and the central values and the uncertainties are listed in Table 19. We also compared these with NNLO perturbative QCD results, which are plotted in Figures 91 and 92. From the QCD prediction, we have found that λ is strongly dependent on P_T, decreasing with increasing transverse momentum of the dimuon. In the $1.0 < P_T < 2.0$ GeV/c range, the predicted lambda is larger than the extracted lambda. We also found weak dependence of the $\cos 2\phi$ modulations at $1.0 < P_T < 2.0$ GeV/c, where QCD predicts a larger dependency.

Continuing in the long tradition of fixed-target Drell-Yan experiments at Fermilab, the E1039/SpinQuest collaboration [26] will use a 120 GeV proton beam from the Main Injector to extract the angular distributions of dimuons in interactions with polarized NH_3 and ND_3. The main physics motivation is to extract one of the Transverse Momentum-dependent (TMD) distribution functions, known as the Sivers' function [75], through the measurement of transverse single-spin asymmetries (TSSA). Extracting the ν parameter from the experiment with optimizing the trigger, particularly for high transverse momentum ($P_T > 2.0 GeV/c$), would provide insights into the contributions from perturbative QCD and the Boer-Mulder function.

REFERENCES

[1] The RooUnfold package and documentation are available from. URL: https://hepunx.rl.ac.uk/~adye/software/unfold/RooUnfold.html.

[2] A. Accardi et al. Electron Ion Collider: The Next QCD Frontier: Understanding the glue that binds us all. Eur. Phys. J. A, 52(9):268, 2016. arXiv:1212.1701, doi:10.1140/epja/i2016-16268-9.

[3] C. A. Aidala and others (SeaQuest). The SeaQuest Spectrometer at Fermilab. Nucl. Instrum. Meth. A, 930:49–63, 2019. arXiv:1706.09990.

[4] A. Alavi-Harati et al. Measurements of direct CP violation, CPT symmetry, and other parameters in the neutral kaon system. Phys. Rev. D, 67:012005, 2003. [Erratum: Phys.Rev.D 70, 079904 (2004)]. arXiv:hep-ex/0208007, doi:10.1103/PhysRevD.70.079904.

[5] S. Arnold, A. Metz, and M. Schlegel. Dilepton production from polarized hadron hadron collisions. Phys. Rev. D, 79:034005, Feb 2009. URL: https://link.aps.org/doi/10.1103/PhysRevD.79.034005, doi:10.1103/PhysRevD.79.034005.

[6] J. Ashman et al. An Investigation of the Spin Structure of the Proton in Deep Inelastic Scattering of Polarized Muons on Polarized Protons. Nucl. Phys. B, 328:1, 1989. doi:10.1016/0550-3213(89)90089-8.

[7] W. B. Atwood. LEPTON NUCLEON SCATTERING. Prog. Math. Phys., 4:1–114, 11 1979. doi:10.1007/978-1-4899-6691-9_1.

[8] Alessandro Bacchetta, Francesco Conti, and Marco Radici. Transverse-momentum distributions in a diquark spectator model. Phys. Rev. D, 78:074010, 2008. arXiv:0807.0323, doi:10.1103/PhysRevD.78.074010.

[9] W. Bartel, B. Dudelzak, H. Krehbiel, J. McElroy, U. Meyer-Berkhout, W. Schmidt, V. Walther, and G. Weber. Electroproduction of pions near the $\Delta(1236)$ isobar and the form-factor $G_M^*(q^2)$ of the $(\gamma N\Delta)$ vertex. Phys. Lett. B, 28:148–151, 1968. doi:10.1016/0370-2693(68)90155-X.

[10] J. D. Bjorken. Asymptotic sum rules at infinite momentum. Phys. Rev., 179:1547–1553, Mar 1969. URL: https://link.aps.org/doi/10.1103/PhysRev.179.1547, doi:10.1103/PhysRev.179.1547.

[11] J. D. Bjorken and E. A. Paschos. Inelastic electron-proton and γ-proton scattering and the structure of the nucleon. Phys. Rev., 185:1975–1982, Sep 1969. URL: https://link.aps.org/doi/10.1103/PhysRev.185.1975, doi:10.1103/PhysRev.185.1975.

[12] J. D. Bjorken and E. A. Paschos. Inelastic Electron-Proton and γ-Proton Scattering and the Structure of the Nucleon. Phys. Rev, 185, 1975. https://journals.aps.org/pr/abstract/10.1103/PhysRev.185.1975. doi:10.1016/S0168-9002(01)02005-8.

[13] E. D. Bloom, D. H. Coward, H. DeStaebler, J. Drees, G. Miller, L. W. Mo, R. E. Taylor, M. Breidenbach, J. I. Friedman, G. C. Hartmann, and H. W. Kendall. High-energy inelastic $e-p$ scattering at 6° and 10°. Phys. Rev. Lett., 23:930–934, Oct 1969. URL: https://link.aps.org/doi/10.1103/PhysRevLett.23.930, doi:10.1103/PhysRevLett.23.930.

[14] D. Boer and P. J. Mulders. Time-reversal odd distribution functions in leptoproduction. Phys. Rev. D, 57:5780–5786, May 1998. URL: https://link.aps.org/doi/10.1103/PhysRevD.57.5780, doi:10.1103/PhysRevD.57.5780.

[15] D. Boer and W. Vogelsang. Drell-Yan Lepton Angular Distribution at Small Transverse Momentum. arXiv:hep-ph/0604177.

[16] Daniel Boer. Investigating the origins of transverse spin asymmetries at RHIC. Phys. Rev. D, 60:014012, 1999. arXiv:hep-ph/9902255, doi:10.1103/PhysRevD.60.014012.

[17] Daniel Boer and P. J. Mulders. Time reversal odd distribution functions in leptoproduction. Phys. Rev. D, 57:5780–5786, 1998. arXiv:hep-ph/9711485, doi:10.1103/PhysRevD.57.5780.

[18] W Bokhari, J. G. Heinrich, N. S. Lockyer, and F. M. Newcomer. The asdq asic [central outer tracker cdf upgrade application]. 1998 IEEE Nuclear Science Symposium Conference Record. 1998 IEEE Nuclear Science Symposium and Medical Imaging Conference (Cat. No.98CH36255), 1:445–446 vol.1, 1998. URL: https://ieeexplore.ieee.org/document/775180.

[19] M. Breidenbach, J. I. Friedman, H. W. Kendall, E. D. Bloom, D. H. Coward, H. DeStaebler, J. Drees, L. W. Mo, and R. E. Taylor. Observed behavior of highly inelastic electron-proton scattering. Phys. Rev. Lett., 23:935–939, Oct 1969. URL: https://link.aps.org/doi/10.1103/PhysRevLett.23.935, doi:10.1103/PhysRevLett.23.935.

[20] Stanley J. Brodsky and Feng Yuan. Single transverse-spin asymmetries at large x. Phys. Rev. D, 74:094018, Nov 2006. URL: https://link.aps.org/doi/10.1103/PhysRevD.74.094018, doi:10.1103/PhysRevD.74.094018.

[21] R. Brun and F. Rademakers. ROOT: An object oriented data analysis framework. Nucl. Instrum. Meth. A, 389:81–86, 1997. doi:10.1016/S0168-9002(97)00048-X.

[22] C. G. Callan and David J. Gross. High-energy electroproduction and the constitution of the electric current. Phys. Rev. Lett., 22:156–159, Jan 1969. URL: https://link.aps.org/doi/10.1103/PhysRevLett.22.156, doi:10.1103/PhysRevLett.22.156.

[23] Stefano Catani, Leandro Cieri, Giancarlo Ferrera, Daniel de Florian, and Massimiliano Grazzini. Vector boson production at hadron colliders: A fully exclusive qcd calculation at next-to-next-to-leading order. Phys. Rev. Lett., 103:082001, Aug 2009. URL: https://link.aps.org/doi/10.1103/PhysRevLett.103.082001, doi:10.1103/PhysRevLett.103.082001.

[24] Stefano Catani and Massimiliano Grazzini. Next-to-next-to-leading-order subtraction formalism in hadron collisions and its application to higgs-boson production at the large hadron collider. Phys. Rev. Lett., 98:222002, May 2007. URL: https://link.aps.org/doi/10.1103/PhysRevLett.98.222002, doi:10.1103/PhysRevLett.98.222002.

[25] Wen-Chen Chang, Randall Evan McClellan, Jen-Chieh Peng, and Oleg Teryaev. Lepton angular distributions of fixed-target drell-yan experiments in perturbative qcd and a geometric approach. Phys. Rev. D, 99:014032, Jan 2019. URL: https://link.aps.org/doi/10.1103/PhysRevD.99.014032, doi:10.1103/PhysRevD.99.014032.

[26] Andrew Chen et al. Probing nucleon's spin structures with polarized Drell-Yan in the Fermilab SpinQuest experiment. PoS, SPIN2018:164, 2019. arXiv:1901.09994, doi:10.22323/1.346.0164.

[27] P. Chiappetta and M. Le Bellac. Angular Distribution of Lepton Pairs in Drell-Yan Like Processes. Z. Phys. C, 32:521, 1986. doi:10.1007/BF01550774.

[28] J. H. Christenson, G. S. Hicks, L. M. Lederman, P. J. Limon, B. G. Pope, and E. Zavattini. Observation of massive muon pairs in hadron collisions. Phys. Rev. Lett., 25:1523–1526, 1970. doi:10.1103/PhysRevLett.25.1523.

[29] J. Cleymans and M. Kuroda. Comparison of angular distributions in $\pi^- n \to \mu^+\mu^- + \ldots$ with lowest order qcd. Physics Letters B, 105(1):68–70, 1981. URL: https://www.sciencedirect.com/science/article/pii/0370269381900435, doi:10.1016/0370-2693(81)90043-5.

[30] John C. Collins. Simple prediction of quantum chromodynamics for angular distribution of dileptons in hadron collisions. Phys. Rev. Lett., 42:291–294, Jan 1979. URL: https://link.aps.org/doi/10.1103/PhysRevLett.42.291, doi:10.1103/PhysRevLett.42.291.

[31] John C. Collins and Davison E. Soper. Angular distribution of dileptons in high-energy hadron collisions. Phys. Rev. D, 16:2219–2225, Oct 1977. URL: https://link.aps.org/doi/10.1103/PhysRevD.16.2219, doi:10.1103/PhysRevD.16.2219.

[32] John C. Collins and Davison E. Soper. Parton Distribution and Decay Functions. Nucl. Phys. B, 194:445–492, 1982. doi:10.1016/0550-3213(82)90021-9.

[33] J. S. Conway et al. Experimental Study of Muon Pairs Produced by 252-GeV Pions on Tungsten. Phys. Rev. D, 39:92–122, 1989. doi:10.1103/PhysRevD.39.92.

[34] Paul A. M. Dirac. The quantum theory of the electron. Proc. Roy. Soc. Lond. A, 117:610–624, 1928. doi:10.1098/rspa.1928.0023.

[35] J. Dove et al. The asymmetry of antimatter in the proton. Nature, 590(7847):561–565, 2021. [Erratum: Nature 604, E26 (2022)]. arXiv:2103.04024, doi:10.1038/s41586-022-04707-z.

[36] S. D. Drell and Tung-Mow Yan. Massive Lepton Pair Production in Hadron-Hadron Collisions at High-Energies. Phys. Rev. Lett., 25:316–320, 1970. [Erratum: Phys.Rev.Lett. 25, 902 (1970)]. doi:10.1103/PhysRevLett.25.316.

[37] G. D'Agostini. Improved iterative Bayesian unfolding. arXiv:1010.0632.

[38] G. D'Agostini. A multidimensional unfolding method based on Bayes. Nucl. Instrum. Meth. A, 362:487–498, 1994.

[39] I. Estermann, O. C. Simpson, and O. Stern. The magnetic moment of the proton. Phys. Rev., 52:535–545, Sep 1937. URL: https://link.aps.org/doi/10.1103/PhysRev.52.535, doi:10.1103/PhysRev.52.535.

[40] C. Morris et al. Tomographic imaging with cosmic ray muons. Science and Global Security, 930:37–53, 2008.

[41] J. Pumplin et al. New Generation of Parton Distributions with Uncertainties from Global QCD Analysis. JHEP, 012:0247, 2002.

[42] S.-H. Shiu et al. FPGA-based trigger system for the Fermilab SeaQuest experiment. FERMILAB-THESIS-2019-12, 802:82–88, 2015. doi:10.1016/j.nima.2015.09.001.

[43] Stephen Pate et al. DYNNLO Calculation of DY Angular Coefficients. 2024. docdb:10771.

[44] Professor Sir E. Rutherford F. R. S. LIV. Collision of α particles with light atoms. IV. An anomalous effect in nitrogen. Phil. Mag. Ser. 6, 37(222):581–587, 1919. doi:10.1080/14786440608635919.

[45] S. Falciano et al. Angular Distributions of Muon Pairs Produced by 194-GeV/c Negative Pions. Z. Phys. C, 31:513, 1986. doi:10.1007/BF01551072.

[46] R. W. Fast, E. W. Bosworth, C. N. Brown, A. M. Glowacki, J. M. Jagger, S. P. Sobczynski, and D. A. Finley. 14.4-m Large Aperture Analysis Magnet with Aluminum Coils. IEEE Trans. Magnetics, 17:1903–1906, 1981. URL: https://lss.fnal.gov/archive/test-tm/1000/fermilab-tm-1034.pdf, doi:10.1109/TMAG.1981.1061361.

[47] Richard P. Feynman. Very high-energy collisions of hadrons. Phys. Rev. Lett., 23:1415–1417, Dec 1969. URL: https://link.aps.org/doi/10.1103/PhysRevLett.23.1415, doi:10.1103/PhysRevLett.23.1415.

[48] Sean Gavin and Joseph Milana. Energy loss at large x_f in nuclear collisions. Phys. Rev. Lett., 68:1834–1837, Mar 1992. URL: https://link.aps.org/doi/10.1103/PhysRevLett.68.1834, doi:10.1103/PhysRevLett.68.1834.

[49] Murray Gell-Mann. The Eightfold Way: A Theory of strong interaction symmetry. 3 1961. doi:10.2172/4008239.

[50] Murray Gell-Mann. A Schematic Model of Baryons and Mesons. Phys. Lett., 8:214–215, 1964. doi:10.1016/S0031-9163(64)92001-3.

[51] S. Gorbunov and I. Kisel. Primary vertex fit based on the Kalman filter. CBM-SOFT-note-2006-001, 2006.

[52] M. Guanziroli et al. Angular Distributions of Muon Pairs Produced by Negative Pions on Deuterium and Tungsten. Z. Phys. C, 37:545, 1988. URL: https://link.springer.com/article/10.1007/BF01549713, doi:10.1007/BF01549713.

[53] E. A. Hawker et al. Measurement of the light anti-quark flavor asymmetry in the nucleon sea. Phys. Rev. Lett., 80:3715–3718, 1998. URL: https://journals.aps.org/prl/abstract/10.1103/PhysRevLett.80.3715, arXiv:hep-ex/9803011, doi:10.1103/PhysRevLett.80.3715.

[54] Robert Hofstadter and Robert W. McAllister. Electron scattering from the proton. Phys. Rev., 98:217–218, Apr 1955. URL: https://link.aps.org/doi/10.1103/PhysRev.98.217, doi:10.1103/PhysRev.98.217.

[55] R.L. Jaffe and Aneesh Manohar. The g1 problem: Deep inelastic electron scattering and the spin of the proton. Nuclear Physics B, 337(3):509–546, 1990. URL: https://www.sciencedirect.com/science/article/pii/0550321390905069, doi:10.1016/0550-3213(90)90506-9.

[56] E. Jastrzembski. Trigger Supervisor v2 (TS), JLab.

[57] J. Kubar, M. Le Bellac, J. L. Meunier, and G. Plaut. QCD Corrections to the Drell-

Yan Mechanism and the Pion Structure Function. Nucl. Phys. B, 175:251–275, 1980. doi:10.1016/0550-3213(80)90053-X.

[58] C. S. Lam and Wu-Ki Tung. Systematic approach to inclusive lepton pair production in hadronic collisions. PhysRevD.18.2447.

[59] C. S. Lam and Wu-Ki Tung. Parton-model relation without quantum-chromodynamic modifications in lepton pair production. Phys. Rev. D, 21:2712–2715, May 1980. URL: https://link.aps.org/doi/10.1103/PhysRevD.21.2712, doi:10.1103/PhysRevD.21.2712.

[60] Martin Lambertsen and Werner Vogelsang. Drell-yan lepton angular distributions in perturbative qcd. Phys. Rev. D, 93:114013, Jun 2016. URL: https://link.aps.org/doi/10.1103/PhysRevD.93.114013, doi:10.1103/PhysRevD.93.114013.

[61] Kun Liu. Step-by-step walkthrough of kTracker. docdb:1283, 2015.

[62] R. W. McAllister and R. Hofstadter. Elastic scattering of 188-mev electrons from the proton and the alpha particle. Phys. Rev., 102:851–856, May 1956. URL: https://link.aps.org/doi/10.1103/PhysRev.102.851, doi:10.1103/PhysRev.102.851.

[63] Randall Evan McClellan. Angular Distributions of High-Mass Dilepton Production in Hadron Collisions. FERMILAB-THESIS-2016-14, 2016. doi:10.2172/1294516.

[64] E. Mirkes and J. Ohnemus. Angular distributions of Drell-Yan lepton pairs at the Tevatron: Order $\alpha - s^2$ corrections and Monte Carlo studies. Phys. Rev. D, 51:4891–4904, 1995. arXiv:hep-ph/9412289, doi:10.1103/PhysRevD.51.4891.

[65] Shou Miyasaka. Study of Vertex Finding Method in kTracker. docdb:1185, 2015.

[66] G. Moreno et al. Dimuon production in proton - copper collisions at $\sqrt{s}$ = 38.8-GeV. Phys. Rev. D, 43:2815–2836, 1991. URL: https://journals.aps.org/prd/abstract/10.1103/PhysRevD.43.2815, doi:10.1103/PhysRevD.43.2815.

[67] Kei Nagai. Recent Measurement of Flavor Asymmetry of Antiquarks in the Proton by Drell–Yan Experiment SeaQuest at Fermilab, Ph.D. thesis, Rutgers U. FERMILAB-THESIS-2017-05, 2017. doi:10.2172/1346822.

[68] Kenichi Nakano. Effect of Hadronic Interaction in Dump on Beam Proton. 2023. docdb:10678.

[69] Yuval Ne'eman. Derivation of strong interactions from a gauge invariance. Nucl. Phys., 26:222–229, 1961. doi:10.1016/0029-5582(61)90134-1.

[70] S. F. Pate et al. Estimation of combinatoric background in seaquest using an event-mixing method. JINST, 18(10):P10032, 2023. arXiv:2302.04152, doi:10.1088/1748-0221/18/10/P10032.

[71] B. Povh, K. Rith, C. Scholz, and F. Zetsche. Particles and Nuclei. An Introduction into the Physical Concepts. Germany, Jul 2006. doi:10.1007/3-540-36686-5.

[72] Paul E. Reimer. Exploring the Partonic Structure of Hadrons through the Drell-Yan Process. J. Phys. G, 34:S107–S126, 2007. arXiv:0704.3621, doi:10.1088/0954-3899/34/7/S06.

[73] Caroline Riedl. Probing nucleon spin structure in deep-inelastic scattering, proton-proton collisions and Drell-Yan processes. Acta Phys. Polon. B, 53:5–A2, 2022. arXiv:2204.03684, doi:10.5506/APhysPolB.53.5-A2.

[74] A. Rogozhnikov. Reweighting with Boosted Decision Trees. J. Phys. Conf. Ser., 762(1):012036, 2016. arXiv:1608.05806, doi:10.1088/1742-6596/762/1/012036.

[75] Dennis Sivers. Single-spin production asymmetries from the hard scattering of pointlike constituents. Phys. Rev. D, 41:83–90, Jan 1990. URL: https://link.aps.org/doi/10.1103/PhysRevD.41.83, doi:10.1103/PhysRevD.41.83.

[76] A. S. Tadepalli. Light anti–quark flavor asymmetry in the nucleon sea and the nuclear dependence of anti–quarks in nuclei at the SeaQuest Experiment, Ph.D. thesis, Rutgers U. FERMILAB-THESIS-2019-12, 2019. doi:10.2172/1574838.

[77] O. V. Teryaev. Kinematic azimuthal asymmetries and lam-tung relation, 2020. arXiv:2012.11720.

[78] Bing Zhang, Zhun Lu, Bo-Qiang Ma, and Ivan Schmidt. Extracting Boer-Mulders functions from p+D Drell-Yan processes. Phys. Rev. D, 77:054011, 2008. arXiv:0803.1692, doi:10.1103/PhysRevD.77.054011.

[79] L. Y. Zhu et al. Measurement of Angular Distributions of Drell-Yan Dimuons in p + d Interaction at 800-GeV/c. Phys. Rev. Lett., 99:082301, 2007. arXiv:hep-ex/0609005, doi:10.1103/PhysRevLett.99.082301.

[80] L. Y. Zhu et al. Measurement of Angular Distributions of Drell-Yan Dimuons in p + p Interactions at 800-GeV/c. Phys. Rev. Lett., 102:182001, 2009. arXiv:0811.4589, doi:10.1103/PhysRevLett.102.182001.

[81] L. Y. Zhu et al. Measurement of angular distributions of drell-yan dimuons in $p + p$ interactions at 800 GeV/c. Phys. Rev. Lett., 102:182001, May 2009. URL: https://

link.aps.org/doi/10.1103/PhysRevLett.102.182001, doi:10.1103/PhysRevLett.102.182001.

[82] G. Zweig. An SU(3) model for strong interaction symmetry and its breaking. Version 1. 1 1964.

[83] G Zweig. An SU_3 model for strong interaction symmetry and its breaking; Version 2. 1964. URL: https://cds.cern.ch/record/570209, doi:10.17181/CERN-TH-412.